Fundamental Concepts Associated with Hydraulic Seals for High Bandwidth Actuation

Bullock, Arthur

Award date:
2010

Awarding institution:
University of Bath

Fundamental Concepts Associated with Hydraulic Seals for High Bandwidth Actuation

submitted by

Arthur Bullock

for the degree of Doctor of Philosophy

of the

University of Bath

Department of Mechanical Engineering

July 2010

Abstract

This thesis is concerned with issues relating to the development of an active sealing system for hydraulic actuators where the sealing elements can be radially extended and retracted to vary the friction and leakage characteristics. In order to determine the feasibility of the active sealing concept it is necessary to establish that varying the seal geometry may achieve useful improvements in the friction-leakage trade-off and that a practical method of achieving this seal extension can be realised. Experimental and simulation approaches for seal friction prediction have been developed and active seal prototypes produced to demonstrate the concept.

Experiments were carried out to measure the constant velocity friction for single-lip and double-lip seals over a range of sliding speeds and sealed pressures with special consideration applied to the instroke-outstroke direction dependence. Additional experiments were performed with sinusoid motion to provide an indication of the transient friction characteristics. Friction was shown to increase towards the end of the outstroke cycle and decrease once the instroke motion began.

Tribology simulations were produced based on the results of a FEA simulation of the rod-seal contact pressure. Empirical friction-load relationships and novel contact mechanics approaches for high loads were considered. Simulations based on the Reynolds equation including standard inverse EHL theory and the GW-average Reynolds lubrication are also presented. Experimental agreement could be improved if loading is assumed to transfer to the fluid to maintain a fluid film. A hysteresis friction model was also developed in attempt to improve the prediction of speed dependent friction.

Two active seal prototypes were produced, each with an adjustable external pressure supplied to the outer circumference of the sealing element. Constant velocity friction measurements for different external pressures and the transient response following step changes in this pressure are presented.

Acknowledgements

I would like to express my appreciation for the guidance and support of my supervisors Prof Patrick Keogh, Dr Derek Tilley, Dr D Nigel Johnston and Dr Chris Bowen, my internal examiners Dr Andrew Hillis and Dr Jos Darling and my professional colleague Dr David Branson. I would also like to extend my sincere thanks to Andrew Galloway, Joe Wankowski, Ian Trussler, Stephen Coombes and Viyay Rajput for their technical assistance and advice over the course of this project.

I am also thankful for the support and companionship of my family and friends during this research.

This research has been made possible by the financial support of the Engineering and Physical Sciences Research Council. I am most grateful for being granted the opportunity to explore the scientific and technical issues within this field.

Contents

Nomenclature

a	Hertzian contact radius
a_c	Contact area
c	Effective damping coefficient of element
g	Normal reaction force
h	Film thickness
h_a	Film at critical location on EHL pressure distribution
h_m	Constant of integration in inverse EHL solution to film thickness distribution
h_s	Static film thickness
h_x	Dimensionless mesh spacing parallel to motion
h_y	Dimensionless mesh spacing perpendicular to motion
h_T	Truncated film thickness
k	Effective stiffness of element
m	Effective mass of element
p_c	Asperity contact pressure
p_f	Fluid pressure
p_h	Maximum Hertzian pressure
p_{sc}	Static contact pressure
u	Rod sliding speed
w	Normal reaction force
x	Axial distance along contact length
y	Axial distance along surface parallel to direction of motion
A_c	Real area of contact
A_0	Nominal area of contact
D	Rod diameter
E	Elastic modulus
E^*	Alternative elastic modulus $\frac{E}{1-\nu^2}$
E'	Storage modulus
E''	Loss modulus
G	Shear modulus
H	Dimensionless film thickness wrt roughness height $\frac{h}{\sigma_h}$

H_s	Dimensionless static film thickness wrt roughness height $\frac{h_s}{\sigma}$
H_T	Dimensionless truncated film thickness wrt roughness height $\frac{h_T}{\sigma}$
L	Dimensionless Moes speed parameter $G(2U)^{\frac{1}{4}}$
L_1	Asperity peak spacing
L_x	Axial contact length between seal and rod
L_y	Effective depth of seal for shear deformation
P_c	Dimensionless asperity contact pressure $\frac{p_c}{p_{atm}}$
P_f	Dimensionless fluid pressure $\frac{p_f}{p_{atm}}$
P_{sc}	Dimensionless static contact pressure $\frac{p_{sc}}{p_{atm}}$
P_t	Dimensionless combined pressure $\frac{p_t}{p_{atm}}$
Q	Frictional shear force
R	Asperity radius
U	Dimensionless speed parameter $\frac{\eta_0 u\left(1-\nu^2\right)}{4RE}$
X	Dimensionless distance along surface in direction of motion wrt contact radius $\frac{x}{a}$
Y	Dimensionless distance along surface parallel to motion wrt contact radius $\frac{y}{a}$
α	Pressure-viscosity coefficient
ϵ	Elastic strain
γ	Shear strain
ζ	Damping ratio
η	Asperity density
η	Kinematic viscosity
η_0	Kinematic viscosity at gauge pressure
ν	Poisson ratio
σ	Elastic stress
σ_h	Asperity height
ϕ_{fs}	Patir-Cheng shear stress factor
ϕ_{fp}	Patir-Cheng shear stress factor
ϕ_x	Patir-Cheng pressure factor
$\phi_{s,c}$	Patir-Cheng shear flow factor
τ	Frictional shear stress
ω	Excitation frequency
ω_n	Natural frequency
Δ	Dimensionless asperity deflection $\frac{\delta}{R}$
Ω	Data recording frequency
Ω_n	Data sampling frequency
$\hat{x}$	Dimensionless axial coordinate wrt contact length $\frac{x}{L_x}$
$\hat{\alpha}$	Dimensionless pressure-viscosity coefficient $p_{atm}\alpha$

Chapter 1

Introduction

1.1 Existing hydraulic actuation systems

The research undertaken was part of a three year EPSRC research project "IntAct- Integrated Piezoelectric-Hydraulic Actuator." This overall project was concerned with developing a single actuation system capable of both high static positioning accuracy and high dynamic performance that cannot currently be obtained from any single actuation system. It was sought to develop a system with high bandwidth and rapid step responses to changes in demand position and velocity. This same system was also desired to have favourable static positioning performance where the system would be capable of actuating a load through relatively long strokes with sub-micron accuracy.

Existing hydraulic actuators are able to actuate loads through long strokes and there are few alternatives where strokes of tens or hundreds of millimetres are required together with high forces of the order of 1 kN. Most conventional hydraulic systems have been limited to a positioning accuracy of 10 μm, although a recent investigation by Habibi [1] was able to achieve a significantly improved positioning accuracy of 0.1 μm against an inertia load over a relatively long stroke of 120 mm. This improvement in positioning accuracy was achieved using an adapted electrohydraulic system where a variable speed electric motor was used to drive a fixed displacement gear pump to supply fluid to a cylinder. The cylinder used was a non-standard design reported in [2] where the rod was hollowed out and the pressure to extend the rod was applied to the inside face of the rod. This new actuation system was reported to have a rise time of 0.3 s associated with its response to a step change in position demand, which suggests a reasonable degree of dynamic performance in static positioning.

Hydraulic actuators are generally limited in frequency response by the dynamics of control valves and the compressibility of the fluid. Valve dynamics limit the frequency response when the valve is unable to open fully at higher frequencies and reduced flow rates are supplied to the hydraulic cylinder. Standard servovalves are typically limited to frequencies

of approximately 150 Hz, although certain specialist models of servovalve are available with higher bandwidth. Fluid compressibility results in a loss in the flow supplied to the cylinder, reducing the displacements produced by the actuator. Compressibility losses become more significant relative to the overall flow at higher frequencies where the displacement amplitudes are lower and the flow supplied to the cylinder during each cycle is also reduced. Typical hydraulic systems are not directly suitable for high frequency applications. The current project was partially concerned with how the bandwidth of a hydraulic actuation system could be extended to higher frequencies.

1.2 Current investigation within larger research project

Within the EPSRC project, three key research areas were proposed for improving the combined static and dynamic performance of a hydraulic actuation system. The first was concerned with modifying the control valve to improve its frequency response. It was proposed to achieve this using piezoelectric actuators to displace the valve spool to allow operation at frequencies in the kilohertz range. The main constraint for using piezoelectric actuators to open and close the valve is their limited stroke. In order to achieve the flow rates required it is necessary to either mechanically amplify the displacements or to pursue a valve design that could achieve higher flow rates for a particular spool displacement than conventional valve designs. The second key area focused on mounting fluid displacement devices inside the cylinder to supply the small flow volumes required to produce high frequency actuation. The final key area involved the development of active sealing systems where the piston and rod seals would have adjustable extension. This could improve actuator performance in load cycles involving high speed motion where the use of standard seal types can be problematic. This thesis is concerned with the active seal area of the overall project.

The active sealing research area involves the concept of a hydraulic seal capable of extending and retracting radially to vary the interference or clearance between the seal and rod/housing. Use of an active seal may be able to improve system performance by enabling adjustment of the seal friction and leakage characteristics. Compressing the seal against the housing with a high force would be expected to minimise fluid leakage while increasing the friction level. Retracting the seal to reduce rod-seal interference or produce a clearance would result in low friction and relatively high leakage. It may be possible to use active seals in high speed applications to reduce leakage and improve positioning accuracy and dynamic performance of such actuators. Active seals could also be used to minimise power loss due to friction and improve system efficiency.

1.3 Motivation of current investigation

Part of the active seal research involves the design, commissioning and testing of active seal concepts. This is required to demonstrate whether it is technically feasible to adjust the friction and leakage of a hydraulic seal by varying the seal extension. Firstly, it was necessary to identify a suitable design concept for extending and retracting the sealing element and design a suitable test rig utilising the concept. Once the test rig was produced and commissioned, experimental measurements of the friction levels were obtained for changes in seal extension. Demonstrating that an active sealing concept can be used to vary the friction of a hydraulic seal represents progress towards a deployable active sealing system.

In order to determine the feasibility of the active sealing concept it is necessary to quantify how the friction and leakage can be varied by adjusting the seal extension in addition to demonstrating that these types of adjustments are possible. For high speed applications it is necessary to determine how far positioning accuracy and dynamic performance could be improved by reducing leakage. For efficiency gains in general applications it is necessary to determine how far seal friction can be reduced while maintaining satisfactory sealing performance.

Developing tribology models for seal friction and leakage would allow the behaviour of different types of passive and active seals to be analysed without having to commission additional test rigs. Producing a general simulation for seal tribology may also be useful as a design tool for sealing elements, allowing the performance of different designs to be evaluated more quickly and cost-effectively than with experimentation. It is also desirable to validate the effectiveness of existing tribology models for seal friction to determine whether these techniques could usefully be applied to the current investigation.

This thesis is concerned with progress towards the development of active sealing systems and the tribology of hydraulic seals that relates to the feasibility of the active seal concept. Part of this study focuses on the development and evaluation of models of the tribology behaviour of hydraulic seals in attempt to allow predictions to be made concerning how friction and leakage could usefully be varied in sealing systems. It is also desired to demonstrate that the active sealing can be achieved in practice and to identify and explore the issues associated with practical active seals.

1.4 Aims and objectives

There are three main aspects of the current research; active seal development and the experimental and theoretical investigation of seal tribology. For the active seal area it was sought to demonstrate the feasibility of adjusting the radial seal extension to vary the friction characteristics. It was also desired to gain insights into how the friction characteristics respond

to changes in seal extension and how useful this is for practical applications.

One of the aims for the experiments with passive seals was to verify previous investigations into hydraulic seal tribology and for the apparatus and procedures to serve as a basis for the active seal friction measurements. Established seal friction characteristics were also to be expanded on to include more detail on the direction dependence of friction, which is of particular importance for friction prediction.

The theoretical parts of the current research looked to evaluate the effectiveness of current tribology models for seal friction prediction and determine those that are more appropriate. Additionally, it was sought to develop the existing modelling techniques to improve friction prediction.

The objectives were:

- Produce and commission passive seal test rig and measure passive seal friction characteristics.
- Validate friction predictions of existing tribology models for passive seals.
- Develop alternative tribology simulation tools for predicting seal friction and leakage and verify against experimental data.
- Investigate seal friction during sinusoid motion of seal and relate to constant velocity cases.
- Produce and commission prototype of active rod seal.
- Experimentally demonstrate concept of extendable active hydraulic seal.
- Experimentally investigate steady-state behaviour of active seal under different geometry extensions.
- Investigate dynamic characteristics of active seal to changes in geometry.

1.5 Scope of thesis

Chapter 2 is concerned with the experimental measurement of rod seal friction at constant velocities. This provides an empirical basis for the friction characteristics of sealing elements over a range of operating conditions and serves as a point of reference for measurements taken from active sealing systems. Friction measurements are also used to validate the accuracy of friction modelling to improve the understanding of the tribology processes involved.

Rod seal friction data is provided by seal manufacturers such as reproduced by Hunt [3] with relatively few experimental studies in academic journals. A detailed review of these experimental studies has been carried out by Nau [4]. Several early studies were carried

out by the British Hydrodynamics Research Association (BHRA) in the 1970s, including Kawahara [5] where similar speed dependent friction characteristics to manufacturers' data were reported, with friction shown to initially decrease with rising sliding speed, reach a minimum level, then increase. More recently Rana [6] and Kaneta [7] have also experimentally investigated seal friction. Other investigators such as Kaneta [8] have considered the friction of lubricated rubber pads as an alternative experimental reproduction of seal lubrication conditions.

An important recent development in hydraulic seal experimentation is the establishment of the ISO 7986 standard. This standard aims to improve the repeatability of seal friction measurements between different investigators where the run-in conditions can significantly affect the measured friction values. A recent study was carried out by Papatheodorou [9] based on this standard. This particular study serves as a useful comparison for the experiments carried out in this thesis as the experimental methodologies are well documented and contain many similarities.

In this thesis friction has been measured independently in both directions of stroke. This is useful for validating friction models where differences in friction in different directions of stroke are important such as the mixed lubrication simulations considered in chapter 5. Few previous studies have been carried out into the direction dependence of seal friction due to issues with designing a suitable test rig. Early studies have been carried out by Field [10, 11] with rectangular elastomeric sealing elements where friction was measured in both directions of stroke. More recently Wassink [12] measured lip seal friction in both directions of stroke, reporting issues with accurately identifying the zero of the friction levels.

This thesis expands on previous experimental studies by obtaining extensive friction data for U-cup type seals in both directions of stroke over a large range of sliding speeds and sealed pressures. Experiments have been carried out with single-lip and double-lip seals for a range of sealed pressures between 10 bar and 80 bar and for sliding velocities between creep speeds and the maximum rated speeds of the seals.

Chapter 3 describes the experimental investigation of rod seal friction during sinusoid motion. This was carried out following the observation of significant friction variation across the stroke in experiments with constant velocity motion. The experiments with sinusoid motion provide an indication over how applicable commonly measured friction characteristics at constant velocities are to practical operating cycles.

These experiments were carried out for a range of different frequencies and displacement amplitudes. Friction variation across the sinusoid cycle is related to the variation in friction observed across the stroke in the constant velocity measurements. Inferences are made about the applicability of constant velocity friction data to practical load cycles.

Friction measurements during sinusoid motion are also influenced by the axial flexibility of the sealing elements. For small displacements seal axial flexibility can significantly affect the

measured friction characteristics over a significant proportion of the load cycle. When using friction characteristics from sinusoid motion to help explain the constant velocity friction behaviour it is useful to distinguish between effects from seal flexibility and variation in the rod-seal friction coefficient. Simulations have been produced for mixed sliding and rocking motion during sinusoid excitation for a constant friction coefficient to illustrate the effects of seal axial compliance. These seal flexibility simulations are presented in appendix A.

Chapters 4 to 6 are concerned with modelling approaches for seal friction. This was carried out to investigate the theoretical basis for seal friction characteristics and how these could be affected. Three main lubrication regimes are commonly associated with sliding surfaces; boundary, elastohydrodynamic (EHL) and mixed. EHL lubrication takes place where the surfaces are completely separated by a fluid film and the dominant source of friction is viscous fluid shear stress, boundary lubrication occurs where the fluid film breaks down and friction is generated through shearing of the boundary layers of lubricant that are physically or chemically absorbed by the surfaces. Mixed lubrication is associated with partial fluid films forming where both fluid viscosity and boundary layer lubricity significantly affect the friction characteristics. It is not clear from available literature which of these lubrication mechanisms is dominant in hydraulic sealing applications. This thesis considers models for the different lubrication regimes in attempt to determine which are more appropriate.

Contact mechanics tribology models for seal friction are presented in chapter 4 to explore how far asperity contact could be used to explain the measured friction characteristics. If seal friction is a boundary lubrication phenomenon, an asperity contact approach would be an appropriate modelling technique. Asperity contact models are also relevant to mixed lubrication conditions where asperity contact models are included in other modelling methods as investigated in chapter 5.

Firstly, finite elementanalysis (FEA) models of the seal geometries were produced to simulate the pressure distribution between the seal and the rod. FEA is well established as method for determining the rod-seal pressure distribution, an example being Chung [13] where the simulated pressure distribution for a lip seal was validated as being accurate. Other investigators such as Johannesson [14] have attempted to produce friction predictions based on these pressure distributions. The simulated pressure distributions were used as a basis for determining the friction generated through either asperity contact or other lubrication mechanisms as explored in following chapters.

An investigation of particular relevance to contact mechanics approaches for seal tribology is that by Calvert [15]. Here a FEA study of the contact pressure distribution of pneumatic sealing elements was produced which predicted friction characteristics within 20% of measured values by assuming Coulomb friction conditions. This study suggests the approach of combining a FEA seal model with a dry or boundary friction coefficient may have merit for the current thesis, although the lower pressures and lower levels of lubricant does not

guarantee the technique to work equally well in hydraulic sealing applications.

The appropriateness of Greenwood-Williamson (GW) theory [16] (which produces Coulomb friction) is investigated as this model has found recent use in mixed lubrication studies [17] of seal tribology. Whether the GW model is suitable for the conditions in hydraulic sealing applications is important for evaluating the appropriateness of seal friction models currently in use.

The physical accuracy of one of the assumptions of GW theory (involving the identification of an asperity on the surface profile) has recently been questioned by one of its originators [18], although other investigators such as Ciaverella [19] have suggested the model to have comparable accuracy to more sophisticated approaches.

This thesis considers the appropriateness of the main assumptions of GW theory for the application of hydraulic seal tribology, investigating the model characteristics over the expected range of asperity loading. The physical accuracy of the surface roughness parameters is also investigated with roughness measurements taken as part of this thesis and compared with roughness measurements from other investigations.

An empirical friction relation for dry rubber developed by Thirion [20] is considered as a reasonable experimental agreement with a relationship for dry contact would suggest seal friction could be a dry or boundary lubrication phenomenon. This relation was produced for high loading and may be relevant to sealing applications where the sealing elements are also subject to high loading relative to the material stiffness. The relation proposed by Thirion has been extensively validated with a range of rubbers and gelatines by Denny [21]. How accurately this relation describes seal friction is considered.

Commonly used alternatives for metals loaded outside the accurate range of GW theory include the Chang-Etsion-Bogy [22] (CEB) and Pullen Williamson [23] (PW) models. These models incorporate plastic behaviour at high loadings, hence are less suitable for high strain materials such as seal polyurethanes. In general there are few asperity contact models suitable for the high loading of high strain materials. Investigators such as Komvopoulos [24] and Eid [25] have looked at using FEA geometries with neighbouring asperities to simulate asperity interaction which becomes important at higher contact fractions.

It is explored whether a contact model suitable for high strain materials under extreme loading could be developed. The approach taken is a single asperity model for a sinusoidal rough surface with a uniform rise created from the displaced material as per PW theory. Analytical and numerical approaches involving FEA were used to determine the contact mechanics and expected load-friction characteristics of this surface model.

Tribology simulations based on the solution of the Reynolds equation are presented in chapter 5. This chapter is concerned with EHL and mixed lubrication approaches to seal friction, what insights they offer into the tribology behaviour and whether these techniques could be improved.

The established technique of inverse EHL theory represents an initial approach to simulating seal tribology. Early studies [26, 27, 28] in the 1960s and 1970s applied the technique to analytically obtained pressure distributions and Johannesson [14] used the numerically simulated pressure distribution for an o-ring. Applying the method to many reciprocating sealing elements requires fluid pressure distributions to be assumed for the outlet and inlet, Ruskell [29] assumed a parabola while Nikas [30] assumed a cubic. A recent series of publications by Nikas [30, 31, 32, 33] investigated reciprocating elastomeric seal tribology using EHL theory, suggesting that the concept should be considered as part of any study aiming to further the current understanding of tribology in similar applications.

The mixed lubrication model considered is the GW-average Reynolds model which combines GW contact theory with the Reynolds equation, assuming the pressures associated with the two models to superpose. GW-average Reynolds theory was first proposed by Johnson [34] and later applied to hydraulic seals by Yamaguchi [35]. The model has seen recent use with an alternative numerical technique in a series of publications by Salant [17, 36, 37, 38]. This model is currently well known in the tribology of hydraulic systems, although has yet to be validated against experimental data for reciprocating seal applications.

This thesis validates the friction characteristics predicted from inverse EHL and GW-average Reynolds theory against the friction measurements taken. Methods of modifying the GW-average Reynolds method to improve experimental agreement to allow for high asperity loading with GW contact theory are investigated. An alternative approach to predicting speed dependent friction by assuming a fixed relationship between sliding speed and asperity friction coefficient is also considered.

A novel method of assuming point-contact EHL lubrication at each asperity was developed as an alternative means of explaining the relatively high friction levels observed in hydraulic sealing applications. This approach represents a possible method of using the EHL physical conditions frequently assumed in seal tribology studies to explain the high measured friction levels through the viscous fluid shear of thin films. The method is also an alternative to using empirical boundary friction values and offers the possibility of predicting absolute values for friction.

EHL lubrication of a hemispherical point-contact is quite well theoretically investigated. Early investigators such as Archard [39] used physical simplifications to obtain approximate solutions with adapted Estel-Grubin [40] simplifications. Later investigations were able to obtain exact solutions using more sophisticated numerical methods, Evans [41] with a combined inverse and finite differencing technique and Venner [42] combining two different finite differencing techniques.

This thesis considers whether the standard problem of point-contact EHL can be applied to asperities on the scale of surface roughness to explain seal friction with viscous fluid shear. Viscous friction characteristics arising from surface asperity scale contacts are simulated and

the results combined with an asperity distribution for a rough surface. Details of these point-contact simulations are presented in appendix B.

Chapter 6 considers an alternative friction modelling approach based on material hysteresis from its viscoelastic properties. This is explored as an alternative method of predicting speed-dependent seal friction characteristics. A new approach of including a compliance in the more rigid surface was considered in attempt to improve the experimental agreement at high sliding speeds compared with previous hysteresis models.

Previous investigations of hysteresis friction include Tangena [43] and Bui [44] where contact with viscoelastic parabolic asperities was simulated using FEA. Purushothaman [45, 46] produced a FEA model of sliding contact against triangular asperities and validated the model against experiments with rubber sliding over a surface of triangular prisms. Other investigators such as Yandell [47] and Schapery [48, 49] carried out hysteresis investigations using plane strain Hertzian analysis as an alternative to FEA modelling. These studies predict friction to approach zero at high sliding speeds where the viscoelastic surface approaches having zero contact with the rigid surface.

In this thesis flexibility is included in the non-viscoelastic surface to allow non-zero contact fractions and friction predictions at high sliding speeds. Simulations are presented for a two surfaces in intermittent contact where the relative motion of the wavy surface is represented by a stationary wave.

The relative merits of the different friction modelling approaches are summarised in chapter 7. This provides an indication of which of the different modelling techniques are more suitable for predicting seal friction in active sealing systems and the expected accuracy.

Active seal development and experiments are discussed in chapter 8. This was carried out to demonstrate that varying the seal interference to adjust the friction and leakage characteristics can be achieved in practice and to provide preliminary indications of the response of sealing elements to variation in radial interference.

Previous investigations of active seals have been carried out with mechanical face seals where the seal position was controlled to maintain a clearance between a mechanical end seal and rotating shaft while minimising fluid leakage. Heilala [50] used a position control system with a pneumatic actuator and a thermocouple to detect temperature rises from contact. Salant [51] and Wolf [52] investigated a similar apparatus with a piezoelectric actuation system. Dayan [53] later used eddy current proximity probes to improve the control system. Active hydraulic seals are documented in a textbook on general tribology by Kragelsky [54], although these types of seals are not featured in major public domain journals.

Two different prototypes were produced for an active rod seal where radial variations were achieved by varying an external pressure applied to the outer circumference of the sealing element. One of the prototypes contained a double-lip seal, the other used a rectangular o-ring sealing element. Steady-state friction measurements were obtained for a range of operating

conditions and external pressures. The measured dynamic friction response of each prototype to a step change in external pressure was also measured.

Detailed literature reviews are placed at the appropriate points in the chapters to enable the relevant focus on the particular issues to be applied.

Chapter 2

Constant velocity friction measurement in hydraulic seals

Experimental studies of seal friction measurement have been carried out as part of the current research into seal friction. Rod seal friction has been measured for common single-lip and double-lip rod seals for a range of different sliding velocities and sealed pressures. These experiments identified the friction characteristics of the two different types of hydraulic rod seals and allow experimental data from previous studies with similar types of seals to be verified. The friction measurements taken are also used to validate simulations produced in chapters 4 to 6.

A test rig was developed to measure friction independently in each direction of stroke. Previous experimental studies have tended to consider the combined friction of two rod seals oriented in opposite directions in order to minimise the complexity of the rig design. Including a second sealing element allows sealing to be achieved between the rod and housing on each side of the housing block. In contrast, the current study has used a single-ended housing block to remove the need for fluid sealing on the second end of a housing block. The dependence of stroke direction on friction is relevant for investigating the mixed lubrication studies in chapter 5 where significant instroke-outstroke differences occur. Some early experimental studies of rectangular seals [11] have also suggested the frictional levels to have significant direction-dependence, although the phenomenon has not been extensively investigated.

Experiments were carried out for single-lip and double-lip rod seals with sealed pressures between 10 bar and 80 bar over a range of sliding velocities. An experimental speed range from a creep speed of 0.1 mm/s to the maximum rated speed for the seal of 300 mm/s was used.

2.1 Background

2.1.1 History of reciprocating seal experimentation

A significant amount of experimental investigation was carried out into the friction of reciprocating hydraulic seals by BHRA in the 1970s. For example, Kawahara [5] obtained Stribeck curves for U-cup type seals for sealed pressures up to 50 bar. The rod speed was increased over several orders of magnitude and showed that friction initially falls before reaching a trough after which it increases. It was also demonstrated that the friction coefficient decreases with increasing sealed pressure. Experimental data provided by seal manufacturers [3] also suggest the Stribeck curve to have a single trough and the friction coefficient to decrease with rising sealed pressure.

Friction of reciprocating seals has gained renewed interest in recent years. Kaneta [8] investigated friction in low pressure fluid sealing through experiments with lubricated wedged and "D" shaped polymeric pads against a sliding glass surface. In a following study Kaneta [7] later concluded that a peak frictional force exists in the creep speed range for reciprocating seals. A study by Rana [6] concluded seal friction to be independent of rod speed for speeds of less than 100 mm/s for smooth rods as a result of a fluid film being unable to form at these low sliding speeds. Other investigators suggest seal friction as being significantly higher for lower rod speeds, which may be due to higher rod surface roughness. Nau [4] has suggested that use of rod with a surface roughness height below a critical value results in additional friction and wear, possibly by reducing the propensity for lubricant pockets to be formed between the contact surfaces. It is also possible that, at lower asperity heights, the hysteresis effects on friction from the delayed elastic recovery of the material become less significant.

2.1.2 Dependence of friction on direction of stroke

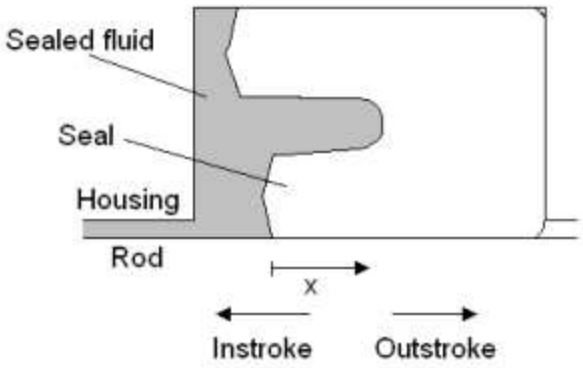

Figure 2-1: Definition of instroke and outstroke for rod motion

The current investigation has applied special consideration to the differences in friction

levels between the two directions of stroke. During rod extension the rod surface is moved from inside the cylinder where the rod contacts the sealed fluid to the surroundings, hence is known as outstroke motion. Similarly, instroke is defined as being equivalent to rod retraction where the rod is retracted into the sealed fluid. This terminology and the velocity sign convention used in the current investigation are illustrated in figure 2-1.

The simplest and most common experimental technique for measuring rod seal friction is to have an enclosed housing with a rod passing through two opposite faces of the housing. Both rod seals are usually orientated in opposite axial directions in order that the pressurised sealed fluid is on the side of each seal that the rod seals are designed to seal from. The combined mean friction from both rod seals can then be obtained by measuring the force required to extend and retract the rod using a load cell. If the directional dependence of friction is to be investigated it becomes necessary to use an alternative housing design.

The simplest procedure for measuring friction in reciprocating seals is to use a disconnected actuator with pressure transducers on the piston and annular sides of the cylinder. During steady motion the total friction force acting on the rod can be obtained by solving a force balance. This allows the total friction from the piston seal and two rod seals to be obtained using simple apparatus consisting of only a hydraulic actuator with mounted pressure transducers. This simple experimental procedure is not suitable if separate data are required for the rod and piston seal friction.

An investigation by Wassink [12] reported experiments to measure lip seal friction that incorporated dependence on the direction of travel. This investigation used a metal sleeve along part of the length of the rod that formed a sealing interface with one of the rod seals. The opposing rod seal produced sealing between the rod and housing rather than the sleeve and housing. This experimental technique allowed the friction of a single rod seal to be isolated and measured in a test rig with two rod seals. Wassink reported significant differences between instroke and outstroke friction, although could not accurately identify the absolute friction values due to uncertainty in the zero of the force transducer. This experimentation was carried out for relatively low sealed pressures of 34.5 bar and 13.8 bar and for a short stroke length of 30 mm.

2.1.3 ISO 7986

2.1.3.1 Emergence of ISO 7986

An ISO standard for seal friction measurement was produced in the mid-1990s in an attempt to improve the repeatability of seal performance measurements. Repeatability between seal friction results from testing programmes is particularly important for the development of new types of seals in order to allow accurate comparison with previous designs. It was necessary to define a common standard with well-defined operating conditions and several repeats for

different seals. ISO 7986 represents the current standard procedure for measuring seal friction and producing results suitable for dissemination.

2.1.3.2 ISO 7986 test procedure

The actuation cycles relevant to the measurement of dynamic friction in ISO 7986 can be summarised as follows:

- Operate for an hour at test reciprocating speed and pressure.
- Measure friction for a minimum of a single cycle.
- Operate at test reciprocating speed and pressure until required number of cycles achieved (200 000 cycles for 150 and 500 mm/s, 60 000 cycles for 50 mm/s).
- Operate for an hour at test reciprocating speed and pressure.
- Measure friction for a minimum of a single cycle.
- Operate at test reciprocating speed and pressure until next required number of cycles achieved (300 000 cycles for 150 and 500 mm/s, 100 000 cycles for 50 mm/s).
- Operate for an hour at test reciprocating speed and pressure.
- Measure friction for a minimum of a single cycle.

2.1.3.3 Adoption of ISO 7986

A seal manufacturer has updated testing procedures to the new standard [9]. This previous investigation was concerned with relatively low reciprocating speeds (1.7 mm/s to 67 mm/s) that are below the value specified for low speed testing (50 mm/s) in ISO 7986. It has been assumed that the study determined the number of cycles for a particular speed by linearly extrapolating from the number of cycles specified for 50 mm/s.

This testing procedure differed in the detail of the run-in times used before taking friction measurements compared with the procedure outlined in ISO 7986. The first sets of measurements were carried out with the rod and seal in "as received" conditions. For a particular sealed pressure the friction levels at different rod velocities and oil temperatures were measured in sequence with no run-in period between different speeds. Then the seal was subjected to a run-in period of 72 hours continuous operation at a fixed sealed pressure of 200 bar and reciprocation speed of 67 mm/s over a 300 mm stroke. Hence 29 000 cycles were used for the run-in period compared with 60 000 cycles suggested in ISO 7986 for a similar velocity (50 mm/s). This difference in the number of cycles may have been expected to produce small differences in run-in seal characteristics compared with the standard procedure.

This investigation by Papatheodorou [9] is the first major public domain study into experimental seal friction to be ISO 7986 informed, although it contains some differences to the standard procedure. The investigation carried out a single run-in period for measurements at a number of different sliding speeds and fluid temperatures in order to reduce testing periods. Additionally, a range of different temperatures and sealed pressures were assessed compared with the standard.

2.2 Methodology for current investigation

2.2.1 Experimental apparatus

2.2.1.1 Main features

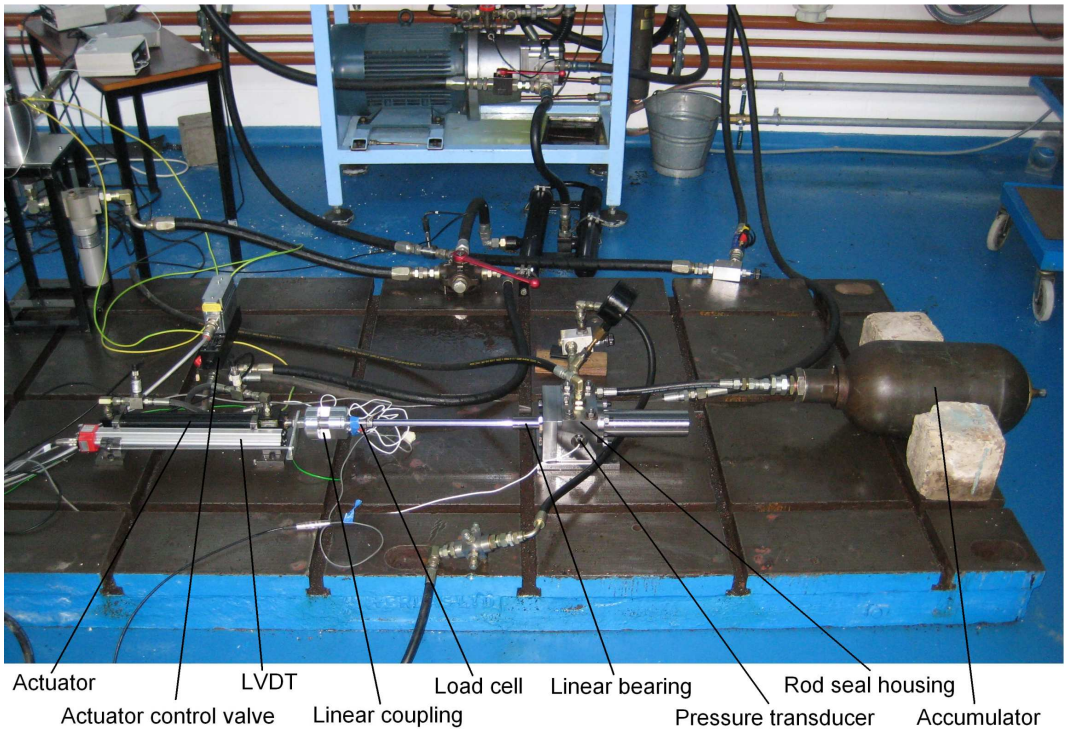

Figure 2-2: Experimental apparatus for passive seal friction measurement

Figure 2-2 shows the experimental test rig used in the current investigation with the important features and internals illustrated in figure 2-3. A rod seal was enclosed in the housing block, through which the rod was extended and retracted using a hydraulic actuator connected to the rod via a linear coupling and load cell. Hydraulic fluid was supplied to the housing and a constant sealed pressure was maintained using a relief valve downstream of the housing. An accumulator was connected upstream of the seal housing to reduce fluctuations

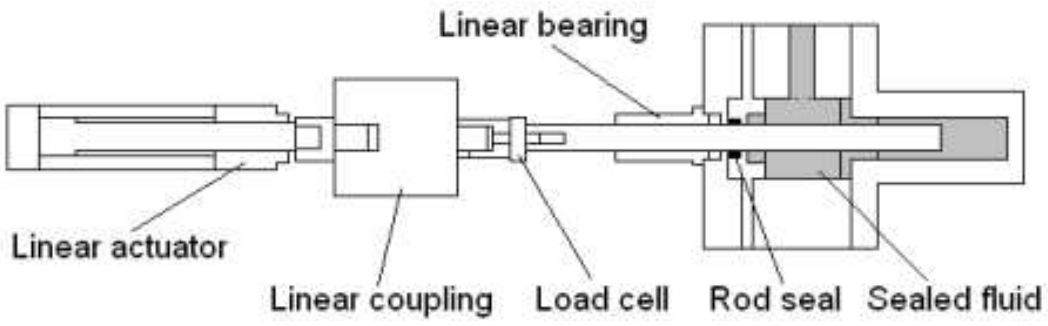

Figure 2-3: Diagram of rod actuation principle for passive seal test rig

in the sealed pressure. A second hydraulic supply was used to drive the hydraulic actuator through a controlling servovalve.

A single rod seal was used with one end of the housing enclosed to remove the need of a second sealing element. The rod seal housing was machined to dimensions and tolerances for a Parker-Hannifin B31624 rod seal [55]. A chrome plated rod was used with a load cell connected in series with a linear coupling and the actuator. The linear coupling acted to minimise the effects of any misalignment between the rod and actuator.

2.2.1.2 Rod seal housing block

The rod seal housing (figure 2-4 with part drawings shown in figures C-1 to C-3) included a seal groove that was located in the central housing block (figure C-2) with one of the faces of the groove formed by the end housing block (figure C-3). A separate housing block (figure C-1) was used to contain the main sealed fluid region and connected to the source of fluid at the required sealed pressure. Two different types of rod seals were considered; a single-lip B31624 (figure 2-5) and a double-lip BS1624 rod seal (figure 2-6).

The housing assembly had a closed end cylinder that exposed the face of the rod to the sealed fluid. This design feature was included to remove the need for a second sealing element. With this housing block configuration it was possible to infer the friction of a single rod seal independently in both directions of rod travel. Account was taken for the force exerted by the pressurised fluid in the friction determination. Other issues include additional loading on the linear coupling and higher flow requirements for the fluid supplied to the housing. During instroke the fluid volume swept by the rod was also required to be either stored in the accumulator or returned to the tank to avoid significantly compressing and raising the pressure of the sealed fluid.

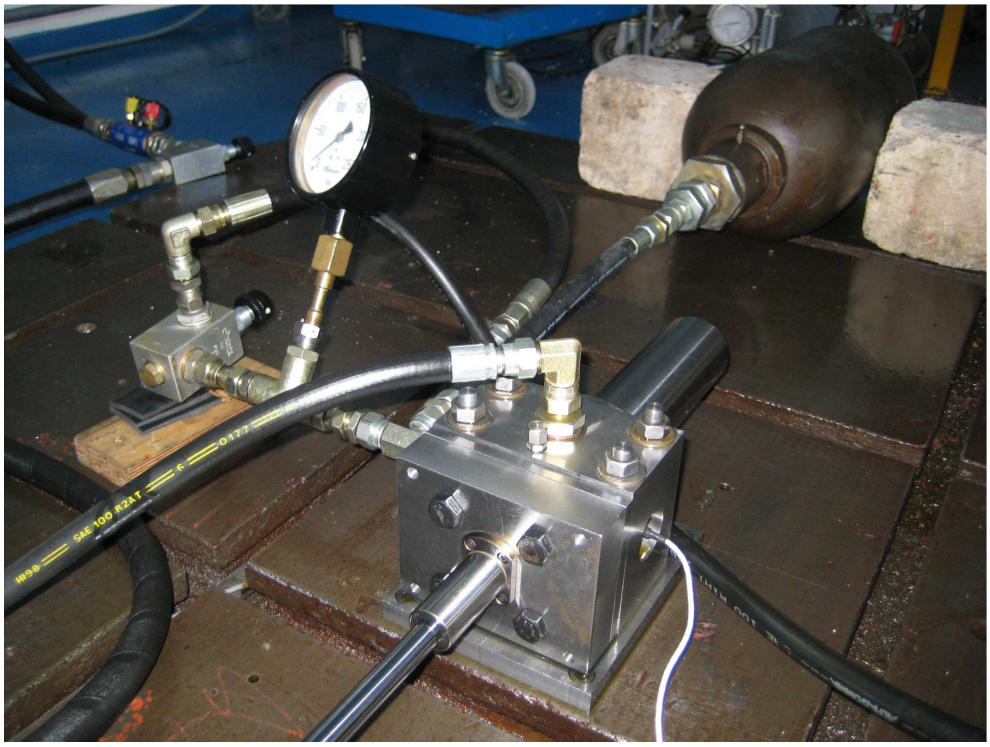

Figure 2-4: Housing block for passive rod seal

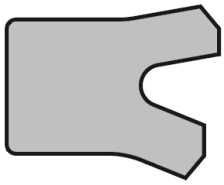

Figure 2-5: Parker-Hannifin B31624 single-lip seal

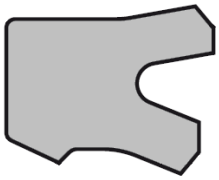

Figure 2-6: Parker-Hannifin BS1624 double-lip seal

2.2.1.3 Housing hydraulics

Figure 2-7 shows the circuit diagram for the hydraulic supply to the seal housing. Mineral oil was used as the supply fluid for the housing block, using a Rexroth internal gear pump of 3.2 cc/rev displacement driven by a 2.2 kW electric motor. This pump had an internal adjustable relief valve connecting the supply line to the return line to bypass the hydraulic circuit if the supply pressure exceeded the cracking pressure of the relief valve. A cracking pressure of 100 bar was set on this valve as a safety measure. Another relief valve was used to set the system pressure for the sealed fluid.

An accumulator was connected into the supply line of the housing block to help provide the differences in flow resulting from the displacement of fluid by the rod as it was retracted and

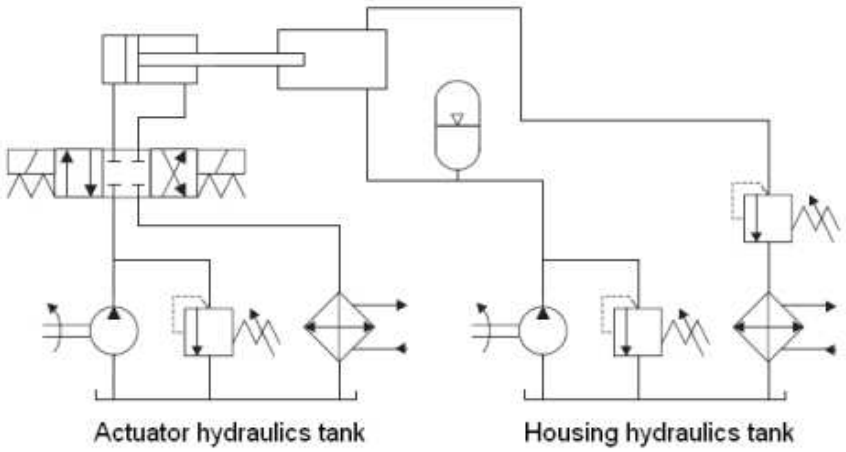

Figure 2-7: Hydraulic circuit to set sealed pressure inside housing block

extended. Without the accumulator the full rate of swept volume by the rod would correspond to variation in flow across the relief valve. As the relief valve had a slight characteristic of increasing pressure drop with flow rate, the fluid displaced by the rod may have resulted in significant variations in sealed pressure between instroke and outstroke.

2.2.1.4 Actuation system

The actuator used was a single-ended 25C-HM1RN24M-300M1-100 linear hydraulic actuator provided by Parker-Hannifin with a stroke length of 300 mm. This actuator had piston and rod diameters of 25 mm and 16 mm, respectively. The stall force of the actuator was dependent on the maximum system pressure in the hydraulics associated with actuation. This maximum system pressure was adjusted by varying the cracking pressure on the relief valve connecting the high pressure line at the pump outlet to the tank. For different sealed pressures acting on the face of the rod the system pressure in the actuation hydraulics was adjusted to maintain sufficient pressure to allow accurate tracking of the demand triangular wave.

Flow to the piston and annulus ports of the actuator was controlled using a Parker-Hannifin DFPlus series D1FP350MA9NB00 proportional servovalve. The spool had zero-overlap, theoretically removing the deadband region of spool displacements where displacement increments produce no additional flow. This design feature enabled a high bandwidth in excess of 100 Hz, which was sufficient for most of the constant speed testing carried out.

A Nexen LC2000 linear coupling was used to connect the actuator rod to the load cell in order to reduce the effects of any misalignment between the actuator and rod seal housing. The coupling was also required to retain sufficient axial rigidity to prevent significant dis-

crepancies between the displacement of the end of the actuator rod measured by the linear variable differential transformer and the displacement of the rod in contact with the seal. The LC2000 series has a maximum rated force of 2 kN, imposing an upper limit on the maximum sealed that can safely act on the rod face. Thus a 16 mm diameter rod would have a corresponding maximum permissible sealed pressure of 99 bar.

The suction line of the pump was connected directly to a 120 litre tank. The pump had a flow rate of 70 l/min when operated at its designed rotational speed. A water cooler was included in the return line to maintain a fluid temperature within a suitable range for the mineral oil. An oil filter was also connected in the return line to maintain satisfactory fluid contamination levels. A silencer was included in between the pump outlet and proportional servovalve to reduce the pressure ripple in the high pressure line from the pump outlet.

2.2.1.5 Sensors

A RDP EP-S-0300M-D60-1-V0 linear variable differential transformer (LVDT) was mounted to the actuator to measure the rod displacement (figure 2-2). The force between the seal and the rod was measured using a RDP model SLC31/01000 load cell, which was connected in series between the rod displacing through the seal housing and linear coupling on the end of the actuator rod. The load cell has a maximum rated force of 2.2 kN that is slightly greater than that of the linear coupling. The maximum sealed pressure was limited by the lower maximum force at which either the load cell or linear coupling could operate. A Kulite ETM-375 (M) piezoresistive pressure transducer rated to 350 bar was mounted inside the seal housing to measure the pressure of the sealed fluid.

2.2.1.6 Data acquisition and control system

The sensor and control signals to the servovalve were processed using a data acquisition system consisting of a PC running dSPACE under Windows XP. A custom control program was used to record the data from the acquisition board and produce a control signal for the position control of the servovalve and actuator. This allowed PID control of the rod position through configurable displacement ramps and repeating triangular signals in addition to manual operation of the valve position.

2.2.2 Test procedure overview

For a particular seal a run-in period was carried out with a sealed pressure of 80 bar. At this pressure the rod was reciprocated as a triangular wave with amplitude 160 mm and speed 300 mm/s for a period of an hour (3 375 cycles). PI position control was used to produce the required triangular wave. Once the run-in phase was completed the load, displacement and fluid pressure were recorded over five cycles of a triangular wave of 160 mm stroke and

0.1 mm/s speed. Five-cycle triangular waves were then run for speeds of 0.2, 0.5, 1, 2, 5, 10, 20, 50, 100, 200 and 300 mm/s with sensor data traces recorded in each case. The sealed pressure was then lowered to 60, 40, 20 and 10 bar in sequence and measurements taken at each pressure for the range of speeds used for 80 bar.

Downsampling was included between the sensor measurements and recorded data in order to maintain manageable results file sizes. A sample rate of a 6 kHz was used throughout testing, details of the data acquisition system are included in section 2.2.1.6. It was necessary to use a large sample interval for the creep-speed experiments where the data recording periods were significantly longer than for the other speeds. An interval of 3 000 received data points between each recorded data point was used for the longest series of tests with a reciprocation speed of 0.1 mm/s. A recording interval of 1 500 points was used for speeds between 0.2 mm/s and 2 mm/s inclusive, an interval of 150 for 5 mm/s to 50 mm/s inclusive and a downsampling rate of 15 for higher rod speeds.

Additional experimental results from three different seal specimens for the double-lip seal have been included to provide a basic indication of the degree of repeatability between different seals. These three seals were tested in as-received condition and reduced stroke lengths were used for speeds of 5 mm/s and less; corresponding to a maximum cycle time of 30 s. The results from these repeatability tests have been plotted separately from the main body of results.

2.2.3 Post processing of friction data

A correction was applied to the measured force at the load cell for each stroke to adjust for the effect of the pressurised fluid on the rod face at the enclosed end of the housing. A linear relationship was assumed to exist between the sealed pressure and force correction as this sealed pressure was known to act over a fixed cross-sectional area: $F(\mathrm{N}) = -19.805 P_s(\mathrm{bar}) + 13.788$ where the negative index indicates the force on the load cell as being compressive as a result of additional fluid pressure. The relationship for the force correction was obtained experimentally using a static test in which the actuator was inactive and the sealed pressure was varied. In this test no pressurised fluid was supplied to the actuator, which was allowed to fully retract under the action of the sealed fluid acting on the rod face. Prior to the testing the accumulator was disconnected from the system to allow easier control of the sealed pressure without the time lags associated with charging the accumulator. The sealed pressure was increased gradually between approximately 0 bar and 100 bar over a period of approximately 20 s by manually adjusting the relief valve downstream of the seal housing. Sensor data from the load cell and pressure transducer were recorded throughout the pressure variation cycle. The linear relationship was obtained using the method of least squares.

2.2.4 Comparison of current procedure with ISO 7986

2.2.4.1 Run-in period

ISO 7986 specifies the friction measurement for a new seal to be taken following an hour of reciprocating at the test speed and pressure. This is similar to the run-in period used in the current study (1 hour reciprocating at 300 mm/s at 80 bar sealed pressure). In the current investigation a single incidence of this particular run-in cycle was followed by measurement periods at all pressures and speeds without replacing the seal or carrying out additional run-in phases for the different pressures and reciprocating speeds. It may be expected for the different sealed pressures and reciprocating to be associated with differing equilibrium surface roughness profiles on the seal. Friction measurements for the lower sealed pressures may not be comparable to those produced with ISO 7986 if there is a significant dependence of loading on the run-in seal characteristics.

The ISO standard specifies friction measurements following two extended periods of operation to provide an indication of the long-term friction characteristics. Shorter testing periods are specified for the lowest reciprocating speed (60 000 cycles and 100 000 cycles at 50 mm/s) that suggest a total experimental period approximately equal to that for the case with the intermediate reciprocating speed. The current study has not experimentally investigated the effects of long run-in periods on friction. There may be expected to be discrepancies between data obtained from ISO standard investigations with long operations and those from the current investigation. Measurements taken from the current study are more comparable to those specified in the earliest measurements with the ISO procedure.

For one of the rod speeds specified in ISO 7986, to meet the standard it is necessary to reciprocate a rod for 100 000 cycles at 50 mm/s with a 500 mm stroke. A total period of 556 hours of reciprocation is required to meet this run-in requirement for a single seal sample. If six separate seals are to be tested as specified in the ISO standard, a period of 3 330 hours (approximately 20 weeks of continuous operation) would be required to produce a final friction measurement for a single speed and sealed pressure. For the current investigation measurements for a range of reciprocating speeds and sealed pressures are required from short-term testing periods. Therefore it is not practical to consider the long run-in periods specified in ISO 7986 in the present study.

2.2.4.2 Rod speeds as independent variable

The three rod speeds (50, 150 and 500 mm/s) specified in ISO 7986 provide too few data points and too narrow a range of speeds to produce detailed descriptions of the Stribeck curve for reciprocating rod seals. It was necessary to expand the number of speeds available in order to capture the Stribeck characteristics. The current study has used a range of rod speeds approximately equi-spaced logarithmically to track the variation in friction across four

orders of magnitude from creep speeds to the highest rated speeds for the seal type.

2.2.4.3 Data recording period

ISO 7986 specifies the friction measurement to be taken at the mid-stroke position for at least a single cycle. The current investigation used an approximation to the mid-stroke friction as the friction level for a particular speed in compliance with this standard. Sensor data were recorded over a total of five instroke-outstroke cycles of a triangular wave and the results processed to produce an estimation of the mid-stroke values of force and pressure. This was achieved by calculating the mean force and pressure values over the range of data points where the demand position was within $\pm 10\%$ of the stroke length from the midpoint (64 mm to 96 mm for the 160 mm stroke used in the current investigation).

2.2.4.4 Stroke length

The 160 mm stroke length used in the current investigation is approximately a third of the 500 mm stroke length specified by ISO 7986. There may be expected to be discrepancies between the current study and experiments carried out to the ISO 7986 standard for cases where there is significant friction variation across the majority of the 160 mm stroke. If this type of friction variation is observed across the shorter stroke, it can be deduced that continuing friction variation may be probable if the stroke is extended. Any friction measurements with significant friction variation across the complete stroke length may not be expected to tally with results produced from the longer stroke procedure. It should also be noted that measuring approximately constant friction levels across most of the 160 mm stroke would not necessarily be indicative of there being no significant change in friction at longer strokes.

2.2.4.5 Breakout friction in ISO 7986

Many contacting surfaces experience a higher static coefficient required to initiate motion than the dynamic friction coefficient occurring during relative motion. Slip-stick behaviour occurs where a discontinuity in speed-dependent friction results in a step change in the net force acting on the system. If static friction is present in an actuation system this can lead to an oscillatory response from a change in demand position or velocity. For a thorough identification of the effects of seal friction on actuator performance it is preferable to include whether higher static friction is present and its characteristics.

ISO 7986 includes a procedure for measuring the breakout friction of a hydraulic seal. In this standard the rod is held in a constant position for 16 hours with the seal pressurised before the measurement is taken. The purpose of the long dwell-time is assumed to be to reach a steady-state condition where the fluid underneath the seal has dried out (either gradually squeezed out or evaporated) and there is relatively dry contact between the rod and seal. It

is well known among authorities in sealing technology ([56] for example) that the friction of a seal increases with time following a suspension of motion as the lubricant dissipates. It is likely that the time constants associated with the reduction in lubrication have relatively poor repeatability. Use of a large safety factor in the dwell-time specified may be intended to ensure the repeatability of the standardised results.

It is questionable whether the ISO 7986 is relevant for the dynamic performance of a hydraulic system where normal operation may not involve extended stationary phases. The main application of the breakout friction measurement described appears to be ensuring an actuator retains a particular net force capacity following a long period without operation. For applications involving repeated changes in direction without extended dwell times the frictional characteristic for a "cold start" is less relevant. The envisioned aims of the current projects are concerned with dynamic response and accuracy in rapidly repeated operations (allowing lubricant to remain under the seal during recommencement of motion). Additionally, it is disputed whether dry rubbers and polymers have different static friction coefficients compared with the dynamic coefficients for low sliding speeds [57]. Experiments involving varying the tangential force between dry rubber and metal contacts have observed creep-speed motion as beginning once a certain tangential load is exceeded, although have not consistently produced clear evidence of any discontinuity in friction force between static and creep-speed cases.

2.3 Results from constant velocity testing

2.3.1 Friction data across stroke

Figures 2-8 to 2-11 show examples of the sensor data from the force and displacement transducers for a range of different sliding speeds, each trace showing the variation in measured friction across the five successive strokes. Also shown in figures 2-12 and 2-13 are examples of the sealed pressure data for cases where these variations are most prominent (discussed in section 2.4.6.1). Figure 2-8 shows a creep speed example at 0.2 mm/s, figure 2-11 shows a high speed case at 200 mm/s while figures 2-9 and 2-10 show intermediate speeds. A sign convention for the sensor data is used for negative displacement and velocity in the instroke direction and compressive load cell forces being positive.

In general, the friction level during instroke decreases as the stroke progresses. This decrease in friction throughout the stroke is more pronounced at creep speeds. Figure 2-8 shows an example at 0.2 mm/s where a decrease in friction level of approximately 40% takes place between the beginning of the instroke motion and the mid-stroke or end positions. At intermediate speeds (e.g. 5 mm/s in figure 2-9) friction continues to decrease throughout the length of the stroke. Less friction variation with time was observed at higher speeds

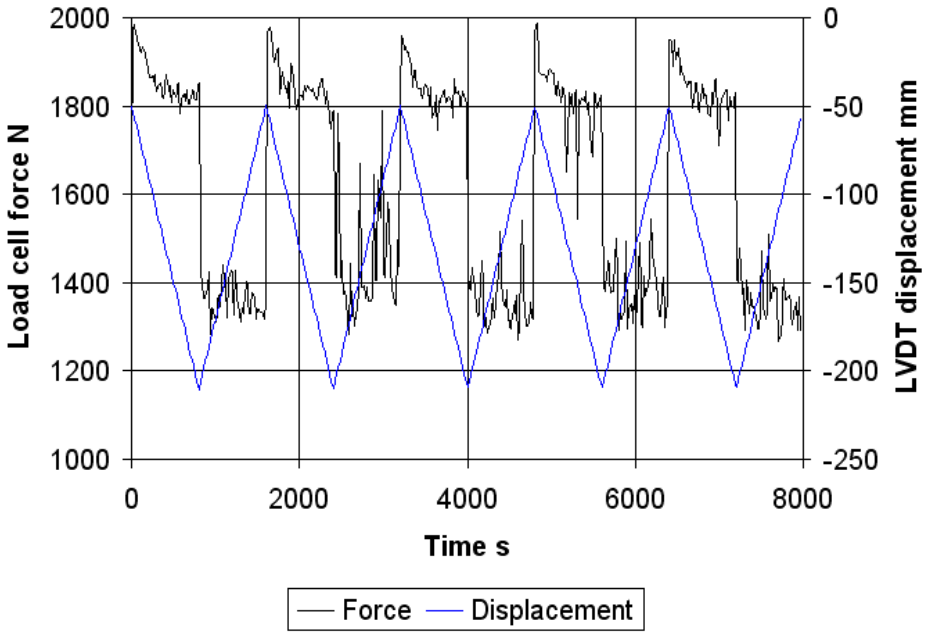

Figure 2-8: Unprocessed load cell and LVDT data for single-lip seal, 0.2 mm/s sliding speed, 80 bar sealed pressure

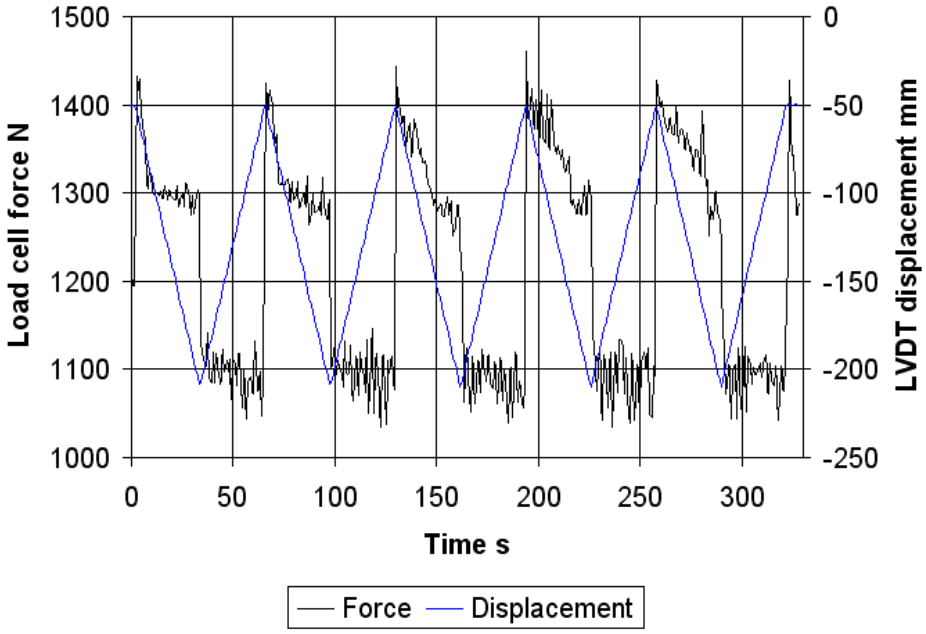

Figure 2-9: Unprocessed load cell and LVDT data for single-lip seal, 5 mm/s sliding speed, 60 bar sealed pressure

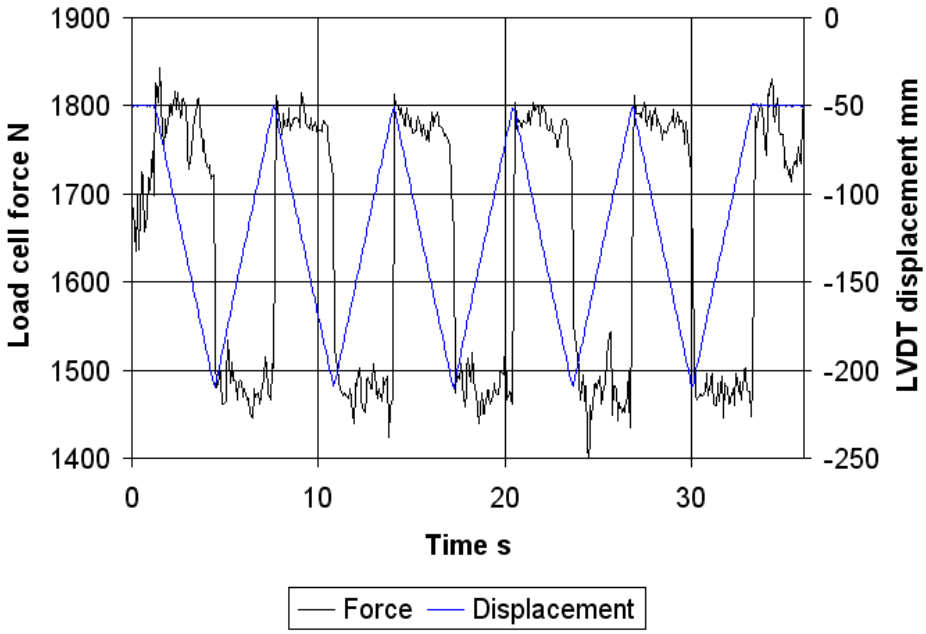

Figure 2-10: Unprocessed load cell and LVDT data for single-lip seal, 50 mm/s sliding speed, 80 bar sealed pressure

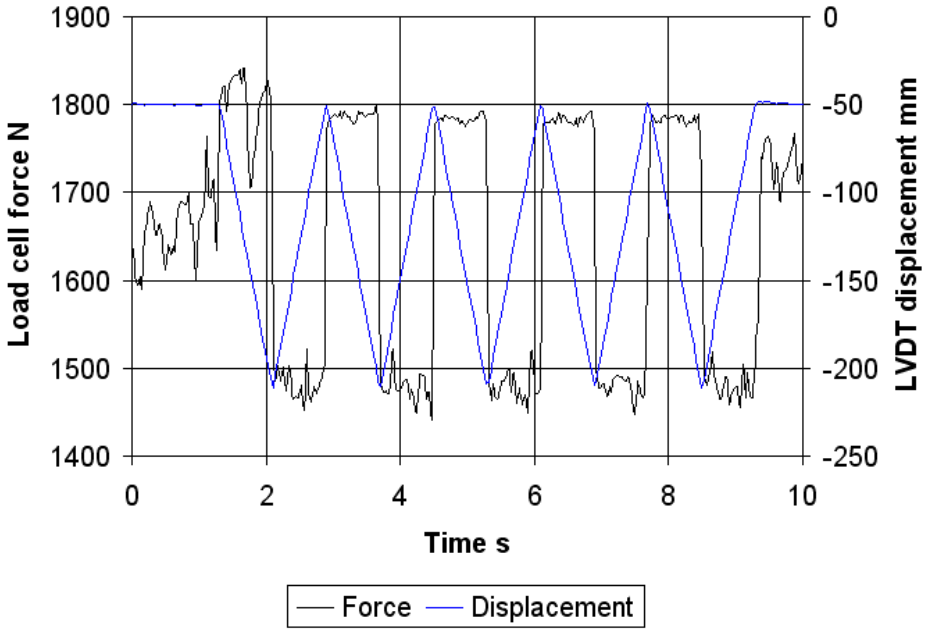

Figure 2-11: Unprocessed load cell and LVDT data for single-lip seal, 200 mm/s sliding speed, 80 bar sealed pressure

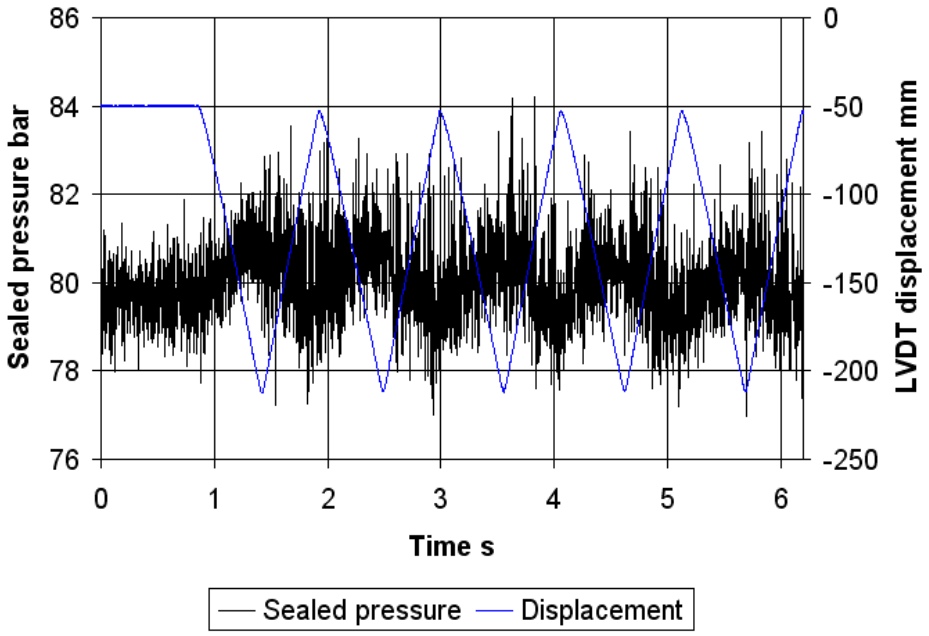

Figure 2-12: Unprocessed sealed pressure and LVDT data for single-lip seal, 300 mm/s sliding speed, 80 bar sealed pressure

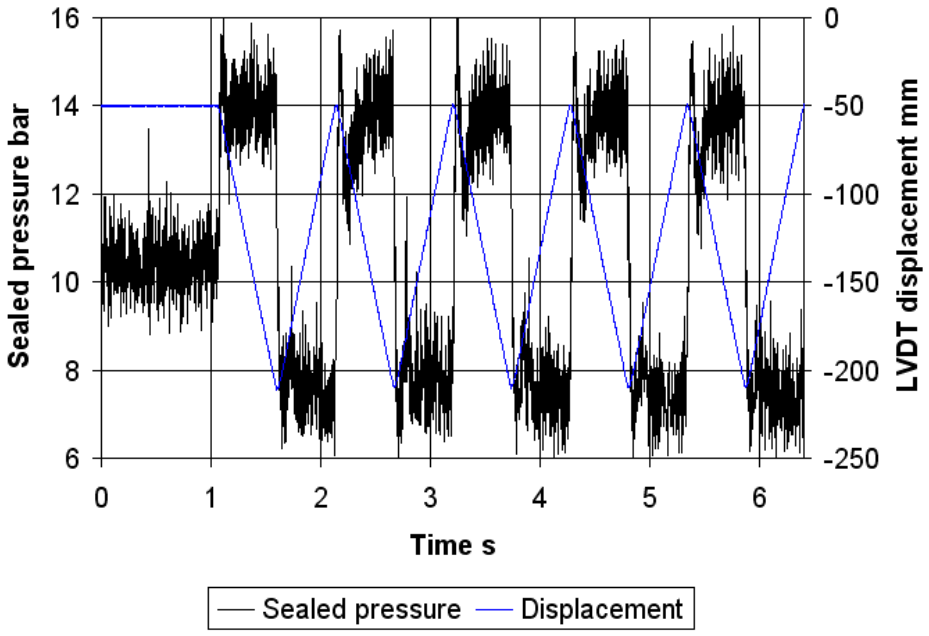

Figure 2-13: Unprocessed sealed pressure and LVDT data for single-lip seal, 300 mm/s sliding speed, 10 bar sealed pressure

(figure 2-10) compared with creep speeds.

During outstroke there is a general increase in load cell force, hence friction, across the stroke. This friction increase across the stroke is pronounced only for lower to intermediate speeds (figures 2-8 and 2-9) while only minimal friction variation is observed at higher speeds (figure 2-10). The magnitudes of these friction variations become significant for a similar range of sliding speeds during outstroke as for the instroke cases. In general, there is a greater magnitude of friction variation across the stroke during instroke than during outstroke. This difference is less pronounced at creep speeds (figure 2-8) where there is significant fluctuation in the outstroke friction, although highly distinctive at lower to intermediate sliding speeds (figure 2-9). There is also significant variation between instroke and outstroke in the length of the stroke over which the initial friction change takes place; at 5 mm/s the friction transition during instroke encompasses the full 160 mm stroke length while the corresponding friction change during outstroke takes place within the initial 10% of the stroke.

2.3.2 Single-lip seal results

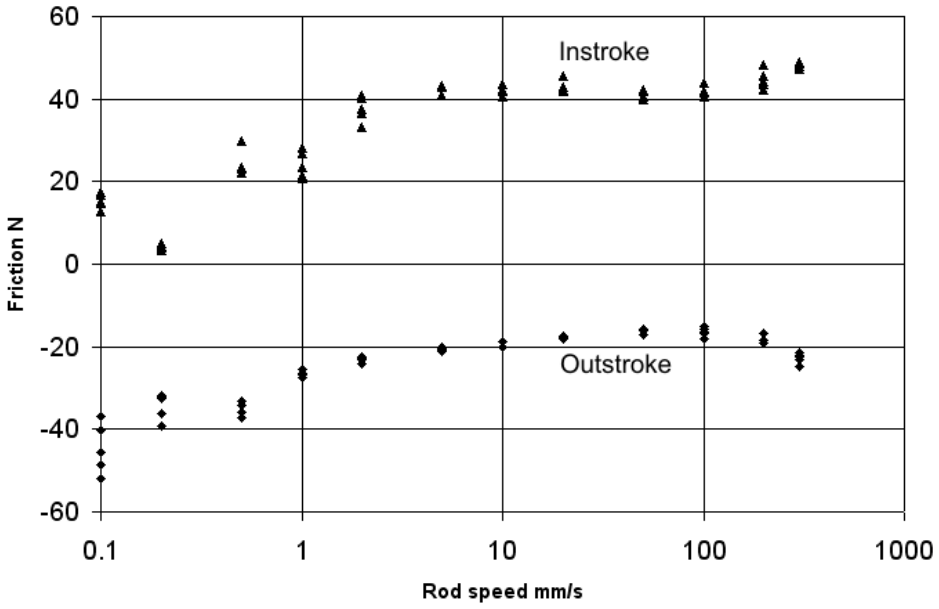

Figure 2-14: Constant velocity friction measurements for single-lip seal, 10 bar sealed pressure

Figures 2-14 to 2-18 show the friction measurements taken over the experimental range of constant sliding velocities for sealed pressures of between 10 and 80 bar for the single-lip seal (figure 2-5). At the higher sealed pressures (figures 2-17 and 2-18) significant reductions in friction occur between creep speeds and intermediate speeds; most of this friction decrease

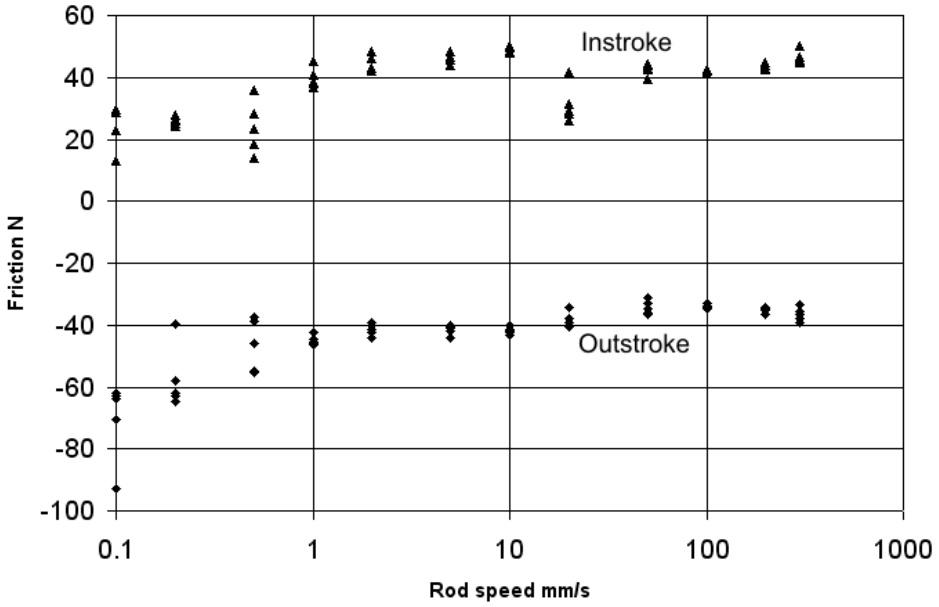

Figure 2-15: Constant velocity friction measurements for single-lip seal, 20 bar sealed pressure

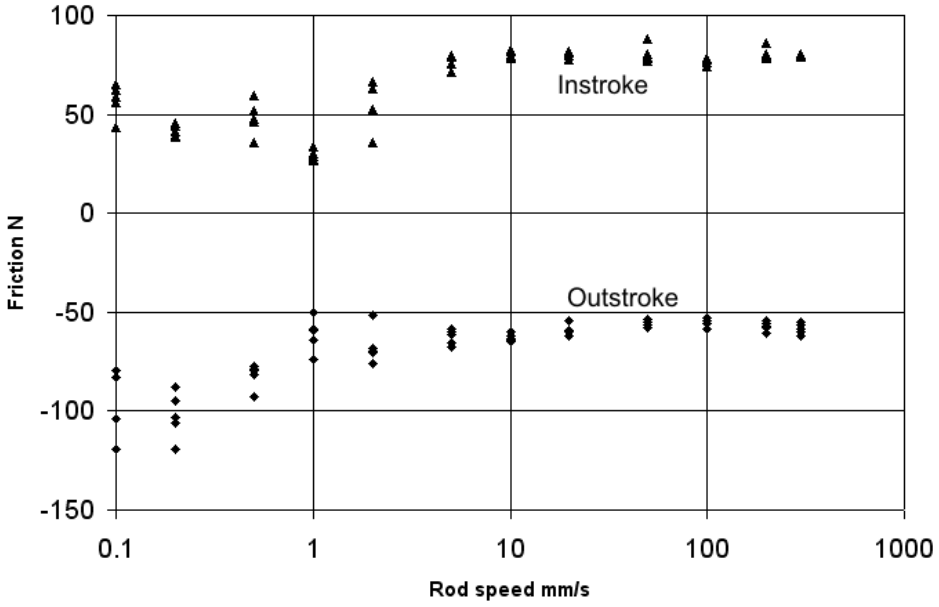

Figure 2-16: Constant velocity friction measurements for single-lip seal, 40 bar sealed pressure

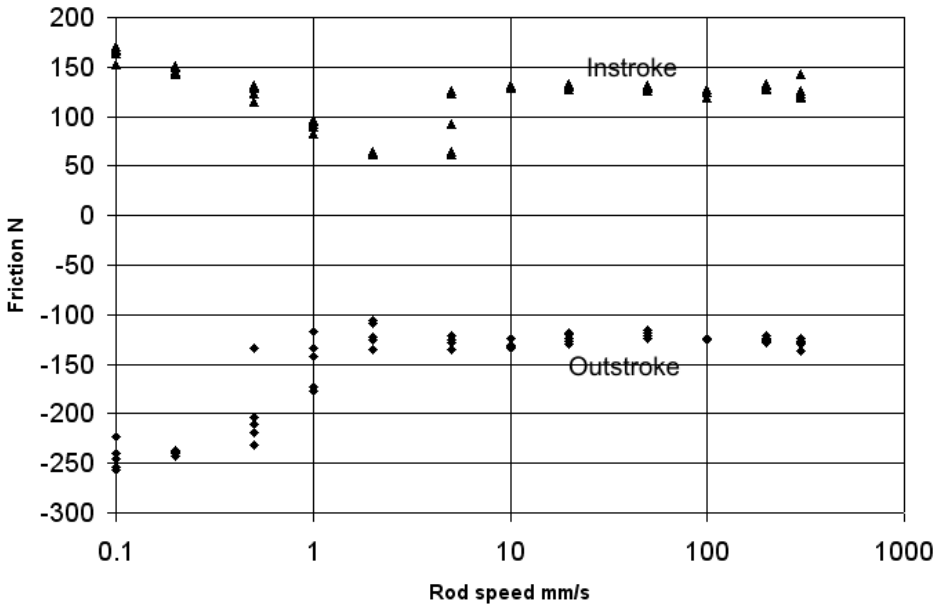

Figure 2-17: Constant velocity friction measurements for single-lip seal, 60 bar sealed pressure

taking place below 2 mm/s. The magnitude of this friction decrease is approximately 50% at the higher pressures. At lower sealed pressures (10-40 bar) no decrease in friction is observed between creep and intermediate sliding speeds during instroke while the outstroke friction variation remains similar to that observed at higher pressures.

An abrupt increase in instroke friction can be observed within a transition region of sliding speeds at intermediate speeds (approximately 2 mm/s to 10 mm/s). A small increase in the magnitude of this friction increase takes place with increasing sealed pressure, although is clearly not proportional to pressure; at 10 bar the step increase in friction is approximately 20-30 N, which rises slightly to 30-40 N at a pressure of 40 bar and beyond. These friction increases are more significant relative to the overall speed dependent behaviour at lower sealed pressures where the absolute values of friction are lower. The transition region for this friction increase shows some minor dependence on sealed pressure, occurring at approximately 2 mm/s for 10-40 bar and at 5-20 mm/s for the higher pressures.

Figure 2-19 shows additional friction measurements carried out over the friction transition region for the single-lip seal in order to provide additional detail concerning the phenomenon. A second pronounced minimum in the friction level is observed at 30 mm/s in addition to the minimum observed between 2 mm/s and 10 mm/s with the measurements taken at three intervals per decade of speed.

Outstroke friction increases with increasing pressure while retaining qualitatively similar

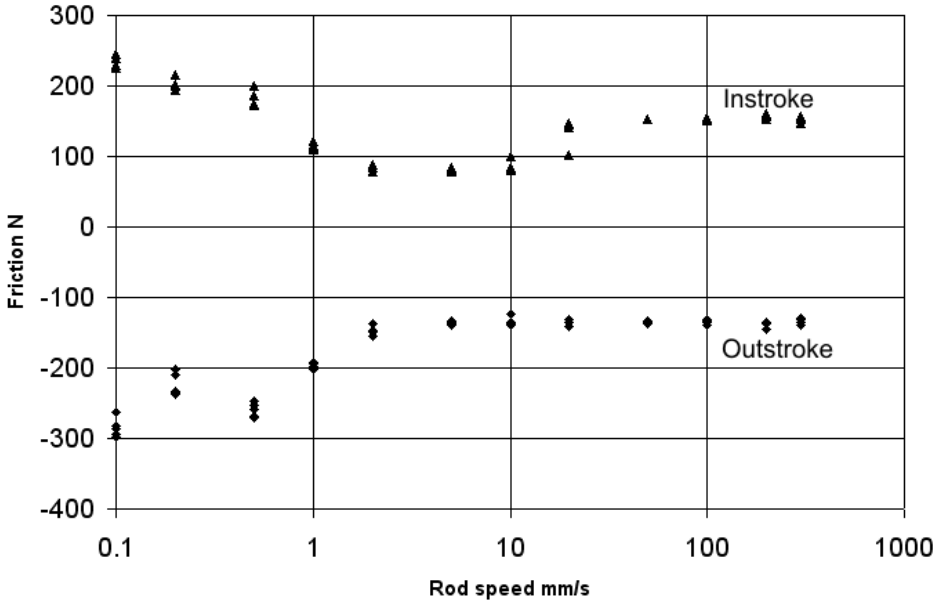

Figure 2-18: Constant velocity friction measurements for single-lip seal, 80 bar sealed pressure

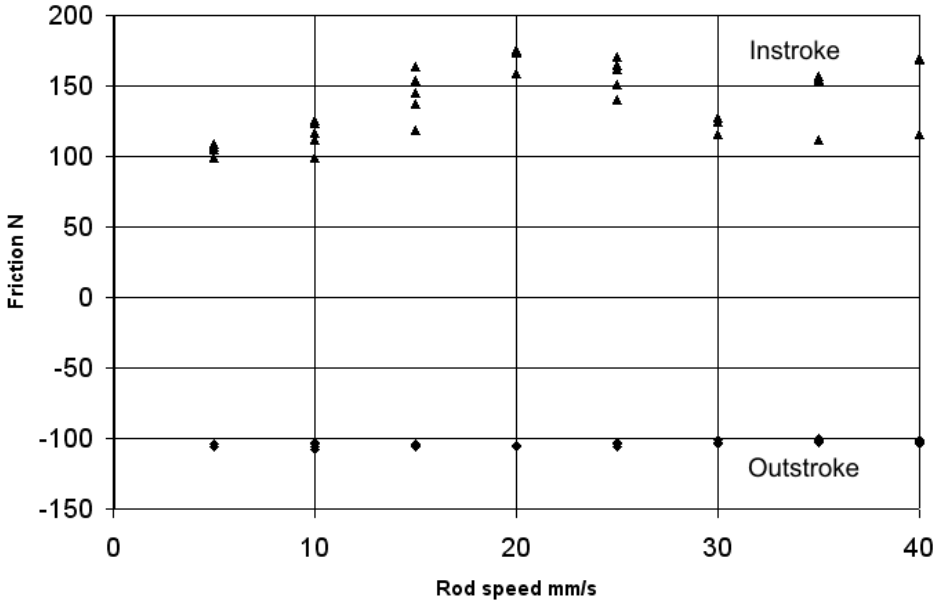

Figure 2-19: Additional constant velocity friction measurements for single-lip seal over intermediate speed range, 80 bar sealed pressure

speed-dependent behaviour. For sealed pressures of 40 bar and lower the relationship between pressure and friction approximates as being linear with creep speed friction doubling from 10 to 20 bar and again from 20 to 40 bar. The proportional relationship between sealed pressure and friction magnitude does not extend to the higher pressures of 60 bar and 80 bar, with greater increases in measured friction between 40 and 60 bar than would be expected with linear extrapolation from lower pressures.

2.3.3 Double-lip seal results

Experimental results were obtained for a Parker-Hannifin BS1624-P5008 rod seal with a double-lip using a similar procedure to that for the single-lip seal. This seal features a second lip protruding from the main body of the seal (figure 2-6) that significantly increases the reaction force and contact area between the rod and seal for lower seal pressures. With the exception of the secondary lip, the geometries of the B3 and BS profile seals used were quite similar and both seals were produced from the same material (Parker P5008 polyurethane).

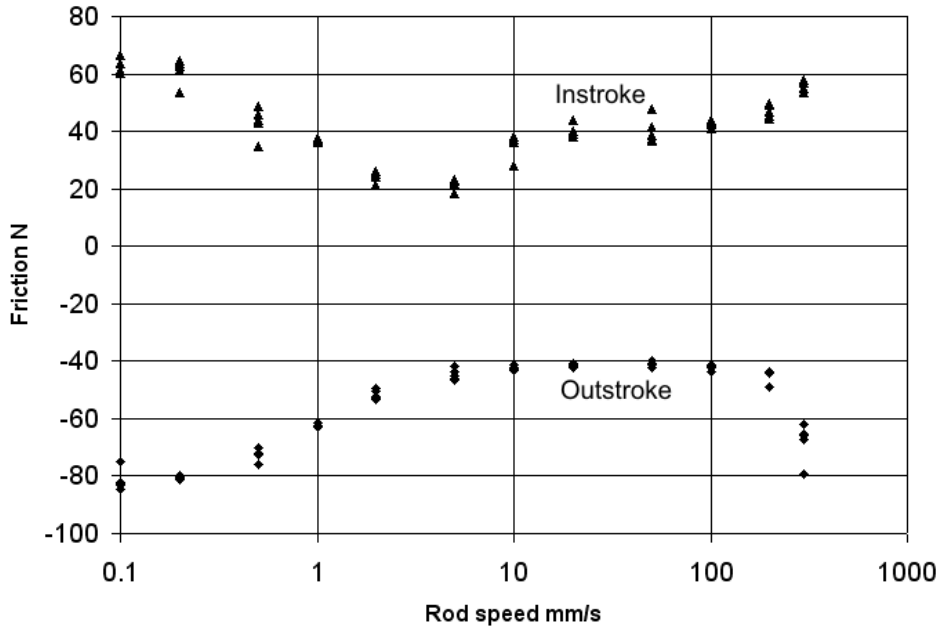

Figure 2-20: Constant velocity friction measurements for double-lip seal, 10 bar sealed pressure

Figures 2-20 to 2-22 show measured friction results for sealed pressures of 10 to 80 bar for the double-lip seal. The results with the double-lip seal have important similarities with those obtained for the single-lip seal. Both seal types exhibit similar increases in friction as the sealed pressure increases and (at sealed pressures of 40 bar or greater) similar speed-

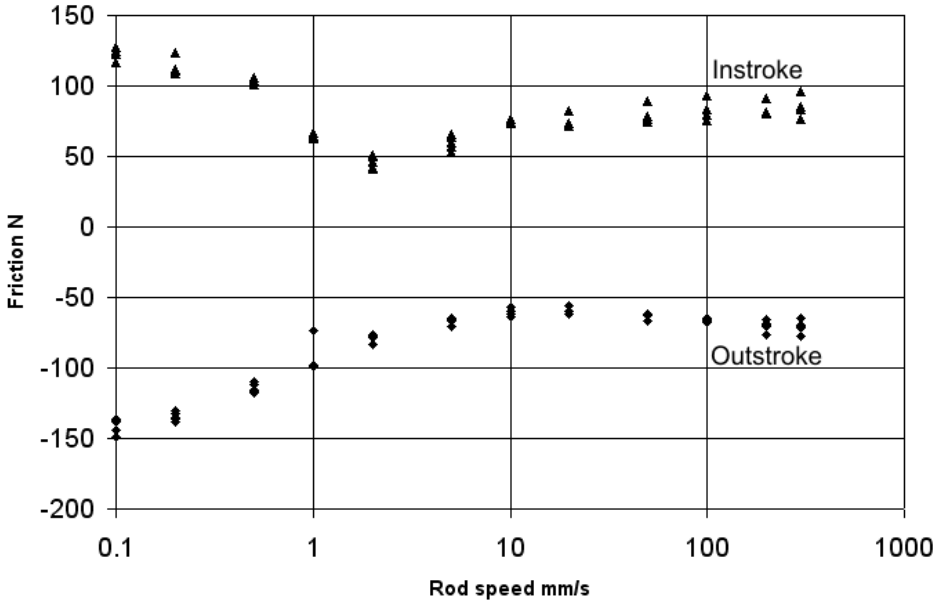

Figure 2-21: Constant velocity friction measurements for double-lip seal, 40 bar sealed pressure

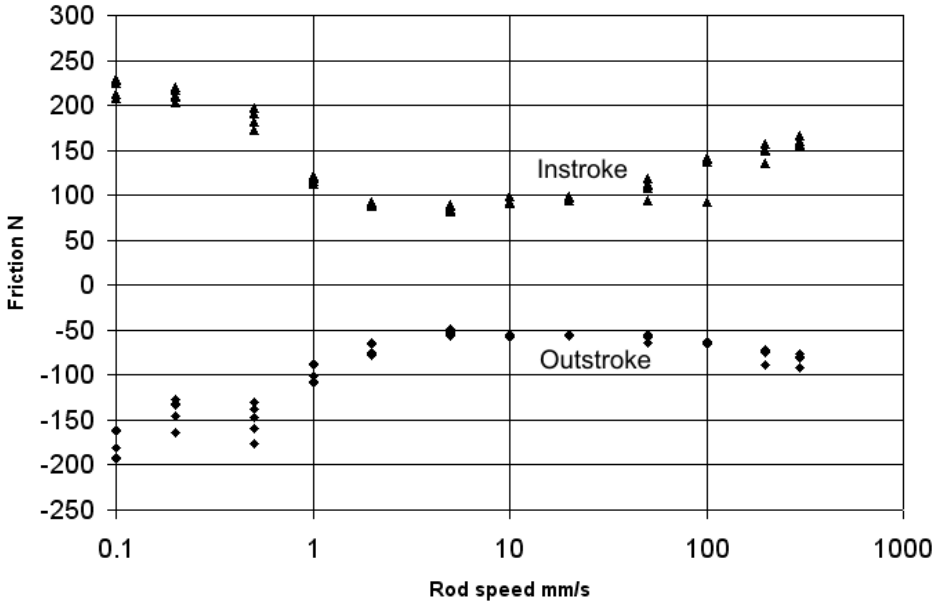

Figure 2-22: Constant velocity friction measurements for double-lip seal, 80 bar sealed pressure

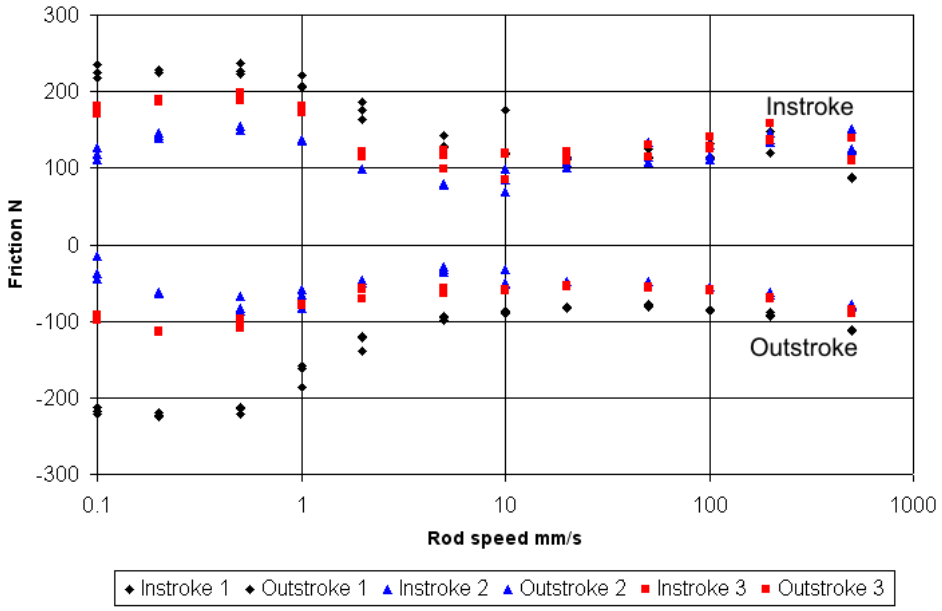

Figure 2-23: Repeatability of constant velocity friction measurements for different double-lip seal specimens, 60 bar sealed pressure, reduced stroke length below 10 mm/s

dependent behaviour. However, there are also some subtle differences in friction from the two seals.

A significant increase in friction with increasing rod speed is observed during instroke over the range of intermediate rod speeds. This increase in friction has similarities to that observed for the single-lip seal. The magnitude of the friction rise has some minor pressure dependence, having magnitude of 30-40 N for 10-40 bar and 60-70 N for an 80 bar sealed pressure.

No abrupt increase in instroke friction with increasing speed is observed for the double-lip seal, differing from the single-lip friction behaviour. Instead, there is a moderate increase in instroke friction at intermediate sliding speeds that took place less abruptly than with the single-lip seal. For the highest pressure investigated (figure 2-22) the increase in instroke friction takes place over a decade of magnitude of sliding speeds, while occurring over a greater range of speeds at lower pressures.

At a sealed pressure of 80 bar (figure 2-22) the double-lip seal maximum friction (mean of instroke and outstroke) is around 200 N. This was significantly lower than the corresponding friction value of 260 N for the single-lip seal. By contrast, at lower sealed pressures (10 bar and 20 bar) the double-lip seal has higher creep speed friction than the single-lip seal. For the double-lip seal the creep speed friction at 10 bar was approximately 0.44 of the corresponding friction level at 80 bar compared with 0.13 for the single-lip seal, indicating the double-lip seal to have a higher offset in the friction-sealed pressure relationship.

Figure 2-23 shows the processed friction-sliding speed results for three different specimens of the double-lip seal. These results were carried out with reduced stroke lengths for 5 mm/s, hence the data points for this range of speeds are not directly comparable with figures 2-20 to 2-22. Overall there is little variation in the qualitative friction characteristics between different seal samples at intermediate-to-higher speeds with moderate variation in the absolute friction levels.

2.4 Discussion of constant velocity friction results

2.4.1 Decrease in friction with rising speed

The decrease in friction with rising speed for 60 and 80 bar sealed pressures (figures 2-17 and 2-18) is quite consistent with most previous experimental studies of hydraulic seals. Two sets of published U-cup friction data from seal manufacturers [3, 9] indicate a decrease in friction of approximately 50% as the sliding speed is increased, which is of similar magnitude to that observed at 80 bar in the current study. However, these investigations show significantly different ranges of speed over which the decrease in friction occurs. In the current investigation the vast majority of the decrease in friction is completed once a rod speed of 2 mm/s is reached, whereas the friction troughs published by Papatheodorou [9] and Hunt [3] occur at approximately 17 mm/s and 100 mm/s respectively.

Differences in seal dimensions may be partially responsible for the discrepancy between the speeds over which the reduction in friction occurs. The study reproduced by Hunt was carried out for a rod diameter of 60 mm and the Papatheodorou paper used a similar 63 mm rod size while the current study used a significantly lower diameter rod of 16 mm. The U-cup seal in the present study also had a correspondingly lower axial length which may have scaled the speed range over which the friction transitions took place. Whether the speed-dependent friction behaviour is affected by the scale of the seal can offer inferences into what type of tribological phenomena is responsible for friction generation. If friction generation is governed mainly by asperity-scale contact mechanics, the Stribeck curve for a particular seal geometry and sealed pressure would be expected to be independent of the scale of the seal dimensions. The axial contact length would be expected to become important if the transport of fluid across the contact region is important. The lower critical speed in the current study suggests the level of fluid entrainment underneath the seal may influence the overall friction properties.

It was considered whether the differences in sliding speeds associated with the friction transitions could have been the result of differences in experimental technique. Papatheodorou's study used a similar B3 profile seal to the current investigation and a well documented testing procedure, allowing inferences to be made concerning the sources of

differences in measured friction with the current study. An obvious possible cause is the difference in stroke length between Papatheodorou (300 mm) and the current investigation (160 mm) where a longer stroke may have allowed a friction level closer to the steady-state level to be reached. However, friction decreases across the stroke (section 2.3.1), indicating a longer stroke to produce lower mid-point friction levels and correspondingly lower speeds would be required to produce a particular decrease in mid-stroke friction. This suggests the difference in friction transition speeds with previous studies cannot be accounted for by differences in the experimental setup and that the B3 rod seal with smaller dimensions can be reasonably identified as having a lower transitional speed.

2.4.2 Creep speed behaviour

No consistent relationships between sealed pressure, sliding speed and friction can be observed over the sub-1 mm/s creep speed region. For example, a minimal decrease in friction at 60 bar was measured as a result of increasing the speed from 0.1 to 0.2 mm/s (figure 2-17), although a large decrease in friction during instroke was recorded at 80 bar for the same change in speed (figure 2-18). This inconsistency in creep speed behaviour between similar pressures suggests either the friction does not have well-defined Stribeck curves in this speed range or that the experimental setup was not suitable to capture these friction characteristics.

Few published investigations exist concerning hydraulic seal friction at creep speeds. The most relevant previous study to the current experiments (Papatheodorou [9]) did not include multiple friction measurements at speeds lower than 1 mm/s and offers useful validation only for higher sliding speeds. Any comparison between the current creep speed experimental results and other studies would have to use previous friction studies that are not specific to hydraulic sealing applications.

Previous studies on dry rubber [44] indicate that friction approaches a discrete value as the sliding speed approaches zero, while others such as Roth [58] measured an increase in friction with sliding speed. Several investigations of dry rubber friction such as Grosch [59] report logarithmic relationships between friction and sliding speed. Lubricated rubber is more complicated to investigate experimentally due to issues in controlling the degree of lubrication and the large variety of available lubricants. One such study of lubricated polymers is Ettles [60] where dry rubber friction was found to decrease over intermediate sliding speeds while the corresponding friction for lubricated rubber showed an increase for the same speed range. This suggests the friction characteristics of polymers and elastomers to be highly dependent on the lubricating conditions and that there is no previous study that would be directly comparable to the measured creep speeds in the current investigation.

There is significant scatter in the force sensor data over the creep speed regions. For a sealed pressure of 80 bar (figure 2-18) and 0.1 mm/s sliding speed the mean standard devia-

tions of the five instroke and outstroke friction data points are 24.4 N and 38.8 N respectively. Similarly, for 0.2 mm/s at the same pressure the corresponding standard deviations are 38.6 N and 78.7 N, indicating significantly greater friction variation during outstroke than during instroke. There are two possible causes of this difference in force scatter between instroke and outstroke; differences in the instroke-outstroke behaviour of the rod seal itself, or unsteady rod motion.

A single-ended (and therefore unequal area) hydraulic actuator was used to extend and retract the rod. Different magnitudes of valve spool displacement were required between instroke and outstroke to achieve a particular constant speed. During instroke (relative to the rod seal and housing block) the extension of the actuator was expected to require a lower valve opening than outstroke where pressurised fluid was supplied to the annular side of the cylinder. The P and I values used in the PI controller were identical for instroke and outstroke and may have been more suitable for achieving steady motion during creep speeds with the lower valve settings associated with instroke motion. Due to the sensor noise in the position sensor data the steadiness of motion at creep speeds could not be accurately measured, hence the cause of the difference in friction scatter between instroke and outstroke cannot be definitively identified.

2.4.3 Abrupt friction increase within intermediate speed range

The unexpected abrupt increase in measured friction at intermediate velocities (approximately 2 mm/s to 10 mm/s) has not been reported in established experimental data for the general U-cup design [3] where only a gradual rise in friction of minimal magnitude is reported at higher speeds. There are limitations to validating experimental results against pre-1990s published results due to the unavailability of detailed experimental procedures and raw experimental data. The curves reported from the data may obscure regions of significant scatter or friction transition regions, while differences in run-in periods or stroke length may significantly influence the results. Therefore the non-appearance of this abrupt friction increase in established seal data does not necessarily discredit this observation in the current study.

The recently published friction study by Papatheodorou [9] is significantly more relevant for validating the current experiments than most previous investigations of seal friction, using a similar seal type and being carried out to the ISO 7986 standard. This study did not report a region of significantly increasing friction while using a range of sliding speeds with an interval of approximately two points per decade in the region of interest (specifically 1.7, 8.3, 16.7 and 25 mm/s). A possible explanation for this difference was that Papatheodorou's study may have had an abrupt increase in friction outside its experimental range of sliding speeds as this larger seal was known to experience other changes in friction level at higher

speeds than the current study (discussed in section 2.4.1). Alternatively, it could be that the abrupt friction increase takes place only with smaller scale seals and the Stribeck curves are not precisely scalable between different scales of seal geometry.

Figure 2-19 shows additional friction measurements carried out over the friction transition region for the single-lip seal, showing there to be a second pronounced minimum in the friction level at 30 mm/s. This is unexpected as Stribeck curves normally have only a single minimum friction level in most applications. Both the friction minima at 2 mm/s and 30 mm/s show a high degree of repeatability with only minimal friction variation between successive strokes, indicating these minimum points to have well defined speeds and friction levels. There is a relatively high degree of scatter between the two minima in friction, showing the friction levels to be less repeatable and well defined throughout a significant amount of the transition region.

2.4.4 Instroke-outstroke comparison

Figure 2-18 indicates there to be some moderate differences in the behaviour of the rod seal friction between instroke and outstroke. One of the main differences is the appearance of a region of increased friction at higher speeds during instroke that does not appear to occur during outstroke. The inability to precisely identify the offset for the friction measurements results in a systematic error in all the friction measurements produced. This inaccuracy in the force offset inhibits producing a firm conclusion of whether friction is higher in instroke or outstroke for most of the range of speeds.

The difference between instroke and outstroke at the higher pressures is significantly different than that previously reported for rectangular section seals [11]. This earlier study reported significantly higher friction during outstroke than in instroke with the fluid film during outstroke appearing to collapse at higher pressures (greater than approximately 30 bar). The current study provides no indication that the fluid film collapses during outstroke only with no evidence of correspondingly different friction characteristics. The earlier study also suggests friction to follow a $u^{0.5}$ power law during instroke in agreement with classical hydrodynamic theory. No evidence of such an increase in friction was observed in the current study where the possible increases in friction at higher speeds have a power law coefficient significantly lower than 0.5.

2.4.5 Friction variation across stroke

Friction decreases during instroke as the stroke progresses with the magnitude of the changes being most significant at creep speeds (figure 2-8). At intermediate speeds (e.g. 5 mm/s shown in figure 2-9) friction is shown to decrease across the full length of the stroke, indicating no equilibrium friction to be reached by the mid-stroke position. This suggests the Stribeck

curves produced may overestimate the minimum steady-state friction at intermediate speeds, hence also underestimate the overall variation in friction with sliding speed. At higher speeds friction variation with time is less significant as can be observed in figure 2-10 where the friction was approximately constant throughout most of the stroke length.

During outstroke there is a distinctive friction increase at creep speeds and lower speeds. This friction increase across the stroke is pronounced only for lower to intermediate speeds. In general there is a greater magnitude of friction variation across the stroke during instroke than during outstroke. This difference is less pronounced at creep speeds (figure 2-8) where there is significant fluctuation in the outstroke friction, although highly distinctive at lower to intermediate sliding speeds (figure 2-9). There is also significant variation between instroke and outstroke in the length of the stroke over which the initial friction change takes place. At intermediate sliding speeds the friction transition during instroke extends to encompass the full 160 mm stroke length while the corresponding friction change during outstroke takes place within the initial 10% of the stroke.

2.4.6 Possible factors affecting experimental friction measurements

2.4.6.1 Sealed pressure fluctuations

A possible source of inaccuracy in the experimental results was the variation in sealed pressure as a result of the variation in net flow into the housing to make up the volume swept by the rod. Inaccuracy from this source was significantly reduced through use of an accumulator as discussed in section 2.2.1.3. For a target sealed pressure of 80 bar the actual pressure does not vary by more than 0.5 bar at the highest speeds (as seen in the measured pressure trace in figure 2-12) with significantly lower variations for most of the speeds used. Variation in sealed pressure is similarly minimal for the other test pressures with the exception of the lowest sealed pressure (10 bar). At this low pressure significant pressure variations occur at the highest speeds (4 bar pressure variation for 300 mm/s as shown in figure 2-13). The pressure variations at 10 bar are less significant at intermediate or lower speeds (less than 0.5 bar for a speeds of up to 50 mm/s). The pre-charge pressure of the accumulator is likely to have been too high to allow charging at a 10 bar working pressure and the accumulator may not have provided any significant action to reduce the pressure fluctuations at this pressure.

Any influence of sealed pressure fluctuations on the friction results is expected to have been limited to the small subset of the highest rod speeds with a sealed pressure of 10 bar. For these cases the actual sealed pressure was significantly higher than 10 bar during instroke due to the fluid displaced by the rod raising the flow rate through the relief valve and restrictions in the downstream fittings. During outstroke the sealed pressure was reduced as a result of the lower flow rate through the relief valve and other restrictions in this line. One expected effect of the increased sealed pressure is an increase in measured friction as the seal is pressed harder

against the rod, which would appear on the Stribeck curve obtained for 10 bar (figure 2-14) as excessively high friction at higher speeds during instroke and lower friction during outstroke. There is no clear appearance of this type of behaviour in the experimental results where moderate increases in both instroke and outstroke friction can be observed for increasing rod speeds between 100 mm/s and 300 mm/s. At low sealed pressures other speed-dependent characteristics of rod seal friction appear to have dominated over the expected contribution from sealed pressure variation.

2.4.6.2 Relevance of sensor uncertainty for measured friction

The most direct source of uncertainty in the measured friction is the repeatability of the load cell. A hysteresis of 0.2% of the measurement range (8.8 N) and repeatability of 0.05% (2.2 N) of the measurement range are quoted for this component [61]. This implies a minimum uncertainty of 10 N in the absolute values of friction for any experiments using this model of load cell. For typical values of friction between 100 N and 200 N the load cell hysteresis introduces an uncertainty of between 5% and 10% to the final friction results. These relatively high uncertainties are a consequence of using a load cell with a significantly higher force rating and measurement range than the typical values of friction. Use of load cell with a rating in the kN range was necessary to withstand the force applied on the rod face by the pressurised fluid. A more ideal design of test rig would have the end of the rod outside the sealed fluid to avoid having high axial forces acting on the rod while retaining the ability to measure both directions of stroke independently.

A further influence of sensor inaccuracy on the zero of the force values arose from the pressure transducer. Data from the load cell were postprocessed to compensate for the force from the pressurised fluid at the rod face. This force correction is based on a measured relationship between the readings at the pressure transducer and load cell (section 2.2.3). The pressure transducer is known to have a typical repeatability of 0.1% of the measurement range (0.35 bar) with an upper limit of 0.5% (1.8 bar) of the measurement range [62]. A 0.35 bar uncertainty corresponds to an approximately 7 N inaccuracy in the corresponding force if this pressure acts over a 16 mm diameter section. Inaccuracy in force measurement from sealed pressure variation is a consequence of having one end of the rod submerged in the pressurised fluid and could be completely eliminated by sealing both ends of the housing and having the rod face exposed to the atmosphere. Pressures sensor based frictional inaccuracy was expected to appear as an additional random error in the final friction values obtained.

2.4.6.3 Issues relating to zeroing of friction results

One of the important sources of inaccuracy in the friction measurements produced is in the correct determination of the friction offset. Inaccuracy in this offset value is equivalent to a

systematic error in all friction values produced. For any sliding speed the friction offset does not affect the force difference between instroke and outstroke (where friction force is taken as positive in a fixed direction regardless of direction of travel). The mean of instroke and outstroke friction is also unaffected. Friction offset directly affects the difference in friction magnitudes between instroke and outstroke. This inaccuracy limits the ability of the data to support quantitative comparisons between instroke and outstroke friction.

An approximation to the maximum uncertainty in the friction offset can be obtained by inspecting the friction measurements for low sealed pressures of 10 and 20 bar (figures 2-14 and 2-14). If negative friction is assumed not to occur, the friction offset in figures 2-14 and 2-15 is limited in range to approximately 20 and 40 N respectively. This suggests an uncertainty in friction offset of ±10-20 N is appropriate for the full experimental range of sealed pressures.

It is not possible to accurately obtain the friction offset through inspection of data from the load cell data due to uncertainty in the loading on this component once the rig was assembled. In the assembly sequence the rod was inserted through the rod seal and housing before being threaded to the load cell. An offset force was applied to the load cell during the attachment of the rod. It was not possible to accurately measure this offset force as it could not easily be separated from the friction between the rod and seal. Both the actuator and seal housing were bolted to the bedplate in positions that prevent the rod from being easily attached to the load cell before inserting the rod through the rod seal. Therefore the preload acting on the rod could not easily be isolated from the force contribution from seal friction.

2.4.6.4 Repeatability of friction measurements

For most of the combinations of sealed pressures and sliding speeds there is a reasonable degree of repeatability between successive strokes with an approximate scatter of approximately ±(5-10) N. This variation in friction at each sliding speeds is significantly lower than the changes in friction that took place over the range of sliding speeds investigated, allowing the speed-dependence of friction to be quantified and for the data to clearly illustrate this speed-dependent behaviour with simple inspection. Repeatability was relatively poor over the creep speed (sub-1 mm/s) range where a mean scatter of several tens of Newtons is present. Possible explanations for the lower repeatability at these creep speeds are discussed in section 2.4.2. Similarly, there is a particularly high degree of scatter at the abrupt increase in instroke friction discussed in section 2.4.3.

2.5 Closure

Experiments have been carried out for the constant velocity friction of single-lip and double-lip rod seals in order to verify simulations for the tribology of hydraulic seals. Special at-

tention was paid to the direction-dependence of friction as distinctive direction-dependence was predicted by standard mixed lubrication simulations and has yet to be extensively verified. The test rig had one side of the rod enclosed by the housing to remove the need for a second sealing element between the rod and housing and allow the friction from the single rod seal to be ascertained. It was necessary to correct for the force exerted on the rod face by the pressurised fluid to obtain the friction values. A different test procedure to the ISO 7986 standard was adopted as it was not practical to carry out the extended run-in periods specified in the standard with the experimental facilities available.

For the relatively high sealed pressures of 60 and 80 bar, friction is shown to significantly decrease at lower to intermediate sliding speeds with most of this friction decrease taking place before a sliding speed of 2 mm/s is reached. Similar friction decreases have been reported in previous experimental studies with larger U-cup seals, although taking place at higher speeds. It is difficult to ascertain accurate friction characteristics in the creep speed region where there is relatively poor repeatability between successive strokes. No reliable inferences can be made over the friction trends or peak friction levels in this region. It is not known whether the high degrees of scatter are due to the seal itself having erratic friction characteristics at creep speeds or whether any of the effect was due to unsteady motion in the actuation system.

There is an unexpected abrupt increase in instroke friction at intermediate sliding speeds. This friction increase shows some minor dependence on the sealed pressure, reaching a maximum magnitude at approximately 60 bar. Previous investigations of rod seal friction have not recorded similar abrupt friction increases, suggesting this phenomenon may be either unique to relatively small sized seals or occur outside the operating speed range in larger seals.

Instroke and outstroke friction have similar speed-dependent characteristics at higher sealed pressures for the single-lip seal. One of the main differences between instroke and outstroke is the unexpected abrupt friction increase that is only present during instroke. Otherwise there is a reasonable qualitative agreement between instroke and outstroke. It is difficult to accurately determine the friction offset and by extension the absolute differences in friction between the different directions of travel.

At low sealed pressures there is no significant decrease in instroke friction between creep speeds and intermediate to higher speeds compared with that observed at higher pressures. During instroke the lower sealed pressures are associated with relatively low creep speed friction levels compared with higher sliding speeds. The outstroke friction continues to exhibit a significant decrease in friction between creep speeds and higher speeds for the lower sealed pressures.

The double-lip seal exhibits broadly similar friction characteristics compared with the single-lip seal. Between creep speeds and intermediate speeds the friction level decreases by approximately 50% which is comparable to the behaviour of the single-lip seal at higher sealed

pressures. No abrupt increase in friction with sliding speed is observed with the double-lip seal, suggesting this unexpected feature in the single-lip seal friction data may not be directly caused by the unusual test rig configuration. There is a moderate increase in friction at higher speeds in both instroke and outstroke instead of an abrupt step increase.

Chapter 3 extends on the measurement of friction for steady-state constant velocity motion to investigate transient friction variation. Significant friction variation across the stroke is observed under certain operating conditions, suggesting transient friction behaviour could be important for general actuation applications. This transient friction variation may also affect the constant velocity friction measurements if steady-state conditions are not reached by mid-stroke. Sinusoid rod motion was used to investigate the transient friction characteristics across the stroke as this type of motion is easily generated and contains fewer variables than repeated ramp inputs or similar alternatives.

Chapter 3

Friction induced by sinusoid motion in hydraulic rod seals

Sinusoid motion provides an alternative assessment of the variation in friction across the stroke compared with constant velocity experiments. It is useful to experimentally ascertain the transient friction characteristics in order to determine under what types of load cycles they become significant.

Experiments for constant velocity motion involve rapid changes in sliding velocity at the limits of each stroke and it is difficult to determine a unique logical velocity profile to use for these velocity transitions. A precise step-change in sliding velocity is not possible due to the required impulse actuation and it is necessary to ramp the sliding velocity. It is possible that the velocity profile during the changes of stroke direction may affect the friction levels in the following transient friction characteristics. In contrast, sinusoid motion involves a well-defined and consistent velocity profile near the limits of each stroke.

Sinusoid motion is often produced by hydraulic actuators, e.g. in high frequency applications such as fatigue testing. Friction during sinusoid motion is directly relevant for such applications where the seal friction acts to reduce the maximum load amplitude the actuator can deliver. During high frequency oscillation seal flexibility can become important as the reduced stroke lengths may become comparable with the deflections due to seal compliance. Under these conditions the friction between the rod and seal may involve significant flexing motion in addition to the relative sliding expected for steady-state motion with constant velocity.

This chapter presents measured friction-velocity and friction-displacement characteristics during sinusoid motion. This has been carried out for low frequency motion with prolonged periods at low sliding speeds and for relatively high frequencies up to 60 Hz. Two different types of rod seal were used; single-lip and double-lip corresponding with the types used in the constant velocity friction measurement in chapter 2.

Simulations are also presented for the transition between rocking and sliding motion where the seal is assumed to flex axially with a particular stiffness, viscosity, inertia and limiting value of static friction. Analysis of the seal material properties, dimensions and possible deformation modes indicates the seals to have natural frequencies in the kilohertz range. This suggests the system would normally operate below its lowest natural frequency. Results are presented for a range of different amplitudes of excitation displacement and for a range of different damping factors to reflect the uncertainty in the damping properties of the seal material. The simulation results are compared with the experimental measurements.

3.1 Experimental procedure

The experimental apparatus was identical to that used for constant velocity friction measurements described in section 2.2.1. Modifications were made to the experimental procedure to allow sinusoidal motion. It was also necessary to adapt the data postprocessing to allow pressure corrections to be applied to the measured force where the sealed pressure varies significantly across the cycle.

The run-in procedure for the seals was unchanged from the experiments for constant-velocity friction measurement. A run-in period of 1 hour (3 375 cycles) of a triangular wave (stroke 160 mm, speed 300 mm/s) at 80 bar sealed pressure was carried out once. Following this single run-in period, tests were carried out for different sealed pressures and frequencies. For each test the required sealed pressure was set by adjusting the cracking pressure on the relief valve. The rod was excited through a sine wave of the required frequency and amplitude for a period of 2 minutes to allow steady-state conditions to be reached, then the sensor data were recorded for a period of 50 complete cycles.

The number of sample intervals between measured and recorded sensor data was varied between different frequencies to avoid excessive file sizes with the low frequency tests. Sampling intervals of 200, 100, 50, 25, 10, 5 and 2 data points were used for respective excitation frequencies of 0.02, 0.05, 0.1, 0.2, 0.5, 1 and 2 Hz and a downsampling rate of 1 (recording all measured sensor data) for sinusoid frequencies higher than 2 Hz. A sampling rate of 6 kHz was used throughout the experiments.

For each sealed pressure a range of intermediate frequencies of 0.5, 1, 2, 5, 10 and 25 Hz was used with corresponding displacement amplitudes 100, 50, 25, 10, 5, 2, 1 and 0.5 mm. This range of frequencies and corresponding displacements corresponded with a demand velocity amplitude of approximately 300 mm/s, creating a range of sliding speeds comparable with the constant velocity investigation. For lower frequencies it was necessary to use lower velocity amplitudes due to the stroke limitation of the test rig. Further tests were carried out at 0.02, 0.05, 0.1 and 0.2 Hz each with a displacement amplitude of 100 mm. Tests were carried out at each frequency for sealed pressures of 10, 20, 40, 60 and 80 bar. An additional series of

tests was carried out at higher frequencies with the gains in the PI controller adjusted to allow an output displacement amplitude closer to the demand signal at higher frequencies. This later series of experiments was carried out at 80 bar with frequencies of 10 Hz to 60 Hz inclusive with 10 Hz intervals. It was not possible to get an accurate sine wave displacements at frequencies greater than 60 Hz with the PI position control system used.

3.2 Data postprocessing

3.2.1 Sensor data filtering

The displacement and pressure data were used to calculate the velocity and force correction profiles throughout the stroke, necessitating the use of filtering to remove the noise addition to these datasets. The displacement and pressure data were filtered in a forward followed by a reverse direction using a second order Butterworth algorithm with a dimensionless cut-off frequency of 0.02. This filtering was applied to the recorded sensor data which had been produced with a particular interval between measured data points. There may have been issues with using the low cut-off frequency for the highest sinusoid frequencies, which are close to the cut-off frequency. For the case of 50 Hz excitation, a cut-off frequency of 120 Hz was used, which is less than an order of magnitude higher than the excitation frequency. Varying the sampling interval between different frequencies has the effect of varying the sampling rate of the recorded data and hence the cut-off frequency used in the filter.

3.2.2 Pressure and inertia corrections and calculation of rod velocities

The velocity profile of the rod was calculated by numerically differentiating the filtered displacement profile using a central differencing method. Similarly, the acceleration profile was then calculated using central differencing from the velocity profile. To obtain the friction force from the filtered load cell data it was necessary to subtract estimates for the force profiles created by the fluid pressure acting on the rod face and the inertia forces from accelerating the rod. The force correction for the pressure effects was obtained from the filtered pressure distribution using the pressure-load characteristic obtained in the constant velocity testing in section 2.2.3. The inertia force correction from the rod was produced using Newton's Second Law with the mass of the rod calculated from its dimensions (16 mm diameter, 300 mm length) and density (7 800 kg/m^3).

To obtain the mean force and velocity values over a single sine wave 50 datasets were created, each with a length of time corresponding to a single period of motion. Following the initialisation of the data recording period, the beginning of the first sine wave was defined as the point where the demand position passed through the mean position with a direction of travel in the outstroke direction. Each dataset contained the sensor measurements for a single

sine wave cycle. For each data point in the datasets the mean force, pressure, displacement, velocity and acceleration were calculated from all fifty datasets. This produced a single dataset containing the mean results trace for a complete sinusoid.

3.3 Results for sinusoid testing

3.3.1 Friction data from sine wave motion

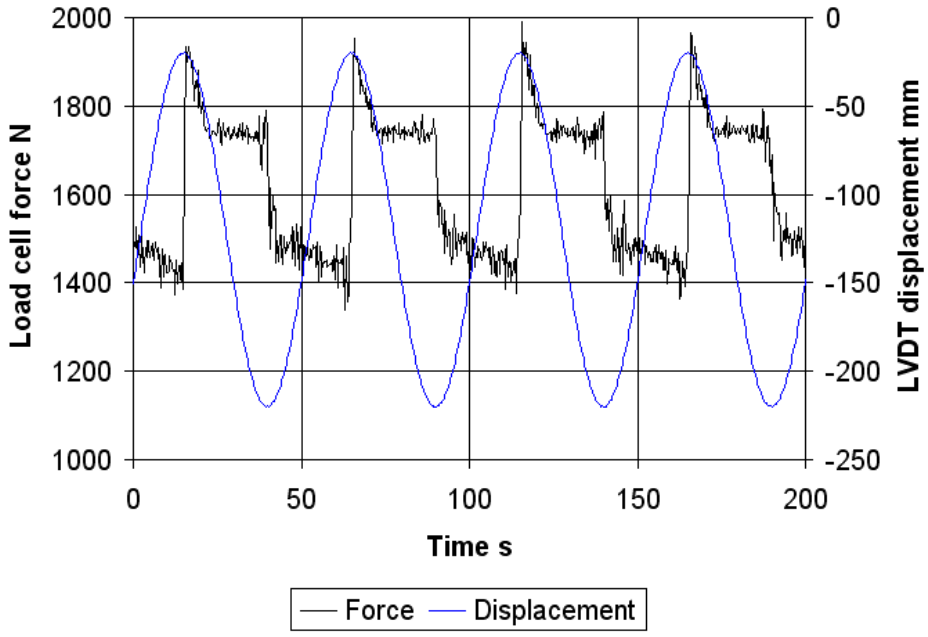

Figure 3-1: Unprocessed load cell and LVDT data for single-lip seal, 0.02 Hz sinusoid motion, 80 bar sealed pressure

Figure 3-1 shows an example of the data recorded from the displacement and load cell transducers, for the first four of the fifty recording cycles at 80 bar with a 0.02 Hz excitation frequency. Similarly to the constant velocity examples in section 2.3.1, the sensor data is plotted with the sign convention that compressive load cell readings are positive and displacement is negative in the direction of actuator extension (instroke relative to the seal and housing).

The force traces in figure 3-1 show distinctive peaks in friction magnitude as the end of the outstroke motion is approached. Once the instroke motion commences the friction magnitude is seen to decrease.

3.3.2 Friction-displacement and friction-velocity measurements from sinusoid motion

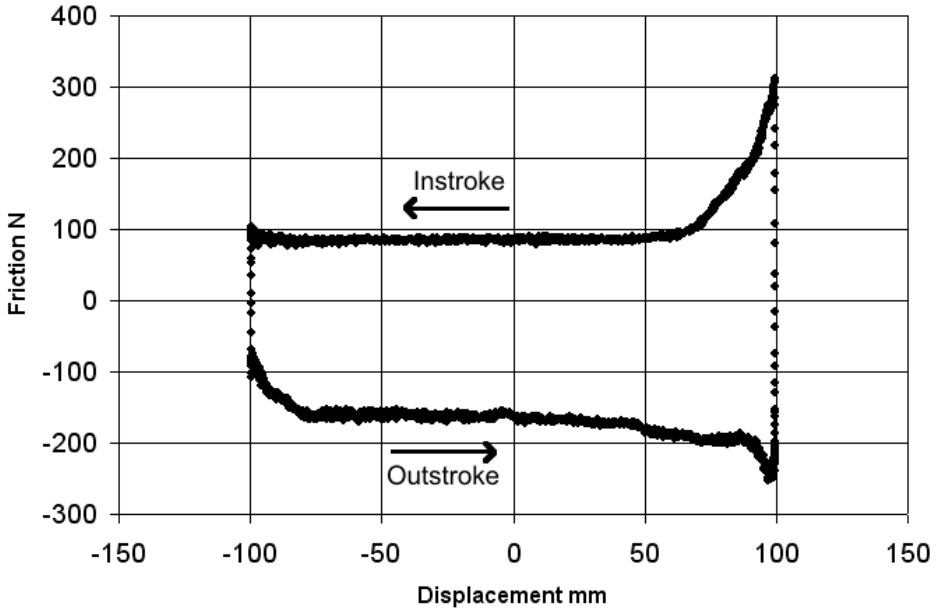

Figure 3-2: Measured friction against rod displacement for single-lip seal, 0.02 Hz frequency, 80 bar sealed pressure

Figures 3-2 and 3-3 show the respective friction-displacement and friction-velocity relationships for the single-lip seal at 80 bar sealed pressure and low frequency (0.02 Hz) sinusoid excitation. Additional friction-displacement and friction-velocity characteristics for a range of excitation frequencies up to 60 Hz are shown in figures 3-4 to 3-14.

At the lowest frequencies investigated (e.g. 0.02 Hz shown in figure 3-2) there is a large region of the stroke where friction is almost constant with the changing rod speed, as expected for Coulomb friction. Maximum friction levels occur near the locations where the rod is at its maximum extension from the seal. As the instroke motion begins the friction decreases until an equilibrium friction level is reached at a particular instroke sliding speed. For different frequencies there is no single consistent critical sliding speed below which the outstroke friction level increases. Comparison between figures 3-3 and 3-5 indicates the outstroke friction to begin to increase below a speed of approximately 10 mm/s for a 0.02 Hz sinusoid while at 0.05 Hz the friction increase begins once the outstroke speed falls below 21 mm/s.

As the frequency of the sinusoidal motion of the rod increases significant changes take place in the friction characteristics. At the highest frequency where a repeating sinusoid could be accurately maintained with the actuation system (60 Hz) there is an approximately linear relationship between friction and displacement (figure 3-14). The hysteresis loop formed on

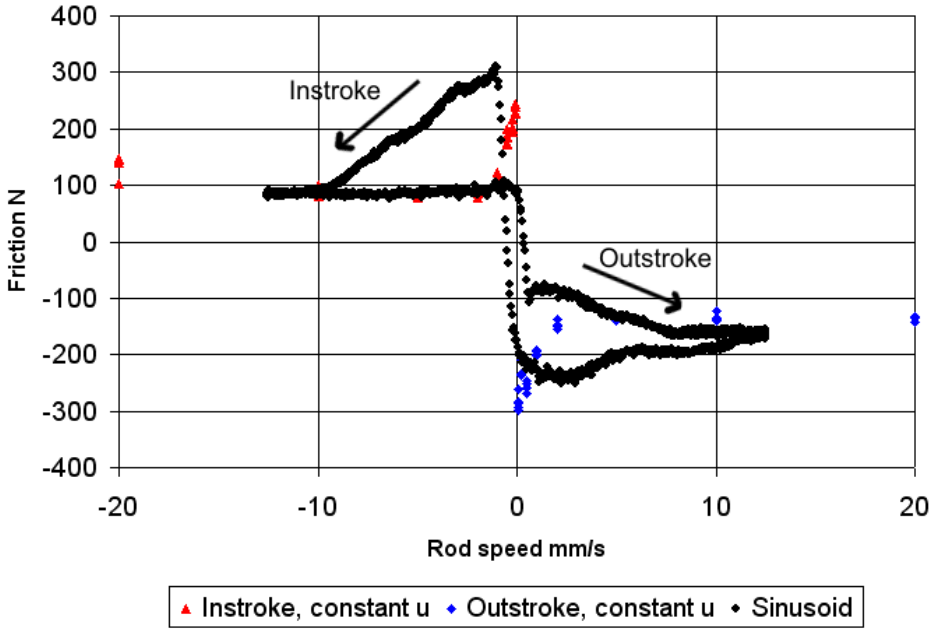

Figure 3-3: Measured friction against rod velocity for single-lip seal, 0.02 Hz frequency, 80 bar sealed pressure

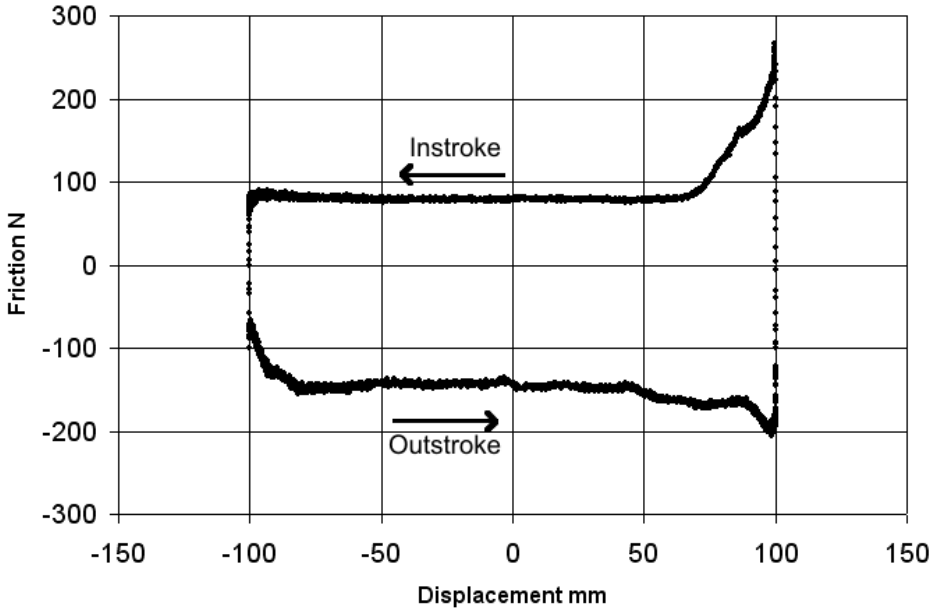

Figure 3-4: Measured friction against rod displacement for single-lip seal, 0.05 Hz frequency, 80 bar sealed pressure

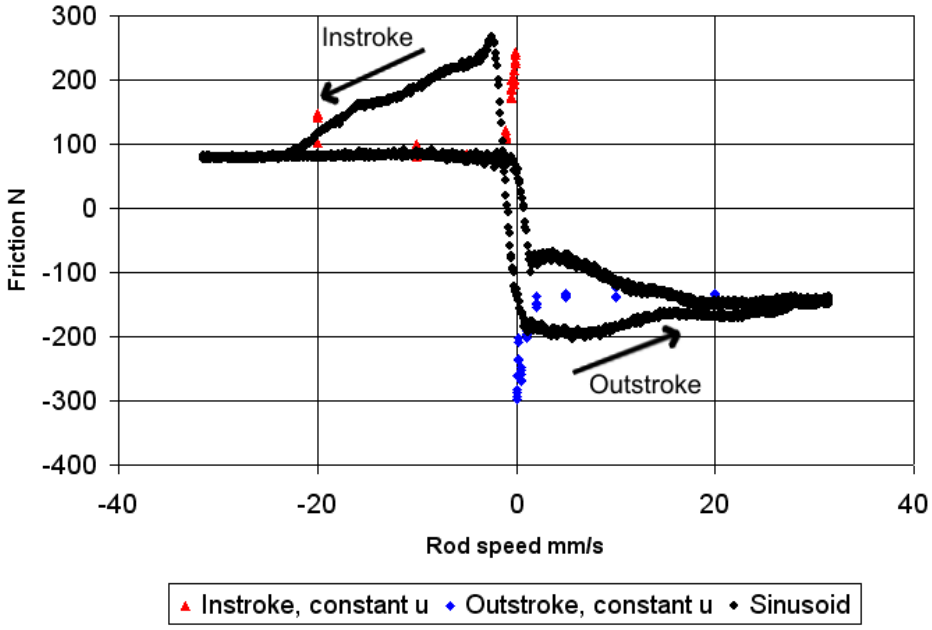

Figure 3-5: Measured friction against rod velocity for single-lip seal, 0.05 Hz frequency, 80 bar sealed pressure

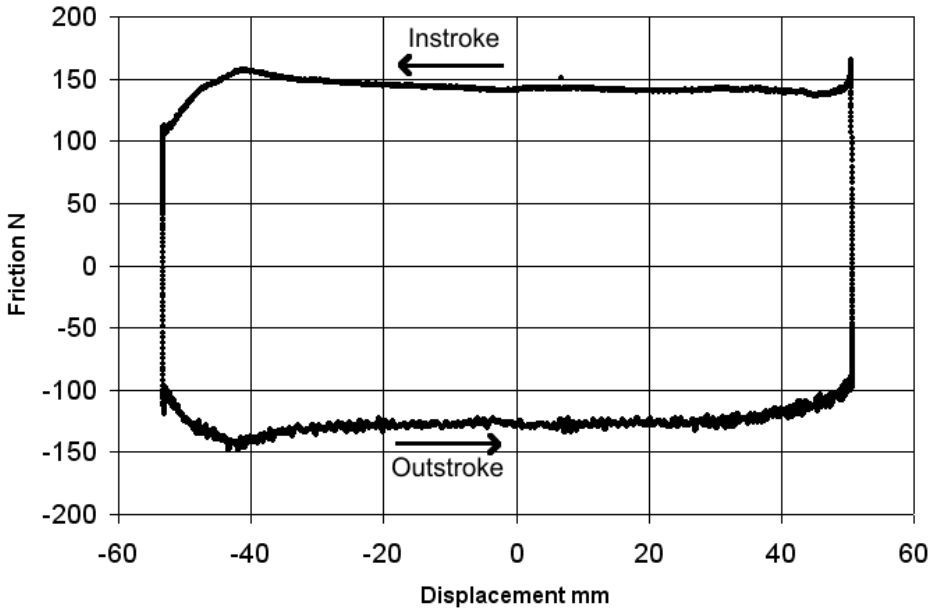

Figure 3-6: Measured friction against rod displacement for single-lip seal, 1 Hz frequency, 80 bar sealed pressure

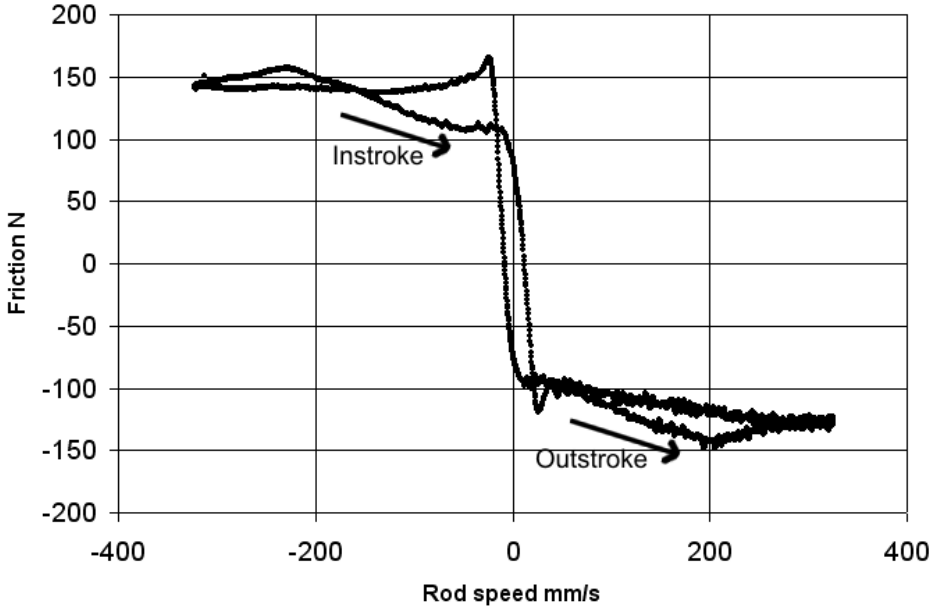

Figure 3-7: Measured friction against rod velocity for single-lip seal, 1 Hz frequency, 80 bar sealed pressure

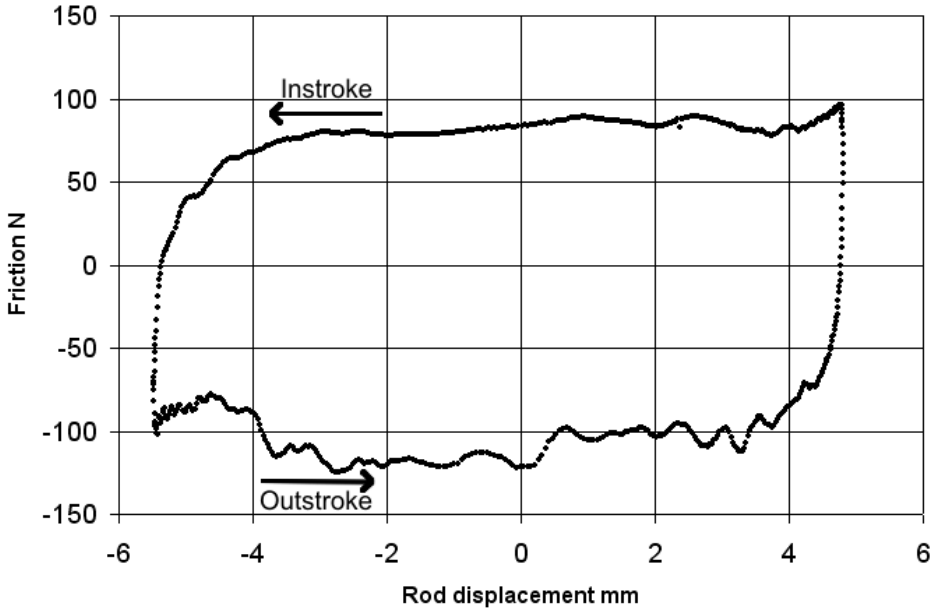

Figure 3-8: Measured friction against rod displacement for single-lip seal, 10 Hz frequency, 80 bar sealed pressure

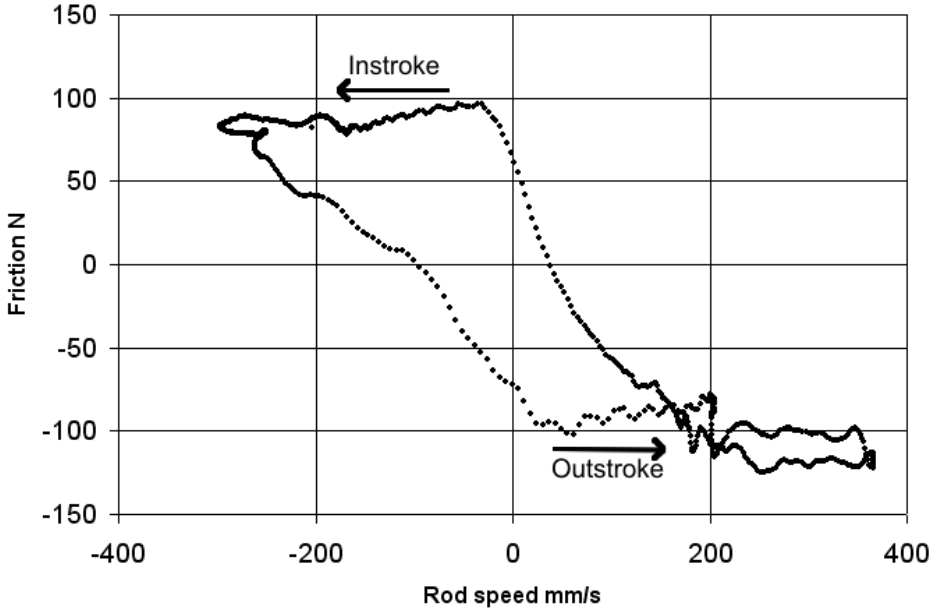

Figure 3-9: Measured friction against rod velocity for single-lip seal, 10 Hz frequency, 80 bar sealed pressure

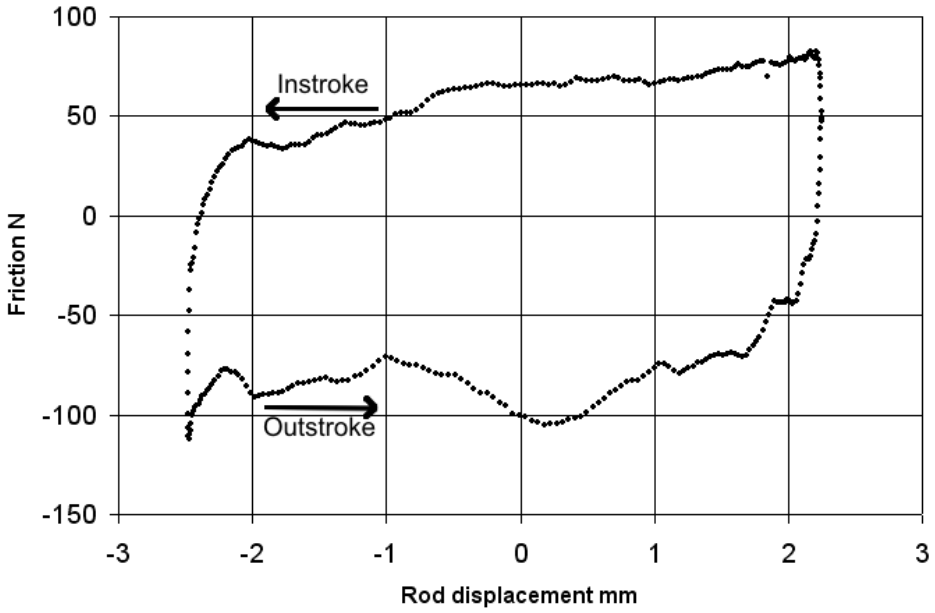

Figure 3-10: Measured friction against rod displacement for single-lip seal, 20 Hz frequency, 80 bar sealed pressure

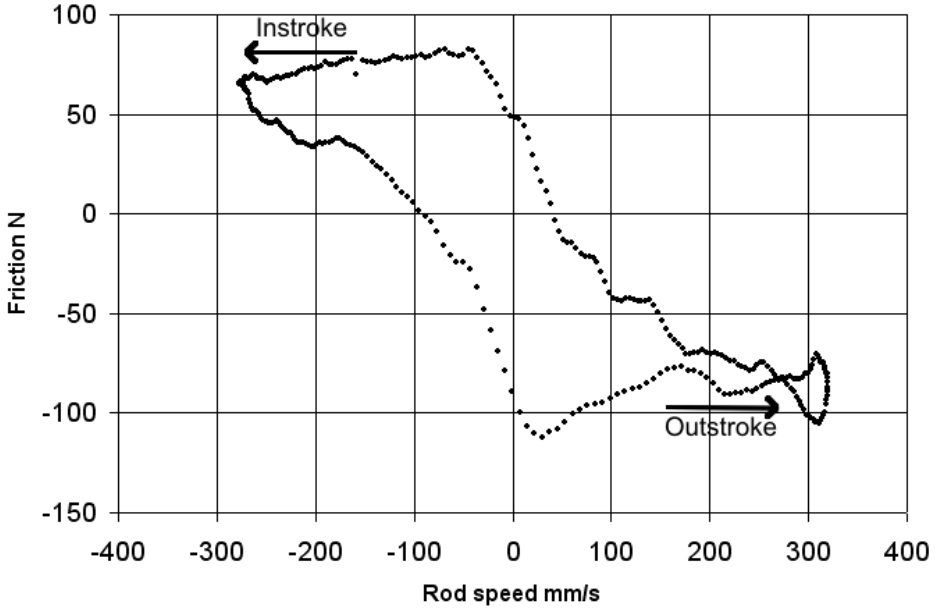

Figure 3-11: Measured friction against rod velocity for single-lip seal, 20 Hz frequency, 80 bar sealed pressure

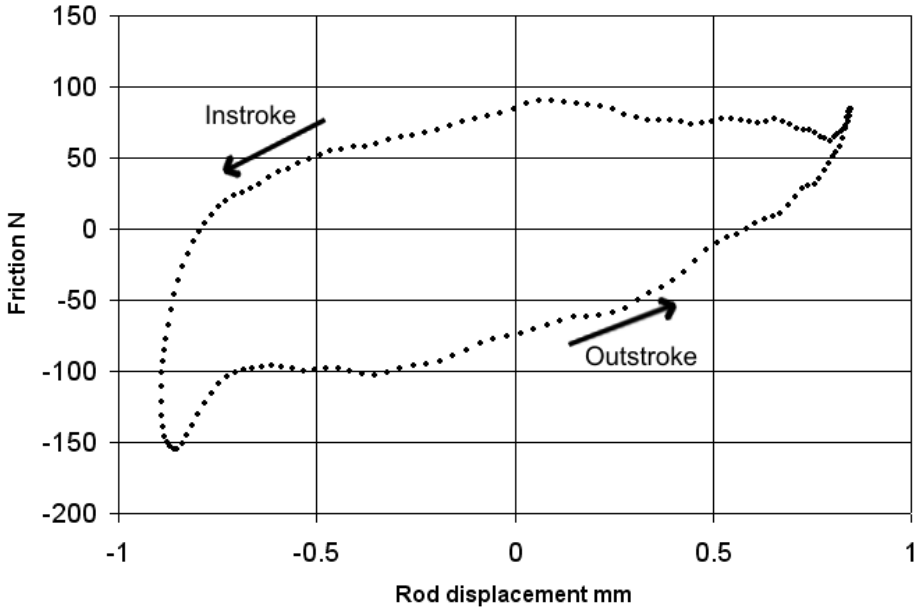

Figure 3-12: Measured friction against rod displacement for single-lip seal, 40 Hz frequency, 80 bar sealed pressure

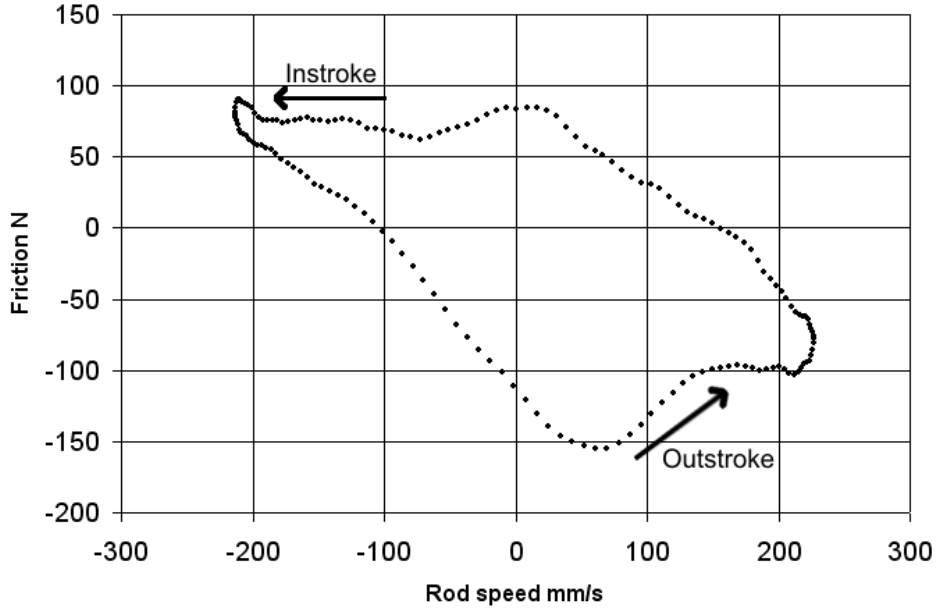

Figure 3-13: Measured friction against rod velocity for single-lip seal, 40 Hz frequency, 80 bar sealed pressure

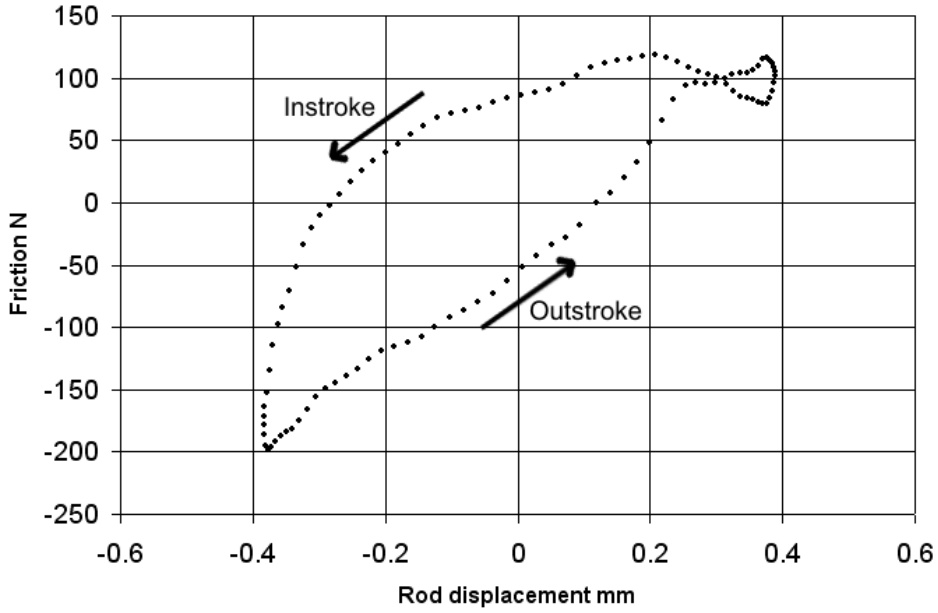

Figure 3-14: Measured friction against rod displacement for single-lip seal, 60 Hz frequency, 80 bar sealed pressure

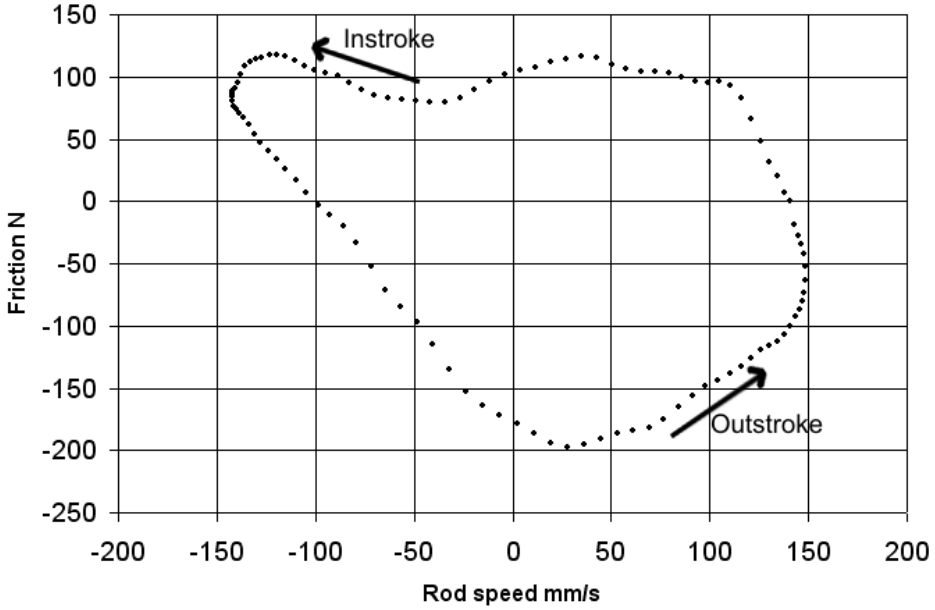

Figure 3-15: Measured friction against rod velocity for single-lip seal, 60 Hz frequency, 80 bar sealed pressure

the force-displacement characteristic at 60 Hz indicates the friction levels not to be identical in both directions of stroke, with greater dissipation during instroke.

Figure 3-16 shows the friction variation across a 20 Hz sinusoid displacement cycle for a range of different excitation amplitudes for the single-lip seal. For displacement amplitudes of 0.4 mm or more the friction-displacement characteristic approximates to a quadrilateral. For shorter strokes the force-displacement relationship does not easily separate into regions of similar friction and near-discontinuities in friction. A gradual increase in the maximum force experienced by the rod takes place as the displacement amplitude is reduced.

3.3.3 Pressure dependence of friction during sinusoid motion

Figure 3-17 shows the measured force-displacement characteristics of low frequency sinusoid motion for a range of different sealed pressures. The results show similar pressure dependent behaviour to that observed in the constant velocity measurements with a rise in friction across most velocities as the sealed pressure is increased. As was the case for the constant velocity testing, the measurements from sinusoid motion also indicate a greater increase in friction between 40 bar and 60 bar sealed pressures compared with pressure rises up to 40 bar. A possible exception to the positive relationship between friction and sealed pressure is the change in instroke friction between 60 bar and 80 bar. In this case there is a reduction in friction with higher sealed pressure for the higher instroke sliding speeds. At the lower sliding

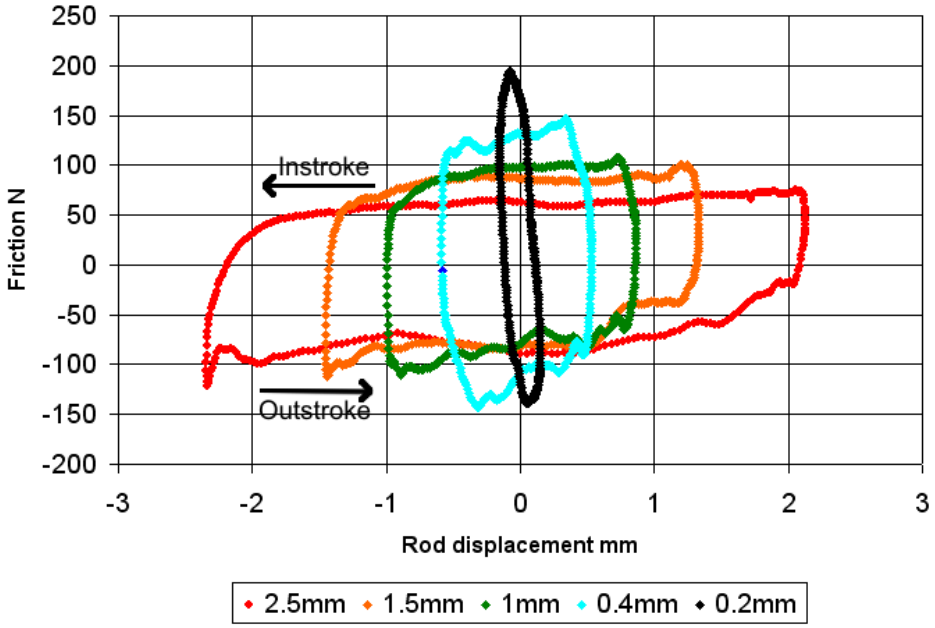

Figure 3-16: Measured friction against rod displacement for single-lip seal, 20 Hz at 80 bar sealed pressure, variable amplitude

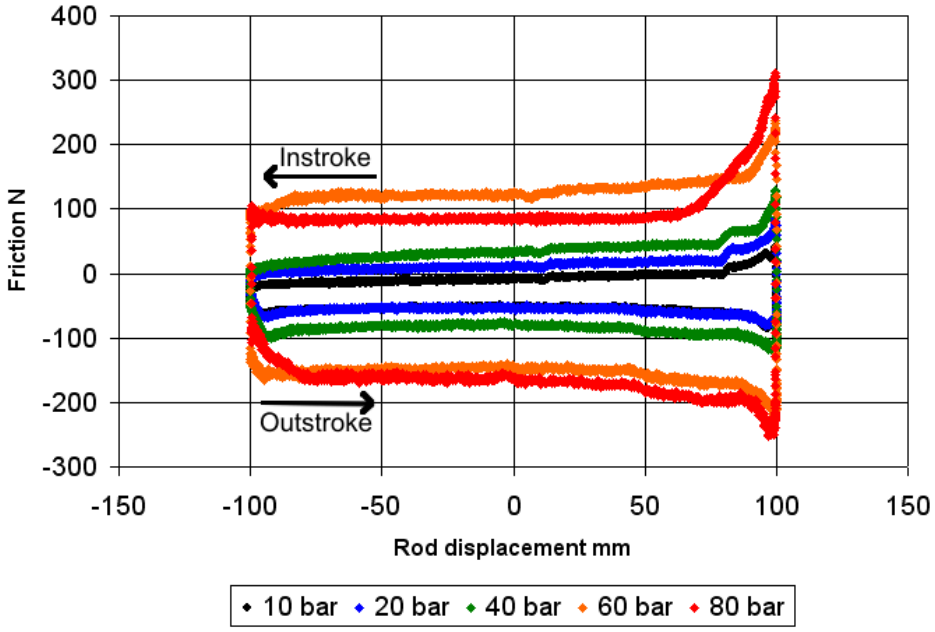

Figure 3-17: Measured friction against rod displacement for single-lip seal, 0.02 Hz sinusoid excitation, 10-80 bar sealed pressure

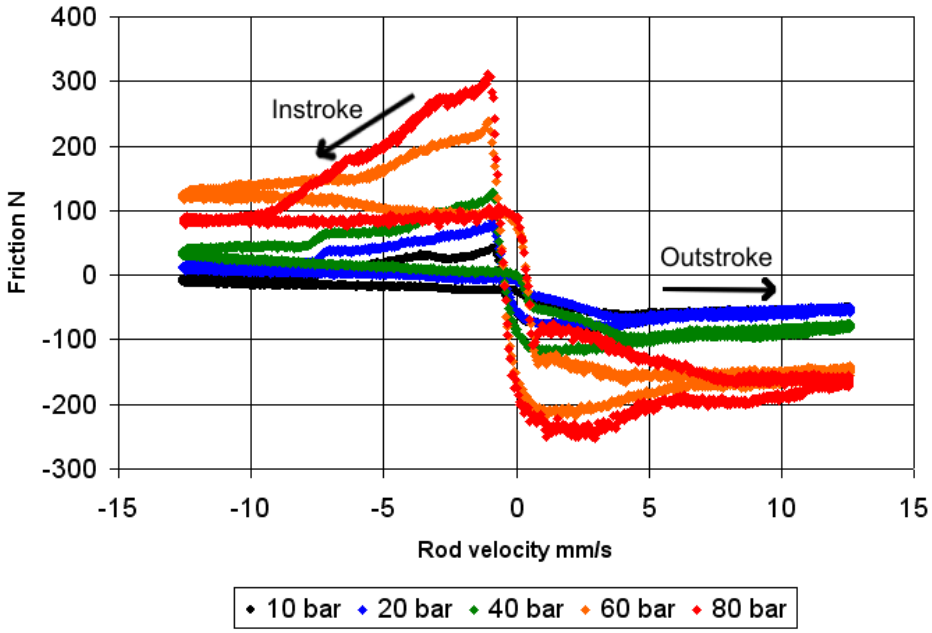

Figure 3-18: Measured friction against rod velocity for single-lip seal, 0.02 Hz sinusoid excitation, 10-80 bar sealed pressure

speeds associated with higher friction there is no decrease in friction between sealed pressures of 60 bar and 80 bar.

3.3.4 Friction results for double-lip seal during sinusoid motion

Examples of the friction measurements from the double-lip seal are shown in figures 3-19 and 3-20, for low frequency motion (0.02 Hz) and higher frequency (10 Hz) respectively, at 80 bar. In general, the friction-displacement relationship for the double-lip seal is comparable to those from the single-lip seal as is seen when comparing figure 3-19 with figure 3-2 and figure 3-20 with figure 3-8. One difference is that the double-lip seal shows less friction variation across the stroke. For the single-lip seal the friction decreases throughout the instroke region (figure 3-2) while the corresponding friction region with the double-lip seal stabilises by the mid-stroke position (figure 3-19).

The higher friction levels during periods of lower sliding speeds are similar for the single-lip and double-lip seals. For the lowest frequencies tested (0.02 Hz and 0.05 Hz), where the higher friction regions are most distinctive, the friction increases begin at similar positions and velocities during the motion and similar proportional changes in friction magnitude take place.

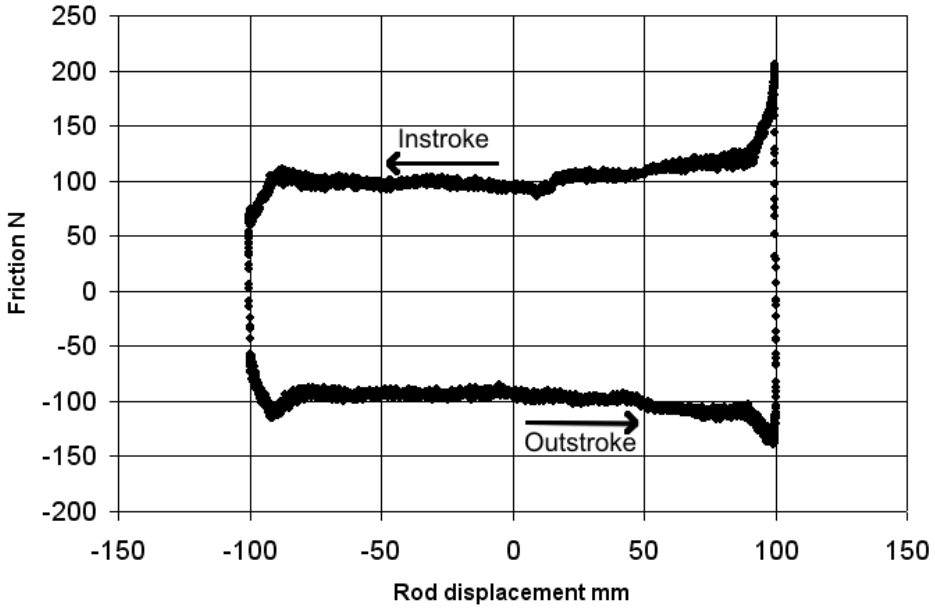

Figure 3-19: Measured friction against rod displacement for double-lip seal, 0.02 Hz frequency, 80 bar sealed pressure

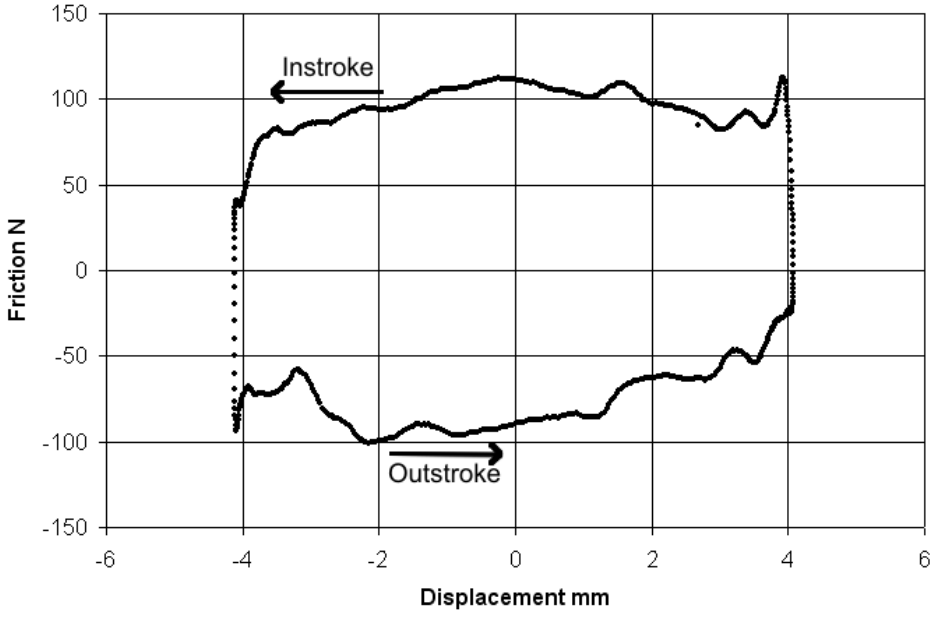

Figure 3-20: Measured friction against rod displacement for double-lip seal, 10 Hz frequency, 80 bar sealed pressure

3.4 Discussion of friction results from sinusoid motion

3.4.1 Frequency dependence of seal friction

The friction-displacement characteristics for low frequency motion (figure 3-2) indicate the friction characteristic to contain transients that cannot be expressed solely in terms of the sliding velocity. The reasonable degree of repeatability between successive constant velocity tests over long strokes in section 2.3.2 suggests that time-dependent friction terms eventually decay. The steady-state location of the increasing friction region during sinusoid motion may have been influenced by the proximity to the limit of the stroke in addition to its dependence on the local sliding speeds.

The force-displacement characteristics at 20 Hz (figures 3-10) and at other intermediate frequencies does not produce a "parallelogram" shape with distinctive regions of sliding with constant friction and rocking with a fixed gradient. Friction is clearly not constant during the sliding motion periods at either of these two frequencies. At 20 Hz excitation the friction increases throughout instroke and decreases during outstroke, indicating the coefficient of sliding friction to vary with time.

The maximum force experienced by the rod is observed to increase as the displacement amplitude is reduced. Friction between the rod and seal increases during instroke motion if the sliding speed falls below a particular level and is maintained below this threshold speed for a sufficiently long period. As the amplitude is reduced while the frequency is held constant, the sliding speed remains below a particular speed limit for a longer period of time. Decreasing the excitation amplitude to 1 mm at 20 Hz produces only moderate increases in the friction amplitude while further decreases beyond this value result in more significant friction increases. The friction amplitudes at lowest displacements tested are approximately double the friction amplitude at higher displacements.

3.4.2 Sinusoidal motion with double-lip seal

The friction-displacement relationships for the double-lip seal indicate there to be less friction variation across the stroke compared with the single-lip seal. This difference in the transient friction behaviour cannot be identified from the processed results for constant velocity friction in section 2.3.3 where only the mid-stroke friction level is quantified. A possible explanation may be that the secondary lip reduces the amount of lubricating fluid getting under the seal, causing the seal to dry out to an equilibrium level more rapidly. It is noted that the higher friction levels during periods of lower sliding speeds are similar for the single-lip and double-lip seals, each experiencing similar proportional changes in friction magnitude. The similarity between the friction characteristics of the two seal types suggests, for reasonably high pressures, the friction behaviour is dominated by the material lubrication properties and

the differences between contact pressure distributions are less significant.

3.4.3 Time-dependent variation of friction

Large speed-dependent increases in friction over low and sustained sliding speeds can be observed for the full experimental range of sealed pressures. For all sealed pressures the friction level begins to increase during the outstroke cycles of motion, reaches at plateau at the stroke limit, then decreases during instroke. There is a similar proportional change in friction between higher and lower sliding speeds for each sealed pressure with the mean of instroke and outstroke friction varying by a approximately factor of two. Inspection of figure 3-17 suggests the friction increase also takes place over a similar region of the stroke length in all cases. The speed-dependent characteristics of seal friction are independent of sealed pressure and loading for the 10-80 bar range investigated.

The results for sealed pressure variation across the sinusoid are compatible with the transient behaviour of the constant velocity experiments discussed in section 2.4.5. For this constant velocity testing the friction was shown to increase during at least the early stages of outstroke motion which is consistent with the friction increase occurring during outstroke for sinusoid motion. For the sinusoid testing the sliding speed did not become sufficiently low to allow a friction increase until near the end of the stroke. Similarly, instroke friction in the constant velocity testing was shown to decrease across the stroke which is compatible with the friction decrease observed following the start of the instroke motion during sinusoidal excitation.

3.5 Simulation of seal flexibility

Simulations have been produced for a flexible system with mixed sticking and sliding motion in order to help explain the measured friction characteristics during sinusoid motion. Suitable parameters for seal flexibility and limiting friction have also been estimated in attempt to quantify the range of frequencies and displacement amplitudes over which the transitions would be expected. This modelling of the effects of seal flexibility on overall friction is attached in appendix A.

3.6 Closure

Experiments with sinusoidal motion at lower and intermediate frequencies show a region at lower sliding speeds where friction reaches approximately double the level at higher sliding speeds. This friction increase takes place at low frequencies where low sliding speeds are maintained for a sufficiently long period. Friction is shown to begin to increase towards the end of the outstroke motion then decrease following commencement of the instroke phase.

This is consistent with previous measurements from constant velocity testing where, at low sliding speeds, friction decreases during instroke and increases during outstroke. There is no consistent threshold speed below which the friction increase begins, suggesting these friction increases to have some form of time delay. Little friction variation is observed over the intermediate speed ranges during low frequency motion. At intermediate frequencies there is significant friction variation throughout most of the sliding regions with the friction increasing towards the end of the outstroke phase and decreasing from the start of the instroke phase. These transient characteristics of the friction result in the simulated "parallelogram" friction-displacement characteristic not occurring in practice.

At the highest test frequency of 60 Hz there is an approximately linear relationship between force and displacement which is consistent with rocking motion below the natural frequency of the seal. There is a significant hysteresis loop present at this frequency, suggesting there may have been other sources of energy dissipation present than the viscoelastic properties of the seal material. An experimental stiffness 3.7 times greater than the predicted value was produced from the rocking motion experiments. This suggests the seal may have flexed in a different manner to the simple shearing assumed in the model. The double-lip seal is shown to have similar friction characteristics to the single-lip seal during sinusoid motion with a slight difference that the friction level for the double-lip seal reaches a constant value earlier in the stroke for most excitation frequencies.

Simulations have been carried out for seal friction characteristics during sinusoid motion for mixed sticking and sliding motion between the rod and seal involving seal flexibility. An adapted mass-spring-damper model was used to represent the flexing of the seal. Suitable parameters for the mass, axial stiffness and damping of the seal were obtained from a bulk parameter model of the seal undergoing shear deflection with the known approximate seal geometry and elastic properties. The seal is predicted to have a natural frequency of approximately 2.1 kHz, suggesting common hydraulic applications to operate significantly below the natural frequency. It is relatively difficult to estimate an accurate material viscosity, therefore a range of different damping coefficients were considered.

The mixed rocking-sliding simulations predicts a transition from proportional friction-displacement relationship at low displacement amplitudes to a "parallelogram" characteristic at higher displacement amplitudes. At high displacement amplitudes the displacement range of the friction transition region is predicted to become less significant relative to the overall stroke length. There are moderate increases in the velocity range associated with the friction transition region with increasing displacement amplitudes as a result of higher sliding speeds occurring at the low displacements. Variation in the damping ratio does not significantly affect the simulation results for excitation frequencies significantly below the system natural frequency. There is predicted to be a minor hysteresis loop during rocking motion at higher damping ratios.

Following the experiments for seal friction during constant velocity and sinusoid motion, chapter 4 switches attention to simulation approaches. Most of the simulations pursued in the following chapters have been concerned with the prediction of steady-state friction levels for constant velocity. The sinusoid motion considered in chapter 3 provides an indication that transient friction effects can be important for short cycles time which could significantly reduce the applicability of constant velocity friction modelling to many practical applications. The simulation of constant velocity friction represents a starting point which could be expanded to include transient effects if the constant velocity predictions prove successful.

Chapter 4 is focused on contact mechanics simulations for seal friction. These models consider whether seal friction can adequately be explained by considering only the direct contact between the rod and seal surfaces without including a fluid film separating the surfaces. The contact mechanics approaches considered do not allow for any speed dependence of friction and may be less suitable for predicting the full experimental range of constant velocity friction levels. However, these simulations may be suitable for applications with low cycle times which the sinusoid experiments identified to experience little transient variation in friction.

Chapter 4

Contact mechanics tribology simulation

One of the approaches to modelling seal friction is to assume a fluid film is not formed between the sliding surfaces and that the dominant source of friction is through direct contact between the surface asperities. This can occur during dry contact and lubricated contact where a boundary layer of fluid forms on each of the surfaces, which acts to reduce friction and surface wear. Under these conditions contact mechanics models can be used to determine the real area of contact between the two surfaces and the resulting adhesive friction from asperity shear. A boundary lubrication approach based on the real area of contact may be able to explain the relatively high friction levels measured in chapters 2 and 3 where viscous fluid shear stress alone cannot account for the friction levels experienced.

It is necessary to simulate the contact pressure distribution between the rod and seal in order to predict seal friction, through a relationship between contact pressure and frictional shear stress in order to predict a level of seal friction. FEA modelling may be applied to the seal geometry to determine the contact pressure distribution. Seal geometries for a single-lip, double-lip and o-ring seal are considered for different sealed pressures. The contact pressure distributions obtained are also relevant for the EHL and hysteresis simulations to be presented in chapters 5 and 6. The curvature at the seal corners are shown to significantly affect the pressure distribution at the seal inlet and outlet, which is important for the EHL analysis. Therefore seal geometries with varying radii at the inlet and outlet corners are also considered.

Greenwood-Williamson (GW) contact theory is used to relate the contact pressure to the real area of contact and friction level as a first approximation. This contact model may be used to determine the real contact area between two rough surfaces and has also been used in previous mixed lubrication studies of seal friction [17]. GW contact theory produces results comparable with Coulomb friction. These simulation results are compared with the

seal friction measurements. The physical appropriateness of the GW model for the loadings experienced is also considered based on measured surface roughness parameters.

An alternative empirical equation for rubber friction coefficients is considered as an alternative to GW and its limitations at higher loads. This empirical equation allows for Coulomb friction behaviour at low loads and a limiting value of friction at higher loading where the real area of contact is expected to saturate. No speed dependence of friction is accounted for in either this empirical relationship or GW theory. Simulation results are compared with the experimental data from the seal test rig.

A theoretical basis for the saturation of contact area is investigated by considering the contact between a rigid flat and a flexible one-dimensional sinusoid representing the rough surface. An analytical approach to this contact model was produced where each node on the sinusoid surface is assumed to have constant stiffness that is independent of deflection at the other nodes. FEA modelling was used to investigate whether these analytical simplifications are physically realistic. The simulated relationship between loading and real area of contact for the sinusoid model is compared with the empirical data to determine whether this is a realistic representation of a rough surface under compression.

4.1 Seal contact pressure FEA

4.1.1 Use of FEA in fluid sealing applications

FEA is commonly used for simulating the contact pressure distribution in dynamic seals. There are several sources of difficulty associated with the FE modelling of elastomeric and polymeric seals. These materials are nearly incompressible with Poisson ratios close to 0.5. This can cause problems with convergence in FE solution methods that minimise elastic strain energy. Many elastomers and polymers also have relatively low elastic moduli resulting in large deformations from small changes in applied pressure that can also cause convergence issues.

An example of FE simulation of a dynamic seal is given in [13] where the reaction force between a radial lip seal and a rod is presented. This study has special interest to the current investigation as the variation of radial interference was considered. In [13] the contact forces predicted by a two-dimensional plane strain analysis of the lip seal were validated against experimental measurements. This suggests that a two-dimensional radial section of a seal under plane strain conditions may be an accurate method of simulating the pressure distribution between a rod and seal.

Several studies have attempted to use FEA of dynamic seals for friction prediction. Johannesson [14] used a FE model of an o-ring to predict the pressure distribution across the contact for use in an inverse EHL model. Calvert [15] used FEA to predict friction in

pneumatic seal to within 10-20% of experimental measurements, by combining a Coulomb friction model with the simulated contact pressure distributions. However, there are additional complications for friction in hydraulic applications compared with pneumatics. Firstly, in hydraulic seals there is a much greater quantity of lubricating fluid available that may act to form a partial or complete pressurised film between the rod and seal and invalidate the Coulomb friction approach. Hydraulic sealing applications are also subject to higher pressure loadings where the friction may not be proportional to loading. Calvert's investigation was carried out with 8 bar air, which produces stresses much lower than the material modulus, hence only light loading was present. The success of pneumatic seal friction simulation from FEA using a Coulomb approach suggests it is worth considering whether the method can be adapted to hydraulic systems.

A few studies have produced simplified deformation models for elastomeric seals for use in EHL applications. These have been used to obtain approximations to the film thickness for a change in pressure distribution without having to execute a finite element program each time. Ruskell [29] used a linear deformation model for a rectangular seal based on FEA. A later study [17] used a similar method to produce a compliance matrix for a double-lip hydraulic seal. It is necessary to use numerical simulation to obtain the compliance relationships for most practical seal geometries.

There are also issues related to accurately modelling the elastic properties of seal materials. Linear elastic behaviour (equivalent to Hooke's law) may be inaccurate for material properties in cases where high strains are present. The pressures inside the sealed fluid are comparable with the elastic modulus of the seal material, indicating a potential for large strains to be produced inside the seal. However, a significant amount of the pressure loading on a seal is hydrostatic, which does not contribute significantly to material strain. It is necessary to inspect the simulated strain levels to verify whether the linear elastic model is likely to be suitable. A study on elastomeric rectangular seals [63] has suggested the linear-elastic assumption to be accurate for strains of $\pm 10\%$ for elastomeric materials. Non-linear models such as Mooney-Rivlin are available, although they require detailed knowledge of the stress-strain characteristics at higher strains in order to select suitable parameters.

4.1.2 Methodology for contact pressure determination

4.1.2.1 Single-lip seal

A FEA model was produced for the Parker-Hannifin B31624P5008 rod seal used in the experimentation. The geometry and dimensions for the seal model were obtained from the seal diagram in the relevant Parker-Hannifin catalogue (figure 4-1 [55]) and compared with the dimensions measured from a particular example of the seal. Figure 4-2 shows the seal geometry used in the simulations.

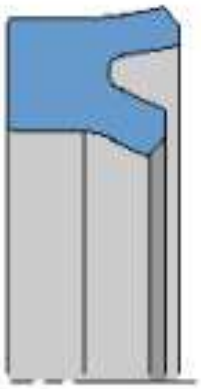

Figure 4-1: Parker-Hannifin single-lip seal

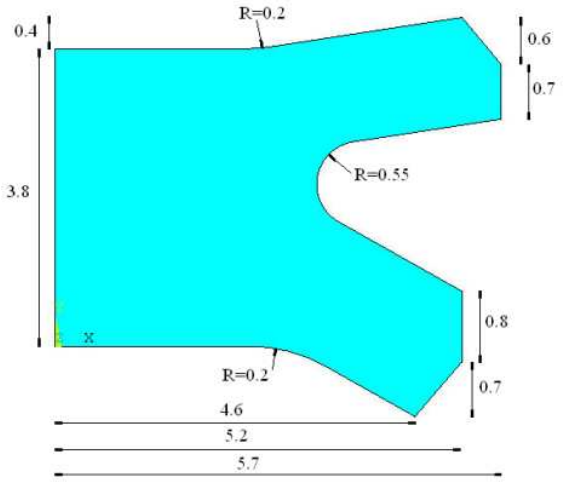

Figure 4-2: Seal dimensions (mm) assumed in single-lip seal FEA model

Two different variations on the geometry shown in figure 4-2 were considered for the single-lip seal to investigate the effect of the curvature at the seal inlet and outlet on the pressure distribution across the contact. The curvature may arise from wear during seal operation and it is not physically realistic for perfectly sharp vertices to remain. The curvature at these locations is important for inverse EHL analysis in where the film thickness is highly dependent on the pressure distribution in the inlet and outlet regions. A set of contact pressure results was produced with no curvature at the inlet and outlet and a second set was obtained with the geometry in figure 4-2 modified with a radius of curvature of 0.4 mm at inlet and outlet corners.

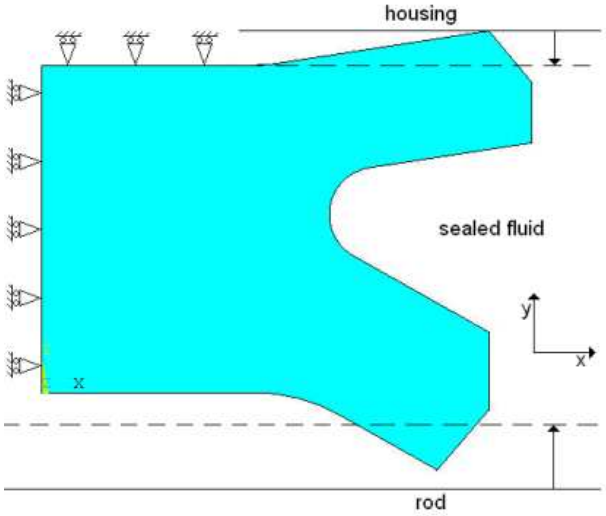

Figure 4-3: Constraints applied in FEA simulation of seal for pre-squeeze

To obtain the contact pressure distribution for the single-lip seal the appropriate geometry shown in figure 4-2 was produced in ANSYS 11. Constraints were applied to the geometry as shown in figure 4-3. The seal edge facing the outer housing (at the top of figure 4-3) was constrained as arising through housing contact. Pairs of contact elements were created between the seal edges with opposing target lines representing the housing in regions where contact was expected. A uniform sealed pressure was applied to the seal faces on the right hand side of the seal in figure 4-3 to simulate the loading from the pressurised fluid. Plane strain conditions were assumed for no hoop strain.

The material was assumed to be linear elastic with Young modulus E =12.1 MPa and Poisson ratio $\nu = 0.49$. Parker-Hannifin P5008 "Ultrathan" polyurethane has a secant modulus for 100% strain of between 11 and 20 MPa according to industrial literature [64].

A mesh was used with local refinement along the rod-seal contact regions as shown in figures 4-4 and 4-5. This mesh had either 146 nodes or 121 nodes across the rod-seal interface for the respective geometries without and with curvature at the inlet and outlet. Plane182 elements were used to allow the use of solvers designed for near-incompressible materials. Contact162 and Target169 elements were used at the contacting faces. The target faces were displaced in 30 substeps in order to minimise convergence problems from over-penetration between the contact and target elements.

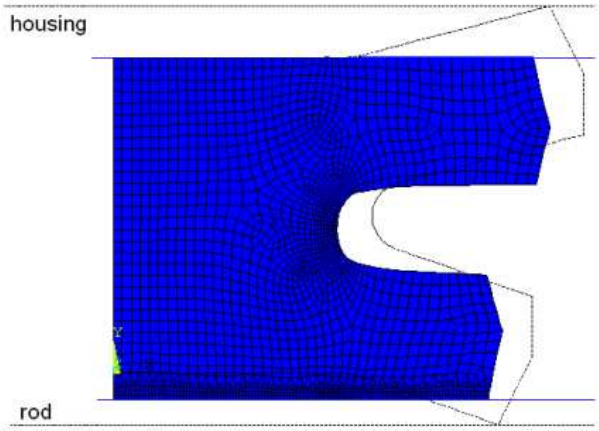

Figure 4-4: Mesh for single-lip seal in FEA simulation, no curvature at inlet and outlet

4.1.2.2 Double-lip seal

A second set of simulations were produced for a double-lip seal geometry. This geometry was based on the Parker-Hannifin BS1624P5008 rod seal. The dimensions used for the geometry are shown in figure 4-6 and are based on the catalogue seal diagrams and measurements taken from a sample seal. A radius of curvature of 0.4 mm was assumed at the secondary lip where the rod-seal contact first occurs. This value of curvature was also assumed at

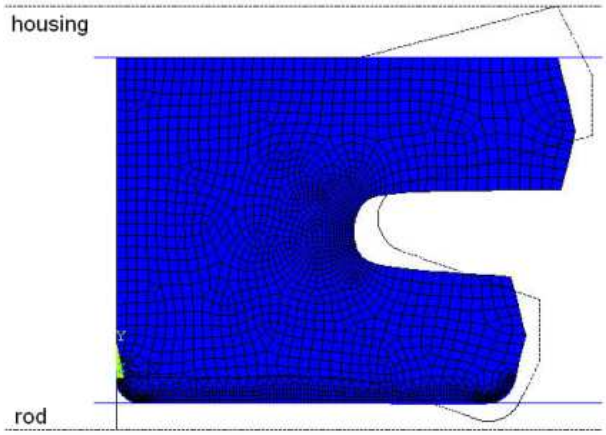

Figure 4-5: Mesh for single-lip seal in FEA simulation, 0.4 mm radius at inlet and outlet

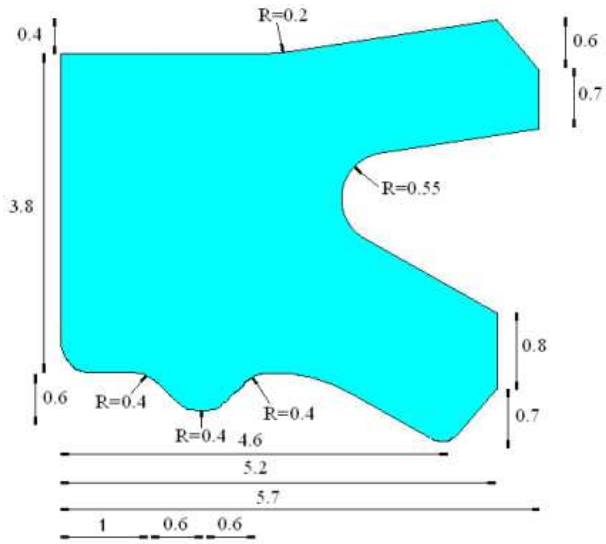

Figure 4-6: Seal dimensions (mm) assumed in double-lip seal FEA model

the two locations where the secondary lip protrudes from the main body of the seal. The geometry was modelled and constrained in an ANSYS 11 simulation in a similar manner to the single-lip seal. A similar mesh density (figure 4-7) was used for the double-lip seal as for the single-lip seal.

4.1.2.3 O-ring seal

A simulation for an o-ring geometry was also produced as a reference case. A circular-section o-ring was simulated with a 2 mm diameter. The simulation was constrained using a semi-circle model as shown in figure 4-8, ignoring the effects of shear stress at the rod-seal interface. Contact elements were used between the seal surface and the two target elements representing

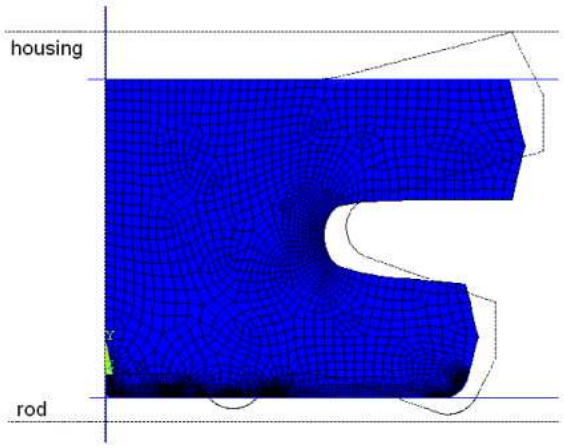

Figure 4-7: Mesh for double-lip seal in FEA simulation

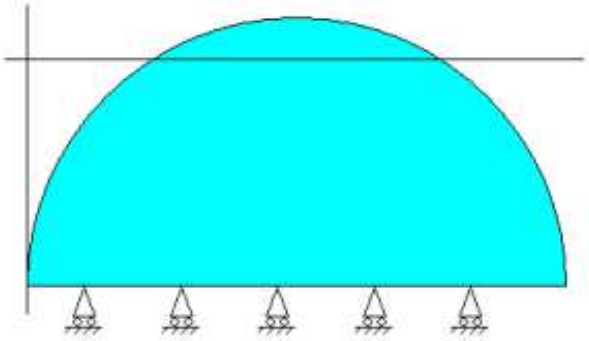

Figure 4-8: Constraints applied to o-ring geometry in FE simulation

the rod and side of the housing. The geometry of the surface and main body mesh of the o-ring geometry under the applied pressure loading is shown in figure 4-9. An elastic modulus of 5 MPa and Poisson ratio of 0.49 were taken as typical for nitrile rubber.

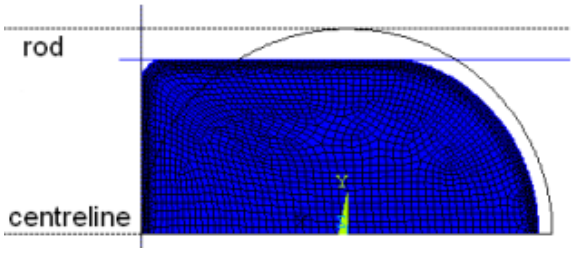

Figure 4-9: Mesh for o-ring in FEA simulation

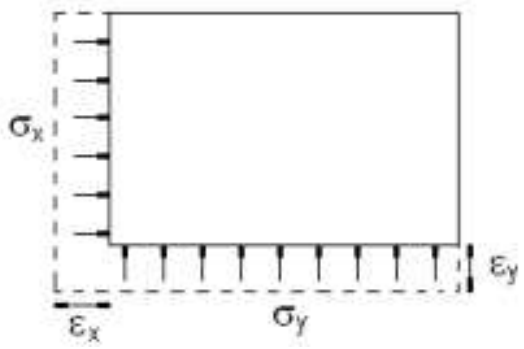

Figure 4-10: Bulk parameter model of seal body under sealed pressure and rod-seal contact pressure

4.1.3 Analytical approach to seal deformation

U-cup type hydraulic seals have a particular feature that contact between the rod and seal is limited to the seal lip at lower sealed pressures. At higher sealed pressures the contact length is increased as the pressurised fluid deforms the main body of the seal towards the rod. It is possible to use an analytical approach to describe the general features of a U-cup seal under different sealed pressures. Figure 4-10 shows a bulk parameter model of the seal geometry where σ_x is the axial stress exerted on the seal by the pressurised fluid and σ_y is the radial stress or mean contact pressure across the full length of the seal. The radial strain ϵ_y represents the radial extension of the seal towards the rod that eventually causes contact between the rod and main body of the seal. For plane strain conditions the circumferential strain ϵ_z is taken to be zero. Hooke's law gives the stresses and strains in the seal as

$$\epsilon_x = \frac{1}{E}\left(\sigma_x - \nu\left(\sigma_y + \sigma_z\right)\right) \tag{4.1}$$

$$\epsilon_y = \frac{1}{E}\left(\sigma_y - \nu\left(\sigma_x + \sigma_z\right)\right) \tag{4.2}$$

$$\epsilon_z = 0 = \frac{1}{E}\left(\sigma_z - \nu\left(\sigma_x + \sigma_y\right)\right) \tag{4.3}$$

Hence

$$\sigma_y = \frac{1}{(1-\nu)}\left(\frac{E\epsilon_y}{(1+\nu)} + \nu\sigma_x\right) \tag{4.4}$$

This relationship indicates that, once full contact between the rod and seal is established and ϵ_y becomes constant, further increases in sealed pressure would create increases in contact pressure proportional to $\frac{\nu}{1-\nu}$. For a perfectly incompressible material where $\nu = 0.5$, increases in sealed pressure produce equivalent increases in contact pressure between the rod and seal.

With the Poisson ratio of 0.49 assumed in the current simulations a near-unity coefficient of proportionality of 0.961 is predicted. Equation (4.4) also indicates that the sealed pressure required to initiate contact between the rod and main body of the seal to be proportional to the maximum radial strain of the seal body. Therefore any variation in the radial separation between the undeformed seal body and housing would produce a proportional change in the sealed pressure required to create contact between the rod and seal body.

4.1.4 Results for seal pressure distribution

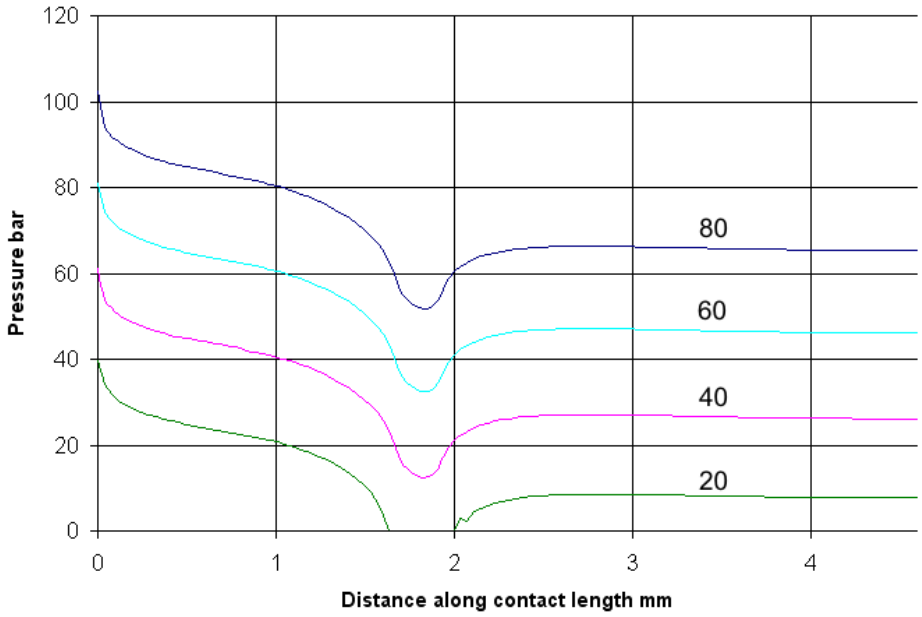

Figure 4-11: Pressure distribution from FEA of single-lip seal, 0.4 mm radius at inlet and outlet. Numerical labels indicate the sealed pressure (bar).

Figures 4-11 and 4-12 show the simulated contact pressure distributions at the rod-seal interface for single-lip seal geometries with and without a 0.4 mm radius at the seal corners that form the inlet and outlet. The pressure peaks (documented experimentally in [65] and [66]) occur as a result of a local region of Hertzian contact forming at the curved surface. Pressing the curved surface against a near-rigid flat creates a Herzian-type parabolic pressure distribution at these corners. Reducing the radius of curvature reduces the contact length along which the major pressure changes take place by reducing the extent of the region with variable radial displacement. However, the curvature at the seal corners has limited effect on the pressure distribution over most of the contact length and the total normal reaction force.

One of the problematic features of the pressure distribution for the single-lip seal is the decrease in pressure at the change in seal geometry near the centre of the contact region

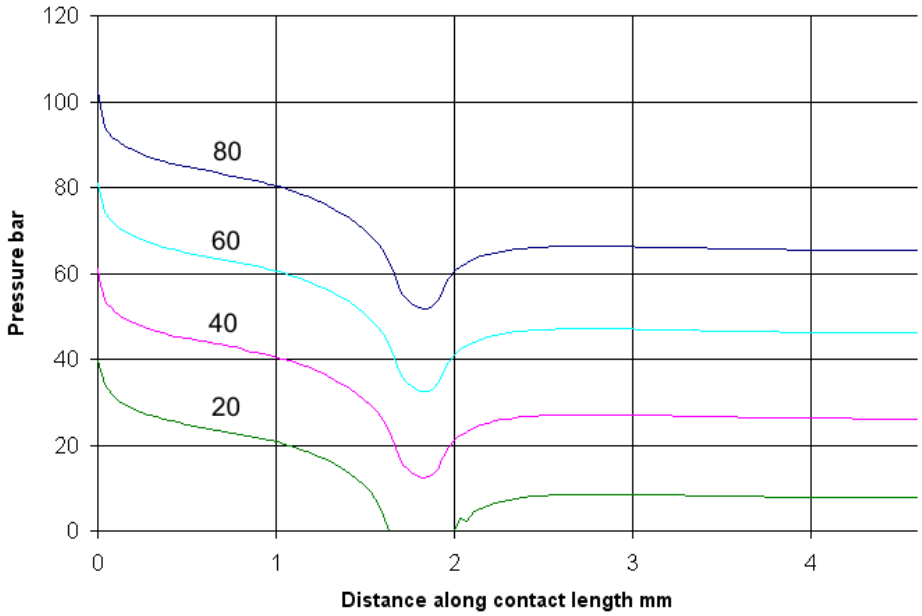

Figure 4-12: Pressure distribution from FEA of single-lip seal, no curvature at inlet and outlet. Numerical labels indicate the sealed pressure (bar).

in figures 4-11 and 4-12 where the seal lip begins to protrude from the main body of the seal. The magnitude of this pressure decrease is dependent on the radius of curvature at this location, with greater pressure decreases occurring at lower radii of curvature. A previous experimental study by Kawahara [5] measured the pressure distribution underneath a similar U-cup type seal to the current study and did not report a significant decrease in fluid pressure at this change in geometry. Kawahara's experimental technique was to create a flow through a small hole in the rod and measure the pressure drop created to maintain the flow as the rod was passed through the seal. It is possible any fluid supplied underneath the seal would be raised to the pressure at the seal boundary in order to maintain flow, disguising any region of lower contact pressure underneath the seal.

Increasing the sealed pressure creates an almost equivalent uniform increase in the pressure distribution across the contact above a critical value of sealed pressure (approximately 20 bar). This suggests there to have been a general relationship between sealed and contact pressure approximately similar to that predicted by the bulk parameter model of equation (4.4). A significantly higher sealed pressure is required to completely flatten the seal against the rod at the change in geometry compared with the lowest sealed pressure required to first induce contact between the rod and main body of the seal. The pressure distribution across the main body of the seal (away from the change in geometry) is approximately constant, suggesting this seal face to remain approximately parallel to the rod throughout its deformation.

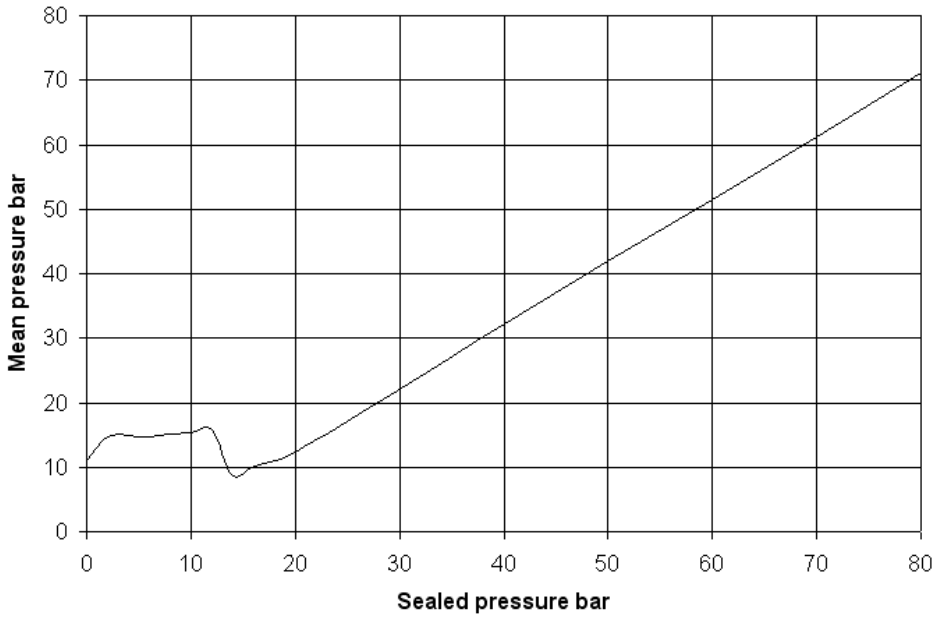

Figure 4-13: Simulated variation in mean contact pressure with sealed pressure for single-lip seal

Figure 4-13 shows the mean contact pressure averaged over the area of contact in each case for a range of sealed pressures. At the lowest sealed pressures the mean contact pressure remains approximately constant with rising sealed pressure as the extension in the contact length is approximately proportional to the increase in overall reaction force. Once a sealed pressure of 12 bar is reached, a fall in the mean contact pressure takes place as a result of the large increase in contact length when the main body of the seal gains contact with the rod. Above the critical sealed pressure (20 bar) increases in mean pressure are approximately proportional to increases in sealed pressure as the contact of length reaches a maximum and the sealed pressure result in hydrostatic changes in the pressure distribution.

4.1.4.1 Results for double-lip seal

Figure 4-14 shows the pressure distributions obtained from the FEA simulations of the double-lip seal. The secondary lip produces a region of significantly higher contact pressure than the remainder of the seal, resulting in correspondingly higher normal reaction forcers. At lower sealed pressures the additional reaction created by the secondary lip is significant relative to the single-lip. For higher sealed pressures the additional contact pressure along the full lengths of the seals reduce the proportional difference in normal reactions between the single-lip and double-lip seals. An approximately Hertzian variation in pressure is produced at the secondary lip, which is due to the relatively large 0.4 mm radius of curvature at this location.

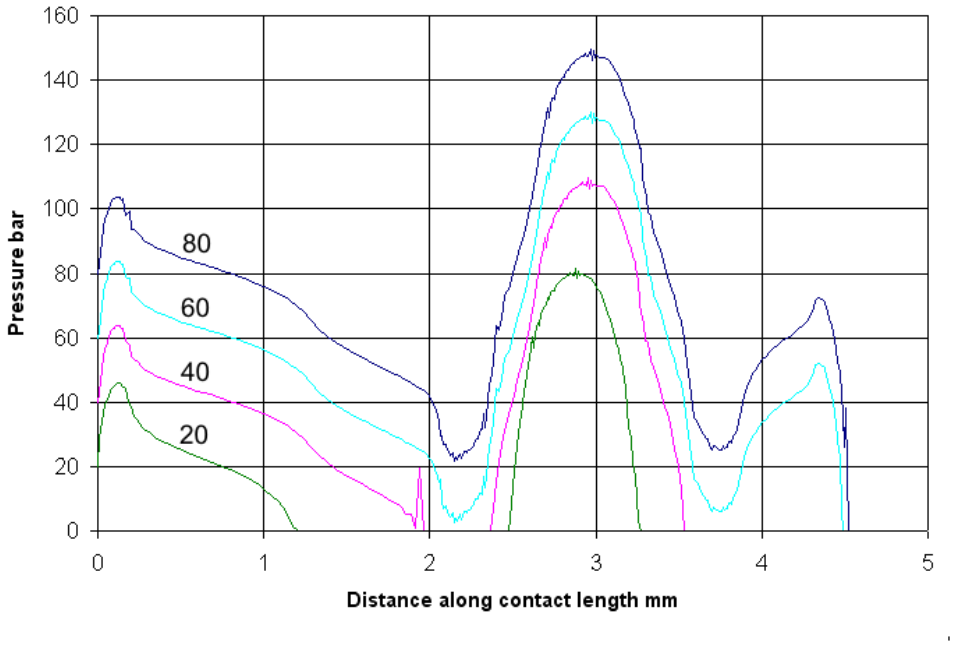

Figure 4-14: Pressure distribution from FEA of double-lip seal. Numerical labels indicate the sealed pressure (bar).

4.1.4.2 Results for o-ring

Figure 4-15 shows the pressure distributions for an o-ring with a range of different sealed pressures. The asymmetry of the pressure distribution is consistent with the air-side of the o-ring being pressed against the housing while the fluid side is unconstrained. Similarly to the single-lip seal, increasing the sealed pressure creates an approximately equivalent increase in contact pressure across most of the length of the contact. This occurs as the near-incompressibility of the material results in most of the change in axial loading producing changes in hydrostatic pressure when the body is constrained from expanding radially or circumferentially. For different sealed pressures there are small differences in the pressure gradients near the pressurised side of the o-ring to allow continuity between the pressure acting on the o-ring surface.

4.1.5 Compliance matrix determination

It is useful to produce a compliance matrix between the pressure distribution across the surface of the seal and the seal deformation for future use in friction simulation. The approach employs a stiffness matrix inversion, differing from previous EHL investigations of seal friction [17, 29] where a flexibility method was used. In the current study the stiffness method was found to be more convenient to set up as the initial deflections applied for the condition of

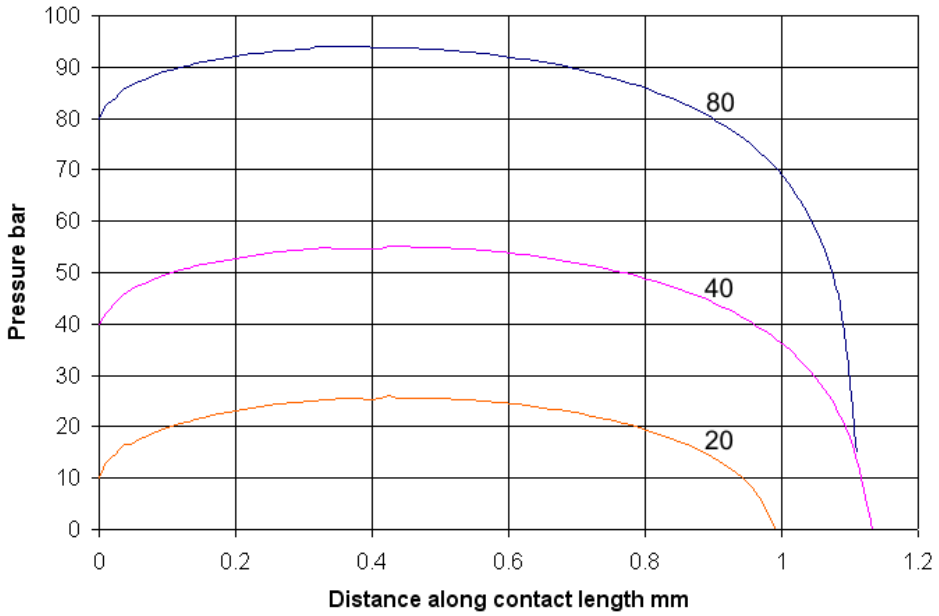

Figure 4-15: Pressure distribution from FEA of o-ring. Numerical labels indicate the sealed pressure (bar).

zero film thickness were relatively easy to determine from the undeformed geometry.

The stiffness matrix was produced through modification of the ANSYS 11 simulation for the static contact pressure distribution. An APDL algorithm was produced to automate the processes used for determining the coefficients in the stiffness matrix. The procedure involved applying a radial displacement to the nodes on the seal surface along the contact length. These nodes were radially displaced to positions corresponding with zero separation between the rod and seal, then the nodal reaction forces across the contact length obtained. For each node along the contact length an additional radial displacement of 0.1 μm was applied at the node in question with no additional deflections applied at the remaining nodes along the contact length. The changes in reaction forces for the nodes along the contact length were recorded as a column in the stiffness matrix. This procedure was repeated for additional deflections applied at each node along the contact in turn in order to obtain the complete stiffness matrix. This stiffness matrix was exported into MATLAB and numerically inverted to give the corresponding compliance matrix.

4.2 Boundary and dry contact modelling approaches

4.2.1 Rough surface background

Once the pressure distribution between the rod and seal is established it is appropriate to determine the resultant shear frictional forces. Coulomb friction would simply be proportional to the overall normal reaction force from the contact pressure distribution. However, hydraulic seals are known to have non-Coulomb friction behaviour under common operating conditions, necessitating the use of alternative friction models. This section considers contact mechanics approaches where the local friction levels are determined by the degree of asperity contact between the rod and seal surfaces.

Engineering surfaces generally have significant surface roughness on the micron scale with localised peaks that can be characterised as asperities. In most practical cases where there is contact between two surfaces, the real area of contact is significantly lower than the nominal area of contact, limited to patches. The real area of contact is particularly important in friction determination. For dry contact one of the important mechanisms of resistance to motion is adhesive friction where a particular shear stress is required to overcome the intramolecular adhesive bonds that form between the contacting surfaces. If the adhesive bonds are of approximately constant shear strength, the total shear force required to initiate or maintain motion is expected to be proportional to the real area of contact. Therefore surface roughness is considered to be important for friction determination in any situation where there is significant direct contact between the two surfaces.

The presence of a pressurised fluid film may keep surfaces partially separated. If the two surfaces are not completely separated by the fluid film, boundary lubrication takes place. Here the lubricant either chemically reacts with the surface or becomes physically absorbed by the surface porosity to form a boundary layer with a lower shear strength than the dry surface, which aids lubrication. It has been suggested by Lansdown [67] that mild boundary conditions occur in hydraulic pistons and cylinders. Under boundary lubrication conditions the deflection of asperities and real area of contact may be similar to the dry case with a thin boundary layer covering the surfaces. Dry contact models may be applicable to boundary lubrication cases with lower shear strengths associated with the real contact areas.

4.2.2 Greenwood-Williamson (GW) contact model

4.2.2.1 GW model overview

The Greenwood-Williamson (GW) contact model [16] is a standard approach for estimating the contact fraction and nominal contact pressure for contact between rough surfaces. This contact model assumes analytical Herzian contact relationships for the contact load and area at a single asperity. These are combined with a normal probability density function for the

location of the asperity peaks. The nominal contact pressure and contact area of the asperity distribution are then obtained from integration of the contact pressure and area distributions. GW theory is based on several assumptions about the geometry of the rough surfaces; the asperity tips are hemispherical of a single radius, the heights of the asperity tips are normally distributed, asperity deflection is elastic and no asperity interaction takes place. Roughness parameters may be obtained from surface profile measurements.

4.2.2.2 Details of GW model

Contact between two rough surfaces is approximated as contact between an equivalent rough surface and a rigid flat. This assumption is appropriate if the surface gradients are relatively minor and do not reach significant fractions of unity [68]. This model is relevant to the current study where only low surface gradients were expected from measurements of the surface profiles and literature concerning general surface profiling. Details of the surface profile are discussed in section 4.2.3.2.

GW theory assumes each asperity to be hemispherical with a single radius of curvature R. This allows the normal force and contact area for a particular asperity to be expressed in terms of the asperity deflection δ using Hertzian contact theory. From Hertzian contact theory the reaction force between a hemisphere and a rigid flat is given by

$$g = \frac{4}{3}\frac{E}{(1-\nu^2)}R^{\frac{1}{2}}\delta^{\frac{3}{2}} \tag{4.5}$$

The area of contact for a single asperity is

$$a_c = \pi R\delta \tag{4.6}$$

The asperity peaks are assumed to have a Gaussian distribution where the probability density function for the location of the asperity peaks is

$$\phi = \frac{1}{\sigma_h\sqrt{2\pi}}e^{-\frac{z^2}{2\sigma_h^2}} \tag{4.7}$$

where z is the distance from the mean location of the asperity peaks which corresponds to the mean surface location. When a rigid flat is located at a distance h from the mean line, the deflection δ of an asperity with its peak located at a position z from the mean line is $z-h$. The probability density function for the distribution of asperity peaks (equation (4.7)) is then combined with the contact force for single asperity and integrated over the range of distances from the surface where asperities are in contact with the rigid flat. Multiplying the result by the asperity density per unit area gives the effective force generated for a particular number of asperities over this area. This effective nominal contact pressure for the rough surface is

$$p_c = \frac{4}{3}\eta\frac{E}{(1-\nu^2)}R^{\frac{1}{2}}\frac{1}{\sigma_h\sqrt{2\pi}}\int_h^\infty (z-h)^{\frac{3}{2}}e^{-\frac{z^2}{2\sigma_h^2}}dz \tag{4.8}$$

For later analysis it is convenient to express equation (4.8) in terms of dimensionless parameters where mean surface separation h was non-dimensionlised according to the roughness height σ_h and contact pressure p_c according to an ambient pressure p_{atm} as

$$P_c = \frac{4}{3}\frac{1}{(1-\nu^2)}\hat{\sigma}^{\frac{3}{2}}\frac{1}{\sqrt{2\pi}}\int_H^\infty (Z-H)^{\frac{3}{2}}e^{-\frac{Z^2}{2}}dZ \tag{4.9}$$

where $P_c = \frac{p_c}{p_{atm}}$ and $H = \frac{h}{\sigma_h}$. Carrying out a similar integration combining the area of contact for an asperity (equation (4.6)) with the probability density of the asperity distribution (equation (4.7)) gives the area of contact for a Gaussian rough surface. As a fraction of the nominal contact area, the real area of contact is

$$\frac{A_c}{A_0} = \int_H^\infty \eta\sigma_h\pi R\frac{1}{\sqrt{2\pi}}e^{-\frac{Z^2}{2}}dZ \tag{4.10}$$

GW theory uses a three-point asperity model for determining the surface roughness parameters from the measured surface profile. This method uses a one-dimensional trace across a rough surface and assumes an asperity to exist at any location that is higher than its two neighbouring points. The accuracy of this assumption has recently been questioned by one of its originators [18]. Surface roughness is known to take place on different length scales and differences in spatial intervals between sampling locations may result in differences in which asperities are captured by the three point model. Investigators such as Sayles and Thomas [69] have demonstrated that roughness properties produced can be highly dependent on the sampling interval length. Alternative models using spectral density functions allow for a range of different surface roughness scales with the shortcoming of increased complexity. A recent study by Ciaverella [19] suggests that the GW model produces the qualitative features of more sophisticated spectral density function models. Therefore GW theory was thought to retain practical suitability approaching that of alternative roughness models while offering greater simplicity.

4.2.3 Measurement of rough surface parameters

4.2.3.1 Previous rough surface measurements

Use of the GW contact model requires suitable values for the parameters of RMS roughness height σ_h, asperity radius R and asperity density η. Estimates for these parameters can be obtained from measurement of the surface topography. One of the problems in obtaining roughness parameters for the GW model is the infrequent measurement of the asperity radius R in previous studies. It has also been questioned whether a single asperity radius of curvature

can accurately represent a practical rough surface. It has been shown [69] that significant changes in the measured asperity curvature take place at very low spatial intervals in the surface profile sampling as roughness characteristics with lower length scales are reached. In the original proposal of the GW model [16] a complete set of parameters was measured from a bead-blasted aluminium surface. Several other previous investigations have been identified that measured all the roughness parameters used in GW contact theory, shown in Table 4.1.

Table 4.1: Roughness parameters measured in previous investigations

	σ_h (μm)	η (mm^{-2})	R (μm)
Greenwood 1966 [16] Bead blasted aluminium	1.37	300	13
Jain 1983 [70] Run-in HD polyethylene	0.5	900	40
McCool 1987 [71] Ground reciprocating surface	0.142	300	12.7
Maser 2006 [72] (Unmeasured)	0.4	10×10^3	1

The reported asperity radii and peak separations were at least an order of magnitude greater than the roughness height for the artificially roughened surface and approximately two orders of magnitude higher for relatively smooth surfaces that had been subject to finishing processes. Typical machined surfaces tend to have gentle slopes that are not usually steeper than 10° with 1° or less being typical [73]. These earlier measurements suggest rough surfaces for metals and polymers in common engineering applications to have asperity densities within the order of 300 mm^{-2} and asperity radii around 13 μm. One feature of interest was that the ground and bead-blasted surfaces were reported to have similar asperity densities and asperity curvature while showing significantly different surface roughness heights. This suggests the asperity curvature and density may not be altered during run-in as significantly as the roughness height. These previously measured values of roughness also provide a useful point of reference for the surface topography measurements made in the present study and whether they are within expected boundaries.

4.2.3.2 Surface topography measurement in current investigation

Surface roughness measurements were taken from a chrome plated rod using a Talysurf-50 surface measurement machine. For each test a one-dimensional trace was taken over a 6.4 mm sample length in the direction of the rod's axis. A cut-off value of 0.8 mm was used for the nodal spacing over which the mean surface profile was assumed to follow. This cut-off value represents the approximate wavelength of surface waviness over which macro-scale variation in the surface profile was assumed to take place. The effective height of the profile was determined from the deviation between the measured profile and the mean profile connecting points with cut-off length spacing. Three separate traces were taken longitudally across the rod at different locations and the mean roughness parameters calculated over the three sets of measurements. The roughness parameters of interest for the current investigation (shown

in Table 4.2) are the RMS roughness height σ_h and mean spacing L_1 of the profile peaks.

An alternative surface roughness measuring technique was used to measure the surface roughness of a Parker B3 1624 P5008 reciprocating rod seal used in the current investigation. The surface profile was measured optically using a non-contact Proscan 2000 surface profiling machine. It was necessary to use a non-contacting method for the soft polyurethane seal material. A 350 μm square section of the seal was analysed at the inside radius of the lip surface. This relatively small size of the sampling region meant it was not necessary to specify a cut-off value for the larger-scale features. The surface profile across this region is shown in figure 4-16 and the measured parameters in Table 4.2.

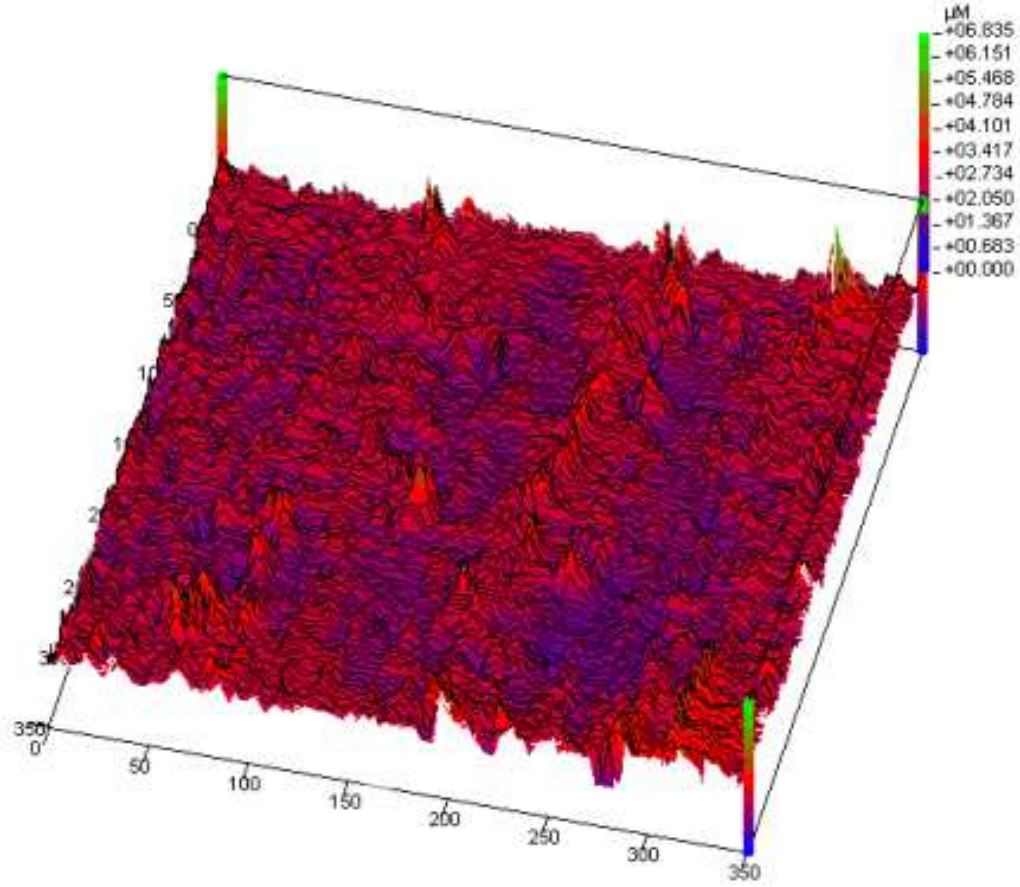

Figure 4-16: Measured surface roughness profile for single-lip seal

Table 4.2: Roughness parameters measured in current investigation

	σ_h (μm)	S (μm)	η (mm^{-2})
Chrome plated rod (run-in)	0.115	49.137	414.4
Parker P5008 seal	0.394	39.979	625.6

The measured asperity density of the rod was within 40% of what previous studies (including those in Table 4.1) have reported for ground and bead blasted steel surfaces. Asperity density for the seal was also within a similar tolerance with the reported density for the previous investigation with the polymeric material. This suggests the measured asperity density of 414 mm^{-2} to be approximately representative of the two surfaces and to be appropriate for use in the GW model. The surface roughness height of the seal material is consistent with the values measured for a run-in seal in a previous studies [6].

4.2.3.3 Use of GW model in seal tribology applications

The contact fractions associated with the expected range of loadings have been examined for the measured surface roughness parameters in order to determine whether the low contact fraction and asperity interaction assumptions of the GW model remain appropriate. A recent investigation of seal tribology by Salant [17] used GW theory as part of a model with an alternative set of roughness values. The characteristics of GW theory with these alternative roughness values have also been considered. Salant's investigation assumed a 0.4 μm for RMS roughness height σ_h, 1 μm asperity radius R and an asperity density of 10^{13} m^{-2}.

There are concerns over whether the GW model is physically accurate for the loads experienced in hydraulic sealing applications. GW contact theory assumes no asperity interaction to take place, which is likely to become invalid if the contact patches form a significant proportion of the nominal area of contact. The sealed pressures of up to 80 bar are similar to the 12.1 MPa elastic modulus of the seal material, suggesting the material may experience high contact fractions to transfer this loading. Numerical solutions of equations (4.9) and (4.10) were produced for a range of different surface separations between 0 and $4\sigma_h$ using the two different sets of roughness parameters identified.

Figure 4-17 shows the relationship between mean surface separation and loading and contact fractions predicted by GW theory for the values of surface roughness assumed by Salant [17] in an investigation of seal friction. With these roughness values the real area of contact is shown to exceed the nominal area of contact at a pressure of 38.6 bar, a value exceeded in seal tribology. Therefore the GW model may not be appropriate for modelling at high sealed pressures if the full amount or a significant proportion of the overall load is assumed to be taken by asperity contact. For higher asperity contact pressures the friction experienced may be lower than predicted by GW theory as the saturation of the real contact area may limit the adhesive friction. The critical pressure and mean separation identified can be interpreted as a limiting value beyond which there would be no further increase in asperity shear stress, although this involves an extrapolation of GW theory beyond low contact fractions.

It was questionable whether the roughness parameters assumed in [17] are accurate rep-

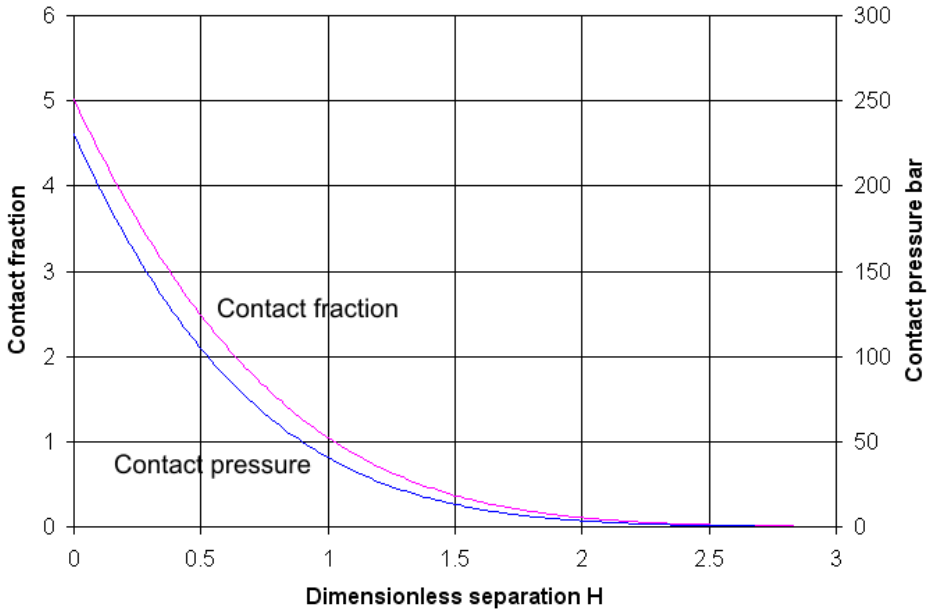

Figure 4-17: GW contact area variation for parameters assumed by Salant [17], σ_h=0.4 μm, R=1 μm, η=10^{13} m^{-2}

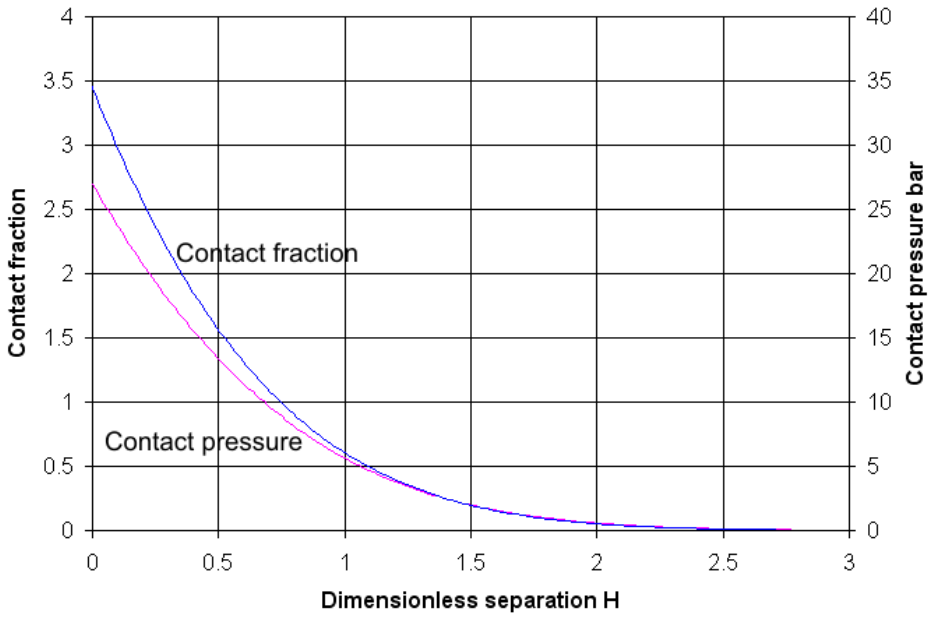

Figure 4-18: GW contact area variation for measured parameters, σ_h=0.115 μm, R=10 μm, η=415 $\times$ 10^6 m^{-2}

resentations of the rod and seal surfaces. An alternative set of relationships between pressure and contact area (figure 4-18) were obtained using the surface roughness measurements taken from the rod in section 4.2.3.2 and comparison also made with previous experimental studies. An asperity radius R of 10 μm was assumed as this value was close to that reported by several previous investigators in Table 4.1 and was similar to that calculated from the proposed relationship between surface roughness parameters developed in section 4.2.5.5. The GW results obtained with these parameters show no improvement in terms of achieving physically realistic contact fractions at higher pressures. With the measured roughness values the real area of contact is predicted to saturate at a lower contact pressure of 11.3 bar. Hence GW theory could be unsuitable for friction prediction for the loading experienced in common hydraulic sealing applications.

One of the more doubtful parameter values assumed in [17] was the asperity density η which was specified as being several orders of magnitude higher than reported from surface measurement in other investigations. Increasing the asperity density (and number of contacting asperities per unit area) increases the nominal contact pressure between the rough surfaces for a particular mean surface separation. At higher asperity densities the surfaces are capable of supporting higher pressure loads while maintaining positive mean separations. Use of an asperity density closer to the measured values reduces the load-bearing capacity of the asperities to below the expected pressures, providing further indication that GW theory does not offer realistic solutions for the high loadings associated with hydraulic seals.

4.2.4 Friction modelling at high loading

4.2.4.1 Previous approaches to high loading

One of the shortcomings of the GW model for hydraulic sealing applications is the expected contact pressure loads predicting unrealistically high contact fractions. Alternative asperity contact models are necessary to accurately model the high contact fractions and levels of asperity interaction experienced in hydraulic seals under practical operating conditions. One of the most commonly used alternatives to the GW contact model is the CEB model [22]. This model is based on GW theory with a modification to incorporate a transition in the asperity contact pressure calculation between elastic and plastic conditions as a function of asperity deflection. CEB theory has been frequently used for heavily-loaded contact between metals, where yielding and plastic deformation occur at low strains, although is less influential in high strain seal materials where approximately linear elastic deformation is expected to be maintained at higher asperity deflections.

A well known alternative model for high loading cases is the PW contact model [23]. This model was developed for contact between metals at high loads where the nominal contact pressure approaches and exceeds the yield stress of the material. PW theory was designed for

contacts dominated by plastic flow, although it has particular features that may be adaptable to the deformation of high-strain materials. No single asperity model is used, instead the contact fraction is derived from the separation between the rigid flat and the deformable rough surface with a Gaussian surface distribution relationship. Material deformation is assumed to be perfectly plastic. Material displaced by the compression of the rough surface is assumed to reappear as a uniform rise in the rough surface with volume conservation applied. The contact pressure is then calculated by equating the plastic work done in the compression with that required for the uniform rise. The concept of a uniform rise in the surface is thought to be relevant to the current investigation. As plastic deformation is a constant volume process the asperity volume displaced downwards is assumed to correspond with the volume in the uniform rise. The seal polyurethane was a near-incompressible material, therefore it was also possible that the displaced material would reappear as a rise in the surface. This uniform rise concept was used to develop a new asperity interaction contact model in section 4.2.5. It was relatively difficult to deduce the pressure required to induce a uniform rise in a high-strain material, therefore the complete PW model could not be used to obtain a load-contact fraction relationship for the seal material.

A few experimental studies for heavily loaded contacts have been carried out that allow the accuracy of the uniform rise assumption to be explored. Experimentation carried out in the original development of the PW model [23] produced a close match between the predicted loading-contact area relationship and the measured values. This study measured the surface roughness of a bead blasted aluminium surface following loading with a polished hardened steel ram at loads up to four times the yield stress of the aluminium. An excellent agreement between the PW theoretical loading-contact area relationship and the measurements taken was reported. However, a later study of high loading [74] carried out similar experiments with aluminium, tin and silver samples and obtained a significantly less accurate agreement than reported by the PW originators (except for during one series of test with a tin material sample). This discrepancy is curious as the repetition with the aluminium sample would have been expected to produce similar results to the original investigation. Relatively few contact mechanics studies have been carried out for high loading. It is therefore difficult to ascertain which of the two investigations is more reliable. The earlier investigation provides some indication that the concept of the uniform rise may occur when asperities are deformed in a constant volume process.

4.2.4.2 Empirical relationships for rubber friction

Various empirical studies have been carried out to quantify the effects of loading on rubber friction. One of the simplest and most accurate empirical relationships for light to heavy loading was first proposed by Thirion [20]. In this relationship the friction coefficient μ for

dry rubber is given in terms of load pressure p and material elastic modulus E by

$$\mu = \frac{1}{C_1} \frac{1}{\left(1 + 15\frac{p}{E}\right)} \tag{4.11}$$

where the parameter C_1 is determined empirically for a particular rubber. This relationship was extensively verified by Denny [21] with several different types of rubber and gelatines through creep speed testing of dry samples on glass. At low loading where $1 >> 15\frac{p}{E}$ the friction coefficient is approximately equal to $\frac{1}{C_1}$ and the load-dependent behaviour is approximately Coulomb in nature. At high loading $1 << 15\frac{p}{E}$ the product μp (i.e. friction force) varies little as the loading is increased. The friction force approaches a maximum value of $\frac{1}{15C_1}E$ at high loading. Friction is expected to approach a limiting value at high loading as the real contact area approaches the nominal contact area. Equation (4.11) is the simplest form of equation that allows for constant μ at low loading and constant μp at high loading to satisfy the expected behaviour in both regions.

The variable friction coefficient in equation (4.11) was integrated over the simulated contact pressures between the rod and single-lip seal for a range of different sealed pressures to produce predictions for the sealed pressure-dependence of friction. The contact pressure distributions were obtained from finite element modelling of a seal geometry described in section 4.1.2. The local friction coefficient and frictional shear stress were calculated at each node across the contact length from equation (4.11). The resulting shear stress distribution was numerically integrated over the contact length using the trapezium rule to obtain the overall friction. This integration was carried out for a range of different values of sealed pressure between 0 bar and 80 bar to correspond with the experimental range of sealed pressures in the current investigation. A suitable value for the C_1 coefficient in equation (4.11) was obtained empirically from the experimental data for seal friction.

For experimental comparison the mean of the modulus of instroke and outstroke friction was calculated for a rod speed of 20 mm/s with sealed pressures between 10 and 80 bar (section 2.3.2). C_1 was estimated by setting the value of simulated friction equal to the experimental value at the highest sealed pressure that was tested (80 bar). The results obtained from integrating the empirical relationship for rubber friction coefficients with the contact pressure distribution simulated from FEA are shown in figure 4-19.

The simulation results show a qualitatively similar relationship between friction and sealed pressure to the experimental results. At lower sealed pressures contact occurs only in close proximity to the seal lip and increases in the sealed and contact pressures produce relatively minor increases in the total reaction force and corresponding friction. Once the sealed pressure is raised sufficiently, contact occurs over the full length of the seal and increases in the contact pressure produce larger increases in the normal reaction force. At higher sealed pressures the friction approaches a limiting value, which is expected as the area of real contact approaches

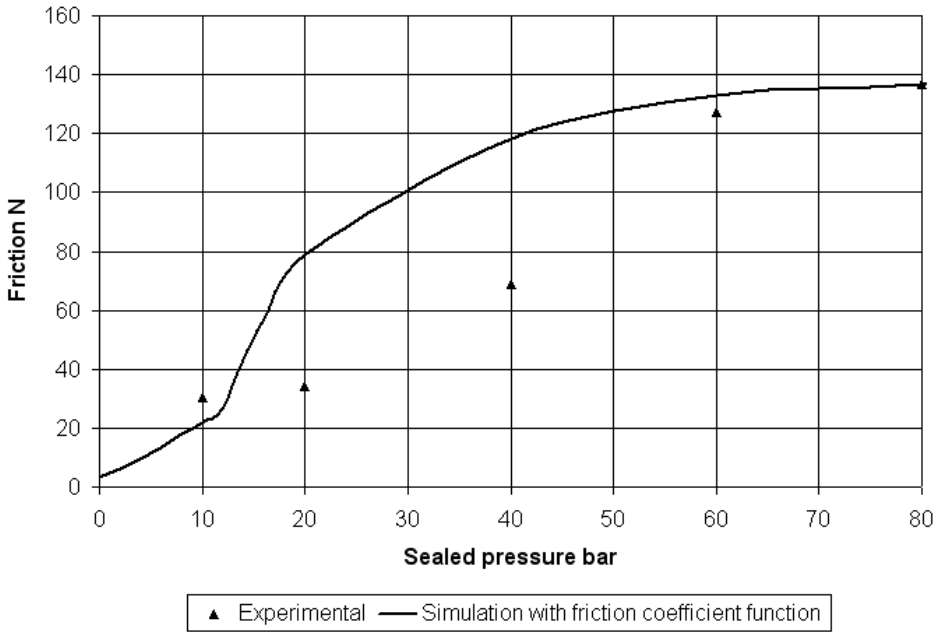

Figure 4-19: Simulated friction for empirical friction coefficient relationship and FEA solution to contact pressure distribution, single-lip seal, experimental data at 20 mm/s

saturation.

One of the significant discrepancies between the simulations and the experimental data is the higher predicted increase in friction at lower sealed pressures. Possible causes may be either inaccuracy in the assumed elastic properties of the seal material or inaccuracy in the seal geometry and clearance between the rod and seal body. The seal geometry used in the FEA simulations assumed a total clearance between the seal body and its limits in radial extension of 0.3 mm and a 3.8 mm seal depth. An inaccuracy of a few tenths of a millimetre in these dimensions would result in significant changes in the radial strain required to initiate full contact between the rod and seal. This would result in contact between the rod and main body of the seal being initiated at a significantly lower sealed pressure than observed in practice.

4.2.5 Development of deterministic approach to asperity interaction

4.2.5.1 Asperity interaction background

The PW plastic contact model assumes a uniform rise in the surface to take place as a result of asperity deflection and the displacement of material. In this model the loading and contact fraction are obtained assuming a Gaussian surface distribution of surface height rather than using a single asperity model. A method of combining a uniform shift in the surface

profile as a result of asperity interaction with a single asperity model has been proposed by Zhao [75]. In this investigation a uniform decrease in the surface profile was assumed to occur from asperity interaction and an elastic-plastic transition model was used for the behaviour of a single asperity [76]. A recent series of papers [77, 78, 79] consider the asperity interaction model proposed by Zhao with an elastic-plastic single asperity model, concluding that neglecting asperity interaction resulted in an over-prediction of friction coefficient at intermediate loads. These elastic-plastic single asperity contact models are not particularly applicable to high strain polymer and elastomer seal materials.

Several investigations have used FEA to simulate asperity interaction. Komvopoulos [24] considered a two-dimensional FEA model for contact between series of cylindrical asperities and a rigid flat under plane strain conditions. An alternative method of modelling an infinitely long series of asperities would be to use symmetry boundary conditions to model half an asperity, significantly reducing the computational requirements. Komvopoulos investigated a range of different asperity spacing to radius ratios between 0.4 and 4, commenting that lower values were appropriate for gentle surface gradients. A different study by Eid [25] looked at a three-dimensional model of two interacting hemispherical asperities.

4.2.5.2 Sinusoid line contact analysis

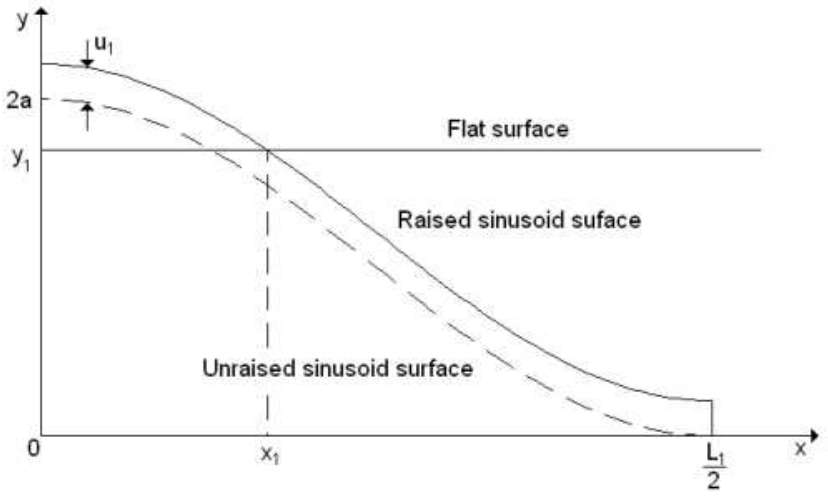

Figure 4-20: Sinusoid surface profile in contact with rigid flat

A single asperity, one dimensional model of the rough surface profile is now considered. The rough surface is assumed to be sinusoidal with RMS height and peak-to-peak spacing corresponding with the measured values presented in section 4.2.3.2. This sinusoid surface is assumed to make contact with a rigid flat as illustrated in figure 4-20. The height of the sinusoid surface, y, includes the uniform shift in surface height and the distance y_0 represents

the mean separation between y and the rigid flat. A uniform rise is assumed to take place in the sinusoid surface to maintain volume conservation in a similar manner to the PW model. For any particular interference between the rigid surface and deformable sinusoid profile the surface profile y outside the contacting regions is given by

$$y = u_1 + a\left(1 + \cos\frac{\pi}{L_1}x\right) \tag{4.12}$$

If volume conservation and a uniform rise u_1 in asperity profile is assumed, the uniform rise is given by

$$u_1 = \frac{V_1}{L_1} \tag{4.13}$$

The displaced cross sectional area is

$$V_1 = \int_0^{x_1} y dx - x_1 y_1 \tag{4.14}$$

Combining equations for volume conservation, uniform rise and asperity profile gives

$$\begin{aligned} u_1 &= \frac{1}{L_1}\int_0^{x_1} u_1 + a\left(1 + \cos\frac{\pi}{L_1}x\right)dx - x_1 y_1 \\ &= a\left(\frac{1}{\pi}\sin\frac{\pi}{L_1}x_1 - \frac{x_1}{L_1}\cos\frac{\pi}{L_1}x_1\right) \end{aligned} \tag{4.15}$$

The surface profile is then given by

$$y = a\left(\frac{1}{\pi}\sin\frac{\pi}{L_1}x_1 - \frac{x_1}{L_1}\cos\frac{\pi}{L_1}x_1 + 1 + \cos\frac{\pi}{L_1}x\right) \tag{4.16}$$

The relationship between the contact fraction $\frac{2x_1}{L_1}$ and the distance from the undeformed centreline to the rigid flat (h, equivalent to y_1) is

$$y_1 = a\left(1 + \frac{1}{\pi}\sin\frac{\pi}{L_1}x_1 + \left(1 - \frac{x_1}{L_1}\right)\cos\frac{\pi}{L_1}x_1\right) \tag{4.17}$$

The mean surface separation $s_1 = h - u_1$ is

$$s_1 = a\left(\frac{1}{\pi}\sin\frac{\pi}{L_1}x_1 + \left(1 - \frac{x_1}{L_1}\right)\cos\frac{\pi}{L_1}x_1\right) \tag{4.18}$$

It is necessary to assume a relationship between material deflection and loading if an analytical solution between contact fraction and nominal contact pressure is to be produced. If the contact pressure at a particular element in figure 4-20 to be proportional to the local with stiffness k_{bulk}, the element reaction force is given by

$$dF = k_{bulk}(y - y_0)dx \tag{4.19}$$

The mean nominal pressure over a single wavelength L_1 was obtained from integrating this reaction over the length of contact:

$$\begin{aligned}
\frac{F}{L_1} &= \int_{x_1}^{x_2} \frac{k_{bulk}}{L_1}(y - y_0)dx \\
&= \frac{k_{bulk}}{L_1}\int_{x_1}^{x_2}\left(a_1 \sin\frac{2\pi x}{L_1} - y_0\right)dx \\
&= \frac{k_{bulk}}{L_1}\left[-\frac{a_1 L_1}{2\pi}\cos\frac{2\pi x}{L_1} - y_0 x\right]_{x_1}^{x_2} \\
&= \frac{k_{bulk}}{L_1}\left(-\frac{a_1 L_1}{2\pi}\cos\frac{2\pi x_2}{L_1} + \frac{a_1 L_1}{2\pi}\cos\frac{2\pi x_1}{L_1} - a_1(x_2 - x_1)\sin\frac{2\pi x_1}{L_1}\right)
\end{aligned} \tag{4.20}$$

As points x_1 and x_2 are equally spaced from the sinusoid peak of y, it follows that the gradient of y at x_2 is the negative of the gradient at x_1. Therefore

$$\cos\frac{2\pi x_2}{L_1} = -\cos\frac{2\pi x_1}{L_1} \tag{4.21}$$

Substituting into equation (4.20) simplifies the equation for nominal pressure to

$$\frac{F}{L_1} = a_1 k_{bulk}\left(\frac{1}{\pi}\cos\frac{2\pi x_2}{L_1} - \left(\frac{x_2 - x_1}{L_1}\right)\sin\frac{2\pi x_1}{L_1}\right) \tag{4.22}$$

From inspection of the locations of the limiting points of contact (x_1 and x_2) in figure 4-20 the contact fraction A_c is given by

$$A_c = \frac{1}{L_1}\left(\frac{1}{2} - 2x_1\right) \tag{4.23}$$

With this relationship the nominal contact pressure (equation (4.22)) can be expressed in terms of the contact fraction as

$$\begin{aligned}
\frac{F}{L_1} &= a_1 k_{bulk}\left(\frac{1}{\pi}\cos\left(\frac{\pi}{2} - \pi A_c\right) - A_c \sin\left(\frac{\pi}{2} - \pi A_c\right)\right) \\
&= a_1 k_{bulk}\left(\frac{1}{\pi}\sin\pi A_c - A_c\cos\pi A_c\right)
\end{aligned} \tag{4.24}$$

This relationship between loading and contact fraction is valid for any uniform shift in the surface profile as the contact pressure is a function of the only the relative positions of rigid flat and the sinusoid surface. Equation (4.18) applies to a uniform rise in the sinusoid

surface as per PW contact [23], no shift in the mean surface or a uniform fall in the surface as assumed by Zhao [75].

4.2.5.3 Sinusoid line contact FEA methodology

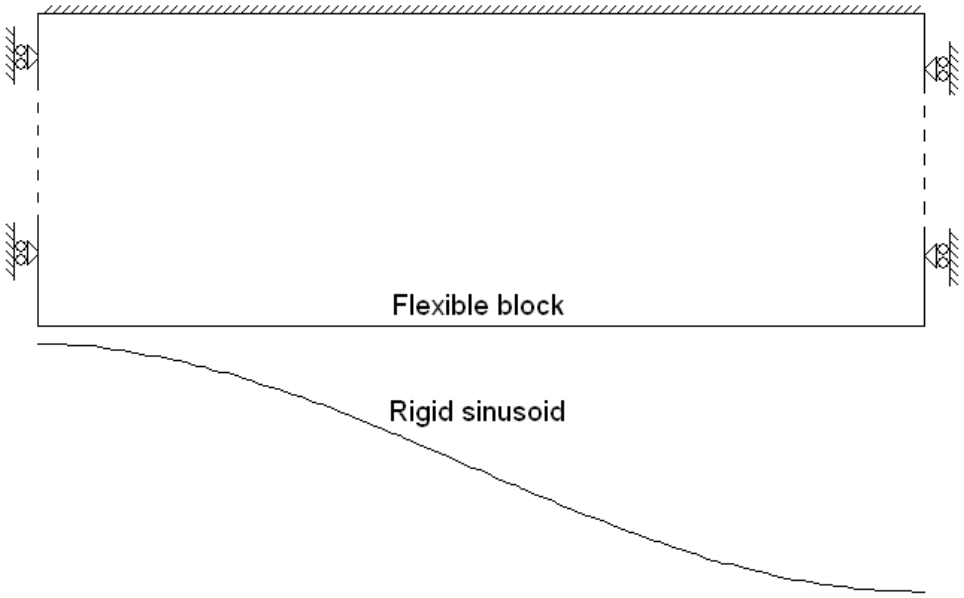

Figure 4-21: Constraints applied to FEA model of deformable sinusoid surface

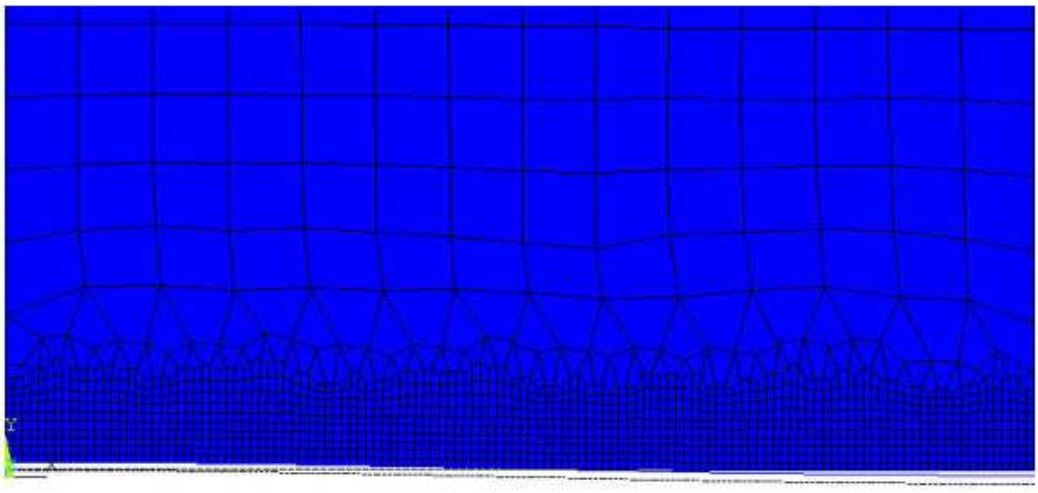

Figure 4-22: Mesh detail at deformable surface in FEA simulation of sinusoid contact, solution for contact fraction of 0.46

FEA simulations were produced to determine whether the analytical model based on a constant axial stiffness is a suitable approximation to the behaviour of a deformed surface

under plane strain conditions. A two-dimensional finite element geometry was produced in ANSYS 11 consisting of a rectangular block of deformable material and a rigid contact surface with a sinusoid profile. This profile was set as having an amplitude of 0.163 μm to correspond with the measured RMS surface roughness height of 0.115 μm and a half-cycle length of 24.55 μm for a peak spacing of 49.1 μm. The dimensions of the deformable block were set to give an aspect ratio of approximately 4 to ensure the location of the constraint in surface deflection did not significantly affect the sub-surface stress distribution. This was achieved using a block height of 100 μm with the 24.55 μm half-cycle length. Plane strain conditions were assumed throughout the simulations. The polymer seal material was assumed to be linear elastic with Young modulus 12.1 MPa and nearly incompressible with Poisson ratio 0.49.

Constraints were applied to the geometry to simulate the symmetry boundary conditions at the sinusoid peak and trough as shown in figure 4-21. A constraint in vertical displacement was applied at the opposite face of the block to the contacting face to allow contact with the rigid flat to deform the block. This constraint was only applied in a vertical direction as no significant horizontal deflection was expected at a long distance from the contact surface where the stresses in the material approach uniformity throughout the length of the block. The rigid surface was constrained horizontally to ensure the limits of the contact coincided with the surface peaks and troughs.

A mesh consisting of plane182 elements was produced for the block with local refinement taking place at (and extending into) the surface facing the sinusoid target. Figure 4-22 shows the near-surface region of the FEA model with this increased mesh density. The contact between the two faces was simulated using contact162 and target169 elements. The required displacement of the sinusoid surface was applied incrementally in 30 substeps to minimise convergence problems associated with large increments in deflection.

4.2.5.4 Sinusoid line contact FEA results

Figure 4-23 shows the contact pressure distributions across the surface in contact with the sinusoid for several different interferences between the rigid sinusoid and deformable block. For the case of contact along the full length of the seal the pressure distribution is close to being a sinusoid. This is similar to that assumed for the analytical approach where the pressure at any node across the surface is modelled as being proportional to only the local deflection. For lower interferences with relatively low contact fractions the pressure distribution is not sinusoidal, suggesting the displaced material does not create a uniform surface rise for lightly loaded conditions. The relationship between contact fraction and nominal contact pressure from the FEA simulation of line contact (figure 4-24) accurately follows the analytical relationship produced from assuming a constant vertical stiffness (equation (4.24)).

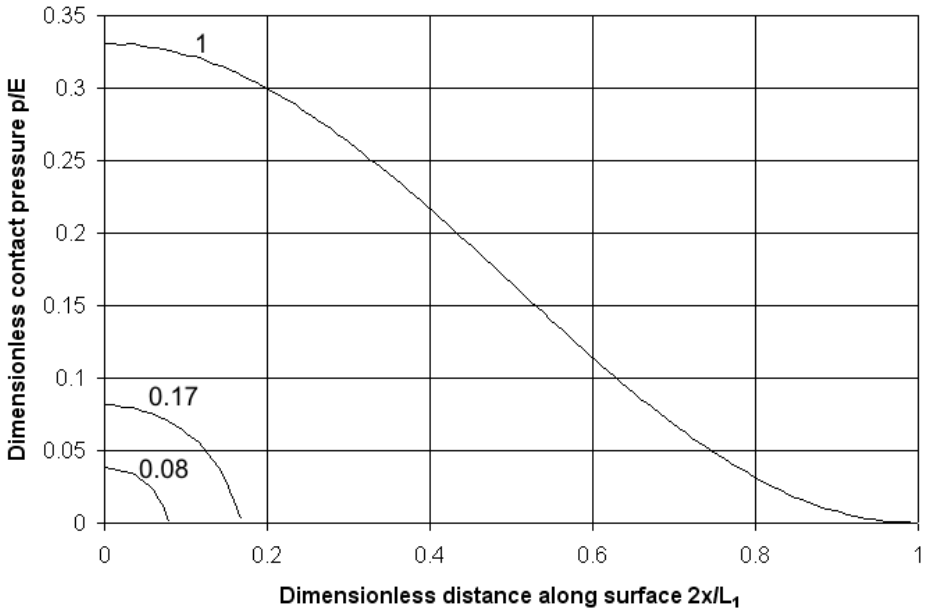

Figure 4-23: Contact pressure distribution across surface for 1D sinusoid contact. Labels on curves indicate contact fraction.

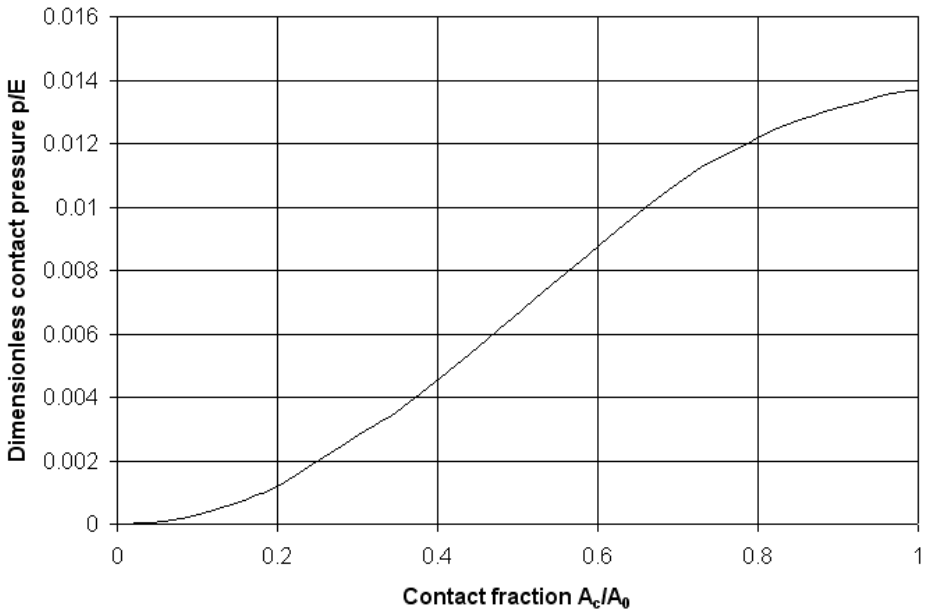

Figure 4-24: Nominal contact pressure and contact fraction for 1D sinusoid contact

Figure 4-25 shows the predicted friction levels for contact between the one-dimensional sinusoidal surfaces as a function of loading where friction is assumed to be proportional to the

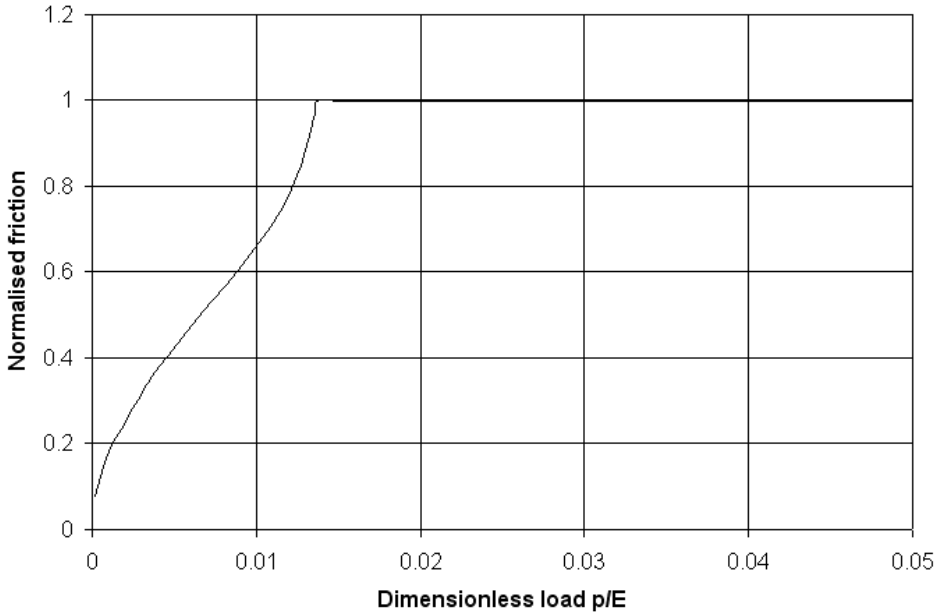

Figure 4-25: Normalised friction level based on contact fraction for 1D sinusoid contact

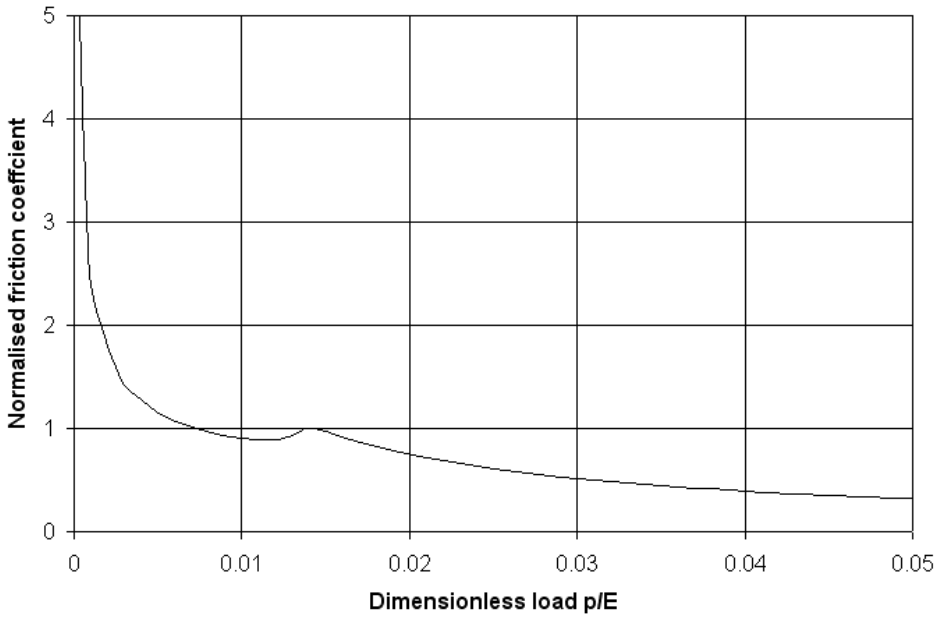

Figure 4-26: Normalised friction coefficient based on contact fraction for 1D sinusoid contact

real area of contact. The friction plotted is non-dimensionalised with respect to the friction level at full contact to give a normalised friction of unity at a contact fraction of unity. At

higher loadings where full contact is approached the contact area and friction increase rapidly with higher loading. As the contacting region approaches the trough in the surface profile and the surface gradient reduces, lower additional deflections are required to further extend the contact area. This results in real area of contact increasing rapidly with increasing load in these regions where full contact is approached. A significant discontinuity results where the rapid increase in friction saturates as the contact fraction reaches unity (shown in figure 4-26). This discontinuity has questionable physical realism and it would be preferable to have an asperity model with more a gradual transition in friction behaviour near the limiting friction level. One problem with deterministic asperity interaction modelling is that any repeating surface profile that has no points of discontinuity in the surface gradient between neighbouring asperities requires a surface gradient of zero between neighbouring asperities. In this region where the surface is nearly flat it is expected for small changes in deflection to produce significant increases in the contact fraction, producing a similar discontinuity in friction characteristic to that observed with the sinusoid profile.

Figure 4-26 shows the non-dimensional friction coefficients for a range of loadings where the friction coefficient is the quotient of the contact fraction over the load. These friction coefficients are non-dimensionlised with respect to the friction coefficient at the limiting full contact condition to give a friction coefficient of unity at the loading where full contact is reached. These results highlight the additional physical shortcoming that high friction coefficients are predicted at low contact fractions. The analytical relationship between contact fraction and loading in equation (4.24) also suggests there to be a region at lower contact fractions where only minor increases in load are expected with increases in the contact fraction. One of the other main limitations of the sinusoid contact simulations for rough surface contact modelling is full contact between the two surfaces being produced at an excessively low nominal contact pressure. The simulations of sinusoid contact indicate full contact and half contact to be reached at a nominal contact pressures $\frac{p}{E}$ of 0.014 and 0.006 7 respectively. The empirical relationship for dry rubber discussed in section 4.2.4.2 suggests a friction level of half the limiting value to be reached at a $\frac{p}{E}$ loading of 0.067. If the empirical friction level is assumed to be proportional to the real area of contact, the sinusoid contact simulation predicts real areas of contact for a given loading that are an order of magnitude higher than occur in practice. Therefore the sinusoid contact model is unsuitable for accurately modelling the contact mechanics of rough surface at high loadings.

The inaccuracy of the load at which the limiting friction is reached could be a result of inaccuracy in the surface geometry as the loading parameters are dimensionless with respect to material properties. If higher surface peaks than assumed with a repeating sinusoid were present, this would be expected to increase the loading required to create full contact by necessitating greater surface deflections. It is possible that rough surface with different scales of asperities imposed on each other may require additional loading to deflect the large scale

asperities in addition to the smaller scale examples. Additional asperities on lower length scales may also act to increase the loading required for a particular real contact area by reducing the effective peak spacing.

4.2.5.5 Asperity curvature proposal

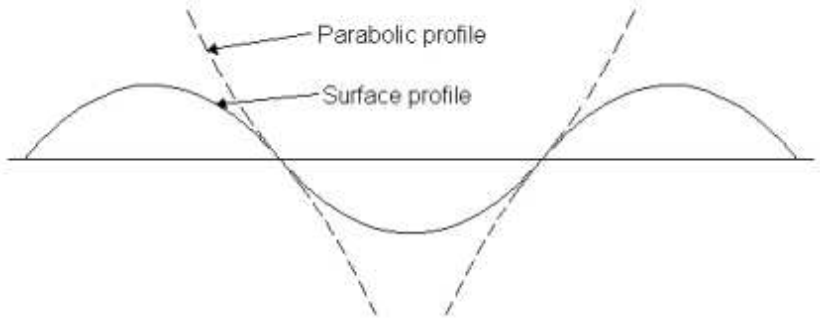

Figure 4-27: Piecewise parabolic approximation to rough surface geometry

A possible extension of the concept of the asperity tips being hemispherical is to consider the surface to have parabolic peaks and troughs with continuous connections as illustrated in figure 4-27. This model represents an alternative to a sinusoid and allows a constant radius of curvature to extend a significant distance from each asperity peak. With this model geometry the profile is determined by two out of the three parameters specified in GW theory (peak separation, asperity height and curvature). As there are uncertainties in measuring an appropriate asperity radius of curvature (which is significantly affected by the sampling length [69]) there are advantages in calculating an approximation to asperity curvature from the measured peak separation and height. Showing that a continuous surface of parabolic peaks and troughs has similar curvatures to previous measurements would at least provide an indication that previously measured asperity radii are compatible with the other measured asperity dimensions.

An asperity separation of 49.1 μm and a RMS roughness height of 0.115 μm as detailed in section 4.2.3.2 are assumed. For a piecewise parabolic profile the relationship between the RMS height σ_h and the peak-to-centreline separation L_1 can be obtained from standard integration techniques. The profile of one of the parabolae in figure 4-27 is given by

$$y = h_1 - \frac{1}{2R^2}x^2 \tag{4.25}$$

Over the length between the asperity tip $x = 0$ and the beginning of the adjacent trough $x = \frac{L_1}{4}$ the RMS value of height is

$$\sigma_h^2 = \frac{\int_0^{\frac{L_1}{4}} y^2 dx}{\int_0^{\frac{L_1}{4}} dx} = \frac{4}{L_1}\int_0^{\frac{L_1}{4}} \left(h_1 - \frac{1}{2R^2}x^2\right)^2 dx = h_1^2 - \frac{h_1 L_1^2}{48R} + \frac{L_1^4}{51200R} \tag{4.26}$$

From equation (4.25) the boundary condition that the distance from the centre-line is zero at the peak-trough transition point ($y = 0$ at $x = \frac{L_1}{4}$) gives the radius as a function of the parabola amplitude

$$R = \frac{L_1}{32h_1} \tag{4.27}$$

Substituting the relationship between the peak curvature and other roughness parameters (equation (4.27)) into the relationship between RMS roughness and the other roughness parameters (equation (4.26)) gives the RMS roughness height as

$$h_1 = \sqrt{\frac{15}{8}}\sigma_h \tag{4.28}$$

The estimation for the radius of curvature of asperity peaks R from the piecewise parabolic model of the rough surface is

$$R = \frac{L_1}{32\sigma_h}\sqrt{\frac{2}{15}} \tag{4.29}$$

For the values of roughness measured from the rod in the current simulation an asperity radius of curvature of 9.74 μm is predicted. This value is close to the values of 10-13 μm quoted from surface topography in previous investigations. However, a shortcoming with the model is its prediction of asperity radius being inversely proportional to curvature. Previous investigations catalogued in section 4.2.3.2 have reported radii of asperity curvature similar to 10 μm for an order of magnitude of asperity heights σ_h, suggesting the asperity profile to undergo changes during finishing that cannot be approximated as a simple scaling of the magnitude of the surface height about the mean separation.

4.3 Closure

A FEA model of a single-lip seal was produced to simulate the contact pressure distribution between the rod and seal for a range of sealed pressures. At lower sealed pressures contact is limited to the region immediately around the seal lip. Above a critical sealed pressure contact is initiated between the rod and main body of the seal, significantly increasing the nominal area of contact. Once full-contact along the length of the seal is reached additional increases in sealed pressure produce approximately hydrostatic changes in the contact pressure distri-

bution. Including a curvature at the seal inlet and outlet produces Hertzian peaks in the contact pressure distribution near the limits of the contact region. Stiffness and compliance matrices were also produced. A double-lip seal and o-ring geometries were also considered, indicating additional contact pressure from the secondary lip which are more distinctive at lower sealed pressures.

The simulated contact pressure distributions for the single-lip seal were combined with an empirical relationship for the friction coefficient of rubbers to predict the pressure dependence of friction in the single-lip seal. A qualitative fit was produced between the simulated friction characteristics and the experimental measurements. As the sealed pressure is increased from low values there is a gradual increase in predicted friction with an abrupt increase occurring where contact between the rod and main seal body is initiated. Simulated friction approaches a limiting value at higher sealed pressures. A significant increase in friction level is predicted to take place at a lower sealed pressure than in the experiments, possibly due to inaccuracy in the initial clearance assumed between the rod and seal body.

GW contact theory is shown not to be accurate for the high loadings expected at the rod seal interface in the current study. Surface roughness measurements were taken from the rod and seal in the current investigation and compared with previous studies involving roughness measurement and friction modelling in hydraulic seals. Measured roughness parameters differ significantly from the values assumed in previous seal tribology investigations involving GW theory. Using either measured or previously assumed roughness values in the GW model produces physically unrealistic contact fractions at the expected loadings. Therefore the GW model is not suitable in its present form for hydraulic sealing applications.

A deterministic contact model was developed for simulating asperity interaction in attempt to improve the theoretical basis for the empirical friction-load relationship. This rough surface contact model consists of a sinusoid in contact with a rigid flat. An analytical approach to the problem was produced where displaced material is assumed to reappear as a uniform rise in the surface profile and the contact pressure at any location is assumed to be proportional to only the local surface deflection. A two-dimensional finite element model was produced to determine the contact properties of the sinusoid surface numerically. The analytical model accurately matches the FEA method for evaluating the mean contact pressure, although was less accurate for determining the local contact pressure variation at lower contact fractions.

Approximating the surface geometry as a sinusoid does not produce an accurate agreement with the contact behaviour of typical rough surfaces. The sinusoid model is not appropriate for the highest contact fractions where the contact fraction rapidly increases as the contact extends across the surface trough. There is also a problem with full contact occurring at excessively low nominal loading compared with practical rough surfaces. It may be important to consider the distribution of asperity heights in order to allow additional load support if a

physically accurate contact model is to be developed for high loading.

A simple method of obtaining the asperity radius from the measured asperity height and spacing was proposed based on a surface geometry of piecewise parabolae. This simple method reasonably relates the roughness parameters together in the present study, although does not account for how surface roughness height can significantly change during operations without significantly affecting the other roughness parameters.

Following the consideration of asperity contact approaches to friction modelling, chapter 5 considers whether including a film of fluid between the surfaces could improve experimental agreement. Most previous studies of seal tribology have used fluid mechanics approaches where a fluid film is assumed to form, suggesting this type of lubrication should be considered in any comprehensive study. The current chapter has identified that it may be possible to partially explain the measured friction characteristics without considering a fluid film and that an approach using GW theory may not be appropriate for the expected asperity loadings. The following chapter is concerned with evaluating models based on the Reynolds equation, addressing the concerns raised over their physical basis and considering whether these models could be modified to overcome their shortcomings. It is also considered whether boundary contact or mixed fluid mechanics approaches are more suitable to the current application.

Chapter 5

Inclusion of fluid flow in tribology simulation

EHL theory has been used in numerous studies of hydraulic seal tribology and is considered and evaluated as a method of friction prediction in this thesis. In EHL theory a continuous fluid film is assumed to form between the two surfaces and most of the normal loading between the surfaces is transferred by fluid pressure. The fluid pressure and film thickness distributions for a continuous fluid channel of relatively thin thickness are related by the Reynolds equation. EHL theory also allows for the surface separation and equivalent film thickness to be affected by the compliance of the surfaces. The conditions for EHL are normally satisfied when the ratio of the fluid shear stress associated with fluid viscosity to the load pressure is greater than a critical value.

Conventional inverse EHL simulations are presented for the pressure distribution between a rod and seal. The film thickness distribution is calculated from the known pressure distribution without the need to carry out any iterations for how the film thickness affects the required fluid pressure distribution. The friction predictions from the fluid shear stress are compared with the measured friction levels.

A different type of EHL simulation is considered where friction from both fluid shear stress and asperity shear occurs. These simulations assume the total pressure at any node between the surfaces to be the sum of the fluid pressure solution from the Reynolds equation and the asperity contact pressure from the GW asperity contact model considered in chapter 4. This GW-average Reynolds model has recently gained use in seal tribology studies [17], although has yet to be extensively validated.

The GW-average Reynolds model was modified to investigate whether its experimental agreement could be improved and if the physical limitations of the model could be resolved. It is identified in chapter 4 that the GW model may not be suitable for the high loadings expected across the contact region where high contact fractions occur. If the surface asperities

become flattened by the high loading this may be expected to choke off the fluid film if the surfaces come into predominantly direct contact. Alternatively, if the fluid film is maintained during asperity flattening some form of load transfer to the fluid would be expected. As a first approximation a transition to EHL conditions in regions of significant asperity flattening is considered with different residual levels of asperity contact in these regions. A variation of this modification is also considered with a fixed proportion of overall load transferred to the asperities.

A different approach assuming the asperity friction coefficient to be a function of sliding speed is also investigated. In this model a relationship between asperity friction coefficient and speed is assumed. Friction coefficient is assumed follow an exponential decrease with speed with the relevant parameters estimated empirically.

An alternative modelling approach based on the maintenance of a fluid film is also considered to investigate whether it is possible to predict the friction levels at the asperity tips without relying on empirical friction coefficients and shear strengths. This model considers whether the contact at each surface asperity could be modelled using the EHL solution of a point-contact between a hemisphere and a rigid flat. The predicted fluid shear force at each asperity is then averaged over a particular distribution of asperity deflections representing a rough surface and the effective friction coefficient obtained for the overall contact between rough surfaces. It is investigated whether the friction-load and friction-speed characteristics of point-contact offer a better experimental agreement than the standard inverse EHL approach across the seal contact pressure distribution.

5.1 Line-contact EHL simulation

5.1.1 Reynolds equation

5.1.1.1 Standard Reynolds equation

Where a lubricant is present between two sliding surfaces the behaviour of the fluid is often modelled using the Reynolds equation. For incompressible, one-dimensional, viscous dominated flow the Reynolds equation can be expressed as

$$\frac{d}{dx}\left(\frac{h^3}{\eta}\frac{dp}{dx}\right) = 6u\frac{dh}{dx} \tag{5.1}$$

where the relative velocity u is the sum of the velocities of the two surfaces and is equivalent to the rod velocity if the seal surface is assumed to be stationary. The viscosity η is a function of pressure and is expected to vary over the working range of pressures expected in hydraulic systems. For lubricating oils the pressure-dependence of viscosity is often determined by the Barus relation

$$\eta = \eta_0 e^{\alpha p} \tag{5.2}$$

Cameron [80] suggests the coefficient α can be obtained with reasonable accuracy from the Wooster relationship

$$\alpha = (3.5 + 0.965 \lg \eta_0) \times 10^{-8} \tag{5.3}$$

It is also necessary to take account of temperature variation in the gauge viscosity. It has been suggested [81] that the Barus exponential relationship between pressure and viscosity is a reasonably accurate approximation at low and moderate temperatures, although severely over-predicts viscosity at higher temperatures. Seal tribology is concerned with tribological phenomena with relatively low maximum pressures (limited to values similar to the maximum working pressure of the fluid, never higher than 100-500 bar in hydraulic systems). As the rod-seal interface is expected to experience neither extreme pressures nor extreme temperatures, the Barus relationship should be an appropriate model. A pressure-viscosity coefficient α of 2×10^{-8} Pa^{-1} is assumed as this value has been used in previous investigations of seal tribology such as [17].

5.1.2 Previous inverse EHL studies

In elastohydrodynamic problems it is necessary to calculate a film thickness distribution from the surface deformation that is compatible with the fluid pressure solution to the Reynolds equation. For sealing elements it is necessary to account for the deformation of the surfaces under the fluid action. Hydraulic rod seals normally have an initial pre-squeeze between the rod and seal to minimise fluid leakage at low pressures. It becomes necessary for a fluid pressure to deform the seal surface away from the rod to open up a channel for the fluid film if the Reynolds equation is to have positive film thicknesses. Additionally, the polymeric seal material is relatively flexible with an elastic modulus within the order of the expected fluid pressures.

Inverse elastohydrodynamic theory was initially used during a period of increasing interest in seal tribology during the 1960s and 1970s. Investigators (for example [26], [27] and [28]) used inverse EHL to calculate the film thickness profiles corresponding with analytical models of the pressure distribution profiles across a line contact. A later study by Johannesson [14] simulated the pressure distribution under an o-ring using a numerical finite element model and obtained the inverse solution of the film thickness from this pressure distribution.

5.1.3 Previous finite differencing EHL studies

An alternative to inverse EHL for solving the Reynolds equation is the finite differencing method. With this approach the Reynolds equation is discretised using finite difference approximations. The film thickness is then iterated with the corresponding fluid pressure solutions until a converged film thickness is reached.

Finite difference EHL methods are problematic for simulating contacts with elastomers or polymers due to numerical stability issues. The low stiffness of these materials results in large changes in film thickness corresponding with small changes in pressure from the solution of the Reynolds equation. It is necessary to use an iterative scheme that can maintain stability in the adjustment of the film thickness distribution. The common iterative method of the successive overrelaxation of the film thickness does not produce a convergent solution for the Hertzian contact problem [80]. Approximate solutions were first achieved with the Estel-Grubin method [40] which uses the standard inverse EHL solution inside the dry contact region and forward differencing outside this region while also using the dry surface profile to describe the change in film thickness outside the dry contact region. Subsequent investigations were able to obtain solutions of the coupled Reynolds and deformation equations without simplifying the deformed surface profile using Newton-Raphson iteration [82, 83] or a combined finite-difference and inverse solution method [41].

Line contacts associated with elastomer and polymer seals have different characteristics to the classical Hertzian contact in that the contact pressures are low relative to the pressure-viscosity coefficient α and large variations in the fluid viscosity are not expected. A convergent numerical scheme for rectangular seals was developed in [29] where Newton-Raphson iteration was used inside the sealing region and inverse EHL used at the inlet and outlet where the fluid pressure was assumed to be parabolic. A recent study by Nikas [30] produced a solution of two-dimensional EHL in elastomeric seals using finite differencing across the sealing region and inverse EHL at the inlet and outlet where a cubic pressure distribution was assumed. This study was later simplified to a one-dimensional case with no surface roughness in [31] and expanded to include backup rings and composite seals in [32] and [33].

5.1.4 Integrated Reynolds equation

Equation (5.1) may be integrated once with respect to x to give

$$e^{-\alpha p}\frac{dp}{dx} = 6\eta_0 u\left(\frac{h-h_m}{h^3}\right) \tag{5.4}$$

To determine the value of the h_m constant of integration, equation (5.1) is differentiated using the chain rule to produce

$$h^3 \frac{d}{dx}\left(\frac{1}{\eta_0} e^{-\alpha p} \frac{dp}{dx}\right) - \frac{dh}{dx}\left(6u - \frac{3h^2}{\eta}\frac{dp}{dx}\right) = 0 \tag{5.5}$$

and h_m is calculated by considering the solution of equation (5.5) at a convenient location along the contact. This location is the point where

$$h^3 \frac{d}{dx}\left(\frac{1}{\eta_0} e^{-\alpha p} \frac{dp}{dx}\right) = 0 \tag{5.6}$$

This can be identified from the known pressure distribution. At this condition equation (5.5) has solutions of either a film thickness gradient of zero or a particular local film thickness h_a that satisfies

$$h_a = \left(\frac{2\eta e^{\alpha p} u}{\left(\frac{dp}{dx}\right)_a}\right)^{\frac{1}{2}} \tag{5.7}$$

This allows the film thickness h_a at the critical point identified to be calculated from the pressure distribution. To obtain the h_m constant of integration equation (5.7) is substituted for the film pressure gradient in equation (5.4), allowing h_m to be evaluated as $h_m = \frac{2}{3}h_a$. Equation (5.4) can be solved at each node across the contact length using the value obtained for h_m to give the complete film thickness distribution.

Nau [4] supposes that the minimum film thickness in seal tribology can be calculated from the points of inflexion on the contact pressure distribution with a variation of the integrated Reynolds equation. This approach assumes an isoviscous fluid, causing the exponential terms disappear from equations (5.4) and (5.7) and produces minor differences in the location of the critical point and associated film thicknesses. Equation (5.7) indicates the film thickness h_a at the critical point to be proportional to $u^{\frac{1}{2}}$ as the fluid pressure distribution does not vary between different wall velocities in basic inverse EHL analysis.

5.1.5 Simulation of seal tribology with inverse EHL

The pressure distribution across the contact region for a single-lip seal was obtained from FEA modelling of the seal geometry as described in section 4.1.2. A pressure distribution produced from a geometry with 0.4 mm chamfers at the seal corners was used (figure 4-11). Previous EHL studies of rectangular seals have assumed cubic [31] or parabolic [29] pressure distributions over the inlet region with the length of this inlet region specified based on empirical judgement. It is preferable to make predictions about the pressure distribution in the inlet regions. Using the contact pressure results from FEA simulation has a problem that the region of increasing pressure approximates to Hertzian contact with a parabolic pressure distribution. A parabolic pressure profile does not have a location with a second derivative of

zero while the pressure is an increasing function. Therefore it is not possible to find a critical point for h_a on the rising section of the inlet. The current study took the unusual approach of taking the critical point h_a near the outlet on the inside of the outlet Hertzian peak where pressure is also an increasing function. This approach allowed solutions to the integrated Reynolds equation to be obtained without assuming particular pressure distributions near the limits of the contact region.

In order to evaluate the pressure distribution in equation (5.6) to find the critical points it is necessary to find the first and second derivatives of the pressure. This was achieved using the central differencing method and applying smoothing to the functions before carrying out the numerical differentiation. A second order Butterworth filter algorithm with a dimensionless frequency of 0.2 was used with a forward followed by a reverse pass to avoid introducing a phase-lag. Critical points corresponding with h_a in the pressure distribution for 80 bar sealed pressure were found to occur at 0.22 mm from the sealed pressure side and 0.29 mm from the air side.

With the critical points on the pressure distribution identified it is possible to calculate the critical film thickness h_a for different sliding speeds. A range of sliding speeds between 0.1 mm/s and 500 mm/s were simulated to correspond with the experimental speed range. For each sliding speed and critical film thickness the overall film thickness was calculated using equation (5.4) at each node along the pressure distribution. A grid of 146 nodes was used with spacing corresponding to those obtained from the finite element simulation of the seal pressure distribution in figure 4-11. It was not possible to obtain real solutions to the film thickness distribution outside the critical points on the fluid pressure distribution. It is assumed that in these regions near the inlet and outlet with high pressure gradients there would be some transition to low pressure gradients at the boundaries. There was further assumed to be no contribution to total friction from these near-inlet and near-outlet regions.

Once the inverse Reynolds equation is solved the friction may be calculated by numerically integrating the fluid shear stress at the moving surface over the contact length. For the one-dimensional Reynolds equation, the shear force acting on the boundary [84] is

$$S_{zx} = \pi D \int_0^L \tau_{zx} dx = \pi D \int_0^L -\frac{h}{2}\frac{dp}{dx} - \frac{\eta_0 e^{\alpha p} u}{h} dx \tag{5.8}$$

5.1.6 Results from inverse EHL simulation of single-lip seal

Figures 5-1 and 5-2 indicate inverse EHL theory not to be suitable for reciprocating seal friction at higher sealed pressures. For all rod speeds across the operating range the measured fluid shear induced friction is over an order of magnitude higher than the friction levels predicted by EHL simulation. In order to produce a friction coefficient of 0.1, typical of the measured seal friction at 80 bar, it would be necessary to have a nano-scale film thickness

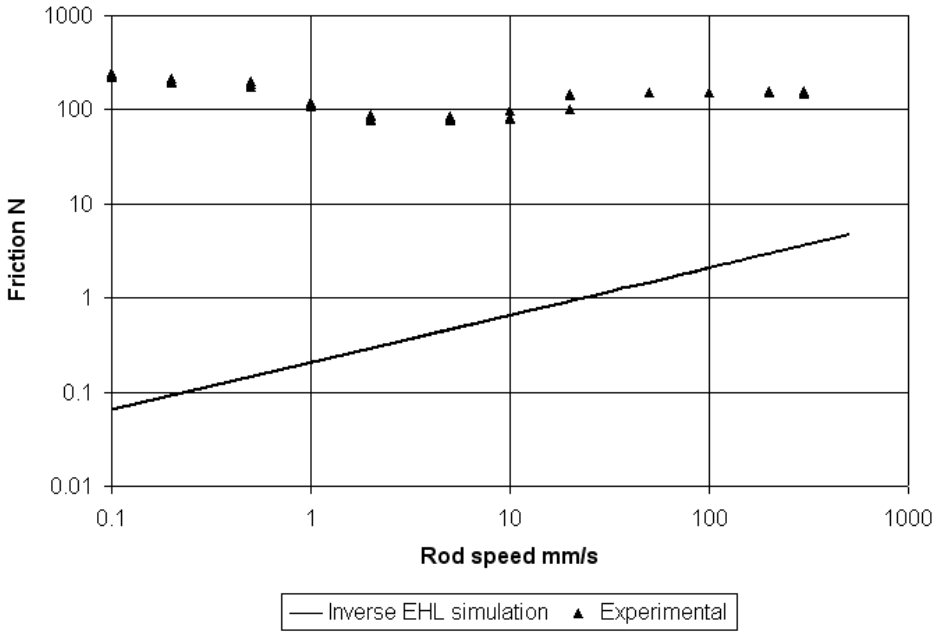

Figure 5-1: Instroke friction results from inverse EHL simulation, 80 bar sealed pressure, single-lip seal. Experimental data are from figure 2-18.

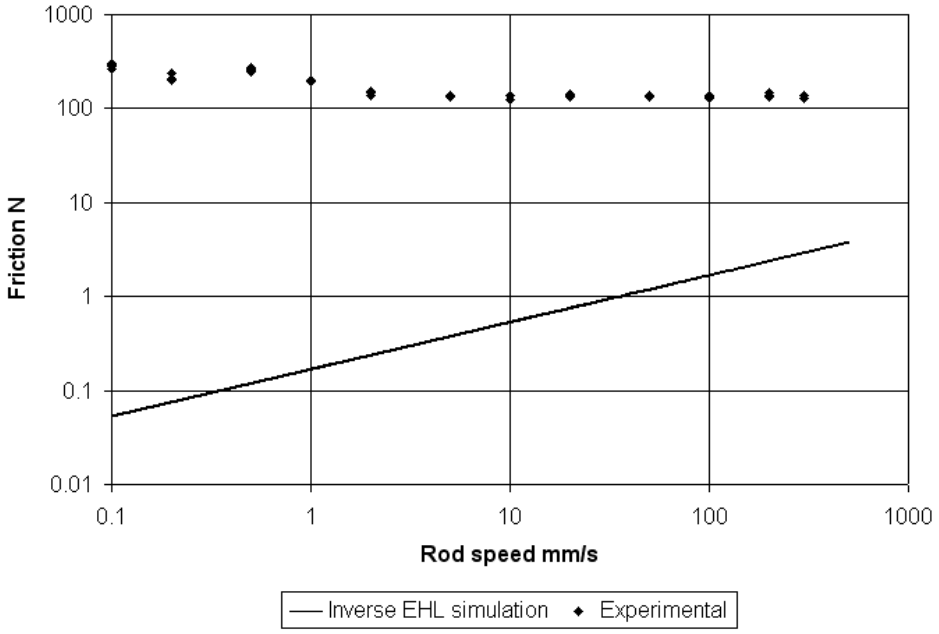

Figure 5-2: Outstroke friction results from inverse EHL simulation, 80 bar sealed pressure, single-lip seal. Experimental data are from figure 2-18.

of 0.5 nm for an intermediate sliding speed of 10 mm/s and 0.043 Pas fluid viscosity. This suggests there to be an additional dominant source of friction between the rod and seal. Boundary friction occurs if direct contact takes place between the two surfaces and shear stress between surface asperities acts to oppose motion. If there is direct contact between the two surfaces the load is at least partially transferred through these contact regions and the Reynolds equation cannot be coupled exclusively with the surface deformation.

It is also noted that the experimental friction force does not follow a $u^{\frac{1}{2}}$ power law. Early experimental studies [5] have noted that the measured friction behaviour suggests boundary friction to be dominant and the fluid film to have collapsed while also having measured oil films on the micron-scale. For the purposes of friction prediction it may be more appropriate to assume boundary friction models if empirically realistic results are required. Any simulations based on the Reynolds equation with micron-scale film thickness would have to include asperity contact with boundary friction if friction predictions within the correct order of magnitude are required. Modelling techniques with mixed asperity contact and EHL lubrication offer a possible means of explaining the higher friction levels.

5.2 Mixed EHL simulation

5.2.1 Mixed EHL methodology

5.2.1.1 Mixed lubrication overview

A mixed lubrication simulation similar to that undertaken by Salant [17] was produced for the current investigation. The method has recently seen significant usage and citation in hydraulic seal tribology and has become a commonly used modelling tool in this field. It is uncertain whether this adoption is justified with the absence of any detailed comparison with experimental data. The current study attempts to experimentally verify the accuracy of the model and determine its usefulness as a predictive tool for the tribology of different seal designs.

The concept of coupling the film thickness for the Reynolds equation with the mean separation in the GW contact model was first proposed by Johnson [34]. Here the inverse solution to the Reynolds equation was combined with GW contact theory over a Hertzian line-contact, iterating the fluid pressure distribution until a converged solution was reached. A similar method was later applied to hydraulic seals in [35]. More recently a novel approach to mixed lubrication and seal friction was proposed by Wassink [12]. This study attempted to quantify the energy dissipation from fluid shear stress, viscoelasticity within the seal material when cycled by the rough rod surface and shearing the intramolecular bonds at the rod-seal interface.

Salant recently produced a GW-Reynolds equationlubrication model for hydraulic seals

[17] in a continuation of [85, 72]. The model is similar to that proposed by Johnson, although uses the alternative numerical technique of iterating the film thickness and calculating the fluid pressure from finite differencing instead of using inverse EHL. Salant's recent study was later modified in [36] and [37] to take account of the two contact regions associated with a double-lip seal. A non-zero fluid pressure is assumed between the two contact regions and the numerical procedure expanded to include iterating the pressure boundary conditions associated with this inter-lip pressure and a film thickness distribution obtained for each contact region separately. The model was later extended to investigate the transient behaviour over a complete operating cycle [38].

The mixed lubrication model assumes both elastohydrodynamic lubrication and GW asperity contact to occur simultaneously. Both the fluid and asperity contact pressures are assumed to be functions of the film thickness distribution with the mean film thickness for the purposes of the fluid mechanics pressure solution assumed to be equivalent to the mean surface separation for the purpose of the GW contact model. It is further assumed that the fluid and asperity contact pressures superpose to give the total pressure distribution. Fluid pressure is calculated from the solution of the average Reynolds equation for the known film thickness and boundary pressures. The asperity contact pressure distribution is determined from GW contact theory. The film thickness distribution is consistent with the fluid and asperity contact pressures. Seal deflection is determined from the total fluid and asperity contact pressures, the static contact pressure where there is no film and the compliance of the seal. The static contact pressure and seal compliance are determined from FE pre-modelling.

The numerical method used for the simulation is illustrated in figure 5-3. To begin the numerical process an initial guess for the film thickness distribution (one from a previous simulation with similar parameters if available) was produced. The asperity contact pressure was calculated simply from the film thickness using a lookup table for the solutions of the GW equations. The total effective pressure was obtained from the sum of the fluid and asperity contact pressure distributions. A film thickness corresponding to this total pressure was calculated from a compliance matrix deformation model.

5.2.1.2 Parameters for GW-average Reynolds equation

Roughness parameters similar to those of [17] were used in the current simulations. It has been considered in section 4.2.3.3 that the values of peak curvature R and asperity density η may not be physically accurate. Use of a significantly larger radius of curvature was found to prevent the asperity contact pressure from being able to support the static contact distribution at higher sealed pressures for positive mean separation.

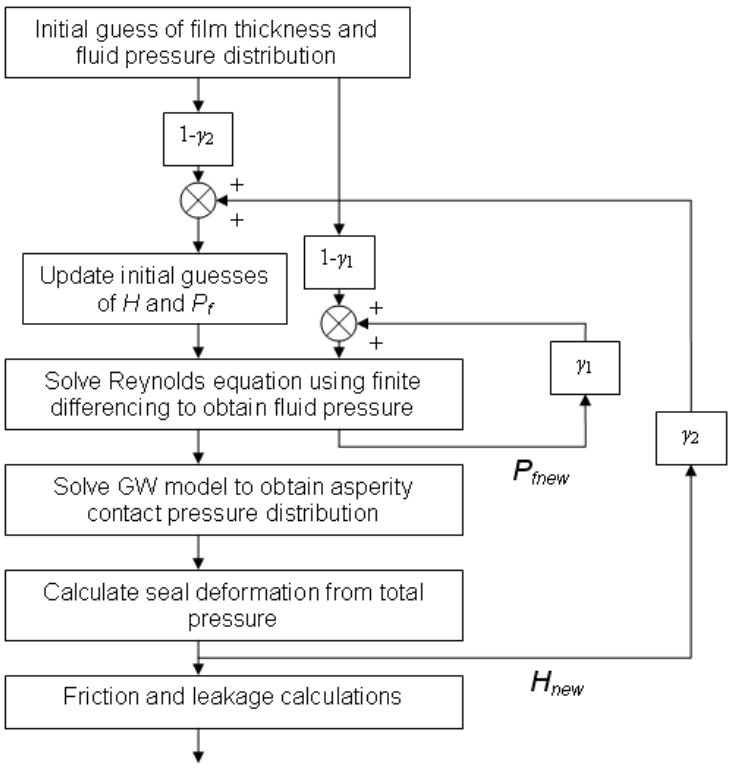

Figure 5-3: Solution procedure for GW-average Reynolds simulation, γ_1 and γ_2 are relaxation factors for respective fluid pressure P_f and film thickness H distributions

5.2.1.3 Solution of average Reynolds equation

The fluid pressure distribution is assumed to be governed by the one-dimensional average Reynolds equation. This assumes cyclic symmetry with no significant eccentricity in the seal and rod alignment and no bend in the rod throughout the stroke. Steady-state conditions are also assumed with no inertia effects in either the fluid or the seal. Fluid flow is assumed to be laminar as the micron-scale film thicknesses are associated with low Reynolds numbers where viscous forces dominate. The average Reynolds equation, with non-dimensional film thickness H, axial distance $\hat{x}$ and fluid pressure P_f with respect to roughness height σ_h, contact length L_x and ambient pressure p_{atm}, is

$$\frac{d}{d\hat{x}}\left(\phi_x H^3 \frac{dP_f}{d\hat{x}}\right) = 6\zeta \frac{\eta}{\eta_0}\frac{d}{d\hat{x}}\left(H_T + \phi_{s,c}\right) \tag{5.9}$$

Use of the semi-empirical flow factors ϕ_x and $\phi_{s,c}$ adjusts for the effects of surface roughness on effective flow. These coefficients were derived by Patir and Cheng [86, 87] from numerical simulations of fluid flow past randomly generated rough surfaces. Each coefficient is a function of only the dimensionless mean surface separation and is therefore simple to cal-

culate for a particular iteration as the film thickness profile is known. For isotropic roughness, the coefficients are

$$\phi_x = 1 - 0.90e^{-0.56H} \tag{5.10}$$

$$\phi_{s,c} = 1.899H^{0.98}e^{-0.92H+0.05H^2} \qquad \text{H} \leq 5 \tag{5.11}$$

$$\phi_{s,c} = 1.126e^{-0.25H} \qquad \text{H} > 5 \tag{5.12}$$

The average Reynolds equation (5.9) does not take account of the effects of inter-asperity cavitation on the flow characteristics. Previous studies [88] have simulated the occurrence of cavitation near asperity surfaces and its effects on overall flow. Additional correction factors for the phenomenon have been produced that can be applied to the average Reynolds equation for particular operating conditions. However, there are no general semi-empirical relationships between film thickness and the coefficients for inter-asperity cavitation. Inter-asperity cavitation cannot be implemented into the general average Reynolds equation as simply and readily as the Patir-Cheng roughness correction factors. Previous studies of hydraulic seals with GW-average Reynolds have not included inter-asperity cavitation and it was not thought necessary to consider its effects in the current investigation.

The average Reynolds equation (equation (5.9)) becomes nonlinear when combined with the pressure-dependent viscosity relation in equation (5.2). To discretise the equation the exponential terms were assumed to be functions of a known pressure distribution. During the solution procedure this assumed pressure distribution was updated with successive results for fluid pressure to obtain an accurate solution. Expanding the combined equation gives

$$\frac{d}{d\hat{x}}\left(\phi_x H^3 e^{-\hat{\alpha}P_f}\right)\frac{dP_f}{d\hat{x}} + \frac{d^2P_f}{d\hat{x}^2}\phi_x H^3 e^{-\hat{\alpha}P_f} = 6\zeta\eta_0\frac{d}{d\hat{x}}\left(H_T + \phi_{s,c}\right) \tag{5.13}$$

This equation may be differentiated with respect to $\hat{x}$:

$$\frac{d\phi_x}{d\hat{x}}H^3 e^{-\hat{\alpha}P_f} + \phi_x\left(3H^2\frac{dH}{d\hat{x}}e^{-\hat{\alpha}P_f} + H^3\frac{d}{d\hat{x}}\left(e^{-\hat{\alpha}P_f}\right)\right) + \phi_x H^3 e^{-\hat{\alpha}P_f}\frac{d^2P_f}{d\hat{x}^2} = 6\zeta\eta_0\left(\frac{dH_T}{d\hat{x}} + \frac{d\phi_{s,c}}{d\hat{x}}\right) \tag{5.14}$$

Equation (5.14) becomes linear once the substitution for the pressure distribution in the exponential term is included. Central difference approximations apply as

$$(\frac{dP_f}{d\hat{x}})_n = \frac{P_{fn+1} - P_{fn-1}}{\delta\hat{x}_n + \delta\hat{x}_{n-1}} \tag{5.15}$$

$$(\frac{d^2P_f}{d\hat{x}^2})_n = \frac{P_{fn+1} - 2P_{fn} + P_{fn-1}}{\delta\hat{x}^2} \tag{5.16}$$

The truncated film thickness terms H_T is

$$H_T = \frac{H}{2} + \frac{H}{2}erf\left(\frac{H}{\sqrt{2}}\right) + \frac{1}{\sqrt{2\pi}}e^{-\frac{H^2}{2}} \tag{5.17}$$

Substituting the central difference approximations (5.15) and (5.16) into (5.14) produces

$$\begin{aligned} P_{fn-1}\{\frac{2A_n}{\delta\hat{x}_{n-1}(\delta\hat{x}_{n-1} + \delta\hat{x}_n)} - \frac{A_{n+1} - A_{n-1}}{(\delta\hat{x}_{n-1} + \delta\hat{x}_n)^2}\} + \\ P_{fn}\{\frac{-2A_n}{(\delta\hat{x}_{n-1} + \delta\hat{x}_n)}(\frac{1}{\delta\hat{x}_n} + \frac{1}{\delta\hat{x}_{n-1}})\} + \\ P_{fn+1}\{\frac{2A_n}{\delta\hat{x}_n(\delta\hat{x}_{n-1} + \delta\hat{x}_n)} + \frac{A_{n+1} - A_{n-1}}{(\delta\hat{x}_{n-1} + \delta\hat{x}_n)^2}\} = \\ \frac{6\zeta\eta_0}{\delta\hat{x}_n + \delta\hat{x}_{n-1}}(H_{Tn+1} - H_{Tn-1} + \phi_{s,cn+1} - \phi_{s,cn-1}) \end{aligned} \tag{5.18}$$

where

$$A_n = H^3 e^{-\hat{\alpha}P_{fn}} \tag{5.19}$$

The relationships in equation (5.18) may be used to assemble a tridiagonal matrix. The boundary conditions for the fluid pressure P_f are taken as the sealed pressure P_s and ambient gauge pressure 0 corresponding with respective distances along the sealing length $\hat{x}$ of 0 and 1. Nodal spacing across the contact length was set as being equivalent to that used in the FE simulation of the static contact pressure distribution. For a known film thickness distribution (and an initial set of values of P_f for use in the exponential terms) a single iteration of the tridiagonal matrix solver produces a new set of values for fluid pressure P_{fnew}. The fluid pressure distribution was then updated using the successive over-relaxation method with a relaxation factor γ_1 of 0.1 according to

$$P_f = \gamma_1 P_{fnew} + (1 - \gamma_1)P_{fold} \tag{5.20}$$

A new fluid pressure distribution was then calculated from the tridiagonal matrix solver using the updated values of fluid pressure in the exponential terms. This process was repeated until the mean absolute nodal change in fluid pressure P_f between iterations was within a specified tolerance of 1×10^{-3}.

5.2.1.4 Cavitation modelling

It is necessary to use a fluid cavitation model to avoid negative fluid pressures. In most tribology literature cavitation refers to either air release from the fluid where the pressure drops significantly below atmospheric pressure or boiling of the fluid where the pressure drops below the vapour pressure of the fluid. Hydraulic or fluid power terminology usually distinguishes between these two phenomena, referring to them as aeration and cavitation respectively. In the current investigation both air release and fluid boiling are referred to as cavitation. Most EHL studies assume cavitation to appear as air release from the fluid while the fluid divides into streamers at the fluid cavitation pressure [80]. Similarly, the current investigation assumes cavitation to take place at a gauge fluid pressure of zero.

There are several different cavitation models for EHL that produce similar fluid pressure distributions. The half-Sommerfield condition allows negative pressures to occur in the solution of the Reynolds equation, although uses a pressure of zero in the cavitated region with negative pressures for the purposes of calculating the surface deformation. An alternative cavitation model is the Reynolds condition where a pressure gradient of zero is assumed at the boundary of the cavitated region. An additional method is the Jakobsson-Floberg-Olsson model [89] where the fluid is assumed to be governed by a different set of equations to the Reynolds equation inside the cavitated regions where the cavitated fluid is modelled simply as having constant pressure and variable density. The current study has used the Reynolds condition cavitation model, implemented by setting all the negative values of fluid pressures to zero in each numerical iteration in the solution of the Reynolds equation.

5.2.2 GW contact solution

The asperity contact pressure distribution was calculated from the film thickness using GW contact theory. It is assumed the dimensionless film thickness for the fluid is equivalent to the mean surface separation used in the GW model (section 4.2.2). A simple lookup table may be used with linear interpolation between data points to determine the contact pressure at each node. This lookup table may also be used to determine the static film thickness from the static pressure distribution.

5.2.3 Seal deformation solution

In order to calculate the deformation of the seal that would open a channel for the fluid film it is necessary to know the static contact pressure occurring at zero film thickness and the flexibility of the seal about this point. The static contact pressure distribution for a particular seal geometry was obtained from FEA modelling (section 4.1.2). For a static contact pressure P_{sc} there is a corresponding static film thickness H_s that occurs when there is no fluid pressure. The static film thickness may be obtained by setting the asperity contact

pressure equal to the static contact pressure and using the lookup table from the GW analysis to find the film thicknesses corresponding to this asperity contact pressure distribution.

A linearised deformation model may be used to calculate the seal deformation under the action of the combined fluid and asperity contact pressures. This model assumes the deflection at a node to be proportional to the change in pressure at each of the nodes along the contact length and is equivalent to a linearisation of the seal compliance. A compliance matrix may be used to represent this relationship between a change in total pressure and deflection or film thickness. For a total pressure equal to the static contact pressure the film thickness is expected to be equal to the static film thickness. This condition may be used to set the offset (equivalent to the static film thickness H_s) in the relationship between total pressure and film thickness. For a particular total pressure the film thickness is given by

$$\mathbf{H} = \mathbf{H_s} + \mathbf{C}(\mathbf{P_t} - \mathbf{P_{sc}}) \tag{5.21}$$

where $\mathbf{C}$ is the compliance matrix, $\mathbf{P_t}$ is the column vector of combined fluid and asperity contact pressures across the contact. $\mathbf{H}$, $\mathbf{H_s}$ and $\mathbf{P_{sc}}$ are the respective column vectors of the H, H_s and P_{sc} distributions along the contact length.

5.2.4 Film thickness computation

The successive over-relaxation method was used to iterate the film thickness until fluid and asperity contact pressures were converged to that produced the required film thickness in the surface deformation model. The film thickness was updated with a relaxation factor γ_2 of 0.21×10^{-3} according to

$$H = \gamma_2 H_{new} + (1 - \gamma_2) H_{old} \tag{5.22}$$

This outer loop iteration of film thickness was carried out until the mean of the absolute changes in the dimensionless film thickness at each node fell within the tolerance for convergence. A tolerance of 0.1×10^{-3} was found to be sufficient to avoid any significant differences in the converged solution compared with higher tolerances.

5.2.5 Postprocessing procedure

Friction and leakage were calculated once a converged solution for the film thickness was obtained. The dimensionless leakage is given by

$$\hat{q} = \phi_x H^3 e^{-\hat{\alpha} P_f} \frac{dP_f}{d\hat{x}} + 6\zeta\eta_0 (H_T + \phi_{s,c}) \tag{5.23}$$

The friction was calculated from the fluid and asperity shear stress. From the standard features of the Reynolds equation the fluid shear stress at a point on the rod surface is given

by

$$\tau = \frac{-\eta_0 e^{\alpha P_f} u}{H\sigma_h}(\phi_f - \phi_{fs}) - \phi_{fp}\frac{H\sigma_h p_a}{2L_x}\frac{dP_f}{d\hat{x}} \tag{5.24}$$

Central differencing was using to obtain the pressure gradients at each node for use in equation (5.24). The correction factors in this equation (obtained by Patir and Cheng as semi-empirical relationships) are

$$\phi_f = \frac{1}{\frac{3}{256}\{35 + z(128 + z(140 + z^2(-70 + z^2(28 - 5z^2))))\}} \qquad \left(z = \frac{H}{3}\right) \tag{5.25}$$

$$\phi_{fs} = 1.11H^{2.31}e^{-2.38H+0.11H^2} \qquad H \leq 7 \tag{5.26}$$

$$\phi_{fs} = 0 \qquad H > 7 \tag{5.27}$$

$$\phi_{fp} = 1 - 1.40e^{-0.66H} \tag{5.28}$$

Asperity shear stress is assumed to follow a Coulomb friction law. A friction coefficient of 0.25 was assumed for the asperities. This friction relationship is expressed as

$$\tau_c = -f_c P_c p_a \frac{u}{|u|} \tag{5.29}$$

The combined fluid and asperity shear stress was numerically integrated over the contact length obtain the total friction.

5.2.6 Results from GW-average Reynolds simulation

5.2.6.1 Single-lip seal results

Figures 5-4 to 5-6 compare measured friction levels with those simulated with the GW-average Reynolds model. During instroke there is an increase in simulated friction with sliding speed which approaches a limit at a sliding speed of approximately 10 mm/s. For outstroke there is a significant decrease in simulated friction which approaches a limit at 2 mm/s. This produces a qualitative agreement between the simulations and experiments during outstroke, although the agreement is poor during instroke.

The higher simulated friction during instroke took place as a result of a reduction in fluid pressure and appearance of a cavitated region near the air side of the seal. Figure 5-7 shows a typical fluid and asperity contact pressure distribution during instroke, indicating a significant cavitated region to extend inwards from the air side of the seal. The higher asperity contact

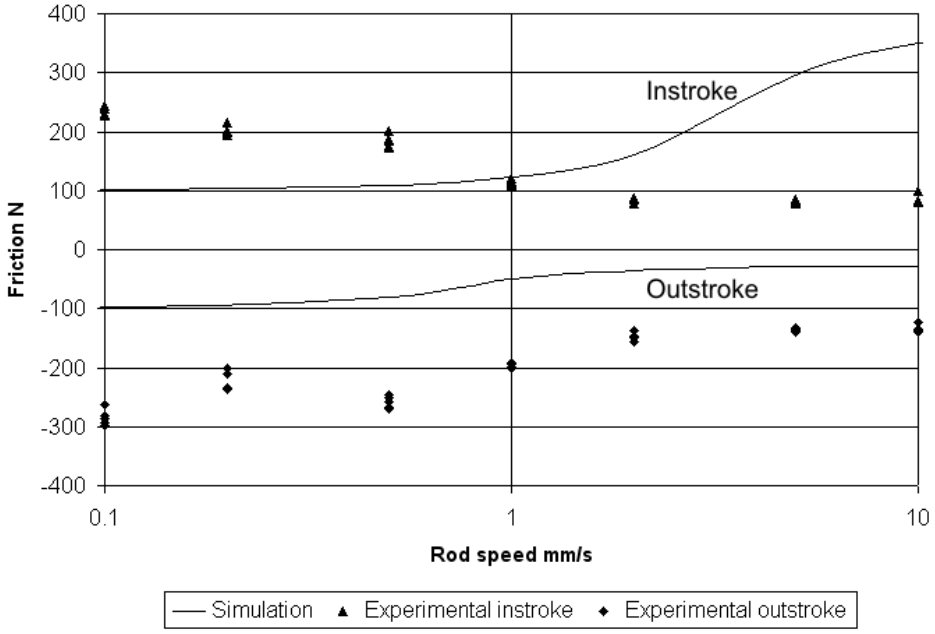

Figure 5-4: GW-average Reynolds simulation of single-lip seal, 80 bar sealed pressure

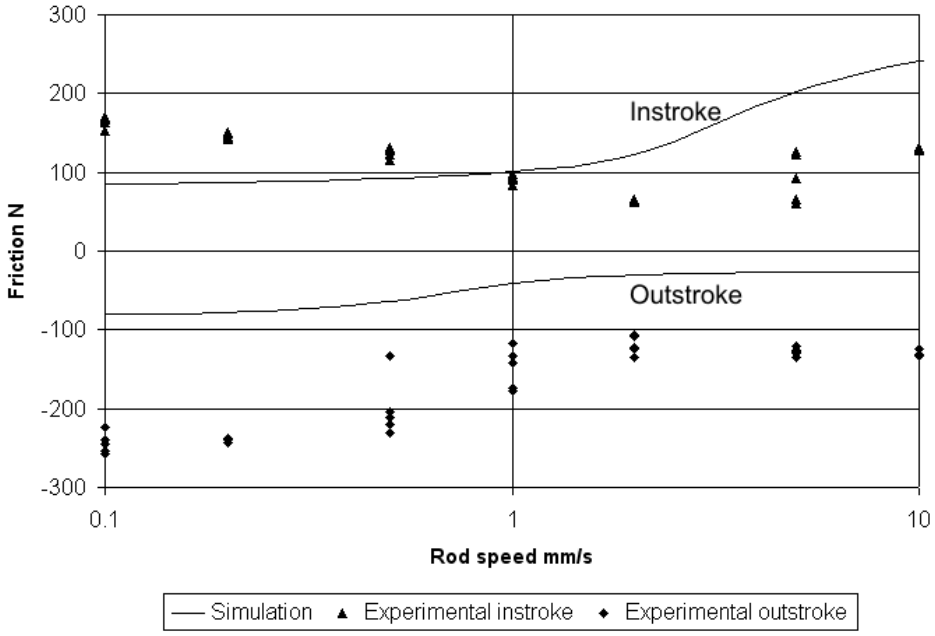

Figure 5-5: GW-average Reynolds simulation of single-lip seal, 60 bar sealed pressure

pressure and shear stress from these cavitated regions results in higher overall friction levels as asperity shear dominates over fluid shear stress as a source of friction.

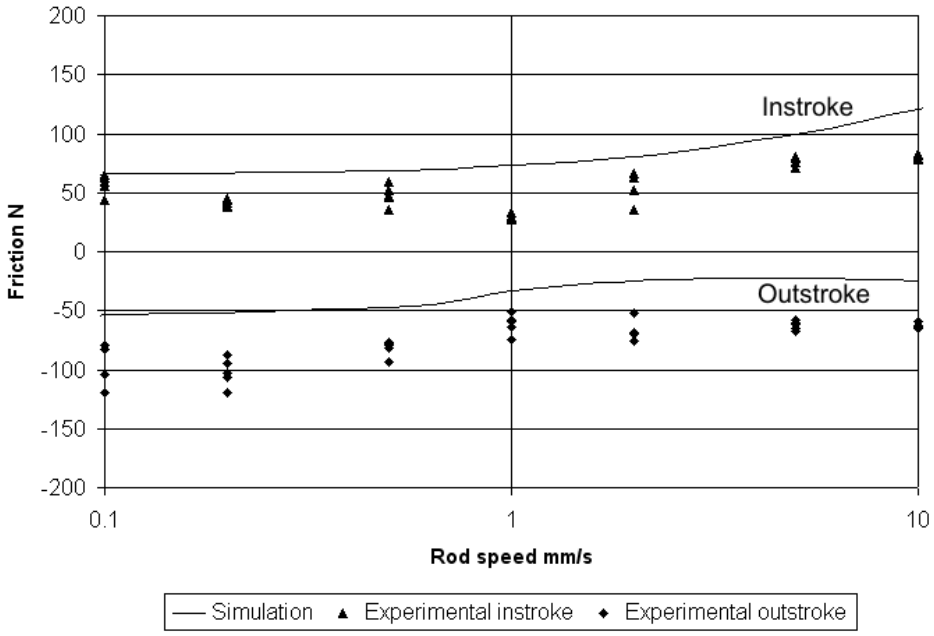

Figure 5-6: GW-average Reynolds simulation of single-lip seal, 40 bar sealed pressure

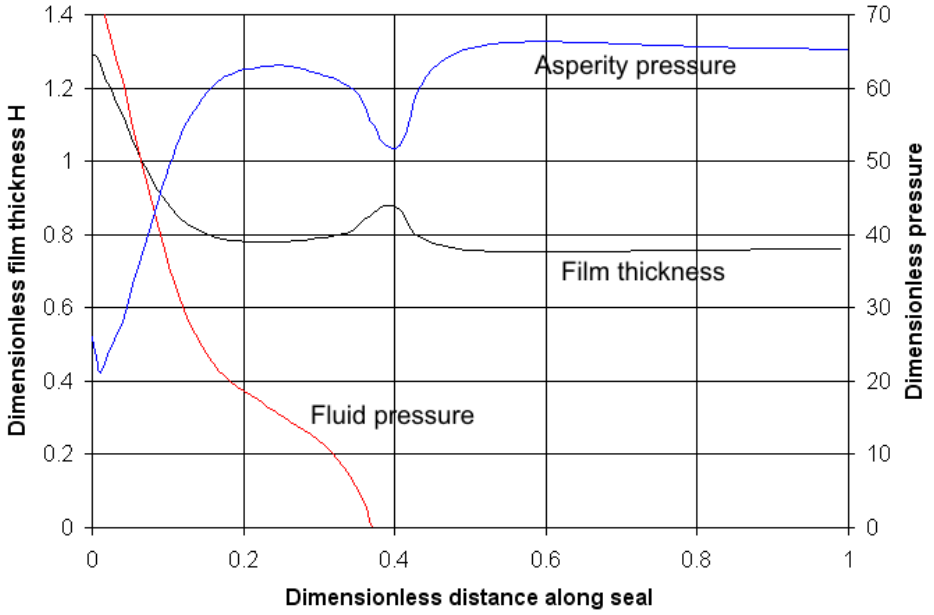

Figure 5-7: Fluid and asperity pressure distributions for mixed lubrication simulation, base parameters, 80 bar sealed pressure, u=-10 mm/s (instroke)

In the outstroke case (figure 5-8) the fluid pressure maintains higher values across the length of the seal, decreasing rapidly near the outlet to meet the air side pressure bound-

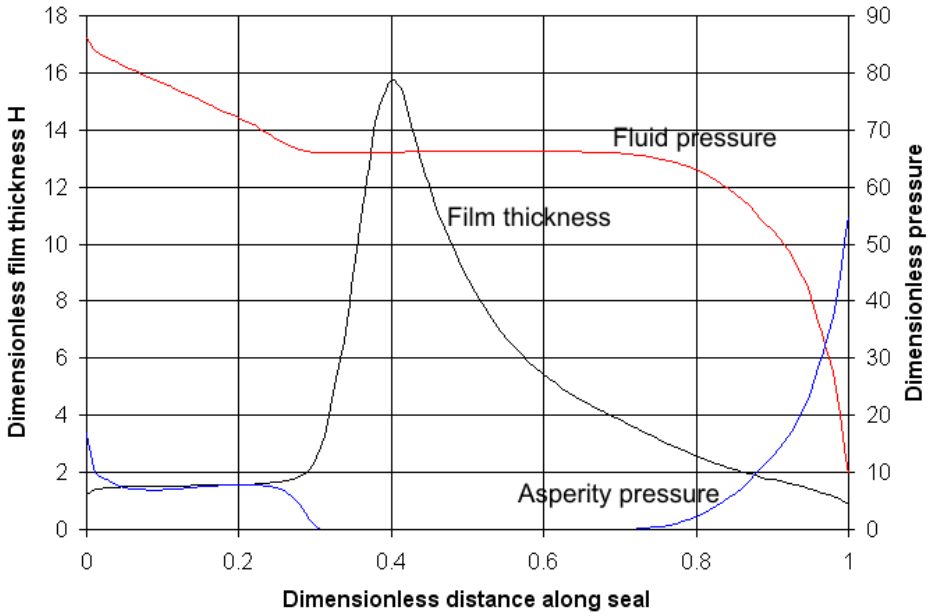

Figure 5-8: Fluid and asperity pressure distributions for mixed lubrication simulation, base parameters, 80 bar sealed pressure, u=2 mm/s (outstroke)

ary condition. With the higher fluid pressures and correspondingly lower asperity contact pressures there was a reduced asperity shear contribution to friction, hence a lower overall friction during outstroke. The extended region of higher fluid pressure may be caused by the divergent film shape between the sealed side and air side of the seal (shown as H on figure 5-8). Inspection of the Reynolds equation (equation (5.1)) indicates the Poiseuelle flow due to pressure to vary with the cubic of film thickness while the relative velocity-induced Couettte flow is proportional to film thickness. For a diverging film a lower pressure gradient is required further downstream to maintain flow continuity, necessitating a negative second derivative of fluid pressure. This prevents significant negative pressure gradients at or near the inlet in order that positive fluid pressures can be maintained until the ambient pressure boundary condition at the outlet.

Varying the sealed pressure over intermediate to higher pressures is shown to affect mainly the magnitude of the friction levels (figures 5-4, 5-5 and 5-6). Between these cases the effect of increasing the sealed pressure is to create a proportional increase in simulated friction without significantly affecting how the relative friction varies with sliding speed. For sealed pressures between 40 bar and 80 bar the rod and seal are predicted to be in uninterrupted contact with a single contact region. Above a critical sealed pressure increases in sealed pressure appear approximately as an increase in hydrostatic pressure across the static contact pressure distribution and do not significantly affect the simulated speed-dependent behaviour.

Overall the simulation results for the GW-average Reynolds model show a poor agreement with the experimental data. At higher sealed pressures no extreme differences were measured between instroke and outstroke friction while much higher friction levels were predicted during instroke (figure 5-4). The higher friction during instroke may have been a result of a convergent film being created through allowing GW contact pressure to take part of the load and reducing the direct influence of fluid pressure on film shape. It is not possible to prevent the increasing friction during instroke while maintaining the load sharing principle and using a static contact pressure corresponding with the seal geometry.

5.2.6.2 Sensitivity analysis

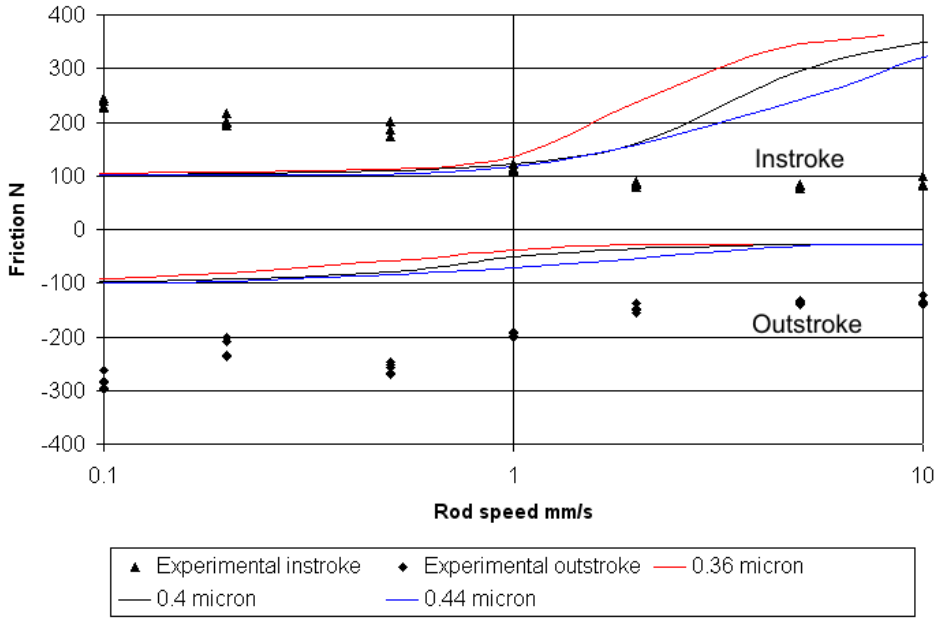

Figure 5-9: Sensitivity of GW-average Reynolds simulation to σ_h, single-lip seal, 80 bar sealed pressure

Figure 5-9 show the effect of varying the RMS roughness height σ_h on the results from the mixed GW-average Reynolds simulation. Decreasing the roughness height reduces the transition region of sliding velocities over which the changes in friction level occur without significantly affecting the limiting values of friction. Similarly, at the higher roughness height the transition range of sliding speeds is expanded. These differences in behaviour between different roughness heights occur as a result of changes in dimensionless rod speed with respect to film thickness. For the lower roughness height the absolute static film thickness h_s reduces in order to maintain a particular static contact pressure distribution. With the correspondingly thinner films the Couette flow in the Reynolds equation is expected to be

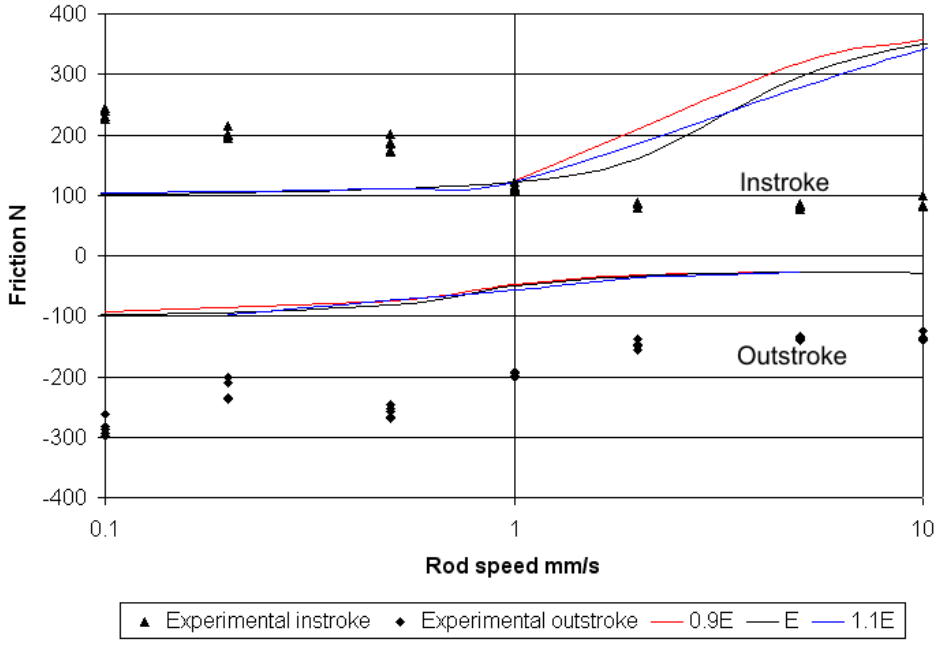

Figure 5-10: Sensitivity of GW-average Reynolds simulation to material E, single-lip seal, 80 bar sealed pressure

reduced less than the Poiseuille flow, resulting in a lower relative velocity being required to produce a particular pressure gradient in the Poiseuille term.

The simulation results were shown to be relatively insensitive to moderate changes in elastic modulus of the seal material. Figure 5-10 indicates reducing the elastic modulus to produce a small reduction in the range of velocities over which the change in friction occurs without significantly affecting the limiting friction values. This change in transition speed range occurs through a similar mechanism to that identified from reducing the asperity height. For lower elastic moduli the dimensionless static film thickness H_s reduces as further deflection of a rough surface are required to maintain a constant load with the lower material stiffness. With the thinner films the Couette term in the Reynolds equation would also be reduced less than the Poiseuille term for a fixed sliding speed, also necessitating higher pressure gradients to maintain continuity.

5.2.6.3 O-ring results

GW-average Reynolds simulation of an o-ring geometry produced similar speed-dependent friction behaviour to that observed in the single-lip seal (figure 5-11). There is a significant rise in friction during instroke as a result of cavitation and reduced fluid pressure extending significantly into the contact region from the air side boundary. This cavitation effect is caused

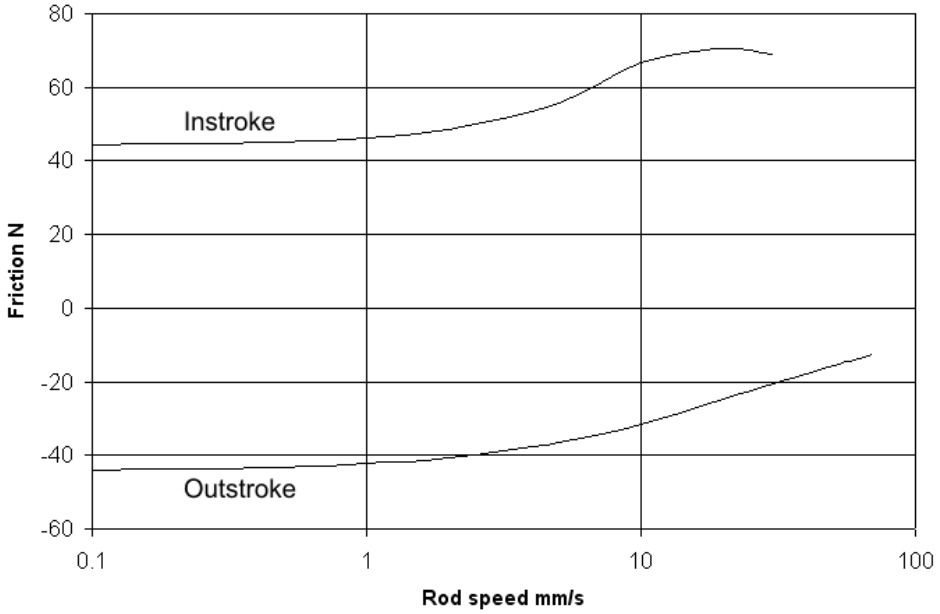

Figure 5-11: GW-average Reynolds simulation of o-ring, 80 bar sealed pressure

by a similar mechanism as for the single-lip seal where it was proposed that the divergent film between the pressure and air sides created a positive second derivative of fluid pressure in this same direction during instroke motion. The transition region of speeds over which the friction variation took place is greater for the o-ring simulations than the single-lip seal. This could be partially explained by the lower elastic modulus assumed for the elastomeric o-ring material (assumed 5 MPa for nitride rubber) compared with the 12.1 MPa assumed for the polyurethane seal material.

5.3 Modification to GW-average Reynolds simulation

5.3.1 Maintenance of fluid film during asperity collapse

One of the main limitations identified with the GW-average Reynolds model is the high loading of the asperities, which may exceed the accurate range of GW contact theory. This is discussed in section 4.2.3.3 where it is shown that commonly assumed surface roughness parameters could result in unrealistic contact fractions for the expected range of asperity contact pressures. There are two possible consequences of simulating excessive contact fractions; excessive friction prediction and GW theory suggesting that the surfaces are able to maintain a significant mean separation when this is not the case. At higher loadings where the contact fraction is a significant proportion of unity an uninterrupted fluid channel may

not be able to exist around the regions of asperity contact. Under these conditions it may not be possible to have both a fluid film between the surfaces and a high degree of asperity contact.

There are two possible approaches to modelling regions of high asperity loading where high contact fractions are expected. The more obvious approach is to assume the fluid film collapses in regions where the asperity contact pressure and contact fraction exceed a critical value. With this assumption the fluid film would disappear at any location with high asperity contact pressure and, in order to maintain flow continuity, any one-dimensional model of the contact region could not have a fluid film at any location along the contact. Under these conditions the fluid film would be expected to collapse across the full contact region and the Reynolds equation would not be valid. If there is no fluid film between the rod and seal the friction characteristics would be expected to be determined by asperity contact only and contact mechanics approaches would be appropriate (chapter 4).

An alternative approach to modelling high asperity loading where the rough surface becomes flattened is to assume the fluid film is maintained. In order for the fluid film to be maintained under these conditions it would be necessary for the film to form between the flattened regions between the two surfaces, reducing the real area of contact between the surfaces. Under these conditions the real area of contact and resulting asperity shear stress would reduce and loading would be transferred from the asperities to the fluid. If this maintenance of EHL conditions is assumed to take place it is necessary to determine under what conditions the reformation of the fluid film takes place and how far the degree of asperity contact is reduced.

One of the possible justifications for assuming a fluid film to be maintained between the two sliding surfaces is that previous studies of hydraulic seals have reported significant fluid films. Ruskell [29] and Field [10] measured fluid film thicknesses in the order of a micron during experiments with elastomeric seals, suggesting there to have been a substantial layer of fluid between the surfaces. Boundary layers at the surfaces are normally expected to be around a single molecule thick, hence the existence of a relatively thick layer of lubricant is unusual if boundary lubrication is the dominant lubrication mechanism.

The simplest approach to allowing the fluid film to be maintained through regions of flattened asperities is to assume a total transition to EHL lubrication between smooth surfaces. This simple approach has the obvious shortcoming in terms of physical realism of creating an unusual relationship between asperity load and friction. A single point along the contact would be expected to experience a consistent increase in frictional shear stress with increasing asperity loading until a critical load is reached where the friction would significantly reduce. It is possible that there may be no unexpected discontinuity in the Stribeck curve for the whole seal if reduced asperity contact pressures in some regions of the contact are compensated for by increased asperity contact pressures in other regions. However, the existence of

a severe limitation in the fundamental physical principles of the model suggests some degree of residual asperity contact and friction should be allowed for at high loadings.

In order to reduce the near-disappearance of friction at high asperity loads it may be justified to assume mixed lubrication conditions to remain following the transition with a residual level of friction from asperity contact. With this approximation the regions of the rod-seal interface with high contact fractions are assumed to retain a minimum degree of contact following the load transfer to the fluid. This residual degree of contact and resulting asperity shear would be expected to form the main component of friction inside the regions with super-critical asperity loading. One method of implementing this residual asperity friction inside the EHL regions is to assume the asperity shear stress in these regions to be a fixed proportion of the maximum asperity shear stress at the EHL transition. Setting this limiting asperity shear stress to zero would produce the equivalent of the simple EHL transition. Assuming a limiting asperity shear stress equal to that at the transition to EHL would produce equivalent friction predictions to unmodified GW-average Reynolds theory with an upper limit to asperity shear. Use of a limiting asperity shear stress between these two extremes could potentially produce an intermediate friction characteristic with less experimental inaccuracy than either limiting case.

A different modification to the GW-average Reynolds model was produced as an alternative means of reducing the discrepancy between instroke and outstroke friction and the proportional change in friction between low and high sliding speeds. This alternative approach is to assume a fixed proportion of the overall load would be transferred from the fluid to the asperities over and above what would take place during the standard GW-average Reynolds load sharing principle with the EHL transition above a critical asperity contact pressure. This additional asperity loading has similarities with the modification for allowing a residual asperity shear stress over the contact area, although applied the additional asperity load across the entire contact region and the resulting additional asperity shear stress would not reach an upper limit with increasing sealed pressure. Transferring a fixed proportion of overall load to the asperities represents an alternative method of maintaining a limiting level of asperity shear across the contact while a transition to EHL takes place in regions of a super-critical asperity contact.

5.3.2 Procedure for simulating asperity collapse

The GW-average Reynolds simulations were modified to include a transition to full EHL lubrication where the asperity contact pressure exceeds a critical value. The standard GW-average Reynolds simulation was solved using the procedure described in section 5.2.1.3. For the fluid and asperity contact pressure distributions obtained the total load is then assumed to transfer from the asperities to the fluid at each node where the asperity contact pressure

exceeded the critical value. EHL conditions are assumed throughout the regions where the asperity contact pressure was removed and the film thickness inside these regions calculated from the inverse EHL theory described in section 5.1. This inverse EHL method was modified to take the known film thickness in equation (5.4) as being the film thickness at the boundary between the standard GW-average Reynolds solution and EHL conditions.

The critical value of asperity contact pressure was determined from the analysis of GW theory with the previously assumed parameters in section 4.2.3.3. In this analysis the real area of contact was shown to exceed the nominal area of contact at an asperity contact pressure of 38.6 bar. Once this asperity contact pressure was exceeded the load was assumed to switch to the fluid in order to maintain a surface separation and the fluid film. Simulations were carried out for static contact pressure distributions corresponding with the single-lip seal with sealed pressures of 20, 40, 60 and 80 bar. Instroke and outstroke sliding speeds between 0.1 and 10 mm/s were used in accordance with the procedure used for the unmodified GW-average Reynolds simulations in section 5.2.1.3.

The asperity friction throughout any regions with a transition to EHL was calculated by assuming the asperity shear stress in these regions to be a fixed proportion of the maximum asperity shear stress. Coefficients of proportionality of 0, 0.25, 0.5, 0.75 and 1 were considered. For each case the combined asperity and fluid shear stresses were integrated across the rod-seal contact length to obtain the overall friction using the procedure described in section 5.2.5.

An alternative set of simulation results were produced assuming the residual level of asperity shear stress was not limited to regions where the transition to EHL took place. These simulations begin with the solution to the modified GW-average Reynolds approach with a transition to EHL conditions above an asperity contact pressure of 38.6 bar and no residual asperity shear within the EHL regions. A fixed percentage of the total load is assumed to be transferred to the asperities and add cumulatively to the asperity contact pressure distributions from the modified GW-average Reynolds solutions.

5.3.3 Results for modified GW-average Reynolds simulation

5.3.3.1 GW-average Reynolds with residual asperity shear in cut-off region

Figures 5-12 to 5-15 show the friction results for the modified GW-average Reynolds simulations where load is assumed to be transferred from the asperities to the fluid above a cut-off asperity contact pressure and different levels of residual asperity shear are allowed in these regions. For reasonably high sealed pressures (e.g. figure 5-15) there is a qualitative agreement between the simulations and experiments. If the assumption of a fluid film being maintained is valid, this model may represent a partial approximation to mixed lubrication conditions where the unrealistically high degree of asperity contact during instroke is avoided. The mechanism of the load transfer between asperities and the fluid is uncertain,

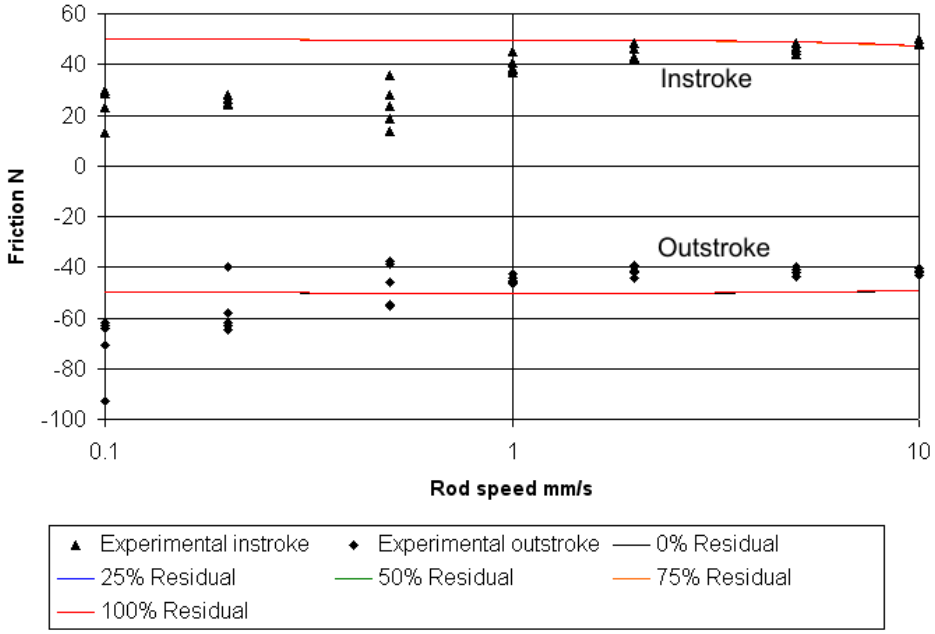

Figure 5-12: GW-average Reynolds simulation with load transfer to fluid at critical P_c, different residual asperity shear stresses during load transfer, 20 bar sealed pressure

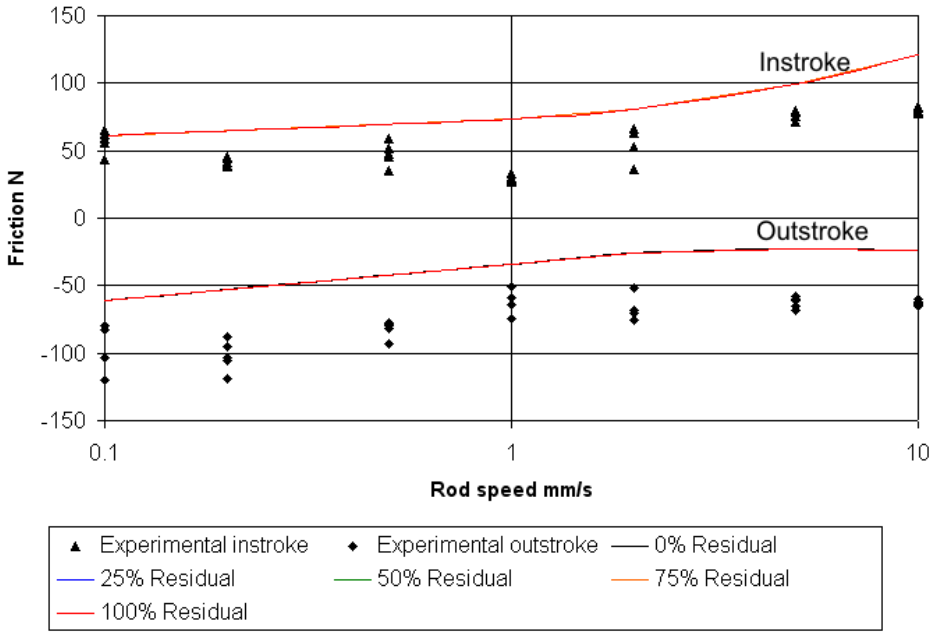

Figure 5-13: GW-average Reynolds simulation with load transfer to fluid at critical P_c, different residual asperity shear stresses during load transfer, 40 bar sealed pressure

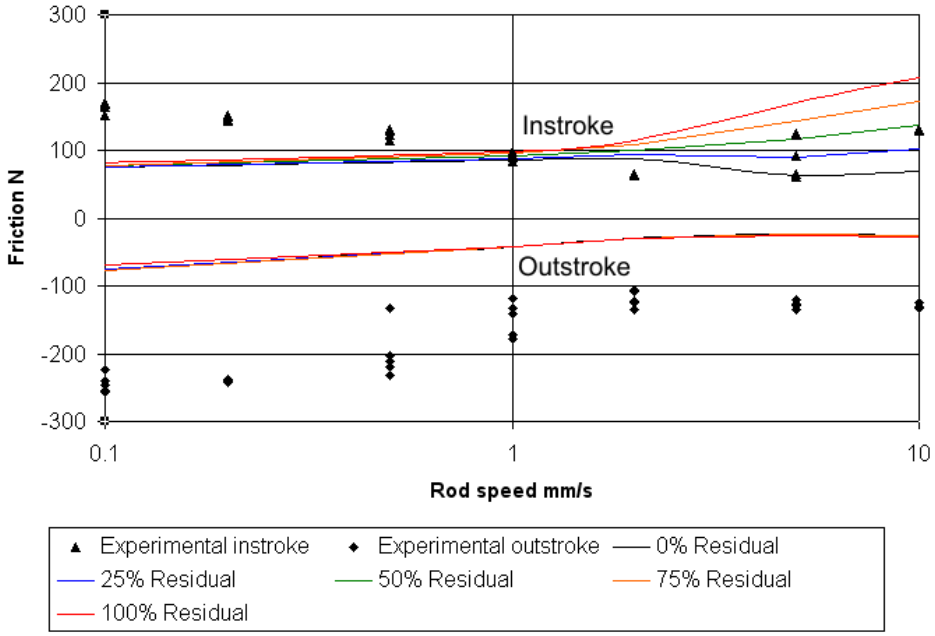

Figure 5-14: GW-average Reynolds simulation with load transfer to fluid at critical P_c, different residual asperity shear stresses during load transfer, 60 bar sealed pressure

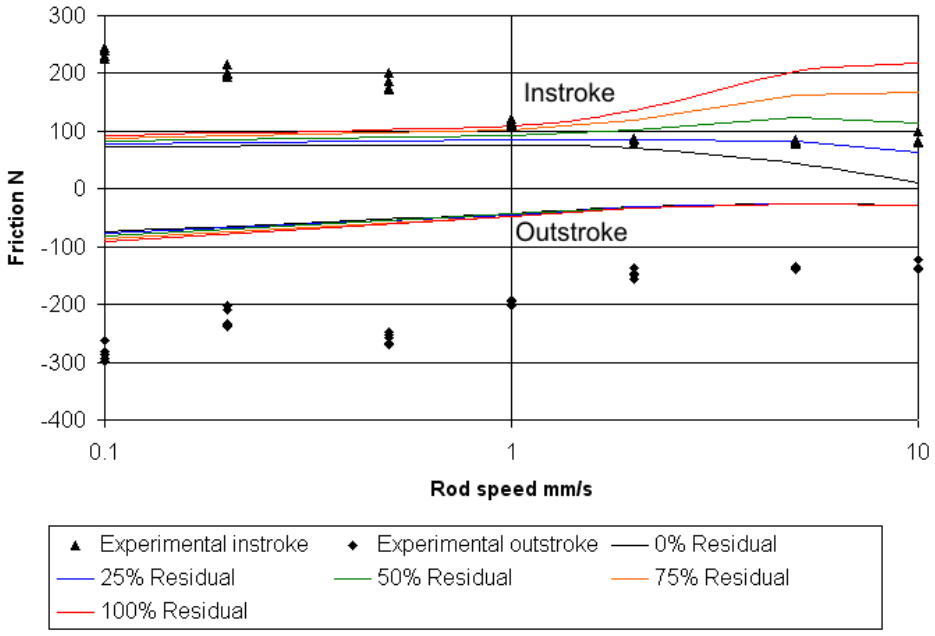

Figure 5-15: GW-average Reynolds simulation with load transfer to fluid at critical P_c, different residual asperity shear stresses during load transfer, 80 bar sealed pressure

although the simple approach of disregarding the asperity contact pressure once its levels become physically unrealistic may represent a first approximation. The physical realism of this mixed lubrication model is dependent on whether there is a fluid film present or if the lubricant present consists predominantly of the surface boundary layers.

Allowing a residual level of asperity shear stress inside the regions involving a transition to EHL allows some improvement in the experimental agreement. Figure 5-15 suggests using a residual asperity shear stress of 25% of the limiting value to reduce the shortcoming of excessively low friction levels during instroke with the transition to EHL modification. Including the residual level of asperity stress would also be expected to improve the physical realism of the model at higher sealed pressures where the limiting asperity contact pressure would be exceeded over greater proportions of the contact region. Use of a higher level of residual asperity shear is shown to reduce the severity of the excessive friction during instroke in unmodified GW-average Reynolds theory, although no reduction in friction with sliding speed could be obtained. This indicates there to be a trade-off between realistic friction levels at high sealed pressures and qualitatively accurate speed dependent friction predictions as a result of varying the residual asperity friction level.

One of the main shortcomings in the experimental agreement is the predicted instroke friction decreasing more significantly at higher sliding speeds than the outstroke friction. This takes place as a result of the simulated cavitated region extending over a significant proportion of the contact length where the asperity contact pressure reaches high values and exceeds the critical value in the modified simulations. During outstroke the fluid pressure remains close to the static contact pressure across most of the contact length and prevents the asperity contact pressure from exceeding the critical value. As a result it is not possible to affect the outstroke friction levels by varying the residual level of asperity friction following the EHL transition.

For the sealed pressure of 40 bar (figure 5-13) the friction characteristic with the EHL transition modification does not produce the reduction in friction with sliding velocity during instroke that was simulated at higher sealed pressures. Instead, the simulated Stribeck curve continues to shows the higher friction during instroke as without the modification. This takes place because the critical asperity contact pressure was not exceeded with the lower static contact pressure distribution associated with the lower sealed pressures. However, the change in measured friction behaviour at sealed pressures of 40 bar and below avoids any severe qualitative disagreement in speed-dependent characteristics between the simulation and experimental results.

The simulated relationship between sealed pressure and friction levels is shown in figure 5-16 with a limited agreement with experimental data. During outstroke the experimental friction increases significantly more rapidly with sealed pressure than the simulated friction. This lack of increase in simulated friction takes place due to the static contact pressure and

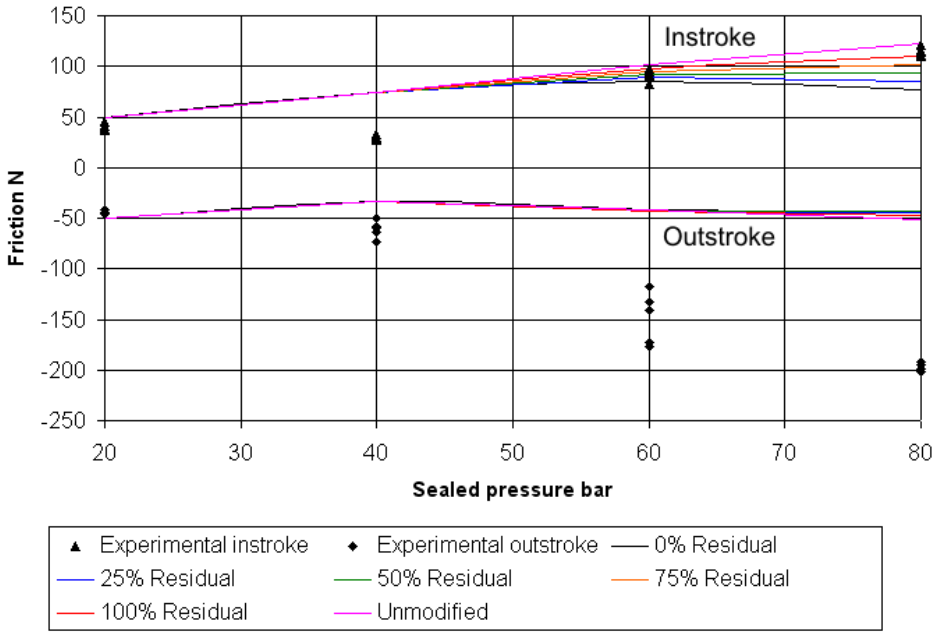

Figure 5-16: GW-average Reynolds simulation with load transfer to fluid at critical P_c, u=1 mm/s, different asperity shear stresses during load transfer

fluid pressure boundary condition increasing with the sealed pressure with corresponding increases in fluid pressure across a significant proportion of the contact length. As a result the asperity contact pressure distribution increases only minimally with increasing sealed pressure, hence only minor increases occur in overall outstroke friction. The non-appearance of this approximately invariant friction in practice raises questions over whether a fluid film behaving according to the Reynolds equation is present during outstroke.

Simulated instroke friction is more dependent on the critical asperity contact pressure and residual asperity shear than the outstroke case. The broad increase in measured friction during instroke with increasing sealed pressure was approximately replicated by the simulations, although an accurate quantitative agreement was difficult to obtain. A more accurate friction-sealed pressure relationship could be obtained by assuming relatively high residual friction levels to remain in the EHL regions. However, the residual friction levels required (50-75% of the maximum asperity shear stress) are significantly higher than those required to simulate reasonable speed dependent friction characteristics.

Adjusting the critical asperity contact pressure at which EHL transition is set to occur would affect the value of sealed pressure at which the simulated Stribeck curves change appearance. Use of a lower critical pressure results in this asperity contact pressure being exceeded during instroke at lower sealed pressures, removing the higher friction that occurs without the limiting asperity contact pressure. In general, lowering the critical pressure

would reduce the simulated friction levels by expanding the regions of contact over which the critical pressure is exceeded and asperity shear reduced. Using a critical asperity contact pressure significantly higher than the value calculated in section 4.2.3.3 would produce results equivalent to the unmodified GW-average Reynolds simulation results for the range of sealed pressures investigated. Therefore there was not much scope for improving experimental agreement by increasing the critical pressure.

5.3.3.2 Additional modification with overall load transfer to asperities

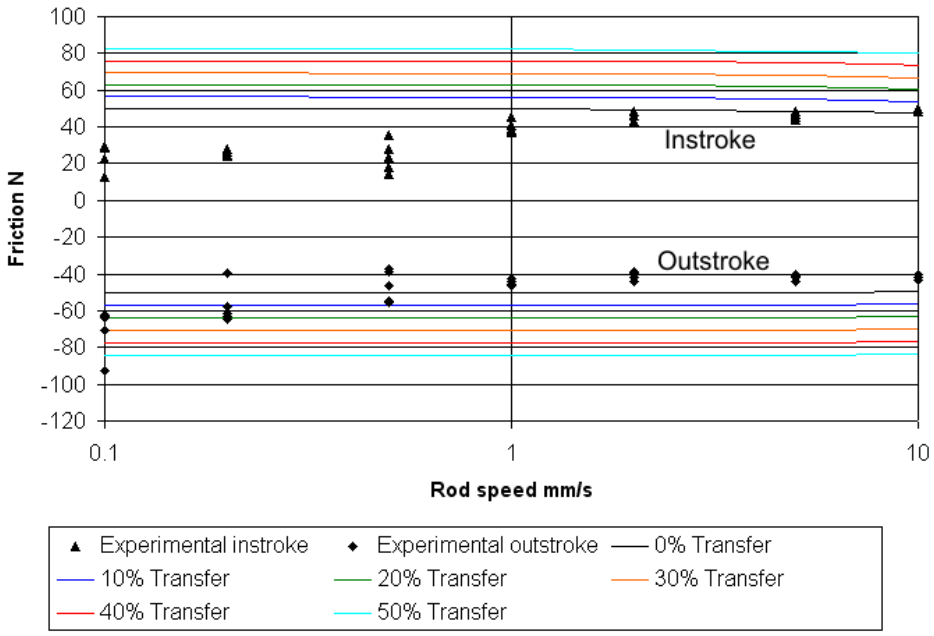

Figure 5-17: GW-average Reynolds simulation with load transfer to fluid at critical P_c, different additional percentage transfers of overall loading to asperities, 20 bar sealed pressure

Figures 5-17 to 5-20 show the simulation results when assuming a fixed proportion of overall load to be transferred to the asperities of the modified GW-average Reynolds model. An improved experimental agreement can be obtained compared with allowing a residual asperity shear stress confined to the regions with the EHL transition. Transferring an additional 30% of the total load from the fluid to the asperities across the contact length produces a reasonable quantitative experimental agreement across the 20-80 bar range of sealed pressures. For this particular percentage of load transfer the speed-dependent relationships in outstroke friction show a reasonable quantitative agreement. There is also an approximate experimental agreement at the highest sealed pressure during instroke (figure 5-20), although the agreement is not as accurate as for outstroke.

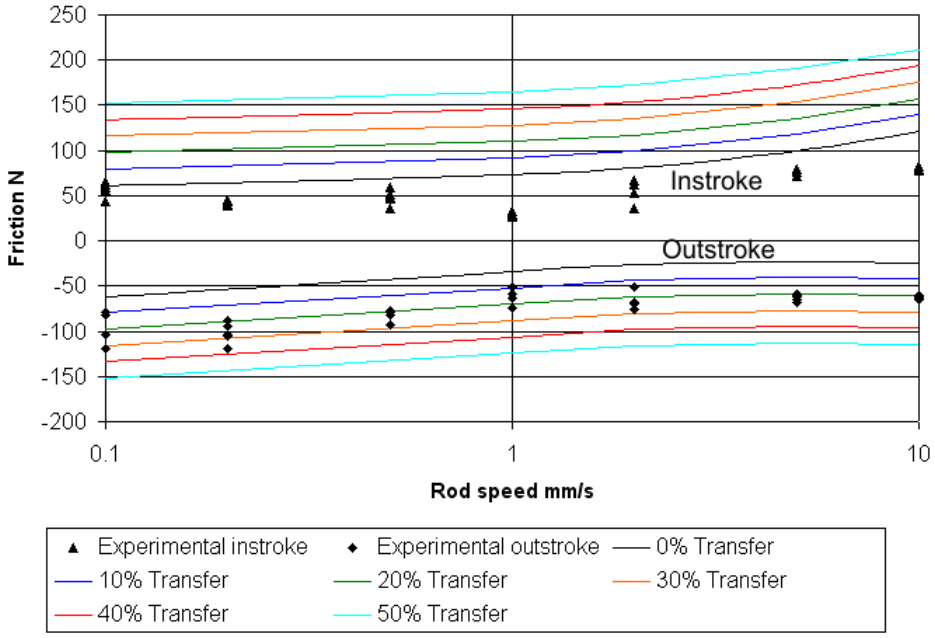

Figure 5-18: GW-average Reynolds simulation with load transfer to fluid at critical P_c, different additional percentage transfers of overall loading to asperities, 40 bar sealed pressure

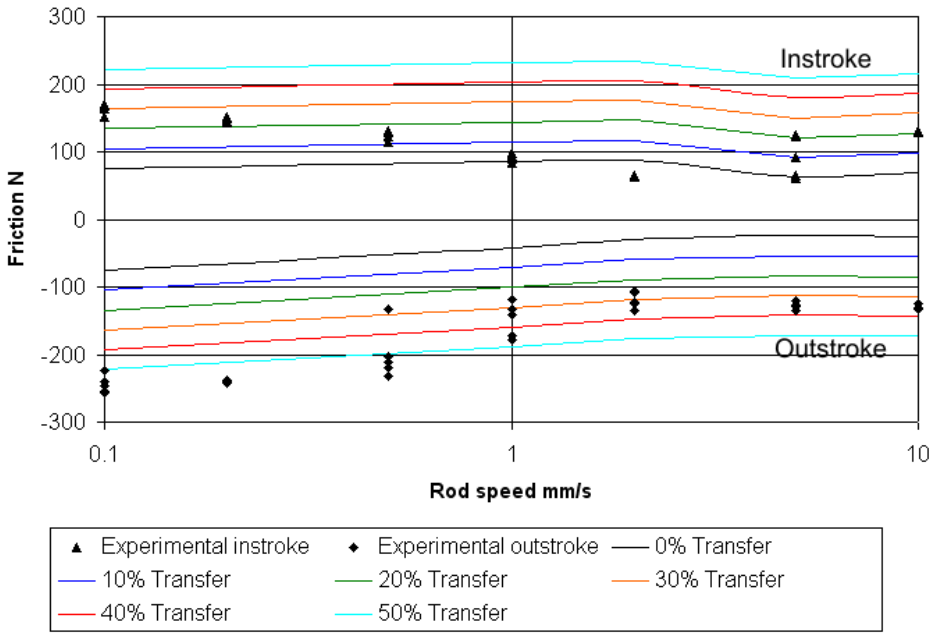

Figure 5-19: GW-average Reynolds simulation with load transfer to fluid at critical P_c, different additional percentage transfers of overall loading to asperities, 60 bar sealed pressure

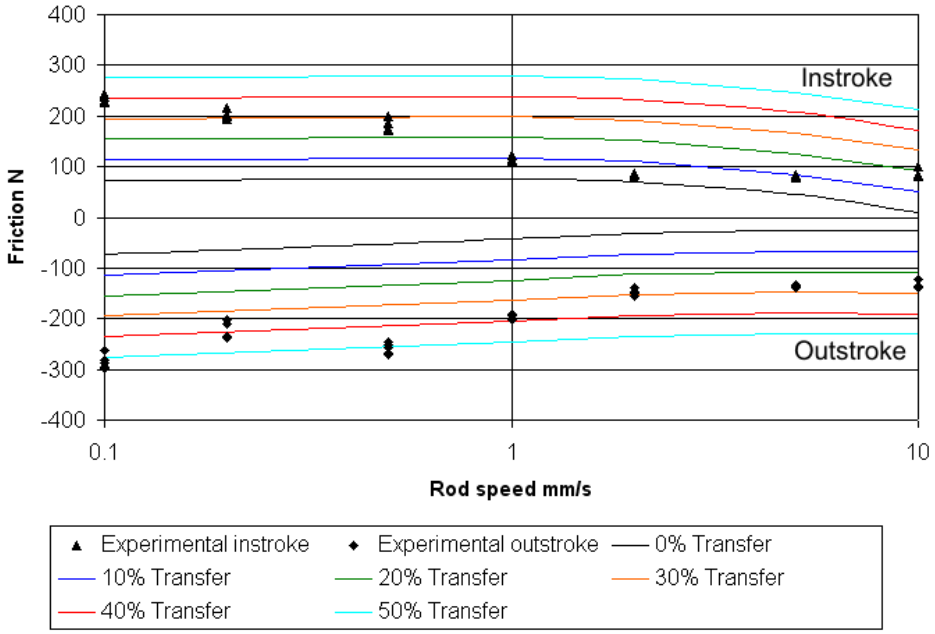

Figure 5-20: GW-average Reynolds simulation with load transfer to fluid at critical P_c, different additional percentage transfers of overall loading to asperities, 80 bar sealed pressure

At sealed pressures lower than 80 bar the experimental agreement is less accurate, although there are no large discrepancies as a result of the increase in measured instroke friction at sliding speeds greater than approximately 1 mm/s. If this increase in instroke friction is a reliable observation (discussed in section 2.4.3) this modified model may be considered to have reasonable accuracy up to the 80 bar experimental range.

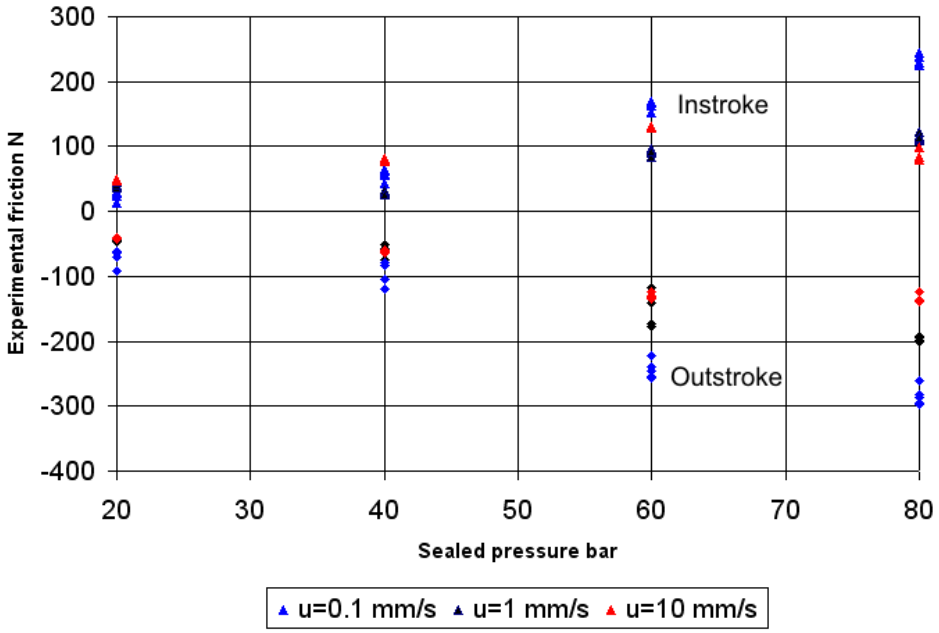

Figure 5-21: Measured friction levels for different sealed pressures and sliding speeds, single-lip seal, triangles are instroke, diamonds are outstroke

Figures 5-21 and 5-22 show the experimental friction measurements and simulation results for the modified GW-average Reynolds simulations as a function of sealed pressure. The proportion of overall load required to be transferred from the fluid to the asperities to produce an agreement between these two figures are shown in figure 5-23. The target experimental friction levels were taken as the mean of the five tests at a 1 mm/s sliding speed for each of the different sealed pressures. These results indicate additional load transfer to the asperities to be required at higher sealed pressures during outstroke while significant load transfer is needed away from the asperities during instroke at lower sealed pressures. The high additional asperity loads required during outstroke are the result of high levels of simulated fluid pressure being maintained across the contact. As discussed in section 5.3.3.1, a similar simulated asperity load was maintained across the contact during outstroke for different sealed pressures.

The necessity of reducing asperity load at lower sealed pressures for an accurate experimental agreement could also be explained by the assumptions within the modified model not corresponding with the physical system. At lower sealed pressures the critical asperity

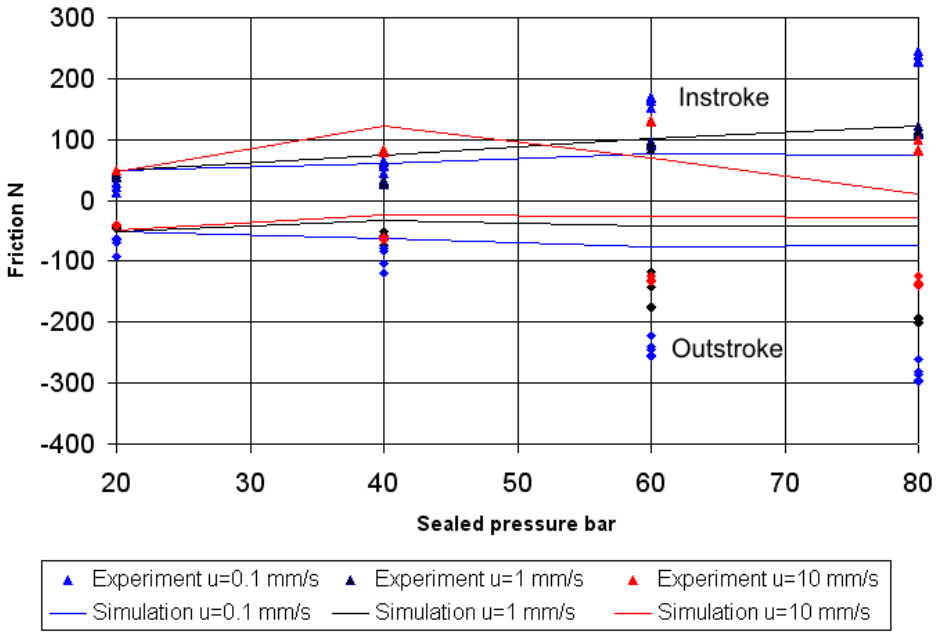

Figure 5-22: GW-average Reynolds simulation with load transfer to fluid at critical P_c, single-lip seal, different sealed pressures and sliding speeds, triangles are instroke, diamonds are outstroke

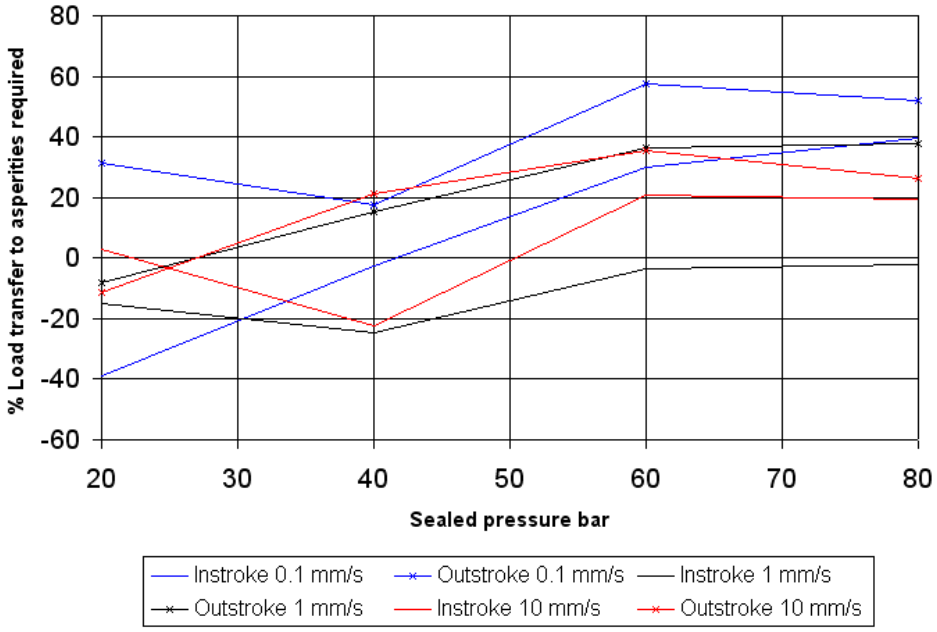

Figure 5-23: Required percentage load transfer to asperities for experimental agreement with GW-average Reynolds simulation, single-lip seal

pressure is never exceeded during instroke, resulting in relatively high predicted levels of asperity contact as a proportion of overall load. Once the critical asperity contact pressure is exceeded and significant load transferred to the fluid, it is necessary to compensate for this by transferring additional load to the asperities for an accurate experimental agreement. The reduction in asperity contact pressure above a critical sealed pressure was a fundamental feature of the modified model and its questionable appearance in practice suggests the modified approach may not be physically realistic.

One of the limitations of assuming a fixed proportion of total load to be transferred to the asperities is that experimental agreement may not be maintained for sealed pressures greater than 80 bar. Many industrial hydraulic systems can operate at sealed pressures of up to 200 or 350 bar and any seal friction model should be capable of reasonable predictions over this extended range of sealed pressures. Assuming a fixed proportion of total load to be transferred would result in an approximately proportional relationship between friction and sealed pressure. This friction-sealed pressure relationship is known not to extend to sealed pressures significantly higher than 80 bar [9]. Therefore this load transfer approximation would not be suitable for applications with higher sealed pressures.

Varying the proportion of load transferred to the asperities has a similar effect to introducing an additional friction offset into both the instroke and outstroke friction levels. This friction increase acts to reduce the relative differences between instroke and outstroke friction increases when the value of additional friction is significant relative to the base friction levels. As a result, the discrepancy between absolute friction levels in instroke and outstroke is significantly reduced. The alternative method of assuming a residual friction level in the EHL regions did not allow the friction levels to be increased as far without significantly affecting the speed-dependent relationship of friction.

5.4 Variation in asperity friction coefficient

5.4.1 Inclusion of speed-dependence in asperity friction coefficient

Throughout the current investigation the asperity friction coefficient has been assumed not to vary with sliding speed. For the lubricated contact of polymers there may be expected to be significant changes in the surface material properties through thermal effects or significant viscoelastic energy dissipation. Any absorbed boundary layer of lubricant between the surfaces may also significantly affect the speed-dependent changes in friction. It is possible that the friction coefficient for asperity contact in seal tribology exhibits significant speed-dependence. It has been considered whether and how effectively speed-dependence of the asperity friction coefficient could be incorporated into the current simulations.

Using an empirically determined friction coefficient in this manner is expected to allow a

reasonable experimental agreement to be obtained, although has the disadvantage of reducing any assurance that variation in asperity friction coefficient is the cause of friction changes in the measured data. Including empirical relationships in any simulation also reduces the predictive value of these simulations if experimental data is required in order to produce accurate predictions.

An empirical relationship for the asperity friction coefficient is taken as an exponential decrease with sliding speed towards a limiting value. This relationship is the simplest decaying exponential function that would allow limiting friction values to be approached at high and low sliding speeds. The friction coefficient function is taken as

$$\mu = a_{c1}(1 - a_{c2}e^{-\lambda|u|}) \tag{5.30}$$

where the coefficients a_{c1}, a_{c2} and λ may be estimated from the experimental data for the single-lip seal friction in section 2.3.2. A maximum friction coefficient a_{c1} is taken as 0.2 to produce a low speed friction of approximately 300 N at an 80 bar sealed pressure to produce agreement with the friction measurements in figure 2-18. A proportion of reduction in friction a_{c2} of 0.5 is assumed in accordance with the experimental data discussion in section 2.4.1. An exponential coefficient of λ =1 s/mm is assumed in order that the significant decrease in friction would take place over the empirical 1 mm/s range of sliding speeds. If EHL conditions with a fixed proportion of asperity contact are assumed, the equivalent asperity friction coefficient would be scaled as a reciprocal of the assumed proportion of asperity contact from total load.

5.4.2 Results for speed-dependence in asperity friction coefficient

Figures 5-24 to 5-27 show the results for assuming an asperity friction coefficient given by equation (5.30). A reasonably accurate agreement can be observed between the exponential relationship and the measured friction at higher sealed pressures in figures 5-26 and 5-27. At the lower sealed pressures of 20 bar and 40 bar (figures 5-24 and 5-25) the experimental agreement is less accurate during instroke as a result of the change in experimental friction characteristics of the single-lip seal. Overall, the decaying exponential function offers a reasonable empirical approximation to the speed dependence of friction.

A deterioration in experimental agreement would be expected at sealed pressures significantly higher than the experimental range in the current investigation. As the friction coefficient is assumed not to vary with load excessive levels of predicted friction would be expected at higher sealed pressures. This model would be expected to share the shortcoming at high sealed pressures that is associated with the load transfer modification in section 5.3.3.2. Use of a contact model that allows for load dependence in the friction coefficient such as that considered in section 4.2.4.2 with the speed-dependent relationships may allow an improve-

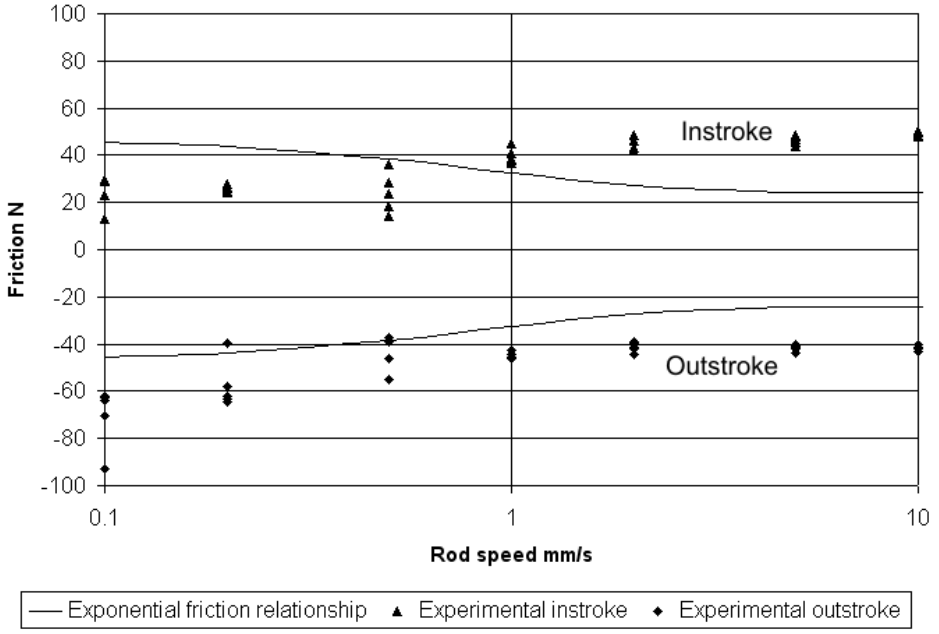

Figure 5-24: Simulations with fixed proportion of load taken by asperities and $a_{c1}(1 - a_{c2}e^{-\lambda|u|})$ asperity friction coefficient, 20 bar sealed pressure

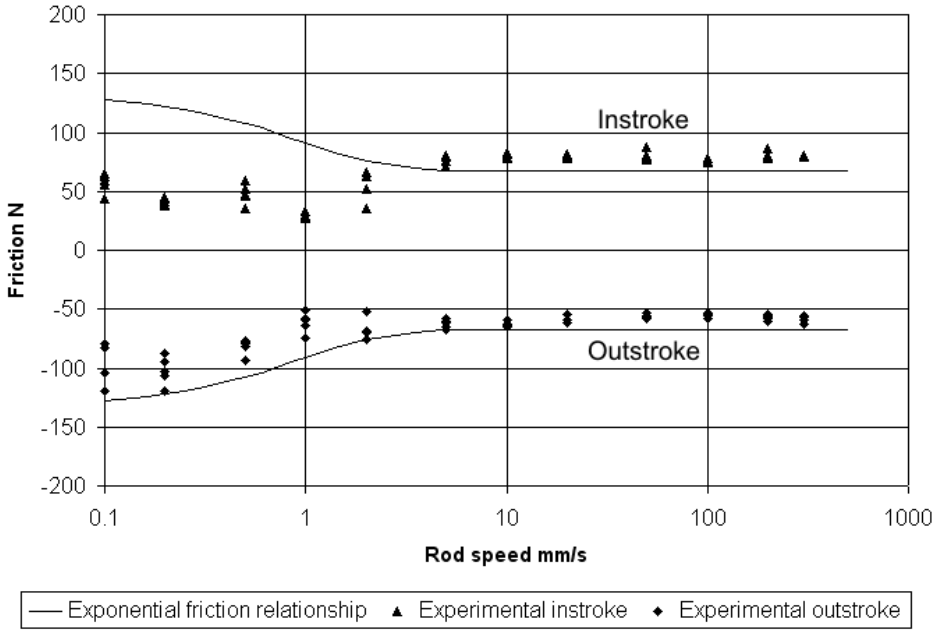

Figure 5-25: Simulations with fixed proportion of load taken by asperities and $a_{c1}(1 - a_{c2}e^{-\lambda|u|})$ asperity friction coefficient, 40 bar sealed pressure

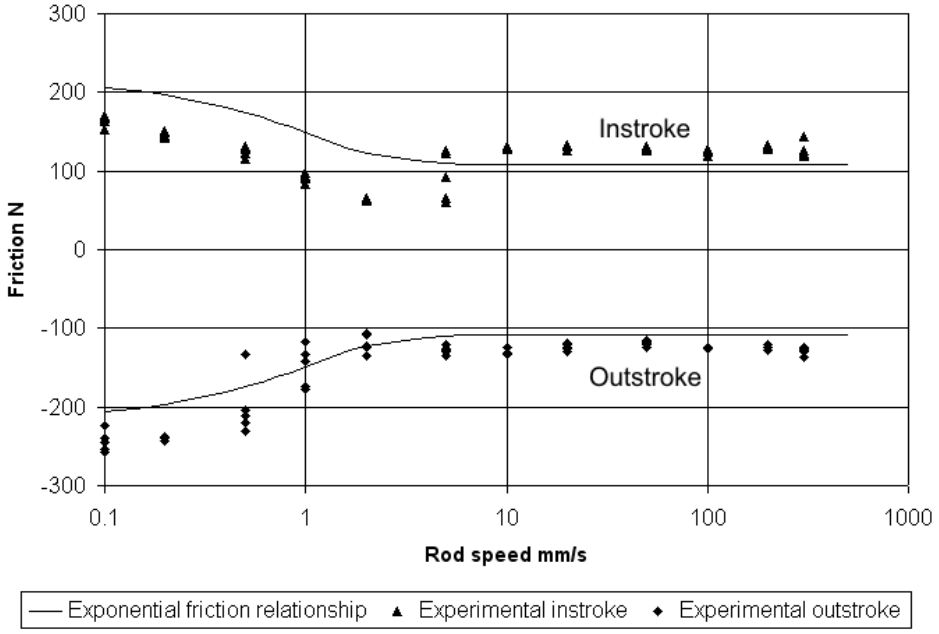

Figure 5-26: Simulations with fixed proportion of load taken by asperities and $a_{c1}(1 - a_{c2}e^{-\lambda|u|})$ asperity friction coefficient, 60 bar sealed pressure

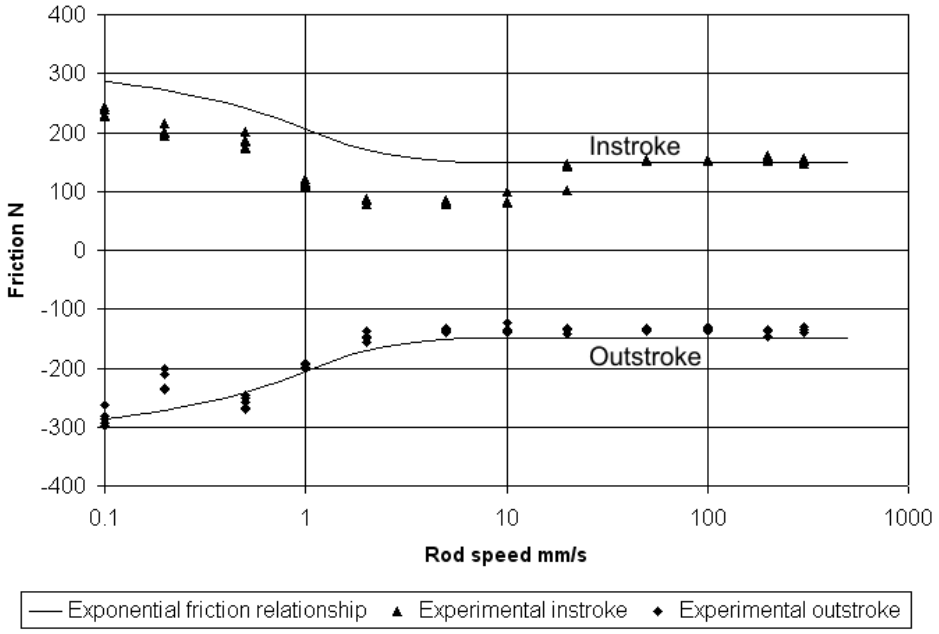

Figure 5-27: Simulations with fixed proportion of load taken by asperities and $a_{c1}(1 - a_{c2}e^{-\lambda|u|})$ asperity friction coefficient, 80 bar sealed pressure

ment in overall steady-state friction prediction.

The main problem with fitting an empirical relationship to a particular model is this does not allow the physical basis for the model to be assessed. It would be preferable to produce a theoretical basis for how friction is expected to vary with sliding speed if the measured variation in friction is to be correctly attributed to speed dependence in the asperity friction coefficients. The load dependence of measured seal friction is shown to approximately follow the known behaviour for asperity contact with dry rubber in section 4.2.4.2. However, it is uncertain whether the velocity dependence of friction could also be attributed to this cause. Methods of predicting the speed dependence of dry and boundary friction are considered in chapter 6 where a hysteresis friction model is developed in attempt to explain this friction variation.

5.5 Point-contact EHL analysis of fluid entrainment underneath asperities

It was investigated whether the principle of fluid entrainment underneath asperity peaks could be satisfactorily modelled using existing point-contact EHL analysis techniques. This allows friction coefficients to be obtained without relying on empirical measurements of the friction coefficient. In the approach considered the EHL simulation of contacting parabolic surfaces is used as an approximation to the fluid entrainment underneath a single surface asperity. The results were combined with an asperity height distribution for a Gaussian rough surface to produce effective EHL friction levels. Details of the simulations are included in appendix B.

5.6 Closure

The standard approach to seal tribology of inverse EHL theory has poor accuracy for friction prediction in hydraulic sealing applications, predicting a $u^{0.5}$ relationship between sliding speed and friction that does not occur in practice. Experimental data suggest a generally negative relationship between sliding speed and friction with much lower sensitivity to sliding speed than predicted by the model. This experimental disagreement suggests EHL conditions are not met and a fluid film is not formed between the rod and seal. Much thinner films than those predicted would be required to generate the measured friction levels through fluid viscosity. Boundary lubrication due to film collapse may have been dominant in producing the higher friction levels, suggesting any physically accurate EHL simulation would have to include mixed lubrication with asperity contact.

The GW-average Reynolds mixed lubrication method is not an accurate method of predicting friction in hydraulic seals. Higher friction is predicted during instroke compared with outstroke as a result of a significant region of fluid cavitation appearing during instroke. This

cavitated region is caused by the divergent film between the sealed and air sides of the seal. During instroke the film is convergent which may necessitate a positive second derivative of fluid pressure between the sealed and air sides. This causes low or near-zero fluid pressure to extend significantly inward from the air side in order to satisfy the fluid pressure boundary conditions. Increasing sealed pressure produces an abrupt increase in simulated friction at lower pressures than observed in experiments. Inaccuracy in the material elastic modulus or seal radial thickness may contribute to this discrepancy. Simulations of an o-ring predict similar speed-dependent characteristics to the single-lip seal.

One of the sources of the experimental inaccuracy GW-average Reynolds model is the questionable suitability of GW contact theory to regions of high asperity contact pressures. The GW-average Reynolds model was modified to force a transition to EHL conditions in regions of high asperity loadings with different residual levels of asperity shear stress. This approach produces moderate improvements in experimental agreement. It is possible to obtain further improvements in experimental agreement over the 10-80 bar experimental sealed pressure range by assuming an additional fixed proportion of the overall load to be transferred to the asperities. However, the physical basis for this latter approach is questionable and the experimental agreement would be poorer at higher sealed pressures. Assuming a simple exponential decay relationship between asperity friction coefficient and sliding speed allows an accurate experimental agreement.

A point-contact EHL study was produced to investigate whether the micro-EHL of fluid entrainment underneath asperities could be used to explain the higher friction measurements without having to rely on empirical boundary friction coefficients. These simulations produce a $u^{0.388}$ power law between friction coefficient and sliding speed. This relationship is not a significant improvement on standard inverse EHL in terms of experimental agreement. The point-contact simulations were carried out for significantly lower material parameters G than most previous point-contact investigations due to the low stiffness of the polymer seal material compared to metals. The sliding speeds in the current study are unusually high relative to the asperity dimensions. This results in a less pronounced pressure spike near the outlet and greater variation in film thickness across the high pressure regions compared with previous point-contact studies. Integrating the point-contact relationships over a distribution of asperity heights for a rough surface does not produce significant improvements with the experimental speed-dependence and load-dependence. Using these results for the asperity friction coefficient in the seal friction simulations was also unsuccessful in improving experimental agreement.

An accurate experimental agreement for steady-state friction can be achieved by using an asperity contact model with an empirical relationship between asperity friction coefficient and sliding speed. This is not particularly satisfactory from a theoretical perspective and it would be preferable to predict this asperity friction-speed relationship. The next chapter

investigates whether a speed-dependent relationship for a boundary friction coefficient can be obtained using a hysteresis approach.

Chapter 6

Hysteresis tribology simulation

A novel contact mechanics model for seal friction based on hysteresis in the seal material is investigated. This approach is considered following the limited success of the static contact models in chapter 4 where the empirical relationship between rubber friction and loading produce a reasonable agreement with the sealed pressure dependence of seal friction, although do not allow for velocity dependence. By considering speed-dependent hysteresis effects a contact mechanics approach may be developed to give reasonable experimental agreement for both the speed and pressure dependence of seal friction. The particular type of hysteresis model developed is one of several unconventional approaches to seal friction investigated as part of the current investigation into the phenomenon. Chapter 5 considers whether the Reynolds equation could be used to explain the speed-dependence of friction while the hysteresis model represents an attempt to explain this through the behaviour of the seal material.

A fundamental approach is taken to hysteresis friction where a stationary sine wave was simulated on a near rigid surface representing the rod which would be in sporadic contact with a flexible surface representing the seal material. Voigt-Kelvin damping is assumed with each node in the flexible surface having a particular stiffness and viscosity. This results in an asymmetrical pressure distribution on the leading and trailing sides of each asperity on the near-rigid surface with a resulting component of hysteresis friction. At high sliding speeds a loss of contact takes place on the trailing side of the asperities, reducing the real area of contact and adhesive friction between the two surfaces.

Previous studies have considered 2D finite element models of the flexible surface while the current approach with a stationary wave providing excitation and a simplified flexible surface deformation model has not been previously published. A relatively novel feature for rubber hysteresis modelling is to include a compliance in the near rigid surface. This compliance results in a particular friction level being reached at high speeds where the flexible material does not have time to undergo significant elastic recovery between successive asperity peaks

and the contact fraction is determined by the deflection of the peaks in the near-rigid surface. Assuming a perfectly rigid surface results in the contact fraction and friction approaching zero at higher sliding speeds which is not predicted if a surface compliance is allowed. This results in a transition in the friction level being determined by the compliance of the flexible surface at low sliding speeds and the by the compliance of the near-rigid surface at high sliding speeds.

Two different approaches are used to simulate the contact between the two surfaces for the hysteresis modelling considered. One method models the deflection of a single point on the seal surface as a series of mass-spring-dampers. A second method considers one-dimensional line contact with a linear inter-relationship between the stresses and deflections at each point across the contact length. A modification was made to the second method to investigate whether the phenomenon of asperity peak truncation during run-in may affect the real area of contact at lower contact pressures. In this analysis the upper parts of the sinusoid representing the rough surface are removed to simulate asperity truncation.

6.1 Hysteresis friction modelling

6.1.1 Background

Hysteresis friction occurs where the delayed elastic recovery of one of the contacting surfaces results in lower contact pressures on the trailing side of the asperities than on the leading side. This asymmetrical pressure acting on the curved surface gives rise to a net tangential force in the summation of all the contact forces. The real area of contact between the two surfaces is also influenced by material hysteresis, affecting the adhesive friction levels. A useful feature of hysteresis friction modelling is that as the relative speed is increased from zero the friction level is expected to rise to a plateau as the contact pressure is reduced on the trailing side of the asperity. Above a threshold speed further increases in speed are expected to reduce hysteresis friction as the flexible material becomes unable to regain full contact with the surface after passing the asperity peak and contact becomes limited to an area nearer the asperity tips of the harder surface. The regions of the surface nearer asperity peaks have relatively low surface gradients, hence the tangential component of the reaction pressure is reduced. With lower real contact areas there is also expected to be a reduction in adhesive friction once contact is lost at higher sliding speeds. Combined adhesive and hysteresis friction is expected to decrease once the sliding speed is increased beyond a critical value. This anticipated frictional behaviour is qualitatively similar to what has been observed in experiments in reciprocating seals, suggesting hysteresis friction modelling may be applicable.

A few studies have attempted to produce models for the hysteresis friction coefficient of

rubbers in contact with a rigid solid using FEA. These hysteresis studies have been focused mainly on tyre friction applications with little consideration of the additional effects of a lubricant between the surfaces. One of the earliest FEA studies was carried out by Tangena [43] where a two-dimensional model of a parabolic asperity was produced. A later study by Purushothaman [45, 46] considered FEA modelling of a two dimensional surface with triangular asperities and carried out experiments to verify the model. These experiments involved measuring the friction of rubber against a brass plate with triangular prisms milled on its surface. A reasonable agreement was produced between these hysteresis simulations and experiments. However, it is not certain how accurately the experimental macro-scale surface geometry of triangular prisms would represent the rod and seal surfaces in hydraulic applications. A more recent study by Bui [44] continued the approach considered by Tangena, producing a FEA model of the contact between two parabolic surfaces in relative sliding motion.

Most studies of hysteresis friction have used FEA to model the surface deformation while few alternative modelling approaches have been considered. Models not involving FEA which made quantitative predictions concerning friction levels include Yandell [47] and Schapery [48, 49] where a plane strain deformation analysis with small perturbations was used. These simulations considered the load and speed dependence of the hysteresis friction coefficient in addition to the surface roughness scales. One of the main shortcomings of existing hysteresis friction models is that none have been shown to produce experimentally accurate results for rubber on metal applications with general rough surfaces. If a suitable hysteresis model is to be developed for the current application it would seem logical to modify simpler approaches that do not involve FEA modelling. Once simplified deformation models are produced for hysteresis friction this may give insights into whether it would be worthwhile developing more complicated FEA models based on similar principles.

6.1.2 Viscoelastic material properties

It has been asserted by Bui [44] that over a range of speeds a plateau in hysteresis friction occurs only if the material is viscoelastic. Rubbers and polymers are generally known to exhibit significant viscoelastic behaviour during shock loading or high frequency operations with high strain-rates. It is possible the viscoelastic characteristics at high frequencies or strain rates may be applicable to the tribological processes occurring on the scale of the surface roughness while no significant viscoelastic behaviour is present in the main body of the material. At the contacting surface of a reciprocating seal the relative speed of the surfaces can be large relative to the asperity spacing, which may result in high frequency oscillations being applied to the seal surface as it runs across the rough surface. For the highest experimental sliding speed (300 mm/s) and approximate asperity spacing (50 μm)

an exciting frequency of approximately 6 kHz would be exerted on the seal material by the rod roughness profile. This suggests high frequency effects on the material properties may be important for the seal behaviour at the rod-seal interface.

6.1.3 Viscoelastic elements

The simplest viscoelastic element is the Maxwell model, which consists of a spring and damper in series (figure 6-1). This element type is designed for modelling the effects of viscoelastic creep has an obvious limitation in simulations with repeated loading where the element can never go into tension. However, it may be possible to use viscoelastic models for the surface response if normal adhesive forces (hence negative reaction forces) are incorporated into the model. For simple cases with only positive reaction forces Maxwell elements are unlikely to be appropriate for the simulating the asperity-scale behaviour of the surface.

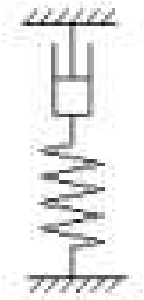

Figure 6-1: Maxwell element

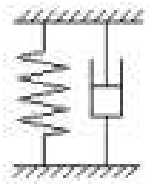

Figure 6-2: Voigt-Kelvin element

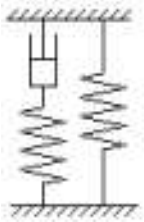

Figure 6-3: Standard linear solid element

An alternative viscoelastic element to Maxwell is the Voigt-Kelvin model (figure 6-2) where the spring and damping elements are in parallel. This type of element is more appropriate for the current simulations looking at asperity-scale contact between the rough surfaces due to its characteristic of retuning to its unloaded position once external loading is removed. When a flexible surface modelled with Voigt-Kelvin elements loses contact with its opposing surface the flexible surface would be expected to return to its original position under the action of the spring stiffness. The Voigt-Kelvin damping model is more suitable that the Maxwell model for simulating the steady-state behaviour of a system with a non-zero mean loading.

An additional damping model is the "standard linear solid" model consisting of a Maxwell system in parallel element in parallel with a spring (figure 6-3). This type of element returns towards its initial position after the load is removed similarly to a Voigt-Kelvin element. The main difference between the standard linear solid and Voigt-Kelvin models takes place at high frequencies where the standard linear solid model experiences lower damping as displacements are transferred from the damper to the spring. The standard linear solid

model may be suitable for avoiding excessive damping at higher frequencies, although requires suitable information on the high frequency behaviour of the material in order to establish suitable parameter values for the damping and stiffness in the Maxwell part.

With the Voigt-Kelvin model the additional stress in an element σ_D associated with the energy dissipation is assumed to be proportional to the strain rate as

$$\sigma_D = \eta_D \dot{\epsilon} \tag{6.1}$$

For an element the spring is assumed to have stiffness equal to the elastic modulus during gradual loading. The viscosity coefficient η_D can also be expressed in terms of the material time constant τ. This time constant is associated with the elastic recovery of a light system following the removal of a load. An instantaneous removal of a load to the Voigt-Kelvin system in figure 6-2 is equivalent to a step change in applied stress. Ignoring inertia effects and resolving the viscous and elastic forces acting on an element produces

$$\sigma = \eta_D \dot{\epsilon} + E\epsilon \tag{6.2}$$

For a step change in applied stress the time response is

$$\epsilon = \frac{\sigma_0}{E}(1 - e^{-\frac{Et}{\eta_D}}) \tag{6.3}$$

The Voigt-Kelvin damping time constant has a quite different physical significance than the Maxwell time constant. The Maxwell model is useful for simulating material hysteresis and its time constant is associated with the stress relaxation under an applied strain. Voigt-Kelvin time constants are related to the elastic recovery of a material. For most viscoelastic materials the Maxwell time constant is much greater than the Voigt-Kelvin time constant, indicating loading has to be maintained for relatively long periods to cause significant hysteresis strain. Both Voigt-Kelvin and Maxwell elements can be used to model energy dissipation during cyclic loading, although (as discussed previously) Voigt-Kelvin elements are more appropriate for simulating non-zero mean reaction forces. Maxwell time constants are commonly quoted in viscoelastic studies in literature ([90] and [44] are examples) with values for rubbers and polymers of tens or hundreds of seconds. Voigt-Kelvin time constants are less commonly used and cannot be inferred from Maxwell time constants.

6.1.4 Viscoelastic simulation methodology

A simple approach to simulating the hysteresis of the flexible seal material in contact with a rigid rough surface is to consider the deformation of a single point on the flexible surface. A one-dimensional model is used to simulate the radial stress and strains in the seal near the contacting surface (figure 6-4). This radial section is divided into multiple elements. The

input displacement profile r is the independent variable and is given by the assumed profile of the rigid surface and the relative surface speeds.

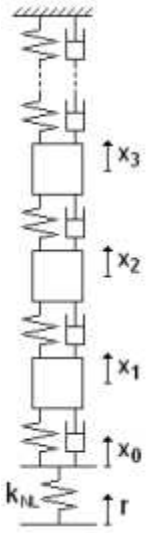

Figure 6-4: One-dimension system used in viscoelastic analysis

A non-linear spring k_{NL} is used for modelling the deflection of the near-rigid surface to model the deflection of the rod surface and allow loss of contact between the two surfaces. This non-linear spring is compressive only, having a constant stiffness of k_{NL} for net compressions and a stiffness of zero for extension. The absence of an extension stiffness models loss of contact by allowing the seal surface to freely displace away from the undeformed rod surface. The value of stiffness during compression is estimated from the relative elastic moduli of the seal and rod and the effective stiffness of the seal surface. This rod compressive stiffness was the product of the ratio of the two elastic moduli and the low strain-rate bulk stiffness of the flexible assembly:

$$k_{NL} = \frac{E_{rod}}{E_{seal}} k_{eff} \tag{6.4}$$

The equations of motion are

$$\begin{aligned} m\ddot{x}_1 + k(x_1 - x_2) + c(\dot{x}_1 - \dot{x}_2) &= F \\ m\ddot{x}_i + k(-x_{i-1} + 2x_i - x_{i+1}) + c(-\dot{x}_{i-1} + 2\dot{x}_i - \dot{x}_{i+1}) &= 0 \\ m\ddot{x}_n + k(-x_{n-1} + 2x_n) + c(-\dot{x}_{n-1} + 2\dot{x}_n) &= 0 \end{aligned} \tag{6.5}$$

The displacement of the surface of the flexible material x_0 is determined by equating the reaction force with the forces in the first spring-damper pair from

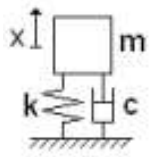

Figure 6-5: Single mass-spring damper element in viscoelastic system

$$-k(x_0 - x_1) - c(\dot{x}_0 - \dot{x}_1) + F = 0 \tag{6.6}$$

This equation can be expressed in the Laplace transform domain as

$$x_0 = x_1 + \frac{F}{k + cs} \tag{6.7}$$

The transfer function in equation (6.7) is treated separately to the system equations that include mass terms (equation (6.5)). The set of (6.5) may be expressed in terms of system matrices

$$\mathbf{M}\ddot{\mathbf{x}} + \mathbf{C_d}\dot{\mathbf{x}} + \mathbf{K}\mathbf{x} = \mathbf{B_N}F(r - x_0) \tag{6.8}$$

where

$$\mathbf{M} = \begin{pmatrix} m & & & \\ & m & & \\ & & \ddots & \\ & & & m \end{pmatrix} \tag{6.9}$$

$$\mathbf{C_d} = \begin{pmatrix} c & -c & & & \\ -c & 2c & -c & & \\ & -c & 2c & -c & \\ & & \ddots & \ddots & \ddots \\ & & & -c & 2c \end{pmatrix} \tag{6.10}$$

$$\mathbf{K} = \begin{pmatrix} k & -k & & & \\ -k & 2k & -k & & \\ & -k & 2k & -k & \\ & & \ddots & \ddots & \ddots \\ & & & -k & 2k \end{pmatrix} \tag{6.11}$$

$$\mathbf{B_N} = \begin{pmatrix} 1 \\ 0 \\ 0 \\ \vdots \end{pmatrix} \tag{6.12}$$

State variables have been set as being the displacement and velocity at each node:

$$\mathbf{z} = \begin{pmatrix} \mathbf{x} \\ \dot{\mathbf{x}} \end{pmatrix} \tag{6.13}$$

The system of equations (6.8) can then be expressed in terms of the state variables as

$$\dot{\mathbf{z}} = \mathbf{A}\mathbf{z} + \mathbf{B}\mathbf{F}(r - x_0) \tag{6.14}$$

where

$$\mathbf{A} = \begin{pmatrix} \mathbf{0} & \mathbf{I} \\ -\mathbf{M^{-1}K} & -\mathbf{M^{-1}C} \end{pmatrix} \tag{6.15}$$

$$\mathbf{B} = \begin{pmatrix} \mathbf{0} \\ \mathbf{M^{-1}B_N} \end{pmatrix} \tag{6.16}$$

The outputs are set as the displacement of the first internal node of the flexible material x_1 and the contact pressure between the two surfaces F. This produces a state-space equation for outputs

$$\mathbf{y} = \begin{pmatrix} x_1 \\ F \end{pmatrix} = \mathbf{C}\mathbf{z} + \mathbf{D}F(r - x) \tag{6.17}$$

where

$$\mathbf{C} = \begin{pmatrix} 1 & 0 & 0 & \dots \\ 0 & 0 & \dots & \end{pmatrix} \tag{6.18}$$

$$\mathbf{D} = \begin{pmatrix} 0 \\ 1 \end{pmatrix} \tag{6.19}$$

Preloading the system to account for the nominal mean contact pressure is achieved by applying a constant contact pressure F_0 against the near-rigid surface in addition to that exerted by the stiffness and viscosity of the adjacent element. The preload is assumed to act as an additional compressive stress that the cyclic stresses from the motion are required to overcome to produce a loss of contact. This effect of preload is expressed by

$$F = k_{NL}(r - x_0) - F_0 \tag{6.20}$$

The state-space system for the repeating components and transfer functions for the behaviour at the surface interface were combined in a Simulink program (figure 6-6).

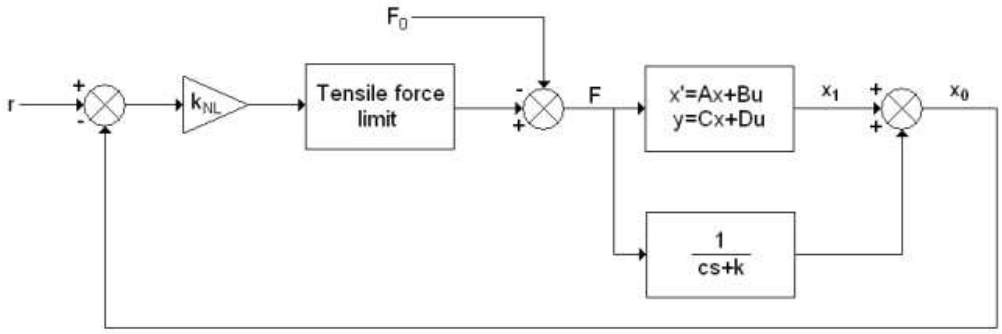

Figure 6-6: Model of 1D viscoelastic system with Voigt-Kelvin damping

6.1.5 Parameter determination

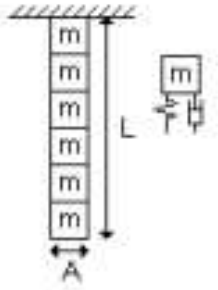

Figure 6-7: Discretisation of 1D block of material in viscoelastic simulation

The values of parameters for use in the simulation are obtained by considering the bulk properties of a block of the flexible material. Figure 6-7 shows a block of the material divided into elements, each represented by a mass-spring-damper that form the complete discretised system illustrated in figure 6-4. The lumped-parameter mass, stiffness and viscous coefficients of the complete block are given by

$$m_{net} = AL\rho \tag{6.21}$$

$$k_{net} = \frac{EA}{L} \tag{6.22}$$

$$c_{net} = \frac{EA\tau}{L} \tag{6.23}$$

giving

$$m = \frac{AL\rho}{n_m} \tag{6.24}$$

$$k = \frac{EAn_m}{L} \tag{6.25}$$

$$c = \frac{EAn_m\tau}{L} \tag{6.26}$$

where n_m is the number of elements.

All parameters for element mass, stiffness and viscosity can be scaled per unit area. Under this condition the force at the spring representing the surface interface becomes the contact pressure. Material density ρ was taken as 1 400 kg/m^3, a value typical for rubbers and polymers. An elastic modulus of 12.1 MPa was assumed in common with previous sections of the current study.

A realistic value for the Voigt-Kelvin time constant is required for the seal material. It is difficult to determine an accurate value as the damping properties of rubbers and polymers are not normally quoted in terms of the Voigt-Kelvin model and there is uncertainty concerning the appropriateness of the model. The time constant is associated with the elastic recovery following the removal of the load, which was used to estimate a reasonable value. A τ value of 0.1 s was selected in order to allow a reasonably rapid retraction from a removed static load. Significant uncertainty exists in the physical accuracy of this damping parameter and it is necessary to consider the sensitivity of the simulation results to different damping coefficients.

A suitable length L for the block was obtained from the simulation results of contact between a sinusoid and a rigid flat in section 4.2.5.4. This analysis suggests full contact to occur between the flat and sinusoidal surfaces at a contact pressure of $0.0274E$. The FEA study from which this value was obtained has similarities to a static case of the geometry used for the viscoelastic model, both being concerned with a flat flexible block contacting a rigid sinusoid. A constant value of stiffness is assumed for the flexible material to produce an equivalent change in contact pressure to the sinusoid FEA. With these assumptions it is possible to set a value for L that would create a bulk stiffness to produce the required change in contact pressure for a gradually applied peak to trough deflection. From elementary me-

chanics the strain in the block following a deflection of the peak to trough sinusoid amplitude is

$$\epsilon = \frac{2a_1}{L} \tag{6.27}$$

Equating this with the known stress in the material from the deflection and Hooke's Law gives

$$\frac{\sigma_{max}}{E} = \frac{2a_1}{L} \tag{6.28}$$

For the hysteresis simulation the value for sinusoid amplitude a_1 can be set arbitrarily providing a block length L was set to satisfy equation (6.28). For simplicity an amplitude a_1 of unity was assumed, corresponding with a block length L of 73.0. It should be noted that the $\frac{2a_1}{L}$ dimensionless number is only valid for the particular asperity profile used in the static finite element simulation. To investigate different sinusoid amplitudes and wavelengths it is necessary to obtain new values of stiffness and recalculate suitable L values for each case.

6.1.6 Postprocessing simulation results

The effective normal pressure acting between the surfaces was calculated by numerically integrating the normal pressure F over a complete cycle and calculating the mean effective contact pressure for this time period. Effective tangential shear stress (the hysteresis component of friction) is calculated using a similar method with the assumed tangential component of the reaction (figure 6-8).

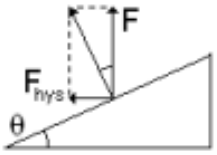

Figure 6-8: Normal and tangential components of reaction force

The local hysteresis component of friction is

$$F_{hyst} = F \tan\theta = F\frac{dr}{dx} \tag{6.29}$$

For a sinusoidal undeformed surface profile r

$$r = A_1 \sin \omega x$$
$$\frac{dr}{dx} = A_1 \omega \cos \omega x$$
$$F_{hyst} = F A_1 \omega \sqrt{1 - \frac{r^2}{A_1^2}}$$

Some inaccuracy in the hysteresis friction calculation is expected due to deformation of the near-rigid surface affecting the local surface gradients. However, this particular source of inaccuracy in hysteresis friction calculation was found not to be significant to overall friction levels as discussed later in section 6.2.1.

To calculate the adhesive friction coefficient it is necessary to obtain the contact fraction or real area of contact. This is achieved by determining the proportion of the complete cycle over which there was a positive reaction pressure F. The adhesive component of friction stress is taken as the product of the contact fraction and the shear strength of the adhesive bonds between the surfaces. A shear strength of $0.1E$ is assumed as this value produces friction results during full contact that were similar to the measurements taken from the seal test rig.

The friction coefficients obtained as a function of preload pressure are integrated over the simulated contact pressure distribution between the rod and seal to allow comparison between the hysteresis simulations and the measured seal friction. The simulated rod-seal interference pressure is obtained from finite element modelling of the seal geometry as described in section 4.1.2 with the resultant contact pressure distributions plotted in figure 4-12.

6.1.7 Analytical consideration of full contact speed range

It is possible to produce an analytical equation for the friction behaviour over the region where full contact is maintained by ignoring the mass of the system. With this approach the block of material is modelled as a lumped parameter system equivalent to a Voigt-Kelvin spring and damper. The dimensionless stiffness of the system is that of the complete block and is given as k_{net} in equation (6.22) and the viscosity from equation (6.23). These dimensionless stiffness and viscosity parameters are then divided by the sinusoid amplitude (0.167 μm) to convert back to standard dimensions. The force response to an applied displacement (including the offset for the preload) is expressed as a Laplace transform

$$\frac{F - F_0}{x} = k\left(1 + \frac{c}{k}s\right) \tag{6.30}$$

For sinusoidal excitation at a frequency ω the complex steady-state response is

$$\frac{F - F_0}{x} = k\left(1 + \frac{c}{k}\omega j\right) \tag{6.31}$$

The corresponding amplitude of the force is

$$\frac{\mid F - F_0 \mid}{\mid x \mid} = k\sqrt{1^2 + \left(\frac{c\omega}{k}\right)^2} \tag{6.32}$$

Loss of contact is expected to occur if the pressure $F - F_0$ expressed in equation (6.32) exceeded the preload pressure F_0. This was predicted to occur at an excitation frequency given by

$$\omega = \frac{k}{c}\sqrt{\left(\frac{F_0}{ck}\right)^2 - 1} \tag{6.33}$$

Using the base parameters assumed for the dynamic mass-spring-damper series simulations a critical frequency of 365 rad/s was predicted for contact to be lost. For a peak-to-peak spacing of 49.1 μm in the sinusoid surface this frequency corresponds to a relative speed of 2.85 mm/s.

6.2 Results for hysteresis simulation of a single point along contact

6.2.1 Comparison between 1D hysteresis simulation and seal experiments

6.2.1.1 Friction coefficient of hysteresis simulation

Figure 6-9 shows the friction coefficients obtained with the hysteresis model of a single point on the seal surface for several different preload pressures. At low sliding speeds (approximately 0.2 mm/s or lower) friction is almost invariant with speed. These lower sliding speeds correspond with a constant contact fraction (unity) and no significant hysteresis friction due to the lower extension and retraction speeds. The velocity range of this region with approximately constant friction increases with increasing preload contact pressure, varying from approximately 0.2 mm/s at a 20 bar preload to 2 mm/s at a 60 bar preload. There is an unexpected discrepancy where the limiting speed of the approximately constant friction decreases as the preload pressure is increased beyond 60 bar, possibly due to the influence of simulated inertia.

A viscoelastic peak can be observed in the friction coefficients for each preload pressure considered. This maximum value of friction occurs at the limiting speed where the two surfaces remain in contact. Before this point, as the sliding speed is increased up to the critical speed, the reduced contact pressure on the trailing side and increased contact pressure

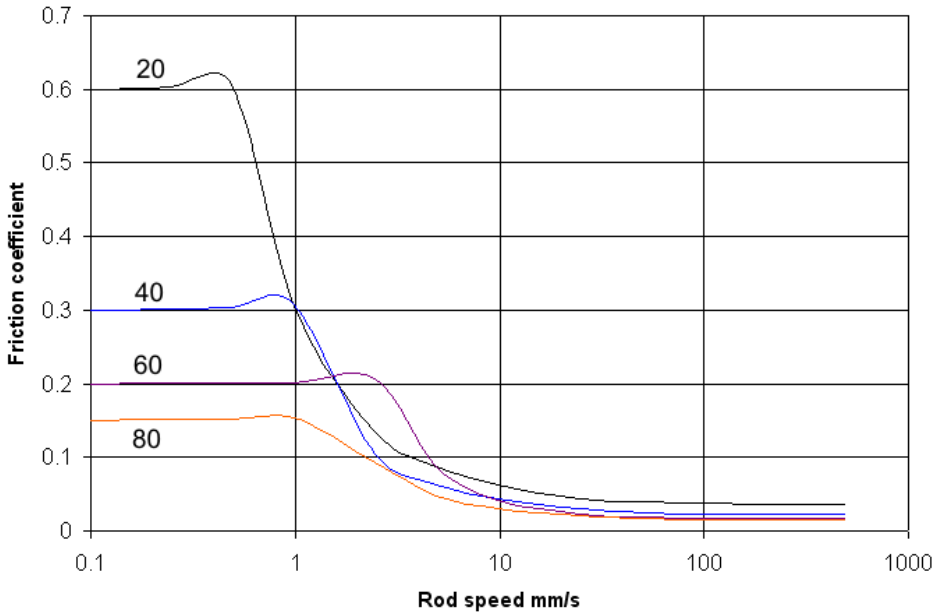

Figure 6-9: Friction coefficients for viscoelastic mass-spring-damper series simulation. Numerical labels show the sealed pressures (bar).

on the leading side result in an increasing hysteresis component of friction. The magnitude of the increase in friction coefficient due to this hysteresis effect is independent of the preload pressure.

At higher sliding speeds the simulated friction coefficients reach a limiting value. Each limiting value of friction coefficient corresponds with a particular flattening of the peaks in the near rigid surface. At high excitation frequencies and sliding speeds the flexible surface effectively becomes flat and rigid as the viscosity of the material prevents any significant elastic recovery in the flexible material between successive peaks in the near-rigid surface. As the near-rigid surface is allowed to deflect, the area of contact between the two surfaces is determined by the compliance of the near-rigid surface. This represents an unusual proposal for the mechanism of speed-dependent friction variation with the flexible surface effectively becoming rigid at high speeds and the friction and real contact area being determined by what is effectively a static contact situation between the rigid flat and near-rigid wavy surface. Use of a compliance in the near rigid surface prevents the friction from tending towards zero at higher sliding speeds which is known not to be realistic for polymeric seal materials.

The simulation results from the hysteresis model indicate the effective friction coefficient at higher speeds to decrease with increasing preload pressure. It is expected for the contact fraction at high sliding speeds to increase with preload due to the additional deflection of the near rigid surface. The decrease in friction coefficient with increasing preload pressure

indicates the proportional friction increase to have been lower than the corresponding proportional increase in loading. A simplified model for the deflection of a sinusoid surface and the relationship between contact fraction and loading was considered in section 4.2.5.2. In this model the contact fraction was predicted to become highly sensitive to loading at the lightest loads.

For all conditions simulated the hysteresis friction contribution to total friction was found to be much larger than the adhesive friction. For the hysteresis simulations the most significant effect of material viscoelasticity is the reduced contact fraction from the loss of contact between the surfaces on the trailing edges of the asperities. This reduction in contact area and adhesive friction is an indirect effect from the hysteresis in the material strain. Hysteresis friction is not capable of accounting for the high friction coefficients expected (of the order of 0.1 or greater) without including effects from adhesion. An upper limit for the maximum possible hysteresis friction can be identified by considering the case where contact occurs only at locations of the greatest slope. For a sinusoid with amplitude 0.167 μm and period 49.1 μm the maximum gradient is 0.021 4 rad. A normal pressure applied by the surface at these locations would have a ratio between tangential and normal components of approximately the tangent of this angle. This indicates the upper limit to the hysteresis coefficient of friction to be around 0.021. Typical machined surfaces do not usually have surface gradients greater than the maximum calculated from this sinusoid model [73].

6.2.1.2 Simulated hysteresis friction for seal geometry

Figures 6-10 to 6-13 show the simulated friction characteristic with the contact pressure distribution between the rod and single-lip seal for 20-80 bar sealed pressures integrated with the friction coefficients from the single-point hysteresis model (shown in figure 6-9). For sealed pressures of 60 and 80 bar the simulation results capture the qualitative trend of a transition between limiting values of maximum and minimum friction at low and high sliding speeds respectively. The most obvious difference between the simulated friction and the measured values is the excessively low values of friction at the higher sliding speeds. At higher speeds the contact fraction and friction level are determined by the deflection of the near-rigid surface and are functions of the preload pressure, near-rigid surface geometry and assumed stiffness. It is possible to increase the contact fraction and friction produced by the simulation by reducing the stiffness assumed for the near-rigid surface or reducing the peak-to-peak height of the sinusoid surface. The sensitivity of the simulation to its input parameter values and how these could be adjusted to produce a more accurate experimental agreement has been discussed further in section 6.2.2.

Figures 6-10 and 6-11 show there to be little experimental agreement for sealed pressures of 20 bar and 40 bar. In both these cases there is no measured decrease in friction with

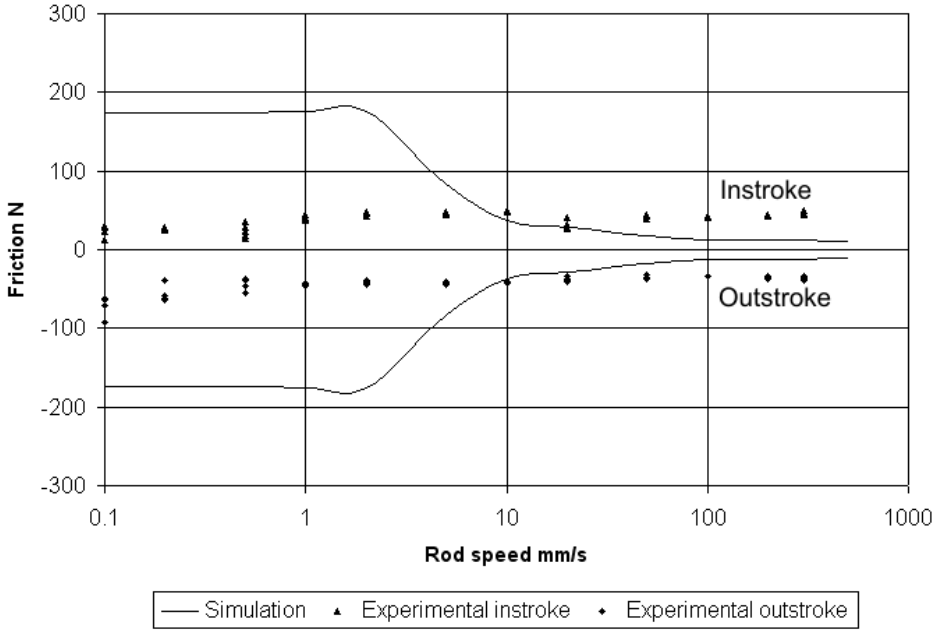

Figure 6-10: Friction of single-lip seal with friction coefficient from mass-spring-damper model, 20 bar sealed pressure

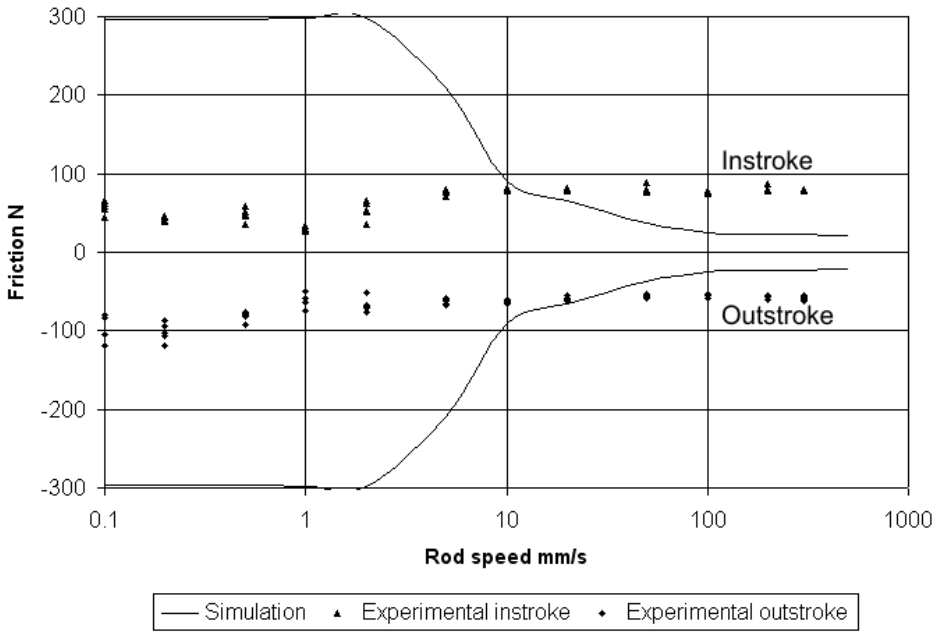

Figure 6-11: Friction of single-lip seal with friction coefficient from mass-spring-damper model, 40 bar sealed pressure

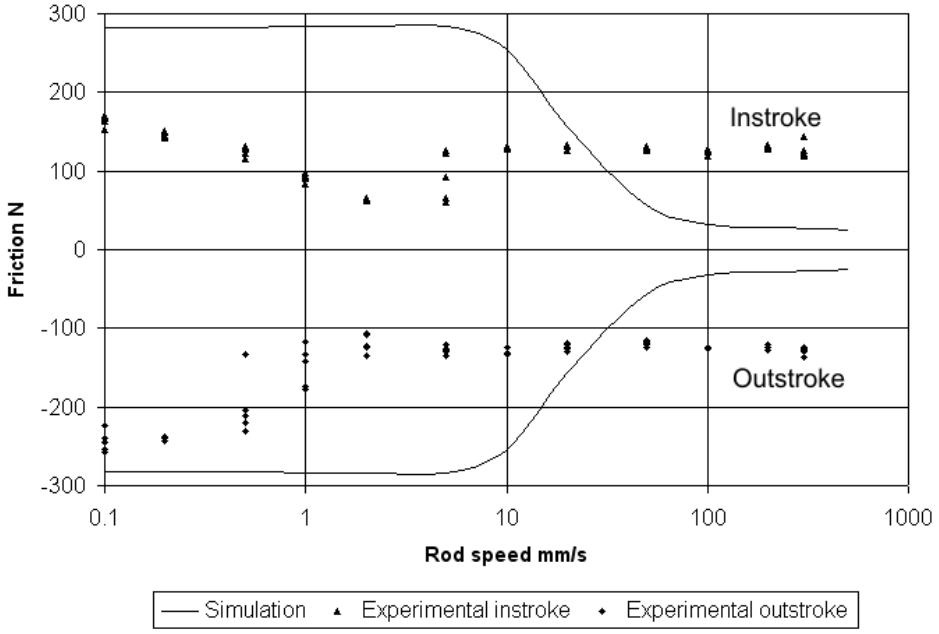

Figure 6-12: Friction of single-lip seal with friction coefficient from mass-spring-damper model, 60 bar sealed pressure

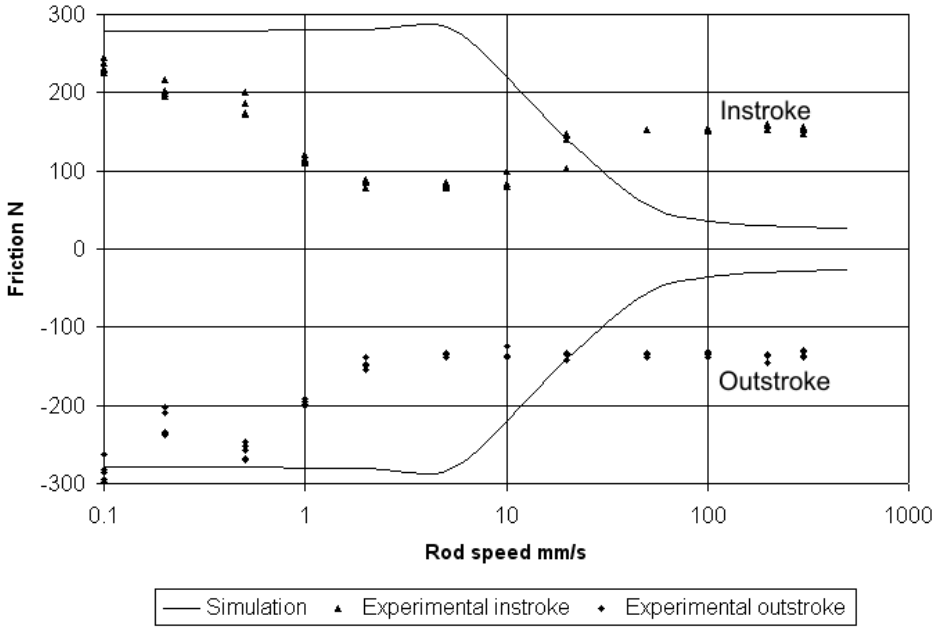

Figure 6-13: Friction of single-lip seal with friction coefficient from mass-spring-damper model, 80 bar sealed pressure

increasing sliding speed while transitions in friction with speed comparable to those at higher pressures are predicted. Excessive friction is predicted for lower sliding speeds at the lower sealed pressures. Inaccuracy in the simulated contact pressure distribution between the rod and seal may partially contribute to the excessive friction predictions at low sliding speeds. Possible causes of discrepancies in the simulated rod-seal pressure distribution are discussed in section 4.1.4.

Figure 6-9 indicates significantly higher friction coefficients to be predicted at lower preload pressures with the hysteresis model which contribute to the excessive friction levels predicted for the seal geometry. These high friction coefficients are the result of contact between the two surfaces in the hysteresis model being maintained throughout the cycle at the lower preload pressures. The simulation results for simulated contact between a sinusoid and a rigid flat in section 4.1.4 suggest full contact as occurring at a nominal pressure of $0.014E$ for the peak heights and spacing deduced from the roughness measurements, which is erroneously low.

6.2.2 Parameter sensitivity

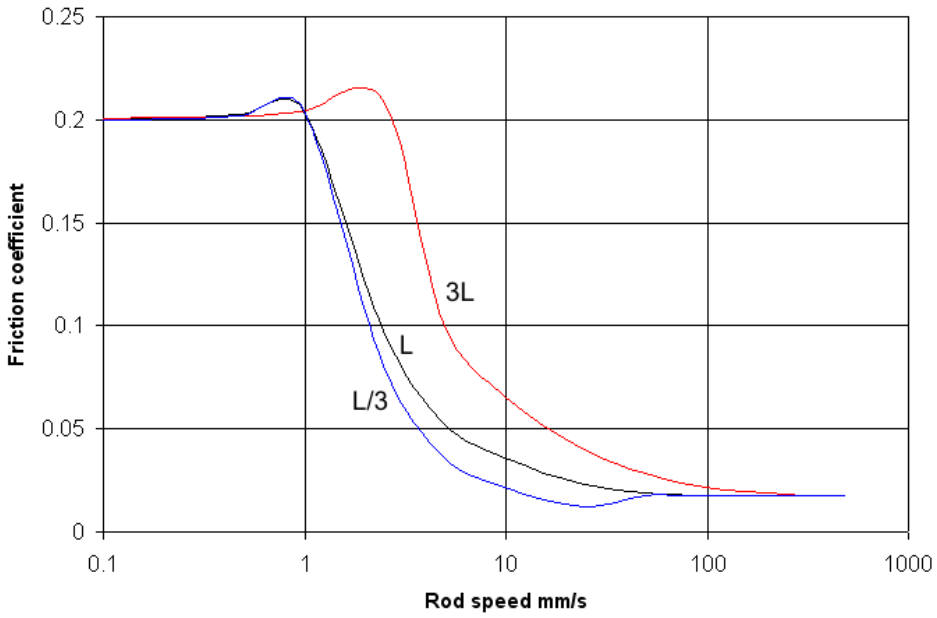

Figure 6-14: Sensitivity to variation in effective length L for viscoelastic mass-spring-damper series simulation

The sensitivity of the hysteresis simulations for a single point along the contact to variation in the parameter values was investigated. As part of this investigation it was considered how each parameter influences the effective mass, stiffness and viscosity of the system as expressed

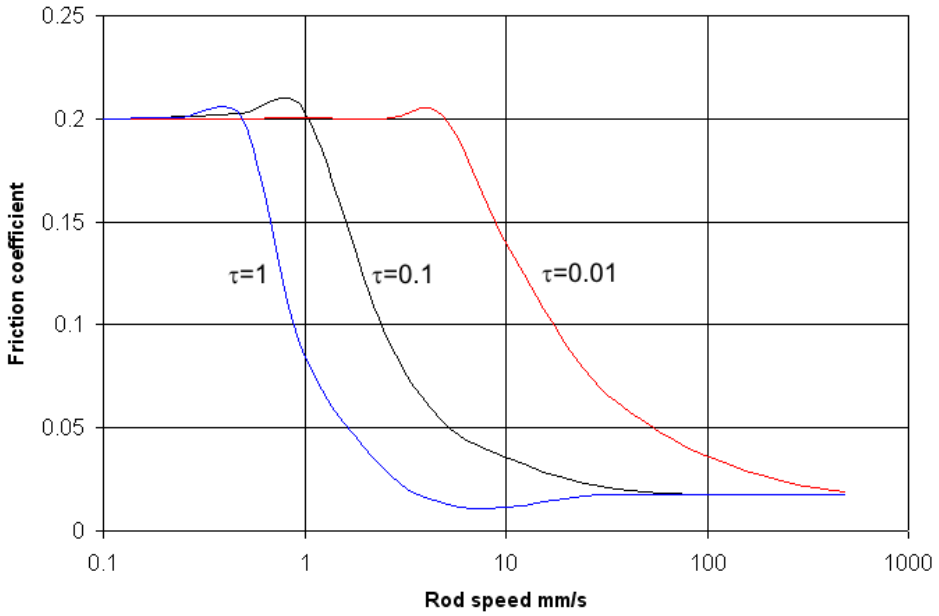

Figure 6-15: Sensitivity to damping time constant τ for viscoelastic mass-spring-damper series simulation

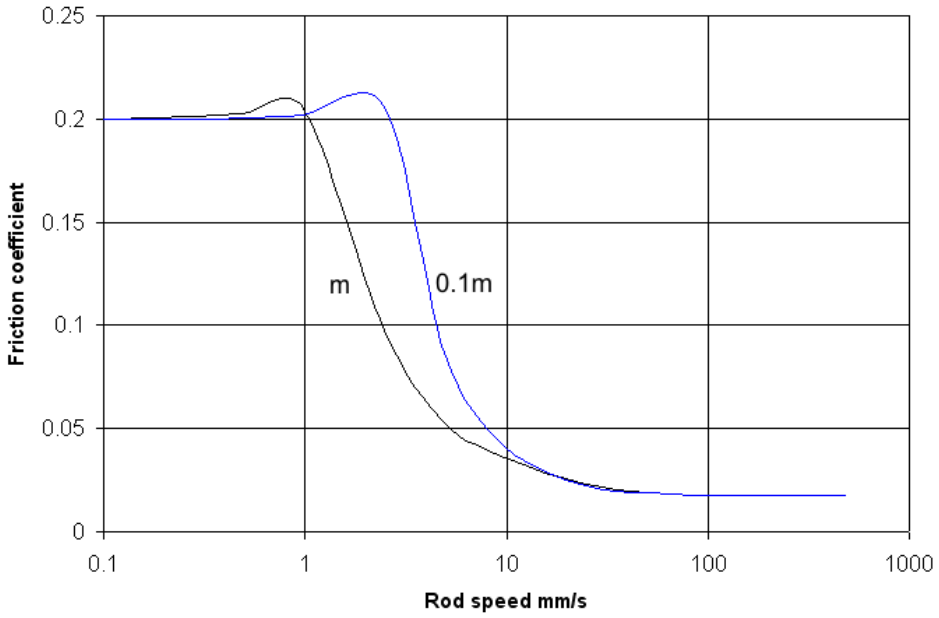

Figure 6-16: Sensitivity to 90% reduction in density for viscoelastic mass-spring-damper series simulation

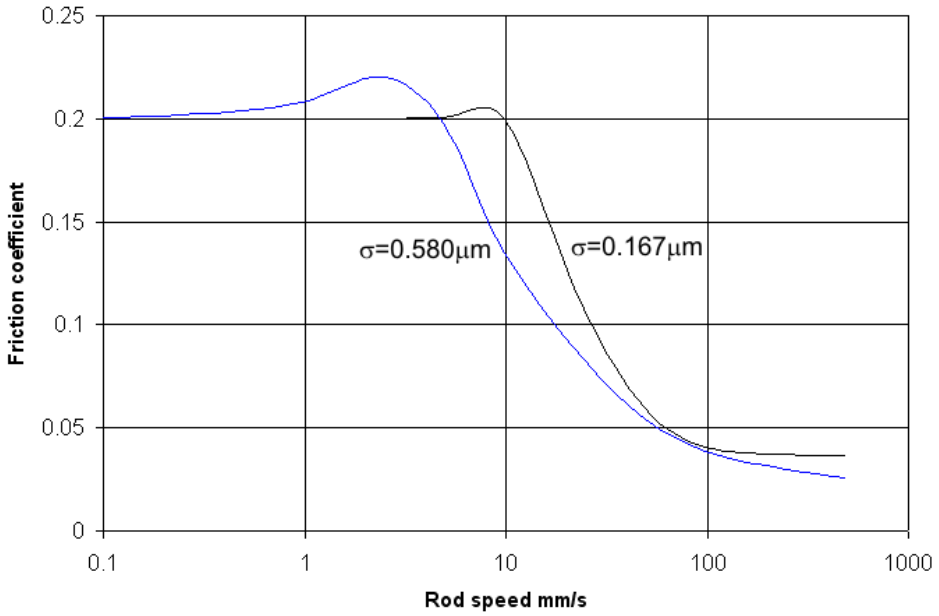

Figure 6-17: Sensitivity to roughness height σ_h increase from 0.167 μm to 0.580 μm for viscoelastic mass-spring-damper series simulation

in equations (6.24) to (6.26). Effective length L has a proportional relationship with the effective mass and a reciprocal relationship to the stiffness and damping. Therefore the ratio between mass and stiffness or damping varies with the square of L. Similarly, it can be inferred that these mass-stiffness and mass-damping ratios vary linearly with density ρ and reciprocally with elastic modulus E. If the elastic modulus is varied the results will only be scalable with other parameters if the preload is also adjusted to maintain a fixed proportion of the elastic modulus. Varying the material time constant τ results in a proportional change in effective viscosity without affecting the mass and stiffness of the block.

The behaviour of the system is expected to be predominantly influenced by the relative values of mass, stiffness and damping to each other. If the effect of varying L is known, it should be possible to infer the effect of variation in ρ and E. The effect of varying the time constant cannot be inferred from sensitivity analysis with different L values. Simulations were carried out with L increased and decreased by a factor of three. These additional simulations were equivalent to altering the density or elastic modulus by a factor of nine. τ was also varied by a factor of ten either side of the base value of 0.1s to produce corresponding changes in the effective viscosity of the system relative to stiffness and inertia. It was felt necessary to look at the effect of varying the parameters over an order of magnitude due to the uncertainty in obtaining accurate values for the effective length and damping time constant. A range of different friction characteristics could be simulated within the uncertainty of the parameters

used and it was considered whether an improved experimental agreement may be obtained within the expected parameter uncertainty.

Figure 6-14 indicates some aspects of the simulated friction coefficient to be moderately sensitive to changes in effective length L. Increasing L creates an approximately proportional increase in the speed at which the significant change in friction occurs. Reducing L from its base value was shown to produce only minor decrease in the critical speed associated with friction transition. The measured results show the friction decrease to begin at lower speeds than in the simulations and this critical speed cannot readily be significantly reduced by varying L. Varying L and the effective stiffness does not significantly affect the high-speed friction levels as under these conditions the contact fraction becomes independent of the properties of the seal material and is determined by only the deflection of the near-rigid surface.

Reducing the elastic modulus of the material produces similar increases in the transition speed as increasing L, although the results were less sensitive to E than to L. Friction at the highest speeds is independent of the flexible material properties and is a function only of the sinusoid amplitude and stiffness of the rod surface. In principle it is possible to adjust the relative stiffness of the two surfaces in order to increase the friction levels at higher speeds and improve the experimental agreement. However, it is difficult to identify a physical justification for a large modification to the effective stiffness of the near-rigid surface.

Frictional behaviour is also shown to be moderately sensitive to material time constant used (figure 6-15). Reducing the viscosity time constant produces an approximately reciprocal change in the speed where the main change in friction begins. Lower viscosities result in moderate increases in the range of speeds of the friction transition region. For lower time constants and associated higher viscosities there is additional resistance to the elastic recovery of the material on the trailing side of the asperity, resulting in a loss of contact a lower cycling frequencies. Adjusting the damping level has little effect on the peak or minimum friction values. It is not expected for the damping level to affect the limiting friction values as these are determined by the assumed shear strength and properties of the near-rigid, non-viscoelastic surface.

The sensitivity of the results to the material density is of limited interest to the present study. Most polymers and elastomers have similar densities and little variation is expected during normal usage. As the density is known to a reasonable degree of accuracy, considering different densities would not be particularly relevant for parameter sensitivity. However, varying the density may be of use for considering the influence of inertia in the model and whether it is necessary to include inertia effects.

6.2.3 Limitations of approach with single point on seal surface

One of the limitations of analysing the deformation of a single point on the surface is the absence of an account for seal material displaced perpendicular to the surface normal. A normal deflection of the surface from contact with an opposing asperity tip may result in material undergoing tangential deflection. As the seal material is nearly incompressible some degree of orthogonal strain is expected to occur in order to maintain a constant volume. Material displaced sideways from the asperities may affect the length of the contact region and contact pressure profiles. A previous study [44] has reported modelling hysteresis effects from a single hemispherical asperity using a two-dimensional FE model that could account for the displaced material. It is not possible to account for this type of material displacement without extending the simulation to include a dimension along the contact surface. Simulating a single point along the contact is a simplified case that could serve as a basis for comparison with more sophisticated models.

A related shortcoming in the simulation methodology is the interaction between strain at one location on the material surface and that of the nearby surface. Points on the surface do not deflect independently and the influence of interaction for a constant deflection is expected to become more significant as the nodal spacing is reduced. The effect of interaction between surface points may be expected to be a reduction in contact fraction and friction for a particular relative speed. Once a point on the flexible material passes an asperity peak on the rigid material the point is likely to experience resistance in retracting from the physical connection with nearby flexible material.

6.2.4 Influence of inertia in hysteresis simulations

The relevance of inertia to the hysteresis analysis can be investigated by obtaining an analytical estimation for the natural frequency. Considering a single element in the system suggests a natural frequency ($\omega_n = \sqrt{\frac{k}{m}}$) of 25.5 rad/s. This frequency is significantly lower than what is often expected in typical metal-based engineering systems due to the low elastic modulus the polymeric seal material. Excitation at the order of this frequency is expected to occur at sliding speeds of around 1 mm/s. It is significant that the calculated natural frequency is also below the frequency at which loss of contact is expected to begin in the analytical model. This suggests inertia effects may be important within a range of speeds that occur in practical applications.

Inertia effects were also investigated by reducing the density of the system by a factor of 10. Results from these simulations are shown in figure 6-16. The reduction in mass produces a moderate increase in the sliding speed and excitation frequency at which the significant friction decrease begins. Inertia is a significant factor in the speed at which the friction decrease begins and the range of speeds over which the decrease occurs. There is no

significant effect on the high and low speed friction values as a result of varying the mass. This occurs because at lower speeds the inertia forces are correspondingly lower and at higher speeds there is little motion of the flexible material surface.

6.3 Hysteresis simulation for line contact

6.3.1 Overview of line contact approach

An alternative simulation was produced to allow for the interdependency of the deflection at different points across the surface of the flexible material. A one-dimensional line contact system is assumed across the surface where each node has a single degree of freedom to displace normally to the surface. Each element is modelled as a simple Voigt-Kelvin element with stiffness and viscosity. Inertia effects are ignored for simplicity. Full inclusion of inertia for line contact would require a two-dimensional FEA model for the block of flexible material, significantly increasing model complexity and processing times.

A line contact length of a single wavelength of the sinusoid profile was considered. The deformed material profile is assumed to repeat over each sinusoid. To simulate this repeating profile the boundary conditions associated with the displacements at the two limits of the line contact region were set to be equivalent in value. The relationship between contact pressure and deformation of the flexible material is determined from a compliance matrix with coefficients derived from an analytical contact model for elastic half-space. Contact pressure from viscosity is assumed to be related to the stiffness and deflection rate as per the standard Voigt-Kelvin model. The flexible material is assumed to be deflected by a near-rigid surface profile in a similar manner to that in the simulations for a single point of contact.

6.3.2 Hysteresis line contact methodology

A one-dimensional line contact model was produced for the surfaces of the flexible and near-rigid material (figure 6-18). Each node of the flexible surface is allowed to displace normally as a Voigt-Kelvin element with stiffness and damping. The stress in a particular element is also assumed to be linearly related to the deflection of the remaining elements. Similarly, the additional stress from viscosity was modelled as being related to the stiffness by the material time constant. A stiffness matrix expresses the relationship between the flexible surface displacements $\mathbf{y}$ and element stresses $\mathbf{F}$:

$$\mathbf{F} = \tau \mathbf{K} \dot{\mathbf{y}} + \mathbf{K}\mathbf{y} \tag{6.34}$$

$$\dot{\mathbf{y}} = \frac{1}{\tau}\mathbf{y} + \frac{1}{\tau}\mathbf{C_K}\mathbf{F} \tag{6.35}$$

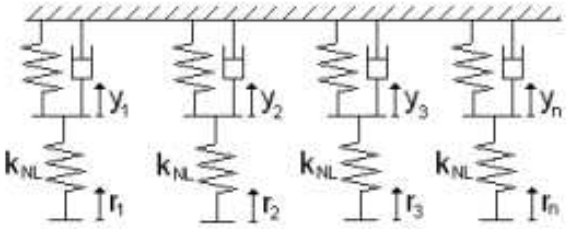

Figure 6-18: Line contact model used with compliance matrix relationship in alternative viscoelastic simulations

The stiffness and compliance matrices are obtained from line contact theory [68]. For an elastic half-space under plane strain conditions, the displacement profile y produced under a uniform pressure applied between $\pm a_p$ is

$$y = -\frac{(1-\nu^2)p}{\pi E}\left((x+a_p)\ln\left(\frac{x+a_p}{a_p}\right)^2 - (x-a_p)\ln\left(\frac{x-a_p}{a_p}\right)^2\right) + C \tag{6.36}$$

where x is the distance from the centre of pressure and a_p is half the node spacing. The constant of integration is the deflection at a reference point (taken to be $x = L_1$ in this case). For a pressure p applied at any node, the displacement at the i^{th} nodes from the source point is

$$y = -\frac{(1-\nu^2)pL_1}{2\pi En}\quad \big((2i+1)\ln((2i+1))^2 - (2i-1)\ln(2i-1)^2 - (2n+1)\ln((2n+1))^2 \\ +(2n-1)\ln(2n-1)^2\big) \tag{6.37}$$

This equation can be used to obtain the coefficients of any particular column in compliance matrix $\mathbf{C_K}$ by inserting different values of i and calculating the corresponding deflections. For each column the deflection is added to the coefficient for $(n-1)$ nodes either side of the leading diagonal where $i = 0$. Once an end of the column is reached the process is resumed from the opposite end of the column and continued until the coefficient adjacent to the leading diagonal was reached. This continuation is used to simulate the repeating boundary condition where the pressure distribution would begin repeating outside the contact length being simulated. For any particular column, the compliance matrix coefficients obtained from equation (6.37) are

$$\mathbf{C_K} = \begin{pmatrix} \vdots & \vdots & \vdots \\ \vdots & y_2 + y_{n-2} & \vdots \\ \vdots & y_1 + y_{n-1} & \vdots \\ \vdots & y_0 & \vdots \\ \vdots & y_1 + y_{n-1} & \vdots \\ \vdots & y_2 + y_{n-2} & \vdots \\ \vdots & \vdots & \vdots \end{pmatrix} \tag{6.38}$$

A state-space equation for the system can be obtained simply from the equation (6.35) with $\mathbf{z} = \mathbf{y}$. For an output of the flexible surface displacement vector y, the state space equations can be expressed as

$$\dot{\mathbf{z}} = \mathbf{A}\mathbf{z} + \mathbf{B}\mathbf{F}(\mathbf{r} - \mathbf{y}) \tag{6.39}$$

$$\mathbf{y} = \mathbf{C}\mathbf{z} + \mathbf{D}\mathbf{F}(\mathbf{r} - \mathbf{y}) \tag{6.40}$$

where

$$\mathbf{A} = -\frac{1}{\tau}\mathbf{I} \tag{6.41}$$

$$\mathbf{B} = \frac{1}{\tau}\mathbf{C_K} \tag{6.42}$$

$$\mathbf{C} = \mathbf{I} \tag{6.43}$$

$$\mathbf{D} = \mathbf{0} \tag{6.44}$$

The deflection of each node on the near-rigid surface is modelled using a non-linear spring with a linear stiffness for compression and no stiffness for extension. A stiffness value for k_{NL} is obtained by considering the bulk stiffness of the flexible surface to a uniform deflection. The bulk stiffness of the near-rigid surface to a uniform displacement is set to be the product of the flexible surface bulk stiffness (for low strain rates) and the ratio of the elastic moduli of steel and the seal material. With this approach a bulk stiffness of 255 $\times 10^9$ Pa/m was calculated for the polymeric seal material with the base parameters. This corresponds with a stiffness for the near-rigid surface k_{NL} of 4.42 $\times 10^{15}$ Pa/m for the base material stiffnesses.

Preload is modelled similarly to the single point hysteresis simulation. It is assumed that the preload pressure would act evenly and have to be overcome before a loss of contact can occur. A vector of the uniform preload pressure is subtracted from the pressure profile from the stiffness of the near-rigid surface to give the effective load pressure acting on the flexible material. The independent variable is the undeformed displacement $\mathbf{r}$ of the near

rigid surface, set to be sinusoidal with a particular frequency. Progressive delays are applied to each point on this displacement vector to simulate a standing sine wave. An amplitude of 0.167 μm is set for this displacement to produce the roughness profile of the rod.

6.3.3 Results for hysteresis line contact

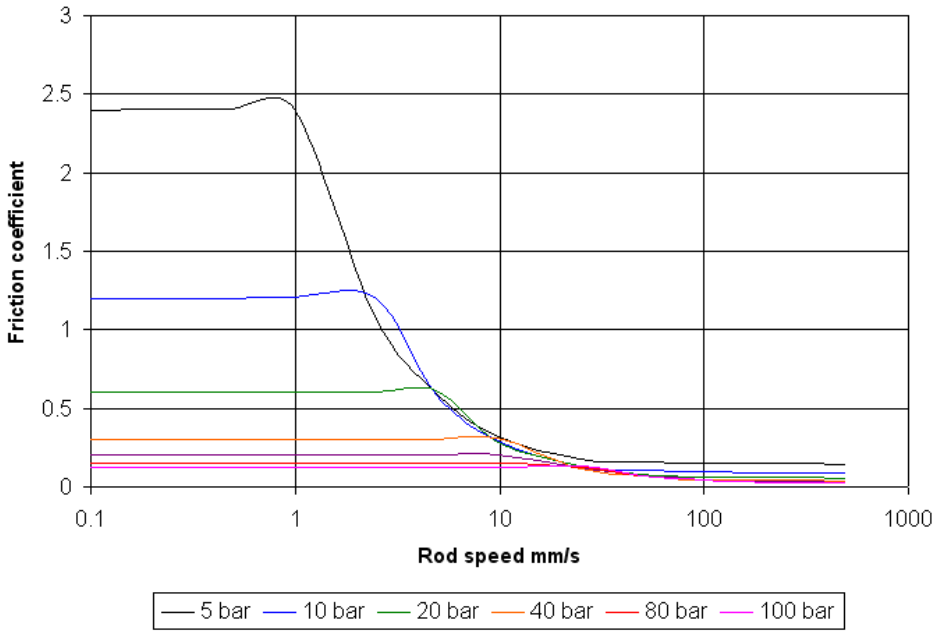

Figure 6-19: Friction coefficients for compliance matrix viscoelastic surface simulation

Figure 6-19 shows the friction coefficients obtained using the compliance and viscosity matrices for hysteresis simulation. The corresponding friction levels for particular pressure distributions between the rod and seal are shown in figures 6-20 to 6-23. Similarly to the single-point simulations, there is a qualitative experimental agreement at the higher sealed pressures where measured friction decreases with sliding speed. For higher sliding speeds the experimental agreement with the compliance matrix approach is slightly improved compared with the simulation for a single surface point. Analysis of the single-point simulation in section 6.2.2 suggests this improvement in experimental agreement may be caused by differences in the relative stiffness of the two surfaces. The flexibility analysis based on elastic half-space contact theory produces a higher bulk stiffness than that from the FE simulation of sinusoid contact. There remains an experimental discrepancy between high and low speed friction with the simulation overpredicting the difference by a factor between two and three. This disagreement can be partially reduced using an alternative roughness height for the asperity amplitude.

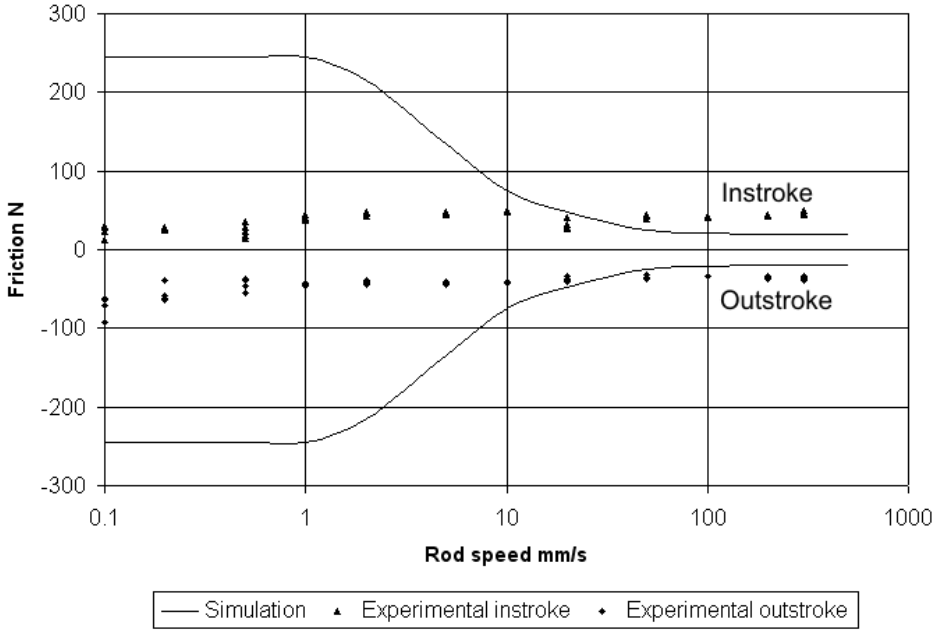

Figure 6-20: Friction of single-lip seal with friction coefficient from compliance matrix surface model, 20 bar sealed pressure

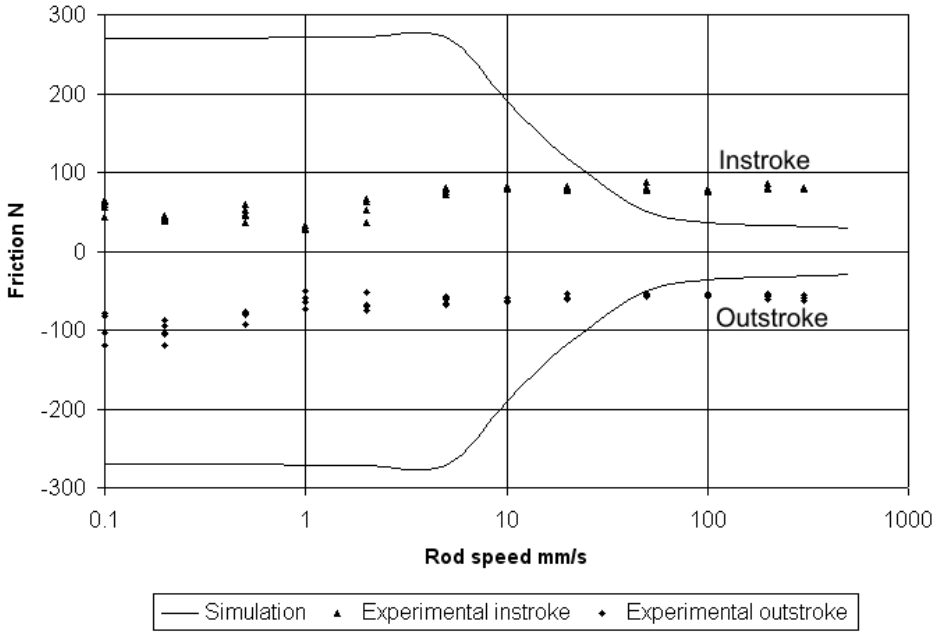

Figure 6-21: Friction of single-lip seal with friction coefficient from compliance matrix surface model, 60 bar sealed pressure

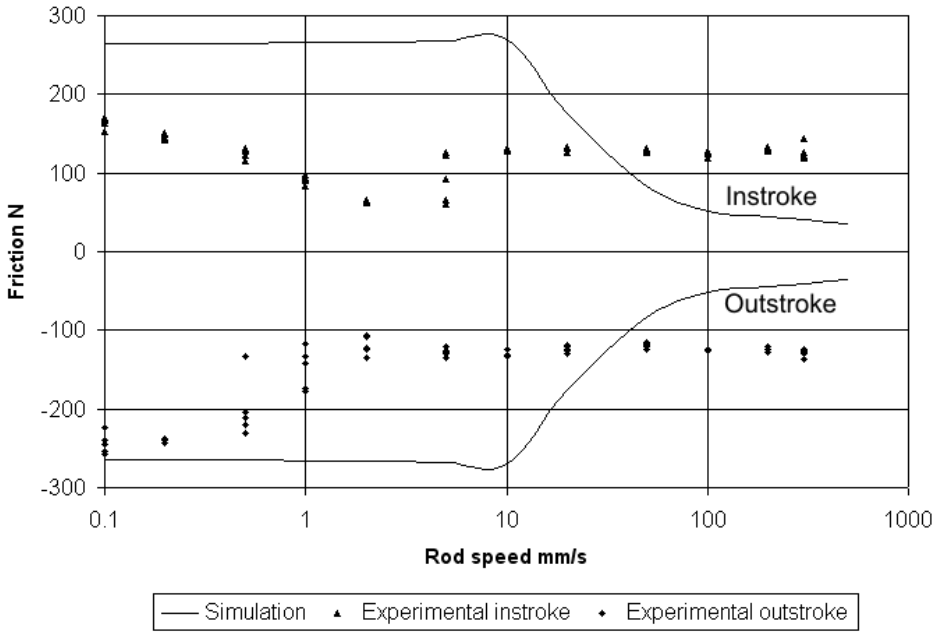

Figure 6-22: Friction of single-lip seal with friction coefficient from compliance matrix surface model, 60 bar sealed pressure

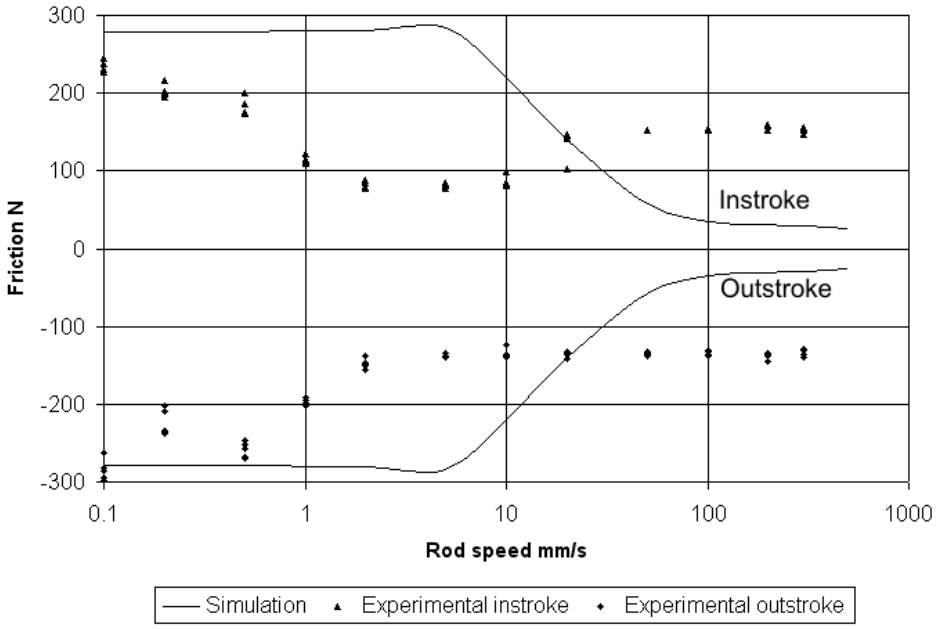

Figure 6-23: Friction of single-lip seal with friction coefficient from compliance matrix surface model, 80 bar sealed pressure

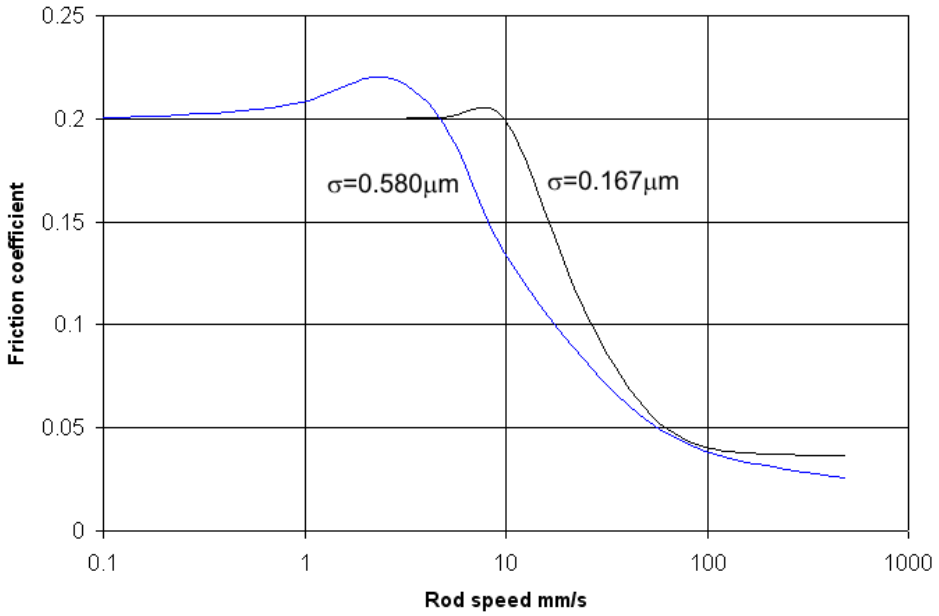

Figure 6-24: Sensitivity to roughness height σ_h increase from 0.167 μm to 0.580 μm for hysteresis simulation with compliance and damping matrices, 60 bar preload

The main transition region in seal friction is predicted to begin at approximately 10 mm/s for the higher sealed pressure (80 bar). For the corresponding experimental measurements this decrease in friction takes place at lower sliding speeds (around 0.5-1 mm/s). This difference is less pronounced in the previous simulations where a single surface point is simulated. It was observed earlier (section 6.2.4) that the inclusion of inertia terms reduces the frequency and sliding speed at which the friction transition begins. It is possible that ignoring the inertia effects may contribute to the discrepancy over the transition region position in the line contact simulations.

An alternative value of roughness height (σ_h=0.410 μm) was also used in the line contact simulation, corresponding with a sinusoid amplitude of 0.580 μm. The alternative roughness height is obtained from the combining the measured seal and rod roughness as described in section 4.2.3. Figure 6-24 shows the simulation results obtained with the greater roughness height. Transition to lower friction levels takes place at a reduced velocity with the increased amplitude of the surface profile. This is expected as the higher amplitude of oscillations would be expected to increase the magnitude of the viscous stresses for a particular excitation frequency, allowing the preload pressure to be overcome at a lower frequency and sliding speed. The increases in friction before partial loss of contact are also more significant with the higher roughness value. At higher sinusoid amplitudes the surface gradients would also be correspondingly higher, producing greater hysteresis friction from the tangential component

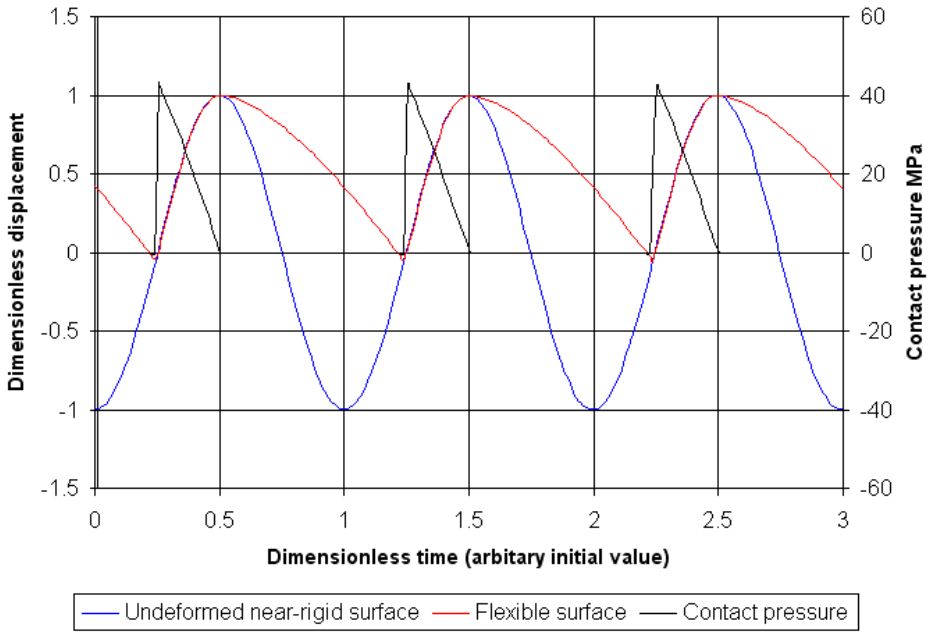

Figure 6-25: Surface displacement over a cycle in hysteresis simulation with compliance matrix, 4.91 mm/s sliding speed, 60 bar preload

of the reaction forces.

Use of the higher value of roughness height reduces the experimental accuracy of the simulation at higher speeds. As discussed previously, the high-speed friction is determined by the stiffness of the near-rigid surface. Where the flexible material does not have time to significantly elastically recover over a loading cycle the peaks of near-rigid material are compressed to form a flat region where contact takes place. If the amplitude is increased relative to the peak spacing a correspondingly greater deflection (and higher loading) is required at the peaks of the near-rigid material to produce a particular contact fraction. While the higher value of surface roughness improves experimental agreement at lower and intermediate speeds, the accuracy is reduced at higher sliding speeds.

6.3.4 Sensitivity of hysteresis line contact to relative compliance of surfaces

The effect of varying the relative compliance of the two surfaces has been investigated. At high sliding speeds there is insufficient time for the flexible material to undergo any significant elastic recovery between asperity peaks. Under these conditions the profile of the relatively flexible material tends towards being flat. The flexible material becomes analogous to a rigid flat deflecting the wavy surface of the near-rigid rod material. For this equivalent problem the real area of contact between the two surfaces is dependent only on the geometry and elastic properties of the rod material. Increasing the stiffness of the rod material reduces the

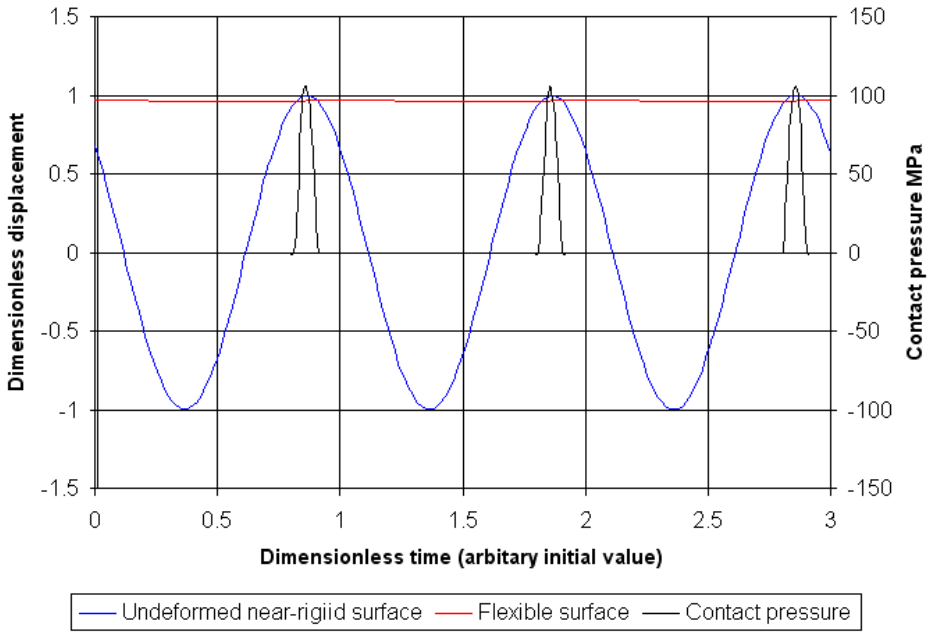

Figure 6-26: Surface displacement over a cycle in hysteresis simulation with compliance matrix, 491 mm/s, 60 bar preload

deflection of the near rigid material at high sliding speeds with corresponding reductions in contact fraction and adhesive friction. Use of a lower value of bulk stiffness for the near-rigid rod surface improves experimental agreement by reducing the difference between low speed and high speed friction. However, it is questionable whether varying this parameter sufficiently to produce a reasonable agreement could be physically justified.

The single most obvious limitation of varying the stiffness of the rod material is the elastic properties of steels are well defined empirically and not subject to significant variation between specimens and temperature over the expected range of operating temperatures. However, it may be justified to reduce the effective compliance of the near-rigid surface if it can be shown that the simplified compliance model used produces an excessively high compliance for the surface deflection it models. The deformation model for the sinusoidal rod surface has been investigated using analytical and numerical methods in section 4.2.5. This analysis suggests it may be justified to decrease the k_{NL} parameter used for the rod profile stiffness by a factor of three to improve the agreement with the FE sinusoid model over the range of deflections with partial contact. Making such an adjustment to the rod stiffness produces a moderate improvement in the experimental agreement between low speed and high speed sliding.

Figure 6-27 shows the proportional changes in simulated friction as a result of proportional changes in E. This indicates the high speed friction levels to be moderately sensitive to variation in the stiffness of the near-rigid material. For the 60 bar preload pressure and

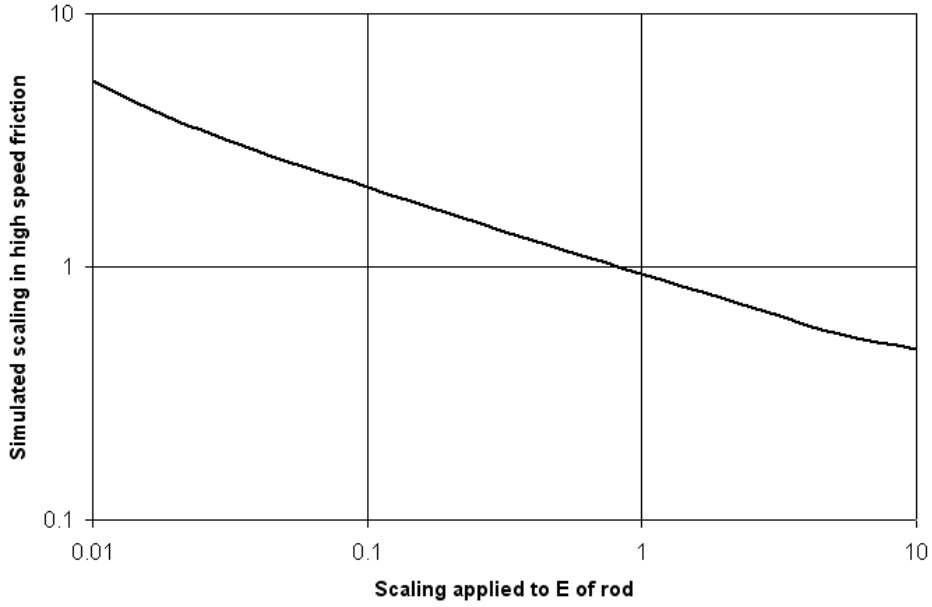

Figure 6-27: Effect of varying E of near-rigid material on high-speed friction in simulation for hysteresis line contact, 60 bar preload, 5 000 rad/s cycle rate (246 mm/s equivalent)

the base rod asperity profile the friction varies with the rod stiffness as approximately $f \propto 10^{-\frac{1}{3}k_{NL}}$ for an order of magnitude either side of the base values. This relationship suggests a reduction in rod stiffness of approximately a factor of 20 to produce an increase in high speed friction by a factor of approximately 2.5. An increase in the high speed to low speed friction ratio of this magnitude produces a quantitatively accurate agreement between the line contact hysteresis simulation and the measurements from the seal test rig at high sealed pressures (figure 6-28). It is difficult to identify a physical justification within the present modelling assumptions that could be used for such a large reduction in rod stiffness. A more modest reduction in rod stiffness of a factor of three (with justification suggested previously) produces an increase of approximately 50% in high speed friction and a moderate improvement in experimental agreement.

6.3.5 Asperity truncation model

6.3.5.1 Use of sinusoid truncation to simulate wear of asperity peaks

A modification was made to the compliance and viscosity matrices approach to hysteresis modelling to allow for the removal of the highest asperity peaks from the rod surface during the run-in period. Removal of material from the rod surface during run-in is expected to be more significant at the higher peaks that form the contact regions than at the asperity

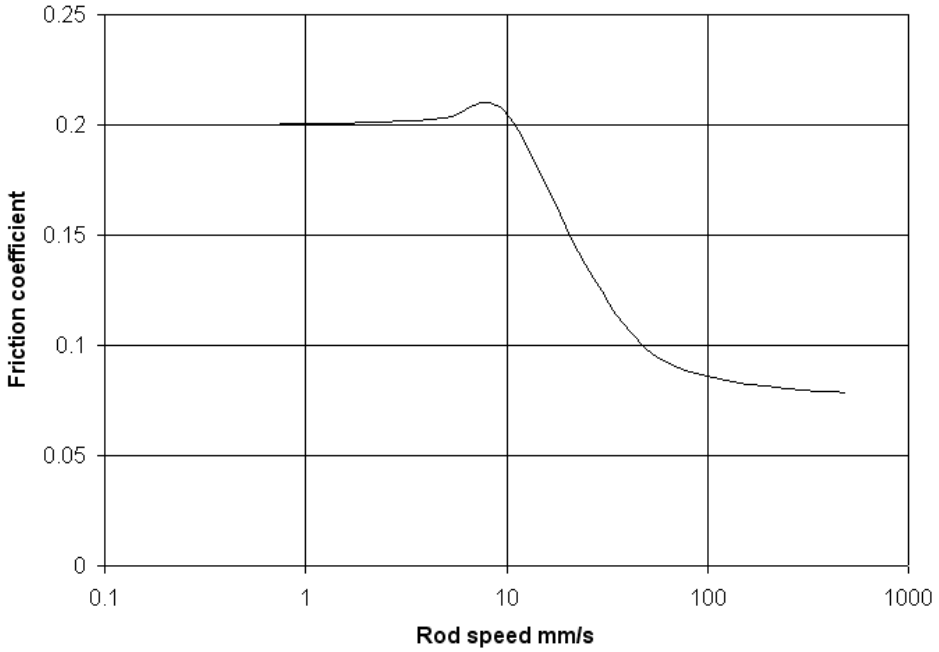

Figure 6-28: Simulation results for line contact hysteresis simulation with rod stiffness reduced by a factor of 20, 60 bar preload

troughs. Similarly, during finishing operations in the manufacture of the rod there is expected to be more material removal at asperity peaks than at troughs in the surface. One modelling approach is to truncate the sinusoid peaks, assuming the surface height to saturate at a particular value.

The depth of asperity truncation is expected to be related to the friction levels at high sliding speeds. At low loading it is expected for the flat region of the truncated sinusoid to remain in contact with the near-rigid surface, producing a minimum friction level at higher sliding speeds. At higher sliding speeds the presence of a flat length is expected to reduce the relative effects of loading on the contact fractions, hence result in less proportional variation in friction with the preload. If adhesive friction is assumed to be the dominant friction mechanism, the proportional difference between friction at high speeds and low speeds is expected to be equivalent to the proportion of the sinusoid that is truncated. As the measured high speed friction was approximately half the creep speed friction at higher sealed pressures it was decided to truncate the asperity peaks about the centreline of the sinusoid. Truncating the repeating signal at its mean point also represents a fundamental condition for investigating the general effects of peak truncation.

One of the anticipated problems with the asperity truncation approach is the expected increase in contact fraction at low loading. Having a particular flat region at the point of

first contact creates a corresponding minimum contact fraction for all loadings. This contact fraction corresponds with a minimum level of adhesive friction for these lower loads, resulting in high friction coefficients that are not observed in practice. Instead, the friction coefficient is expected to approach a limiting value as the loading is reduced as opposed to reaching a particular value of overall friction. This represents a potential limitation in the physical realism of the asperity truncation model and raises questions over whether asperity truncation may be a physical cause of the low speed to high speed friction transition

6.3.5.2 Methodology for asperity truncation model

The asperity truncation model was produced as a modification of the simulation with a sinusoid surface acting against a compliant surface with stiffness and damping matrices described in section 6.3.2. In this procedure a standing sinusoid wave was created in a near-rigid surface and the deflection and pressure distributions obtained at an opposing flexible surface. For the truncation model a maximum value of vertical displacement was set in the sine wave at which the displacement input saturates, equal to the mean of the unmodified sinusoid as a base case. Results were obtained for a range of excitation frequencies and corresponding sliding speeds as in the previous analysis.

6.3.5.3 Results for asperity truncation model

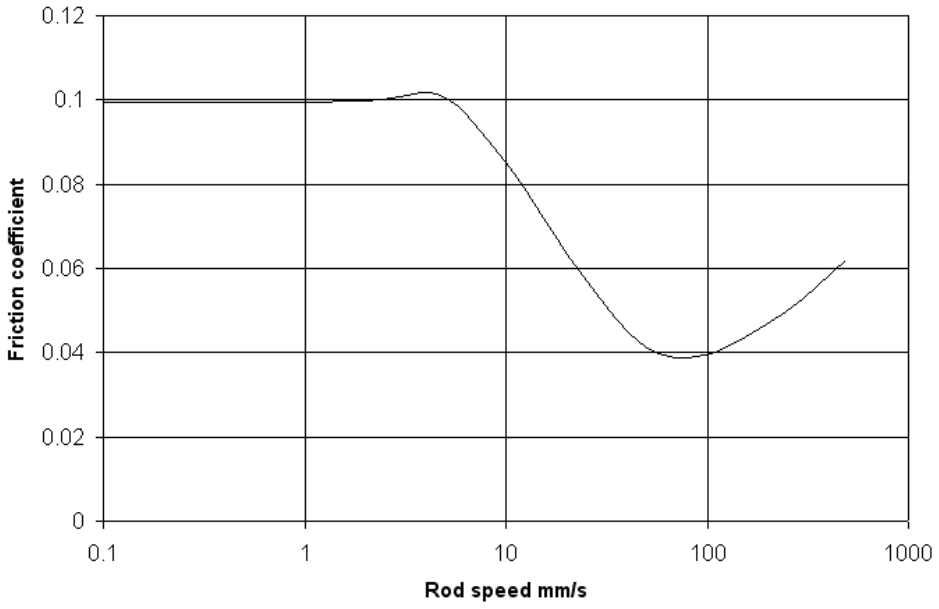

Figure 6-29: Friction coefficient for sinusoidal surface with top half truncated, compliance matrix viscoelastic simulation, 60 bar preload

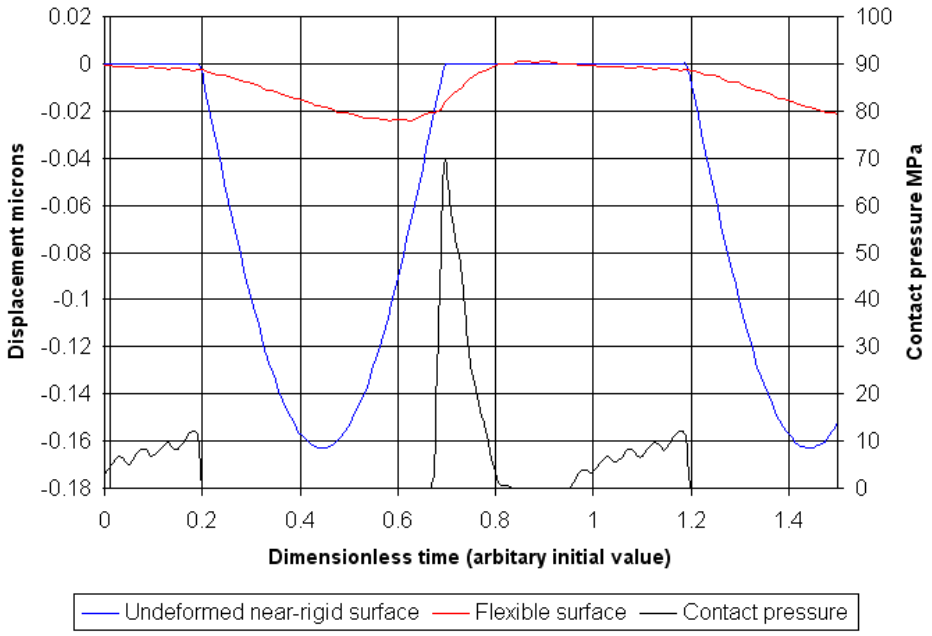

Figure 6-30: Force and displacement trace across a single cycle for truncated sinusoid surface with compliance and damping matrices, 60 bar preload

The results from the truncated asperity simulation (figure 6-29) show a significant reduction in friction between creep speeds and higher speeds. The simulated friction approaches a particular limiting value at low speeds and, following a transition region, shows significantly lower friction levels at higher speeds. At higher sliding speeds no well-defined limiting value of friction is reached within the simulated range of sliding speeds of up to 500 mm/s. The approximate friction level at these higher speeds is approximately half that at creep speeds. This is consistent with the expected halving of friction with increasing speeds with the contact fraction being unity at low speeds and equal to the truncated proportion of the surface at high speeds. For higher sealed pressures there is a reasonable experimental agreement in friction characteristics where the friction level approximately halves in value over a transition region of increasing speeds. At higher loadings the marginal increase in contact fraction with additional load is less significant relative to the initial contact fraction formed by the truncated region.

The transition region of speeds at which the simulated friction decreases begins at a slightly lower sliding speed with the truncation modification than without, with these friction transitions taking place beyond 5 mm/s and 10 mm/s, respectively. In the case of the truncated asperity there is a discontinuity in the sinusoid surface profile on the trailing edge of the peak at the limit of the truncated region. The discontinuity in the extension speed may numerically induce a slightly earlier loss of contact through the simulation integrator. Both

values of sliding speed where friction reduction commences are within an order of magnitude of the corresponding experimental critical speed of approximately 1 mm/s and can both be considered reasonable predictions of this speed value.

Introducing the truncation to the sinusoid surface significantly affects the friction characteristics at the highest sliding speeds simulated. Simulated friction increases moderately towards the 500 mm/s limit of the simulated speed range with the peaks truncated while the results without the truncation are closer to approaching a limiting value. Figure 6-30 shows the locus of a single node with the truncated sinusoid model for one of the higher speeds (200 mm/s), indicating a significant amount of elastic recovery to take place in the flexible surface following the loss of contact. At high speeds the simulation is expected to tend towards the condition where there is no elastic recovery in more flexible surface as it passes between peaks, a condition not reached at the highest speeds simulated with the truncation model. Plots for similar conditions in the simulation without peak truncation (figure 6-26) suggest limiting conditions to have been approached in the corresponding high speed cases where the peaks of the sinusoid were not truncated.

6.4 Closure

The hysteresis simulations based on a single point on the surface with a mass-spring-damper viscosity model produce qualitative agreement with the experimental results for higher sealed pressures. Friction is predicted to undergo a decrease above a critical sliding speed and reach an approximately constant value at higher speeds. This friction decease is caused by the loss of contact on the trailing side of the sinusoid where the damping prevents elastic recovery from maintaining contact during the fall in the sinusoid. Adhesive friction is reduced with the lower contact fraction caused by partial loss of contact. At high sliding speeds the contact fraction is determined by the deflection of the near-rigid sinusoid surface as the relatively flexible viscoelastic surface does not experience significant elastic recovery between successive peaks. For low sealed pressures of 40 bar or lower there was no apparent experimental agreement with these experimental results not exhibiting significant decreases in friction at higher speeds. The hysteresis approach is unsuitable for lower loading conditions.

One of the main experimental disagreements with the hysteresis model is the excessive predicted friction decrease between low and high sliding speeds. The friction transition is also predicted to occur at speeds between one and two orders of magnitude higher than observed in practice. The friction at high speeds is determined by the loading in addition to the stiffness and sinusoid amplitude of the near-rigid surface. Decreasing the stiffness and amplitude of the near-rigid sinusoid surface is expected to produce higher friction levels at high speeds. Varying the inertia, stiffness and viscosity of the flexible material is shown to produce moderate variation in the sliding speeds over which the friction transition takes

place without significantly affecting the limiting friction levels at low and higher speeds. There is significant uncertainty over the accuracy of the base parameter selected and varying these values within the expected uncertainty could produce moderate improvements in the experimental agreement, although not an quantitatively accurate match.

The second set of hysteresis simulations with a line of contact between the surfaces produce minor improvements in the experimental agreement. Use of the line contact model reduces the discrepancy between low and high speed friction which may have been the result of the Hertzian contact theory producing a higher effective bulk stiffness than assumed for the contact of a single point. Experimental agreement between low and high sliding speeds could be improved by reducing the effective stiffness of the near-rigid surface. However, a reduction in this stiffness by a factor of approximately 20 is required to produce an accurate agreement with experimental data. This degree of adjustment is difficult to justify based on the known relative moduli of the rod and seal materials.

Applying an asperity truncation modification to the model produces a speed-dependent friction coefficient that is a reasonable match to the experimental data for high sealed pressures. The proportion of the sinusoid length truncated is shown to be equivalent to the relative sizes of the high speed and low speed friction levels. This is achieved by inducing an approximately constant contact fraction at high speeds. Use of the truncation model significantly reduces the dependence of high speed friction on the loading. The truncation model has a problem of producing high friction levels at low loading that were not physically realistic. The repeating sinusoid model of the rough surface predicts excessively high contact fractions at low loadings which questions whether this modelling approach is suitable for lightly loaded contacts.

Chapter 7

Summary of appropriateness of different modelling techniques

The advantages and disadvantages of the different friction modelling approaches considered is summarised in Table 7.1. It is not apparent which of the different seal friction modelling techniques is most appropriate for the phenomenon. No single simulation considered is able to produce unambiguously accurate matches with experimental data for both the speed dependence and pressure dependence of friction. Using an empirical relationship for the asperity friction coefficient allows an accurate agreement, although using empirical relationships introduces concerns over the theoretical basis. The lack of an accurate theory for comprehensive operating conditions represents a significant limitation of currently available tribology models and the alternative models developed in the present study. However, it is possible to obtain a more reasonable match between simulations and experiments if a reduced range of sliding speeds and sealed pressures is considered.

In general it was easier to obtain a reasonable experimental agreement for the friction-sealed pressure characteristic than the friction-sliding speed characteristic. It may be possible to obtain reasonable friction predictions in applications where only the pressure dependence of friction is important. It was shown in chapter 3 that (with the exception of high frequency rocking motion) significant variation in friction with sliding speed takes place only in cases where the sliding speed was maintained below a relatively low value for an extended period of time. Velocity dependence of seal friction may not be important for many types of load cycles and applications that do not involve these low speeds, hence it may be satisfactory to use models without sliding speed dependence in such cases. Fundamental contact mechanics models may therefore be able to produce practically useful friction predictions in certain applications with low cycle times.

The empirical equation between friction and load for dry rubber friction appears to be the most suitable model for cases where friction is approximately independent of sliding speed.

Model	Advantages	Disadvantages
GW	Approximate agreement at low and intermediate sealed pressures	No friction saturation level at high loadings and sealed pressures No speed-dependence
Empirical friction-load equation	Qualitative agreement for pressure dependence of friction	No underlying theoretical basis No speed-dependence
Sinusoid contact model	Idea for deterministic basis for high loading friction relationship	Underestimation of loading associated with limiting friction Physically unrealistic friction-load behaviour at high contact fractions No speed-dependence
Inverse EHL	Commonly used existing approach to tribology	Unrealistically low friction predictions Inaccurate prediction of speed-dependent behaviour
GW-average Reynolds	Mixed lubrication approach possible explanation for fluid presence and high measured friction levels	Inaccurate prediction of speed-dependent behaviour GW theory questionable applicability at high asperity loading
Modified GW-average Reynolds	Approximate qualitative experimental agreement across range of sealed pressures	Questionable physical realism of transition to EHL lubrication
Point contact EHL	Non-empirical approach to high friction generation	Poor experimental agreement
Hysteresis model	Qualitative experimental agreement at high sealed pressures	Excessive friction at low sealed pressures Excessive difference between low and high speed friction No speed dependence experimental agreement at low sealed pressures

Table 7.1: Relative advantages and disadvantages of different friction modelling techniques

This model produces a qualitative agreement in friction-sealed pressure characteristic for the seal with a rapid increase in friction once a critical sealed pressure is exceeded with a

limiting friction level at high loadings. The experiments in chapter 2 verified the low and intermediate sealed pressure predictions and it has been well documented elsewhere [9] that the seal friction level reaches a limit at higher sealed pressures than tested in the current study. Experimental agreement based on a dry contact relationship suggests asperity contact models may be suitable to explain the friction characteristics without the inclusion of a fluid film.

The friction results from GW contact theory are comparable to those from the empirical equation for dry rubber at lower sealed pressures, although GW theory is less suitable for higher sealed pressures. GW theory is suitable only for low contact fractions and predicts excessive friction and contact fraction at higher loadings. The physical accuracy of the GW model in the current investigation has been discussed in section 4.2.3.3 where the theory is shown to predict excessive contact fractions over the 10-80 bar range of sealed pressures considered. Using measured surface roughness parameters in the GW model further reduces the applicability of this model to the current study. This has implications for the physical accuracy of the mixed GW-average Reynolds model that is also considered.

It has been established that any contact mechanics model capable of accurately predicting hydraulic seal friction would have to be suitable for high contact fractions. If a suitable contact mechanics model could be produced, this would have the advantage of improving the theoretical basis for the empirical equation for dry rubber friction that has some success in predicting seal friction. A deterministic contact mechanics model was produced based on approximating the rough surface as a sinusoid. This approach was shown not to produce accurate results with full contact initiated at excessively low loadings and physically unrealistic friction-load characteristics as full contact was approached. This sinusoid contact model helps explain the excessive friction predictions at low loadings that were observed in later hysteresis friction simulations. It is necessary to consider a non-deterministic distribution of asperity heights in order to avoid excessive contact fractions at lower loadings.

Simulations using the Reynolds equation as a basis were produced to verify and extend on previous investigations of seal tribology where a fluid film is assumed to be maintained. It is uncertain whether an uninterrupted fluid film with Newtonian behaviour is present between the rod and seal and how valid the Reynolds equation is for seal tribology. It is noted in chapter 4 that the friction characteristics could be partially described without modelling a fluid film. Investigating whether any improved agreement could be obtained by including the Reynolds equation may have provided some indication of whether a fluid film was present. The high friction levels from experimental data suggest either a significant amount of asperity breakthrough in combination with EHL lubrication or a collapse of the fluid film and boundary lubrication. EHL theory alone is not suitable for reasonable friction predictions, therefore mixed lubrication approaches were considered.

The mixed GW-average Reynolds equation represents a possible method of allowing a

fluid film to remain present while accounting for the high empirical friction levels through asperity contact. This theory has currently found used in hydraulic seal tribology and it was thought important to investigate the model's suitability. GW-average Reynolds theory is shown not to produce accurate speed dependent friction results, predicting excessive friction during instroke. The theory also has limitations concerning the physical realism of GW contact theory at higher asperity contact pressures. This indicates the model not to be suitable for seal tribology in its established form.

It was considered whether it was possible to modify GW-average Reynolds theory in order to improve experimental agreement. The main source of experimental inaccuracy takes place when regions of high asperity loading and friction formed which also correspond with physically unrealistic asperity contact conditions. EHL conditions were assumed to form in these regions of high asperity contact with a limiting level of residual asperity shear stress, producing some improvement in experimental agreement. Experimental agreement could be further improved by assuming a fixed proportion of total load to be transferred from the asperities to the fluid instead of a residual shear stress in affected regions. However, this later approach has further concerns relating to whether the modification could be physically justified.

An alternative method of modelling the speed-dependence of friction is to assume the coefficient of friction for asperity contact is itself a function of sliding speed. Use of a simple exponential decay function for the asperity friction coefficient produces an accurate agreement with experimental data. The main shortcoming with this approach is that it is not possible to predict the speed-dependence relationship for the asperity friction coefficient. As a result it is not possible to ascertain a strong indication of whether speed-dependence in the asperity friction coefficient is the physical cause of the measured friction characteristics.

Developing a contact mechanics friction model to predict the effects of speed dependence on friction may help verify whether variation in asperity friction coefficient with speed is the dominant cause of the measured change in friction with speed. The apparent partial success of contact mechanics approaches for the load dependence of friction suggests pursuing a contact mechanics model which includes relative motion to be the more conservative approach towards speed dependent seal friction modelling. The current investigation has attempted to develop such a contact model based on the principle of hysteresis friction.

The hysteresis friction simulations produced are not able to replicate the load-dependence success of the empirical equation for rubber friction as a result of inaccuracy in the assumed rough surface profile. It is difficult to avoid this problem without inventing an alternative asperity contact principle that is physically accurate at high contact fractions. A qualitative agreement for speed dependent friction at high loadings was produced, although it was not possible to obtain a quantitatively accurate experimental agreement under these conditions. If a quantitative experimental agreement is to be produced from a hysteresis friction simu-

lation it would be necessary to use more accurate approximations for the surface profile and deformation in addition to improved viscoelastic models for the material.

Closure

For the overall simulation of seal friction the empirical equation based on dry rubbers was found to be the most accurate method for correspondence with experimental data. Experiments with sinusoid motion suggest the higher friction levels at lower constant velocities may not appear in many practical applications without prolonged periods at low sliding speeds. The equation for dry rubber friction with no velocity dependence may therefore often be appropriate. GW contact theory predicts similar results to the dry rubber equation at low loadings, although may be less suitable at higher sealed pressures.

Less success was obtained in producing a predictive tool for speed dependent friction for cases involving low and maintained sliding speeds. If a fluid film is assumed to remain between the rod and seal it is necessary to assume significant asperity contact in order to obtain friction predictions within the correct order of magnitude. GW-average Reynolds simulations do not make accurate predictions for speed dependent friction and have issues with the physical realism of GW theory at high asperity contact pressures.

Modifying GW-average Reynolds theory to include a transition to EHL conditions with a residual asperity shear stress at high asperity contact pressures produces a qualitative experimental agreement. This agreement can be improved by assuming a fixed proportion of total loading to be transferred to the asperities instead of a residual asperity shear stress in regions affected by high asperity contact pressures.

An accurate experimental agreement can be obtained by assuming the coefficient of asperity friction to vary with speed as an empirical exponential function. While offering reasonable agreement for constant velocity friction levels, this approach does not allow the speed-dependence to be predicted without reference to experimental friction measurements. Therefore it cannot be indisputably established that variation in asperity friction coefficient with sliding speed is the cause of the measured frictional characteristics.

Simulations based on hysteresis friction principles were developed in attempt to provide a theoretical basis for how the friction coefficients for asperity contact could vary with sliding speed. These hysteresis simulations produce qualitative experimental agreement at high sealed pressures, although do not produce accurate predictions as a result of inaccuracy in the assumed surface profile and its elastic and viscoelastic properties. It would be necessary to resolve these physical shortcomings if quantitatively accurate contact simulations are to be developed for speed dependent friction.

The partial success of predicting the load-dependence of seal friction based on dry contact relationships for rubber suggests this method may be applicable to the active seals produced.

Predicting the speed-dependence of friction would be more problematic as the simulation approaches considered were largely unsuccessful at predicting the speed dependence of friction. Chapter 8 accordingly includes a brief consideration of modelling the load-dependence of friction.

Chapter 8

Active seal development

Research has been undertaken into whether it is technically feasible to vary seal friction by adjusting the radial extension in addition to the investigation into how to calculate these friction levels. The previous chapters have considered methods of prediction and measurement for the friction characteristics of hydraulic seals over a range of operating conditions. In order to establish the feasibility of an active sealing system it is necessary to demonstrate the concept can in principle lead to improvements in actuator performance and that seal extension and retraction can be achieved in practice. The current chapter focuses on the latter condition of demonstrating the active rod seal concept can be achieved in practice.

Two active seal test rigs have been developed to investigate how applying a variable external pressure to the outer circumference of a sealing element can influence the friction characteristics. One of these test rigs was designed for a double-lip rod seal sealing element and the other for a square-section o-ring. These test rigs were designed to demonstrate it is possible to vary the radial seal extension during operation of the actuator. Steady-state friction was measured in both test rigs for different external and sealed pressures. This allowed the fundamental concept of varying the frictional characteristics by adjusting the radial seal extension to be established. The transient response to step changes in external pressure was also investigated to assess whether varying the seal extension would be able to achieve a significant change in tribology characteristics within a load cycle involving rapid movement.

8.1 Active seal background

The current investigation has attempted to develop an active rod seal for use in hydraulic actuation systems. This active seal was intended to be capable of extending and retracting radially to vary the interference pre-squeeze or clearance between the rod and seal. Creating a high level of pre-squeeze between the rod and seal is expected to minimise fluid leakage while

producing higher friction. Allowing a light level of interference or a separation between the rod and seal is expected to minimise friction while resulting in additional leakage. Excessive friction dissipates energy, reducing the efficiency of the overall hydraulic system and also subjects the sealing elements to higher wear. High leakage can result in control issues in hydraulic systems as there is a less certain actuation response for a particular flow supplied from a flow control valve. The particular application of the system will also determine the maximum acceptable level of leakage from the hydraulics. A trade-off exists between minimising friction and minimising leakage that can be adjusted by varying the seal radial extension. Use of an active seal could potentially improve sealing performance if the seal extension required for the optimal friction-leakage trade-off varies throughout the load cycle.

The original idea of developing an active hydraulic seal in the current investigation was inspired by a previous research project with CarnauldMetalBox. In this project a high-speed hydraulic actuator was required as part of a can-making machine. Over an operating cycle the actuator was subject to approximately a step change in demand position where the load was to be actuated through a long stroke and stopped at an accurate position without overshoot. It was desired to minimise the cycle time in order to maximise the production rate. To minimise the cycle time it was necessary to actuate the load through the long stroke at high speed before stopping the motion with reasonable positioning accuracy. Commercial hydraulic actuators capable of the required linear speeds generally use seal-less designs to avoid the high friction and wear experienced at these high speeds. These seal-less hydraulic actuators experience significant levels of cross-piston leakage. This leakage results in control issues for obtaining the required step response in position. It may be envisaged that the cycle time could be reduced by extending a seal during the deceleration stage to either lower the leakage to improve the motion controllability or assist with braking by increasing the friction. This case study represents an example where improving the trade-off between friction and leakage could significantly improve the performance of the overall system. In general, use of an active seal may be able to improve the performance of hydraulic systems in any application where the trade-off between friction and leakage is a major design issue.

The concept of using an active dynamic seal to control friction and leakage in hydraulic systems has not been widely considered. The few active seal studies to be published in major engineering journals are limited to mechanical face seals. In this application it had been sought to maintain clearance between a mechanical end seal and rotating shaft while minimising fluid leakage. An initial study by Heilala [50] used a relatively simple method for feedback control consisting of a thermocouple that would detect a rise in temperature from friction in the event of contact. Actuation of the face seal was achieved using pneumatics with the position adjusted over periods of minutes according to the measured temperature. Salant [51] considered a similar apparatus, although used a piezoelectric actuator to adjust the position of the face seal instead of a pneumatic system. This experimental setup was

further explored in a following study [52]. As the axial actuation for the face seal is a quite different design problem to the radial seal extension pursued in the present study, these earlier studies offer limited insight for the current investigation.

In a follow-up study [53] a more sophisticated feedback mechanism was incorporated into a mechanical face seal control system. Eddy current proximity probes were used to directly measure the seal clearance, significantly improving accuracy and lowering sensor lag compared with the previous investigations. Recently, there has been further analytical investigation of controlling a mechanical face seal [91] for sealing a gas instead of oil.

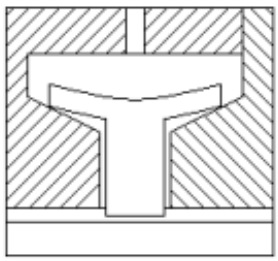

Figure 8-1: T-section inflation-type seal

Previous development of active hydraulic seals has been documented in a textbook on general tribology by Kragelsky [54]. This source refers to what was translated as an "Inflation-type radial seal" where hydraulic fluid is used to radially extend the seal against the rod. Figure 8-1 shows one of these seal examples with a T-section profile. Hydraulic fluid at a certain pressure would be applied at the outer circumference of the seal to control the radial extension of the seal.

One of the reasons for using a T-section profile for the active seal may have been to reduce the problem of radial seal extrusion compared with using a rectangular-section seal. If the sealed pressure exceeds the pressure used to actuate the seal it may be expected for the protrusion on the sealed side of the seal to be slightly lifted off the housing and allow fluid flow between the sealed fluid and outer-circumferential chamber, equalising these two pressures. This mode of seal deflection may be expected to produce only minor changes in strain in the T-section seal. Use of a rectangular-section seal could possibly result in large radial extrusions if the sealed pressure was to significantly exceed the pressure on the outer circumference of the seal.

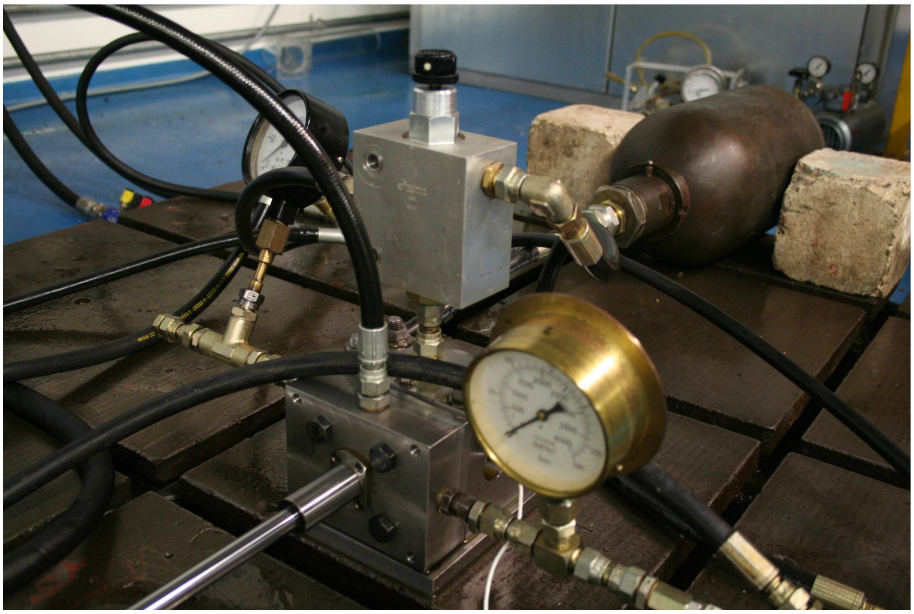

Figure 8-2: Housing block for active rod seal

8.2 Active seal prototype with double-lip seal

8.2.1 Apparatus for radial pressure test

The experimental setup for friction measurement with the passive seals in section 2.2.1 was used as a basis for the active seal experimentation. The rod seal housing block containing the passive rod seal was replaced with an alternative housing for the active seal. This replacement housing block allowed a different pressure to be supplied to the chamber on the outer circumference of the seal than to the main sealed fluid region. A pair of pressure reducing valves was used to set the pressures in each of the two chambers. The linear bearing on the outside of the housing was retained to constrain the rod radially and prevent contact between the rod and the housing blocks.

The detailed design of the active seal housing block is shown in figures C-4 to C-6. These components produce a deeper internal groove facing the outer circumference of the seal, allowing a space for pressurised fluid to directly act on the seal outer circumference. Fluid was supplied to the outer circumferential chamber from a separate source to the main sealed region, each of these two regions set to the pressure downstream of a pressure reducing valve. An additional component was included in the assembly (figure C-6) to constrain the seal in radial displacement and prevent seal extrusion while allowing the controlling fluid pressure to act on the seal outer circumference. A double-lip Parker Hannifin BS1624 rod seal in P5008 polyurethane was used as the sealing element. This type of double-lip rod seal was investigated in the passive seal friction measurements in section 2.3.3. Figure 8-3 illustrates

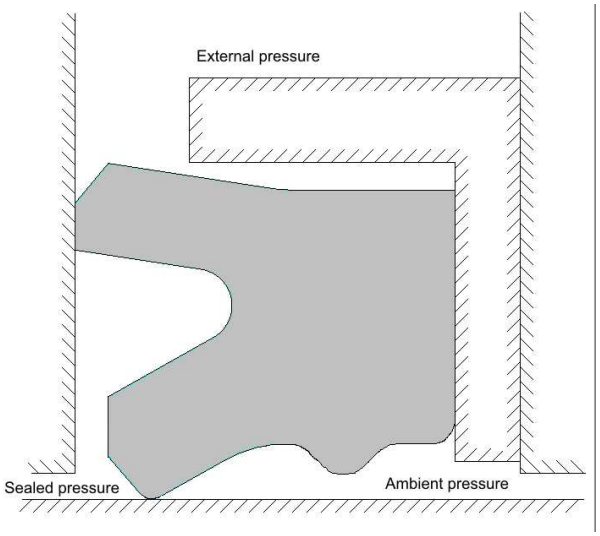

Figure 8-3: Assembled active seal housing block with double-lip sealing element

the assembled active seal housing with the sealing element in place. This assembly produced an axial interference between the seal and housing blocks in order to create sealing between the air side, sealed fluid side and radial chamber where the fluid pressure to extend the seal was applied. Increasing the seal actuation pressure to a level higher than the main sealed pressure would result on the seal being deflected radially inwards on the upper-left hand corner of figure 8-3. This deflection was expected to lift the outside circumference of the seal away from the inside of its groove and allow the fluid at the seal actuation pressure to get between the seal and the housing. The fluid pressure used to actuate the seal was assumed to act on the full area of the seal outer circumference assuming that the actuation pressure was sufficiently higher than the main sealed pressure.

The hydraulic supply system for the active seal housing is shown in figure 8-4. Hydraulic fluid was supplied to the main sealed fluid region from a Sun Hydraulics PBHB KAN pressure reducing valve. Flow from the supply pump was passed through a relief valve with a cracking pressure set at a level to produce a sufficient system pressure to supply the higher of the required pressures at the two chambers in the housing block. This supply pressure was adjusted throughout the experiments to avoid having the pump raise high pressures for the low pressure test runs and the resultant excessive fluid heating. The sealed pressure in the main sealed region was measured with the Kulite pressure transducer used in the passive seal experimentation. Fluid pressure at the outer-circumferential chamber was set using a pair of pressure reducing valves. A Sun Hydraulics PBFB KAN pressure reducing valve was used to supply fluid to the housing when the directional control valve was inactive and a PBHB LAV pressure reducing valve when the directional control valve was activated. A Hagglunds Denison GMBH directional control valve was used to switch the pressure in the outer chamber

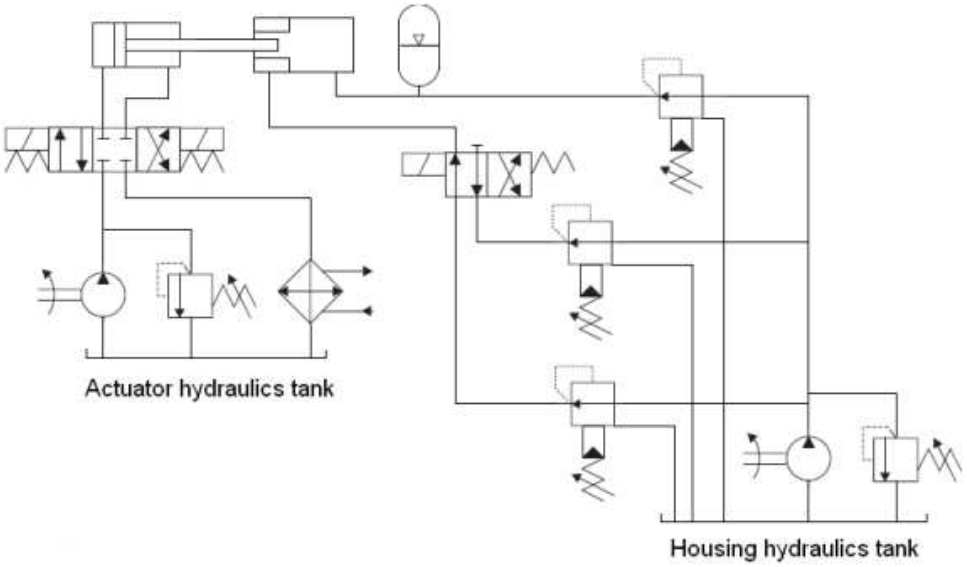

Figure 8-4: Hydraulic supply to active seal housing block

between the two pressure produced downstream of the two pressure reducing valves. This directional control valve was operated only during the series of tests looking at the dynamic response of the active seal and remained in its unactivated position throughout the steady-state friction measurements. A Rexroth HM 17-1X/250-H/1/0/0 pressure transducer was used to measure the fluid pressure in the chamber on the outer circumference of the seal.

8.2.2 Constant velocity experimental procedure

Experiments for the active seal test rig were carried out with a double-lip seal in an as received condition. No extended wear-in process was used due to uncertainty in the expected lifetime of the seal in the modified assembly. It was not known whether the experimental setup would remain stable for periods of hours with the seal subject to pressure loading and sealing requirements significantly different to its design conditions. A similar testing procedure to the passive seal rig was used for friction measurements of steady-state constant velocity. For each pressure combination the rod was displaced through five cycles of a triangular wave profile with 160 mm stroke and a particular speed. Triangular wave speeds of 5, 10, 20, 50 and 100 mm/s were used for each pressure. Creep-speed and high-speed friction were not investigated due to concern over whether the seal setup would be able to withstand repeated high-speed actuation and the long operating periods associated with creep-speed testing. For a particular sealed pressure tests were carried out with the external pressure increased in 20 bar intervals from the sealed pressure to a maximum value of 120 bar. Sealed pressures of 20, 40, 60 and 80 bar were used.

The data acquisition and processing procedure adopted were similar to those used in the

friction measurements for the passive seal. A sampling rate of 6 kHz was used for all tests with a sample interval of 150 between recorded data points for sliding speeds of 50 mm/s or lower and a sample interval of 15 for the tests at 100 mm/s. The mid-stroke force and pressure measurements were taken from the mean sensor readings 10% of the stroke length either side of the midpoint.

8.2.3 Constant velocity results

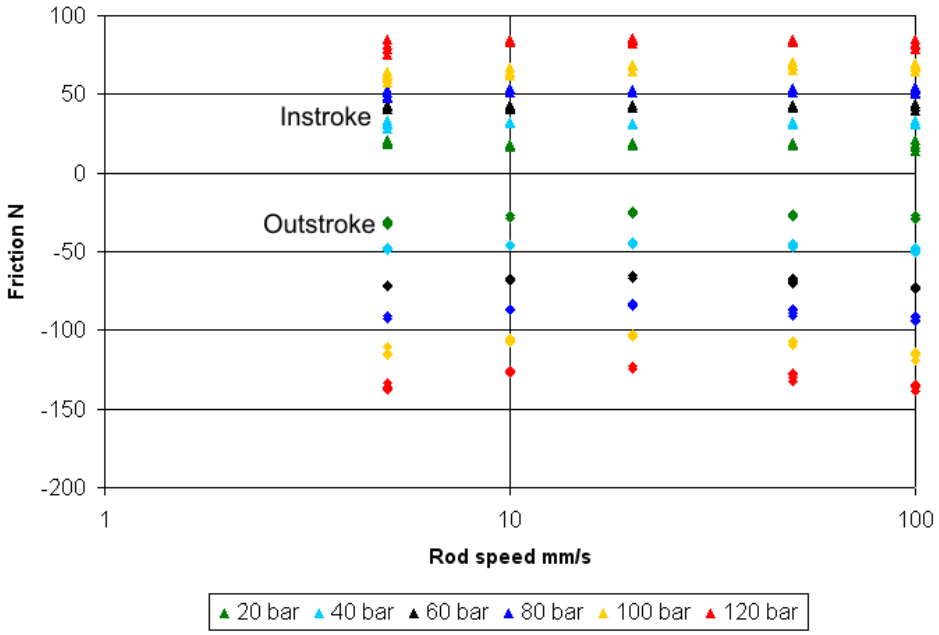

Figure 8-5: Measured steady-state friction for active seal with double-lip sealing element, variable external pressure, 20 bar sealed pressure

Figure 8-5 shows the measured friction to generally increase with the external pressure applied to the outer circumference of the sealing element. These friction levels do not show indications of approaching constant values as the external pressure is increased up to 120 bar. This suggests the seal material did not become sufficiently loaded at the rod-seal interface to produce significantly diminishing additional friction and real area of contact with increasing loading. Previous investigations [9] with a single-lip seal of the P5008 polyurethane material suggested the friction to approach a maximum value for sealed pressures higher than approximately 50 bar. It was not expected for the double-lip seal to continue to exhibit increasing friction with additional external pressure while similar friction increases were not present for corresponding variation in the sealed pressure of the unmodified single-lip seal. This discrepancy may have occurred if the pressures at the rod-seal interface exhibited significantly lower pressure increases than would have occurred if the increases in external pressure produced a

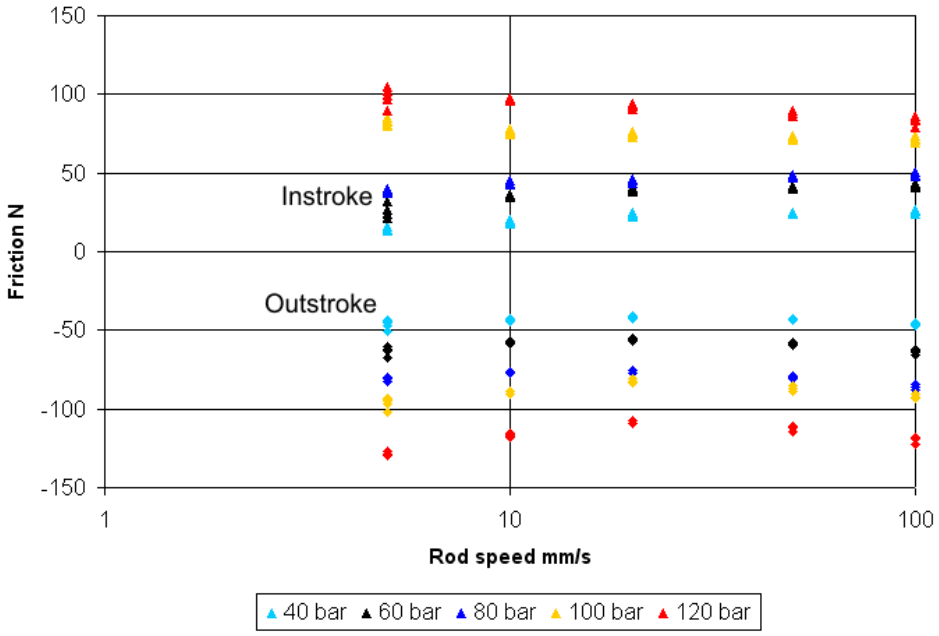

Figure 8-6: Measured steady-state friction for active seal with double-lip sealing element, variable external pressure, 40 bar sealed pressure

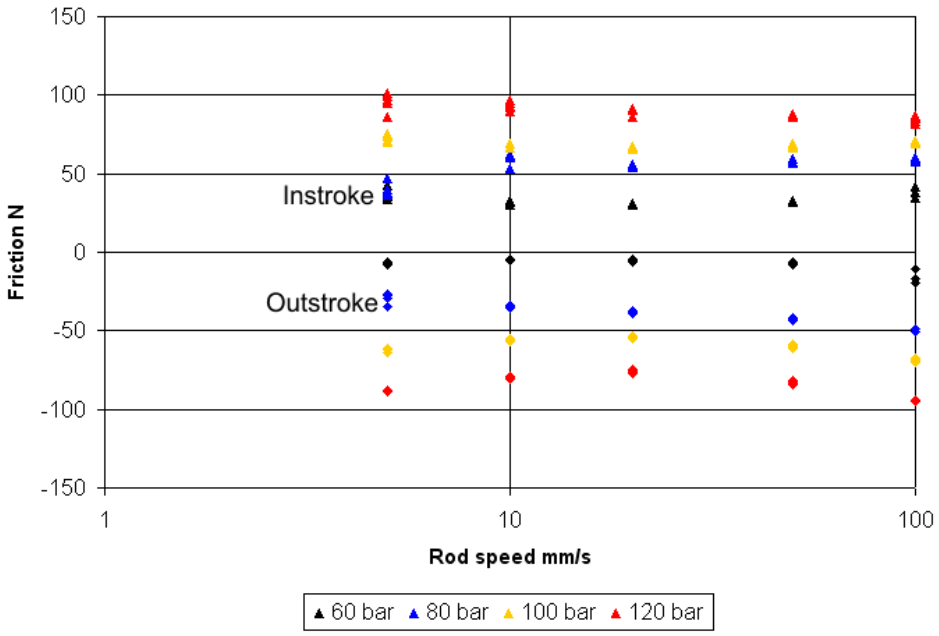

Figure 8-7: Measured steady-state friction for active seal with double-lip sealing element, variable external pressure, 60 bar sealed pressure

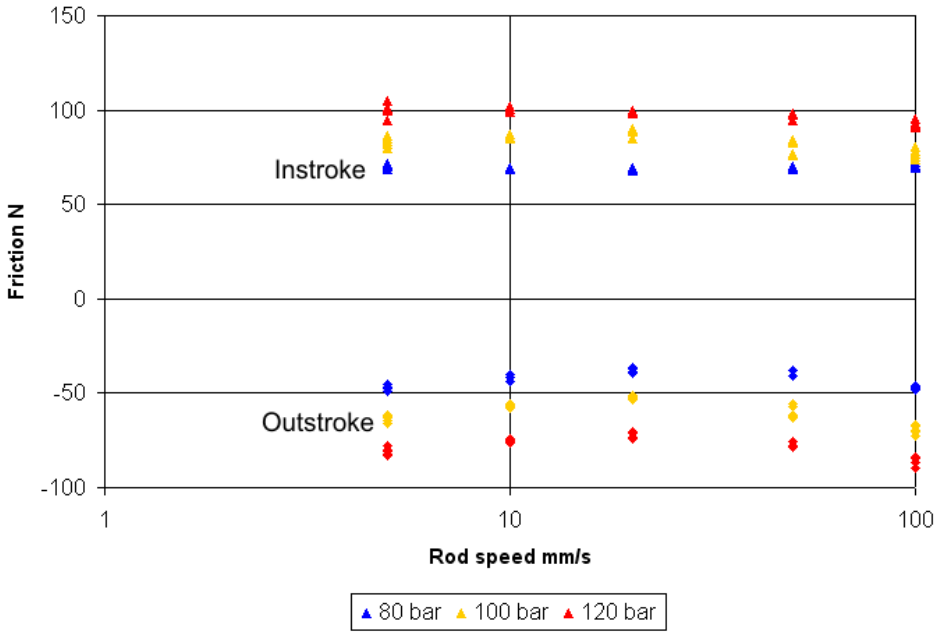

Figure 8-8: Measured steady-state friction for active seal with double-lip sealing element, variable external pressure, 80 bar sealed pressure

hydrostatic pressure increase throughout the seal. The sealing element in the active sealing assembly had an initial axial interference (figure 8-3) that was not produced with standard housings for passive seals. This axial interference may have resulted in additional radial frictional shear stress between the housing and seal as the seal was deflected radially inwards under the external fluid pressure. If a significantly higher radial shear force was acting on the sealing element in the active seal assembly, the radial normal force at the rod-seal interface would be expected to have been correspondingly reduced.

There was shown to be a reasonable degree of repeatability for the friction measurements taken. For most of the pressure combinations and sliding speeds tested the measured friction values appear to fall within a ± 5 N band between successive strokes. The differences in friction level between 20 bar steps in the external pressure are approximately 15-20 N. This reasonable degree of repeatability is consistent with that observed for the double-lip seal in the standard housing over the corresponding range of speeds (figure 2-22). There is more scatter at the lowest speed tested (5 mm/s) than at the higher sliding speeds which is approximately consistent with the high scatter during creep speeds in the passive seal experimentation. Any unsteadiness in the external pressure may have been expected to contribute to variation in rod-seal contact pressure and measured friction.

The experimental results show some indication of lower friction levels being present with the modified housing block compared with the corresponding passive seal cases. For the

cases of 20 bar and 40 bar sealed pressure (figures 8-6 and 2-21) the mean of the instroke and outstroke friction levels is significantly higher for the passive seal than with the active seal assembly with corresponding sealed and external pressures. This difference is also present at 80 bar (figures 8-8 and 2-22), although the proportional difference in friction between the two different seal assemblies is less pronounced. It may have been expected for the friction level to be reduced between the standard passive seal housing and the active seal housing as a greater diameter for the outer groove was used in the active seal assembly. This would have been expected to reduce the level of pre-squeeze between the rod and seal and produce significantly lower reaction forces at lower fluid pressures. It is possible the different run-in periods may have affected the absolute values of friction for the two different housing blocks as the passive seal testing was carried out following a significantly longer run-in period (sections 2.2.2 and 8.2.2). In this case the shorter run-in period for the active seal tests may have been expected to produce higher friction levels. Therefore the differences in run-in periods were not expected to have caused or extenuated the lower friction levels in the active seal assembly.

There is consistently higher friction during outstroke than instroke for all combinations of pressures with the active seal test rig. The results for a 20 bar sealed pressure with variable external pressure (figure 8-5) indicate this difference in friction cannot readily be attributed to inaccuracy in the friction offset. Adjusting the friction offset by more than 10-20 N would result in negative friction levels for the data with a 20 bar external pressure, imposing this limit on the offset variation of all the absolute friction values. At higher external pressures the outstroke friction would exceed the instroke friction for any offset variation within the established margin. This higher outstroke friction was more distinctive than observed in the experiments with the passive seals. The experiments with a standard housing showed higher friction levels at low sealed pressures as a result the higher pre-squeeze levels, lowering the accuracy that could be inferred for the friction offset. The friction measurements from the modified housing block provide some indication that the double-lip seal design generally experiences higher friction during outstroke than for instroke.

8.2.4 Step changes in external pressure methodology

The dynamic response of the active seal to step changes in external pressure was considered as part of the current investigation. In a practical active sealing system it would be expected for the seal to be extended or retracted during a stroke where there would be a finite time associated with how long the lag in the seal response could be if the seal is to improve system performance. The required response speed of the active seal would be dependent on the particular application. It is useful to ascertain how rapidly the current active seal design responds in order to suggest potential applications for this type of active seal. The current investigation has considered how the friction level varies following increases and decreases in

external pressure and the time periods associated with a return to steady-state conditions.

A step change in pressure was achieved using the hydraulic system shown in figure 8-4. Two pressure reducing valves were used, each at a different setting, to create two different downstream pressures corresponding to the initial and final external pressure required for the active seal. These two pressure values were set manually by in turn switching each valve outlet to the seal housing and adjusting the valve setting to give the required pressure according to the pressure transducer ported to the outer-circumferential chamber in the housing. These external pressures were set to an accuracy of 0.5 bar. A directional control valve was positioned downstream of the two outlets from the pressure reducing valves and used to switch its outlet pressure between that from the two pressure reducing valves. The main sealed pressure was set using a different pressure reducing valve that was connected directly to the main housing. An accuracy of 0.5 bar was obtained between the measured sealed pressure and required sealed pressure for all testing.

Each test was carried out over two cycles of a triangular wave of amplitude 160 mm and speed 10 mm/s. An initial cycle with no change in external pressure was included as previous steady-state experiments suggest the initial cycle to sometimes exhibit minor differences in friction compared with subsequent cycles and it was sought to minimise this effect. For a particular set of external pressures one test was carried out with the external pressure switched during the instroke stage of the second cycle. This change in external pressure was achieved by electronically switching the direction of the directional control valve when the rod was near the mid-stroke position. A second test was carried out with the rod set in motion for two cycles where the switch in pressure was applied at the mid-stroke position during outstroke of the second cycle. Two similar further tests were carried out with the two external pressure values reversed. Between each test the rod was reciprocated in a triangular wave for 20 cycles at 100 mm/s in order to obtain steady-state conditions for the initial external and sealed pressure combination before the external pressure was switched. This complete procedure was carried out for a sealed pressure of 20 bar with external pressures switched between 20 bar and 40, 80 and 120 bar. A sealed pressure of 60 bar was also considered with the external pressure switched from 60 bar to 80 and 120 bar.

A sampling rate of 6 kHz with a sampling interval of 15 was used with the data acquisition system throughout the series of experiments with steps in external pressure applied to the active seal. A correction was applied to the load cell force data as a result of the sealed pressure acting on the rod face. This correction was produced from the measured response of the load cell measurements to variation in sealed pressure using the procedure described in section 3.2. This procedure involved filtering the pressure and force data to minimise the noise introduced into the corrected friction data. The pressure data were filtered using a double-pass Butterworth algorithm of order 2 and dimensionless cut-off frequency 0.02, constituting a high degree of filtering in order to remove the electrical noise from the force

corrections. The load cell data was also filtered using a first order Butterworth algorithm, although with a higher dimensionless cut off frequency of 0.1, representing a lower degree of filtering than for the pressure sensor data.

8.2.5 Pressure variation results

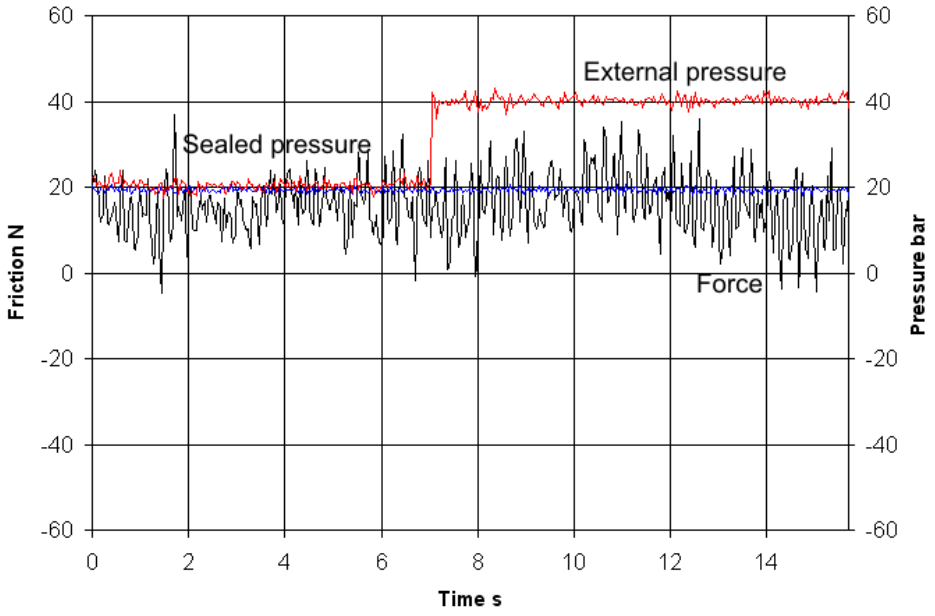

Figure 8-9: Friction for active seal with double-lip sealing element, external pressure step from 20 bar to 40 bar during instroke, 20 bar sealed pressure

Figures 8-9 and 8-10 show the responses to a relatively small step increase in external pressure for instroke and outstroke (20 bar to 40 bar). The highest magnitude of increase in external pressure (20 bar to 120 bar) is shown in figures 8-13 and 8-14. For each case the increase in external pressure is shown to produce a corresponding increase in friction within a period of the order of a tenth of a second after the pressure increase. This indicates there to have been some nearly instantaneous influence on friction as a result of increasing seal extension. There is a greater immediate increase in friction during outstroke than during instroke as a result of increasing the external pressure. This difference in friction changes is particularly distinctive between figures 8-13 and 8-14 where the friction increase during outstroke is approximately three times the magnitude of the friction increase during instroke. It is uncertain why the friction increase was higher during outstroke than instroke. It was found in the sine wave experiments with the passive seals in section 3.3 that friction had a greater tendency to increase during outstroke than instroke once the sliding speed was dropped significantly. The unidentified physical causes for this behaviour may also have

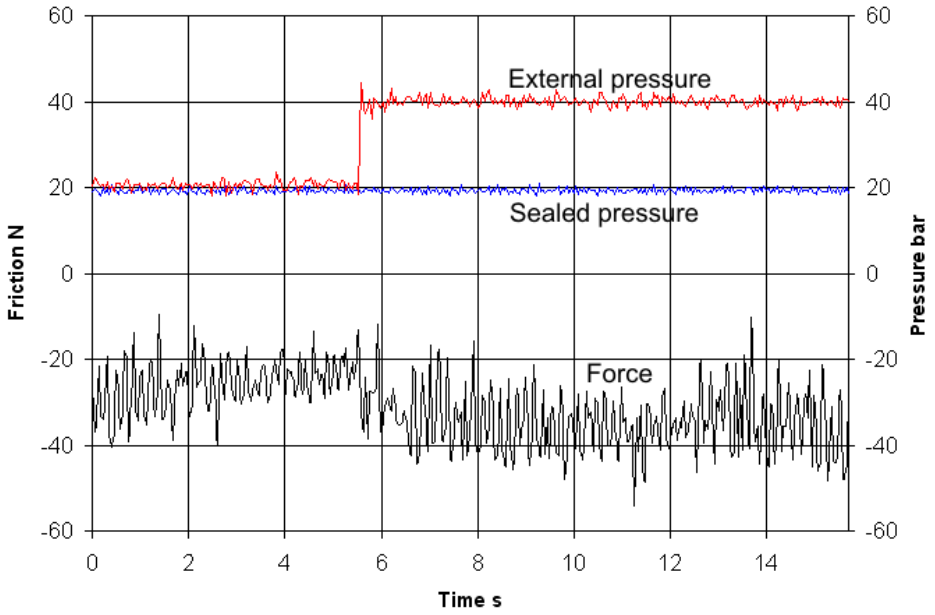

Figure 8-10: Friction for active seal with double-lip sealing element, external pressure step from 20 bar to 40 bar during outstroke, 20 bar sealed pressure

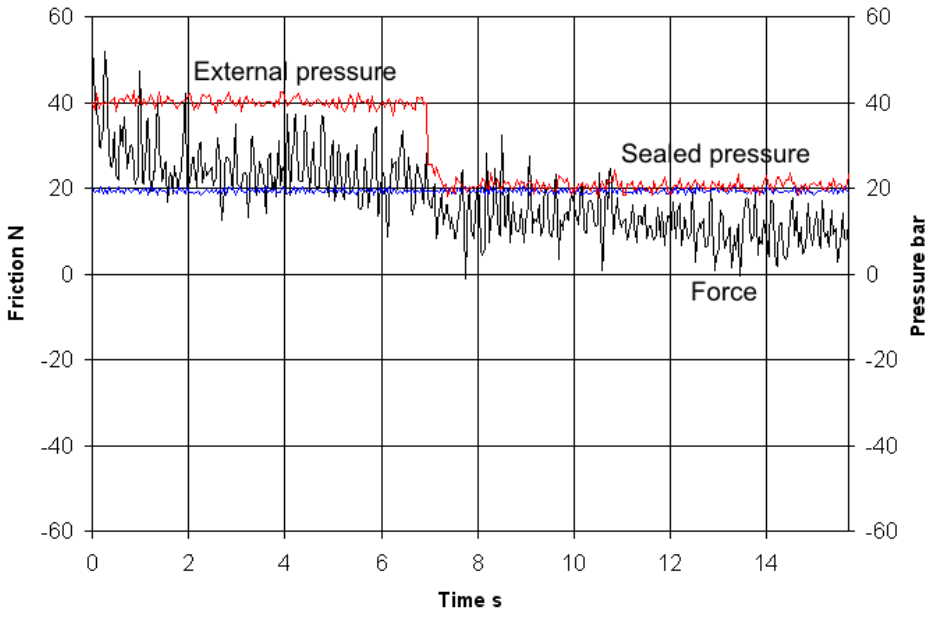

Figure 8-11: Friction for active seal with double-lip sealing element, external pressure step from 40 bar to 20 bar during instroke, 20 bar sealed pressure

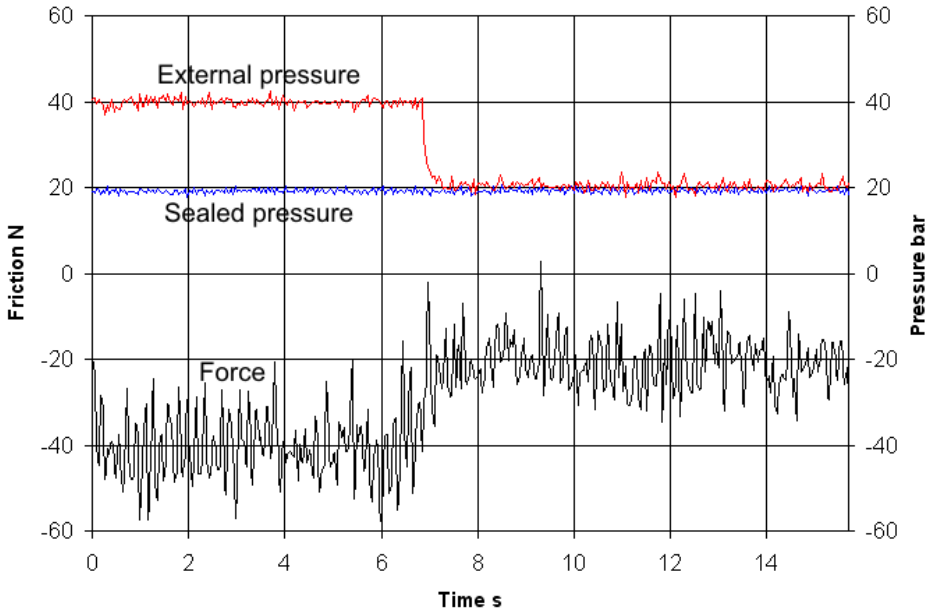

Figure 8-12: Friction for active seal with double-lip sealing element, external pressure step from 40 bar to 20 bar during outstroke, 20 bar sealed pressure

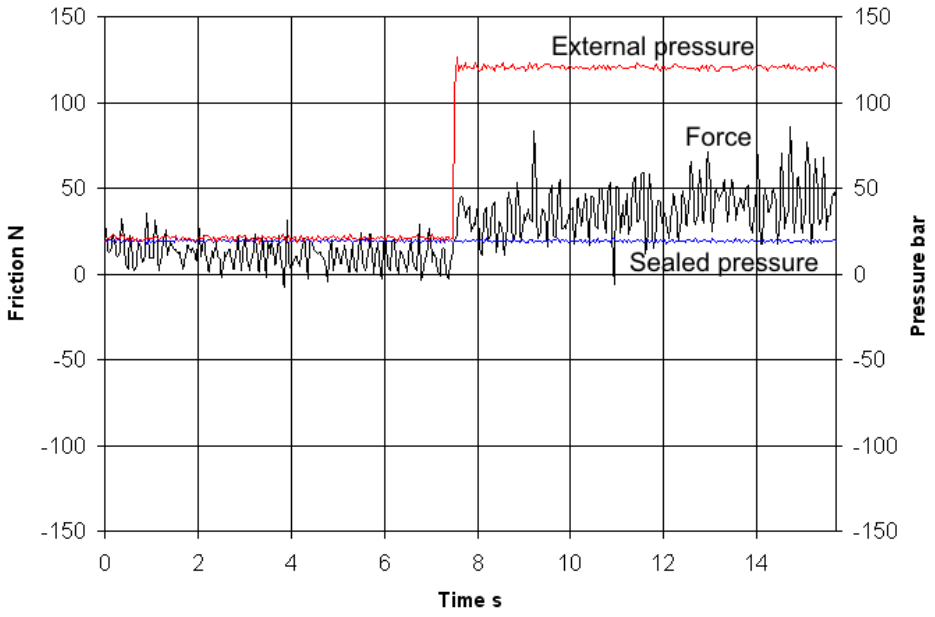

Figure 8-13: Friction for active seal with double-lip sealing element, external pressure step from 20 bar to 120 bar during instroke, 20 bar sealed pressure

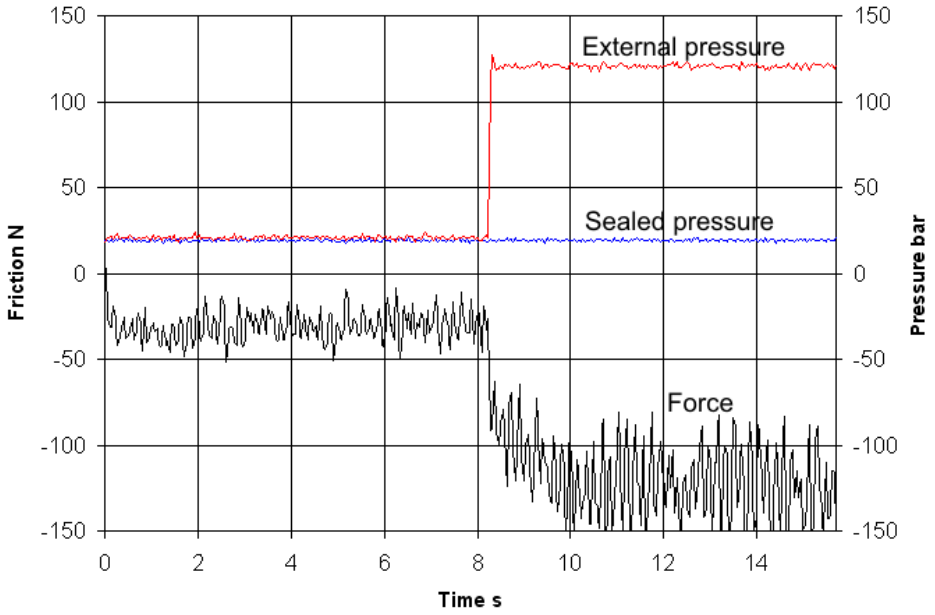

Figure 8-14: Friction for active seal with double-lip sealing element, external pressure step from 20 bar to 120 bar during outstroke, 20 bar sealed pressure

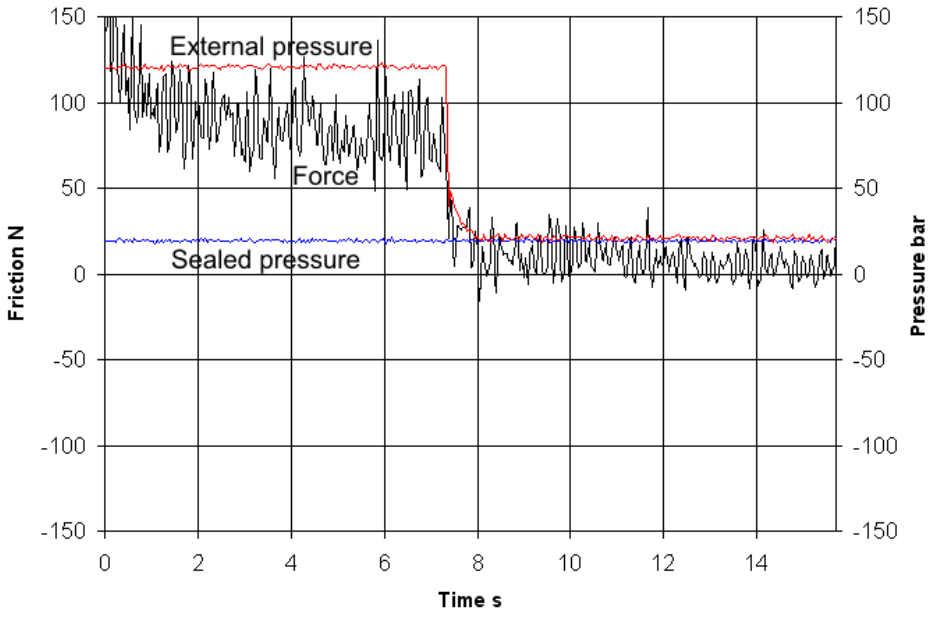

Figure 8-15: Friction for active seal with double-lip sealing element, external pressure step from 120 bar to 20 bar during instroke, 20 bar sealed pressure

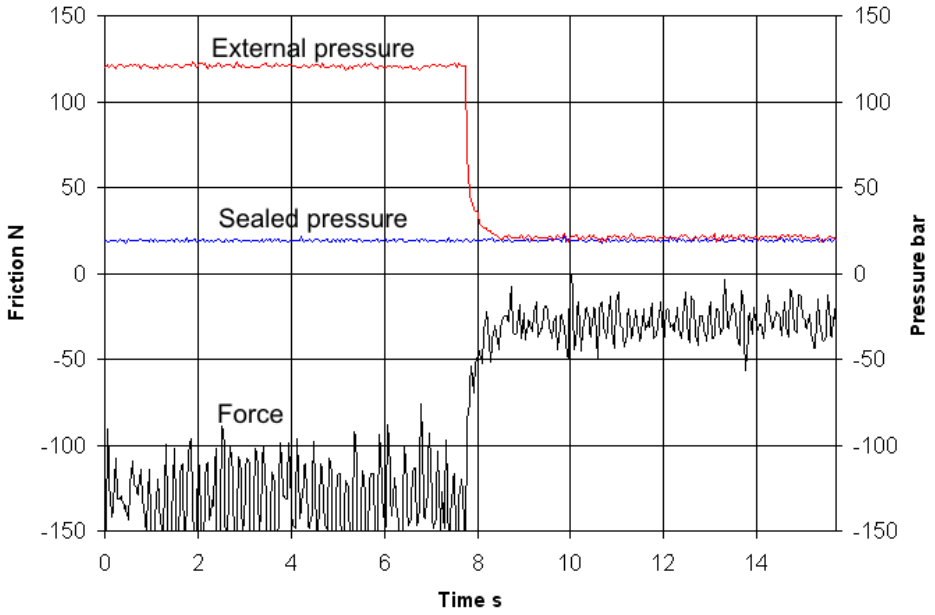

Figure 8-16: Friction for active seal with double-lip sealing element, external pressure step from 120 bar to 20 bar during outstroke, 20 bar sealed pressure

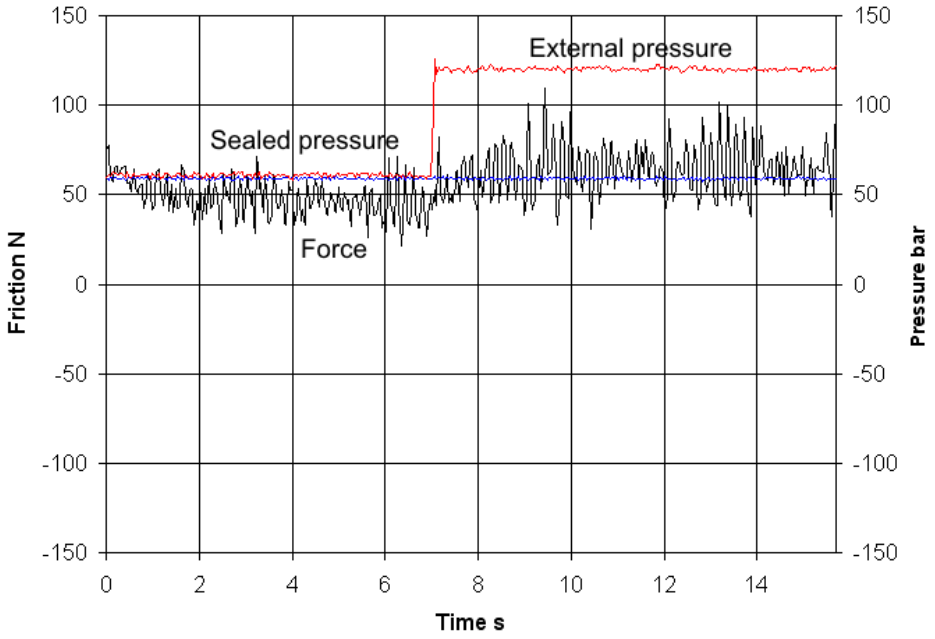

Figure 8-17: Friction for active seal with double-lip sealing element, external pressure step from 60 bar to 120 bar during instroke, 60 bar sealed pressure

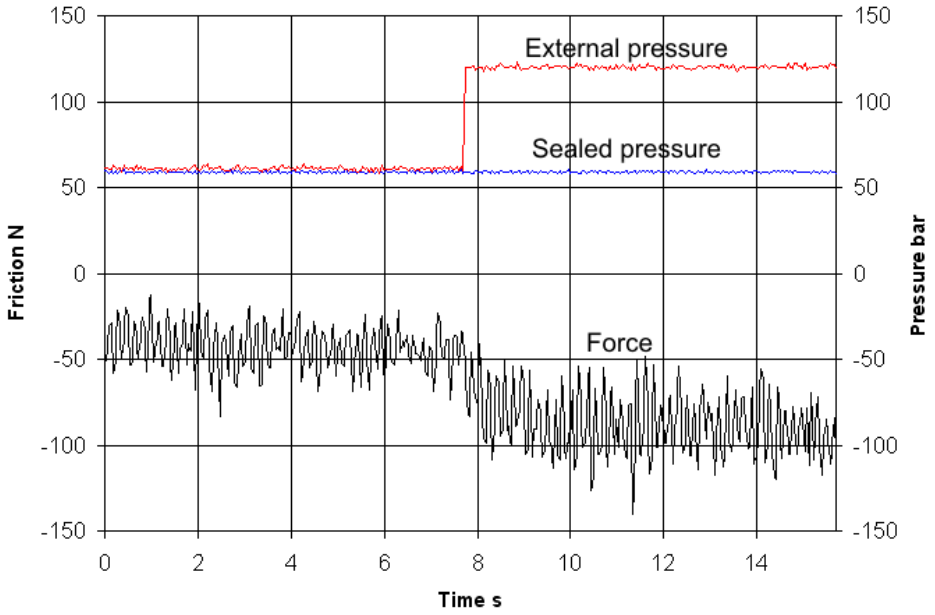

Figure 8-18: Friction for active seal with double-lip sealing element, external pressure step from 60 bar to 120 bar during outstroke, 60 bar sealed pressure

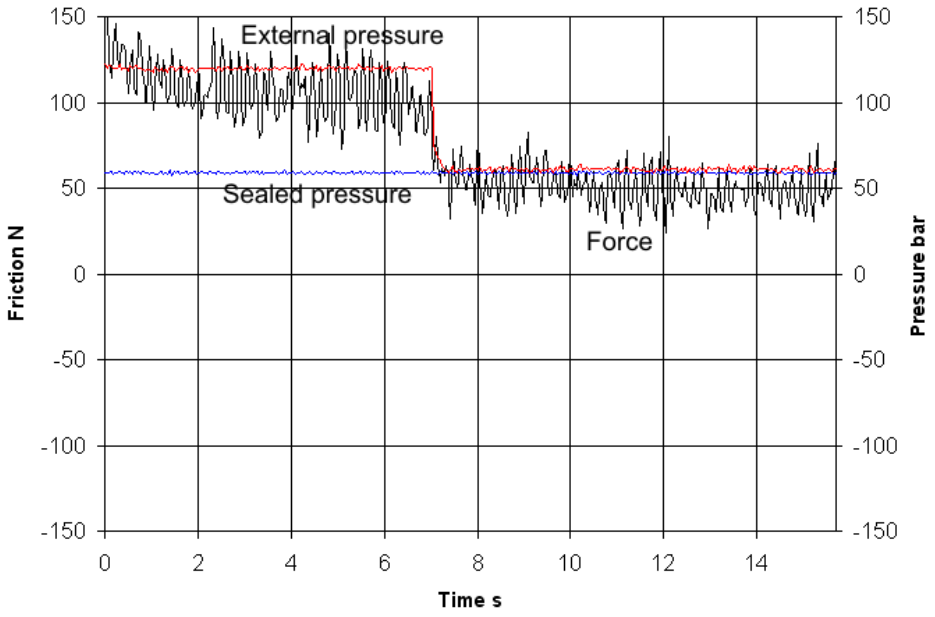

Figure 8-19: Friction for active seal with double-lip sealing element, external pressure step from 120 bar to 60 bar during instroke, 60 bar sealed pressure

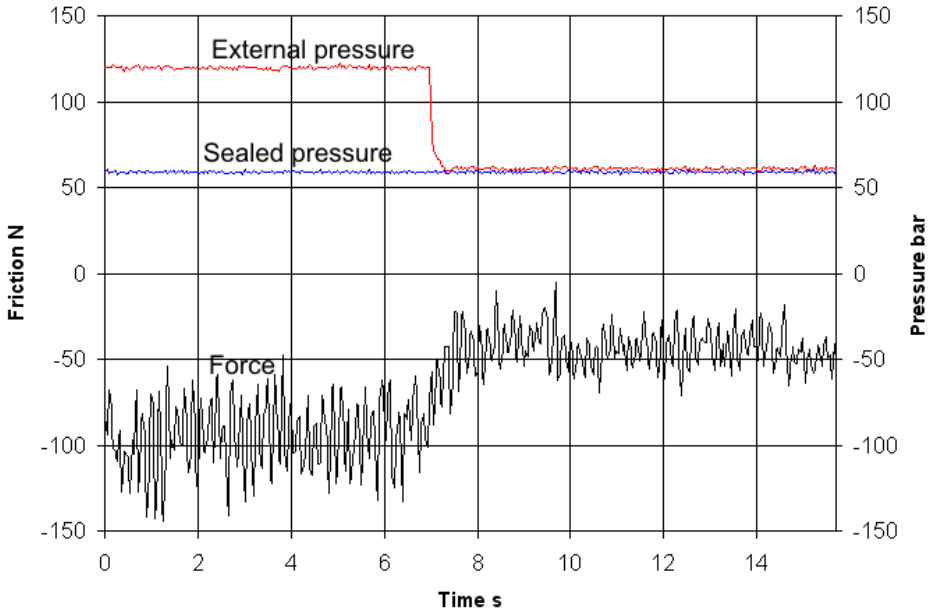

Figure 8-20: Friction for active seal with double-lip sealing element, external pressure step from 120 bar to 60 bar during outstroke, 60 bar sealed pressure

limited the immediate friction increase experienced during instroke as a result of increasing the external pressure.

Reducing the external pressure is seen to produce immediate decreases in the friction level. The time lag associated with the friction transition varies between tests and does not show a consistent relationship between the magnitude of the pressure step and the lag. As an example, an external pressure step from 120 bar to 60 bar (figure 8-20) is associated with a longer delay than in the case of a pressure step from 120 bar to 20 bar (figure 8-16). There is evidence that the friction responds more rapidly to the external pressure decrease during instroke than during outstroke as the cases with a definite lag are limited to outstroke tests. It is possible that this behaviour may be reminiscent of the tests for the standard seal assembly where friction was shown to decrease throughout instroke while increasing during outstroke. If rod seal friction has a disposition to decrease during instroke this may have contributed to the relatively rapid friction reduction following the removal of the external pressure.

For the cases where the external pressure was reduced the friction level falls to levels approximately consistent with steady-state friction for reciprocating motion at the new pressure combinations. Increases in the external pressure did not increase the friction to steady-state levels during instroke during the remainder of the stroke at which the pressure increase was applied. For these cases the friction does not return to steady-state levels until subsequent cycles.

8.3 Active seal prototype with square o-ring seal

8.3.1 Test rig apparatus

A test rig for an alternative active seal design was produced in order to further investigate the feasibility of the concept of achieving seal actuation by varying an external fluid pressure applied to the seal outer circumference. It was intended for the modified design to be more robust in terms of its tolerance to different external pressures by using a sealing element that was more suitable for three different pressures. To achieve this a square-section sealing element was used instead of the double-lip rod seal.

The experimental setup was similar to that for the active seal testing with the double-lip sealing element described in section 8.2.1, although with a modified seal housing block. The detailed design of the housing block for the square-section seal is shown in figures C-7 and C-8. The seal groove formed by the housing blocks creates an axial interference between the seal and the sides of its housing to minimise the leakage of fluid from the external pressure side to the main sealed and air sides. A radial slot is formed in the centre of the groove to allow the fluid at the external pressure to act on the outer circumference of the sealing element. This was intended to minimise the tendency for seal extrusion through the slot if the external pressure fell below the sealed pressure. The presence of the outer groove helped to prevent extrusion occurring in the main body of the seal at low external pressures. The radial distance the seal was free to deflect through between its extended and retracted positions was minimised in order to avoid excessively high strains in the seal material during operation. A square-section nitride rubber o-ring of imperial size S-115 was used as the sealing element. This had small circumferential notches at the centres of each of its four faces, although has been henceforward described as square-sectioned.

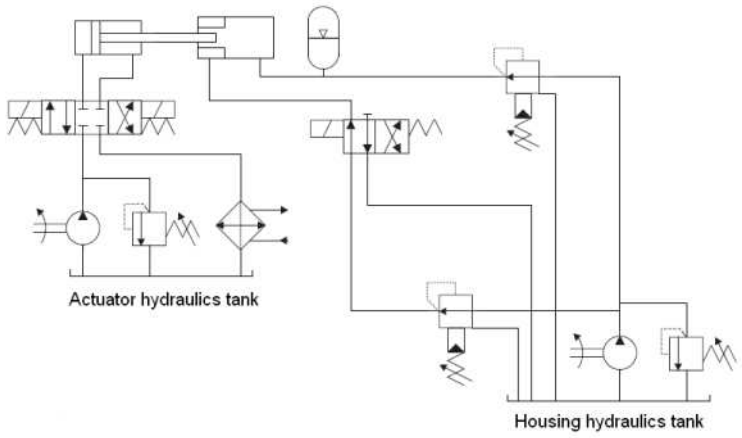

Figure 8-21: Hydraulic supply to active seal housing block for assembly with square-section o-ring sealing element

The hydraulic supply and circuit to the housing was modified to allow the external pressure to be dropped from a particular value of pressure to the ambient level. Figure 8-21 shows this hydraulic circuit with a single pressure reducing valve to set the non-ambient external pressure. A directional control valve was used to switch the pressure at the outer circumferential chamber in the housing block between the outlet of the pressure reducing valve and a return line to the tank at ambient pressure. This valve was not operated during the initial series of tests where the steady-state friction levels were obtained. For these experiments the pressure at the outlet of the pressure reducing valve was directed to the seal housing throughout testing.

8.3.2 Constant velocity testing methodology

Steady-state measurements of the friction levels for the active seal with a rectangular-section sealing element were carried out in order to verify that adjusting the external pressure could affect the friction characteristics. These friction measurements also provide a point of reference for the dynamic behaviour following changes in external pressure. As with the active seal rig with the double-lip sealing element, no period of run-in was carried out prior to the friction measurement experiments. Extended operation for run-in was omitted as it is was not certain whether the sealing element would remain in its intended position and state over extended periods. Friction measurements were obtained for a range of intermediate sliding speeds and combinations of sealed and external pressures in order to produce Stribeck curves associated with the different pressure combinations. For each pressure combination tests were carried out at speeds of 5, 10, 20, 50 and 100 mm/s with a five-cycle triangular wave of 160 mm stroke. Sealed pressures of 20, 40 and 60 bar were considered each with values of external pressure between the sealed pressure and 120 bar in 20 bar increments.

Sensor data was sampled at a rate of 6 kHz with an interval of 150 sampled data points between recorded data points. The effective friction force for a particular sliding speed was taken to be the mid-stroke friction level, obtained from the mean of the recorded data between 40% and 60% of the stroke length. The mean force obtained from the load cell was corrected for the force exerted on the rod face by the fluid using the procedure described in section 2.2.3.

8.3.3 Constant velocity results

Figures 8-22, 8-23 and 8-24 show the measured steady-state seal friction for different external pressures with respective sealed pressures of 20, 40 and 60 bar. In general the results show friction to increase for all sliding speeds as a result of an increase in the external pressure, which was expected from the higher rod-seal reaction forces associated with higher external pressures. During outstroke the friction increases rapidly with external pressure for low pressures of up to 40 bar. At higher external pressures the outstroke friction saturates at a

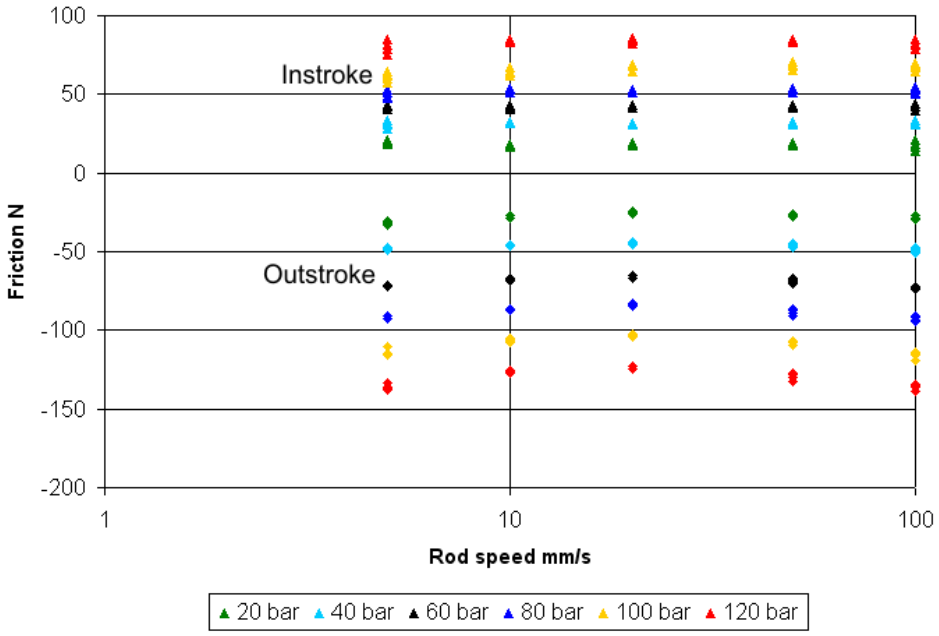

Figure 8-22: Measured steady-state friction for active seal with square o-ring sealing element, variable external pressure, 20 bar sealed pressure

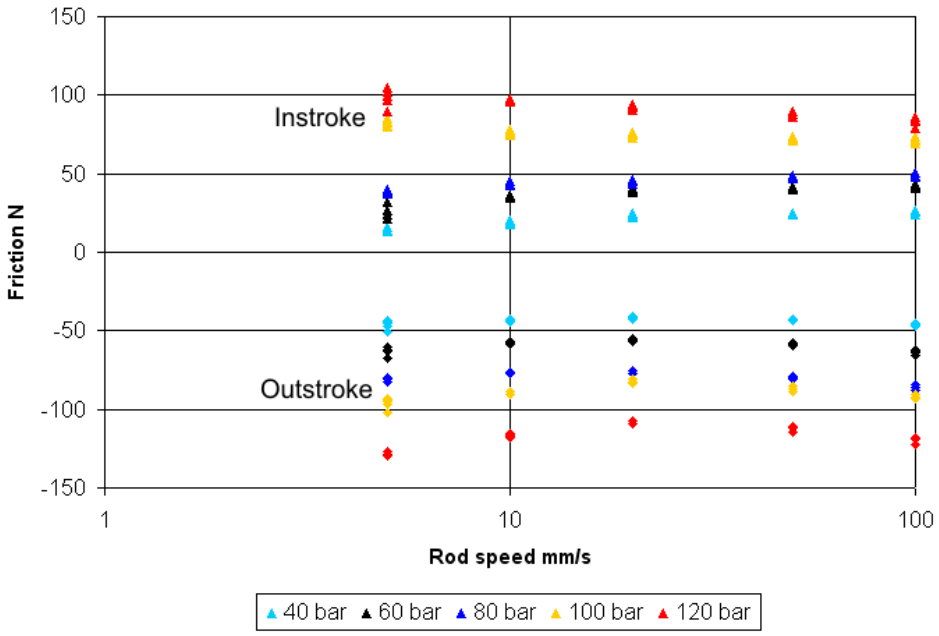

Figure 8-23: Measured steady-state friction for active seal with square o-ring sealing element, variable external pressure, 40 bar sealed pressure

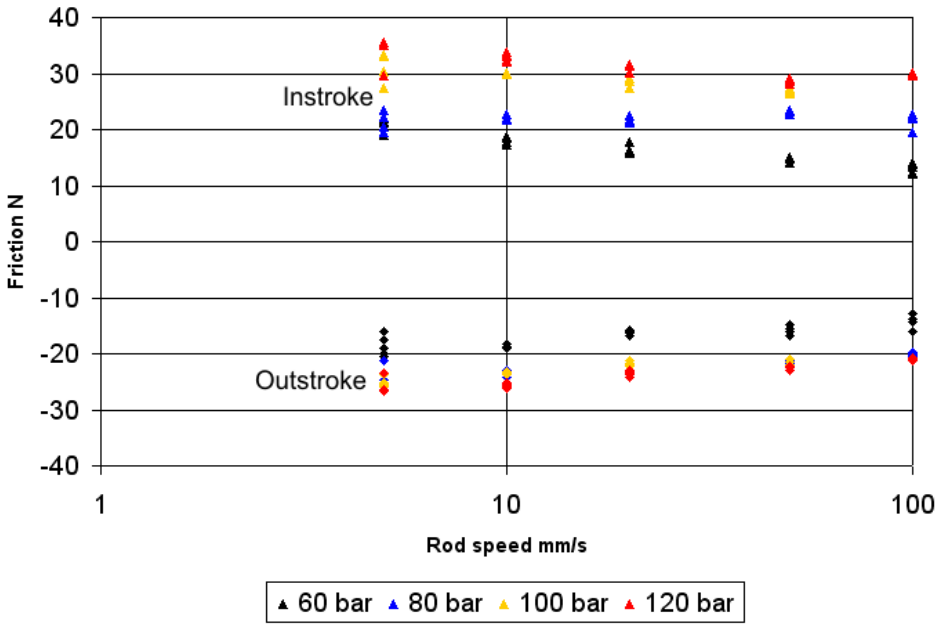

Figure 8-24: Measured steady-state friction for active seal with square o-ring sealing element, variable external pressure, 60 bar sealed pressure

level of approximately 25 N. It was not expected for the friction to be higher during outstroke than instroke at low external pressures. Previous experiments with square-section elastomeric seals [10] have suggest a significant increase in friction over low sealed pressure to take place only during instroke where the film thickness was reported to decrease with increasing sealed pressure. It is difficult to identify a cause of this discrepancy between the earlier study and the current investigation.

Friction increases during instroke over the full experimental range of external pressures (up to 120 bar). The largest friction increase can be observed in figure 8-22 for a change in external pressure between 20 and 40 bar. This suggests there to be a non-linear relationship between external pressure and friction with the highest friction-pressure gradients occurring at lower pressures. It is not possible to identify whether the friction had reached or was approaching a limiting value for external pressures up to 120 bar. The maximum external pressure is several times the elastic modulus of the nitride rubber o-ring material, indicating the rubber to be heavily loaded. From the empirical relationships for rubber friction considered in section 4.2.4.2, friction is not expected to increase by more than a fifteenth of its value at a load equal to its elastic modulus for any higher loading. The proportional increases in friction with external pressure are significantly higher than this proposed upper limit. It was thought that the rectangular seal may have been partially extruded through the narrow clearance between the rod and inner bore of the housing. This effect would have increased the nominal

area of contact between the rod and seal and allowed greater friction levels with a limiting maximum shear stress.

It is noted that the absolute values of friction for varying the external pressure with the square o-ring sealing element are significantly lower than in similar experiments with the double-lip polyurethane seal. There are several possible causes for this friction difference. The polyurethane seal would have had a significantly greater nominal area of contact with the rod than the elastomeric seal with an axial contact length of 5.7 mm compared with 2 mm. This greater area of nominal contact would allow a greater area of real contact and overall shear force at high loadings. As the polyurethane material had a higher elastic modulus it was also thought to continue friction increases over a longer range of absolute loadings. If both materials are assumed to have similar friction coefficients at light loading, the material with the greater elastic modulus would be expected to have higher absolute friction levels at high loads. It is also possible the polyurethane material may have had higher friction coefficients at low loadings in addition to the effects of load-dependence on friction coefficients.

8.3.4 Step changes in external pressure methodology

The response of the active seal with a square-section sealing element to step changes in external pressure was investigated to provide an indication of the dynamic characteristics of this type of design. The procedure used was similar to that for the active seal rig with a double-lip sealing element in section 8.2.4, although focused on sudden decreases in external pressure and involved complete removal of this external pressure. Use of the square-section sealing element allowed stable operation with lower pressures on the outer-circumference of the sealing element than at the main sealed region. The irregular profile on the sealed side of the double-lip seal may be less effective than the square-section seal at sealing the different chambers of the housing from each other. Sealing was dependent on the axial interference between the lips of the U-cup geometry and the housing. These protruding seal lips may have experienced significant radial deflection at higher pressure differences, which may open a fluid channel between the seal and housing. The square-section design is less prone to changes in shape under the effects of the pressure differences.

The external pressure was removed through using the directional control valve to switch the external pressure port on the housing block from the pressure reducing valve to the tank. This hydraulic circuit is shown in figure 8-21. The initial external pressure was set before any recordings were taken by manually adjusting the setting on the pressure reducing valves to an accuracy of 0.5 bar. An electronic switch was used to active the directional control valve and remove the external pressure once the rod approached the mid-stroke position. Each test consisted of two cycles of a triangular wave with a stroke length of 160 mm and speed of 10 mm/s. During the second cycle the external pressure was removed at the mid-

stroke position during either instroke or outstroke. A period of reciprocation consisting of 20 cycles of a triangular wave of speed 100 mm/s was used between tests in order to establish equilibrium initial conditions for each case. Experiments were carried out for a sealed pressure of 20 bar with initial external pressures of 40, 80 and 120 bar and for a 60 bar sealed pressure with initial external pressures of 80 and 120 bar. Separate tests were carried out for the pressure removed during instroke and outstroke for all pressure combinations.

Data were recorded for both triangle wave cycles in each test. A sampling rate of 6 kHz with an interval of 15 measurements between recordings was used throughout testing. A Butterworth filtering algorithm was applied to the pressure sensor data before calculating the effective friction levels as described in section 3.2.1. A Butterworth filter of second order with a dimensionless cut-off frequency of 0.02 was used for the pressure sensors measurements and a dimensionless cut-off frequency of 0.1 for the load cell data.

8.3.5 Pressure variation results

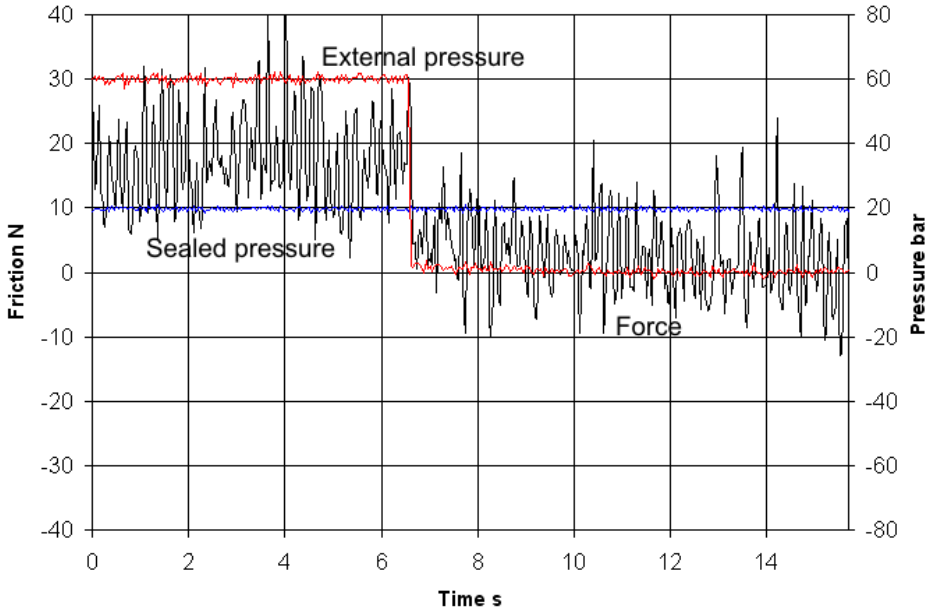

Figure 8-25: Friction for active seal with square o-ring sealing element, step removal of 60 bar external pressure during instroke, 20 bar sealed pressure

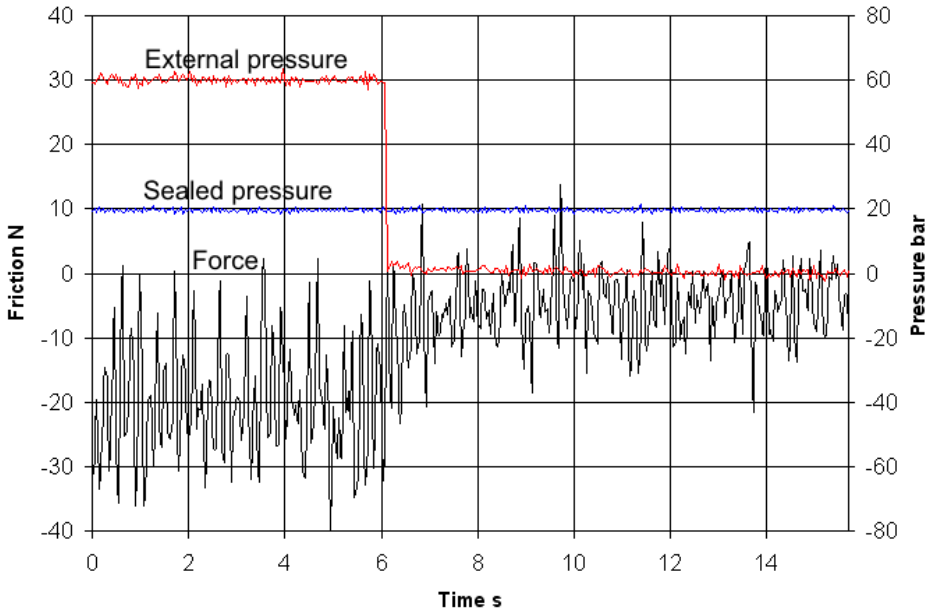

Figure 8-26: Friction for active seal with square o-ring sealing element, step removal of 60 bar external pressure during outstroke, 20 bar sealed pressure

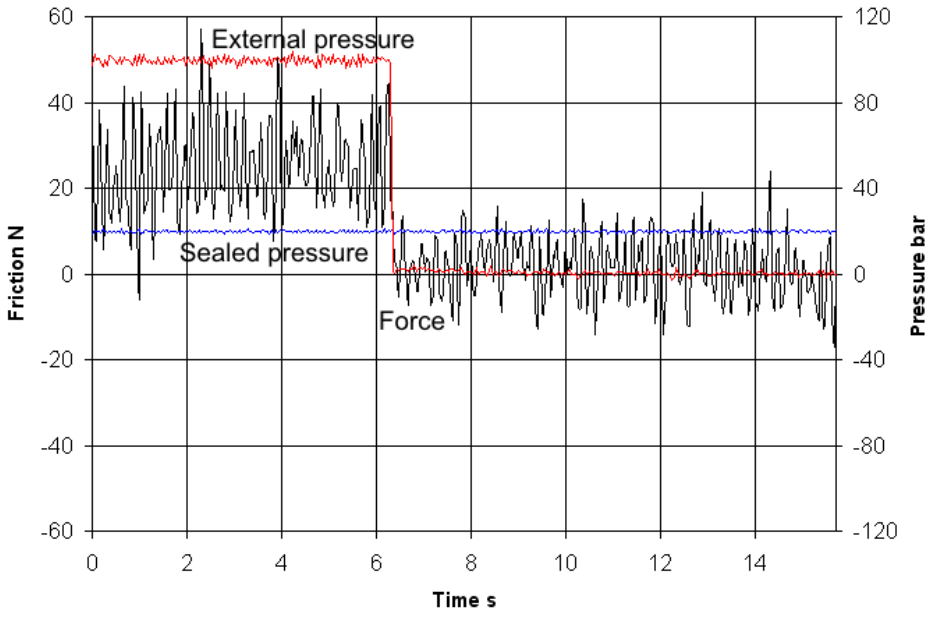

Figure 8-27: Friction for active seal with square o-ring sealing element, step removal of 100 bar external pressure during instroke, 20 bar sealed pressure

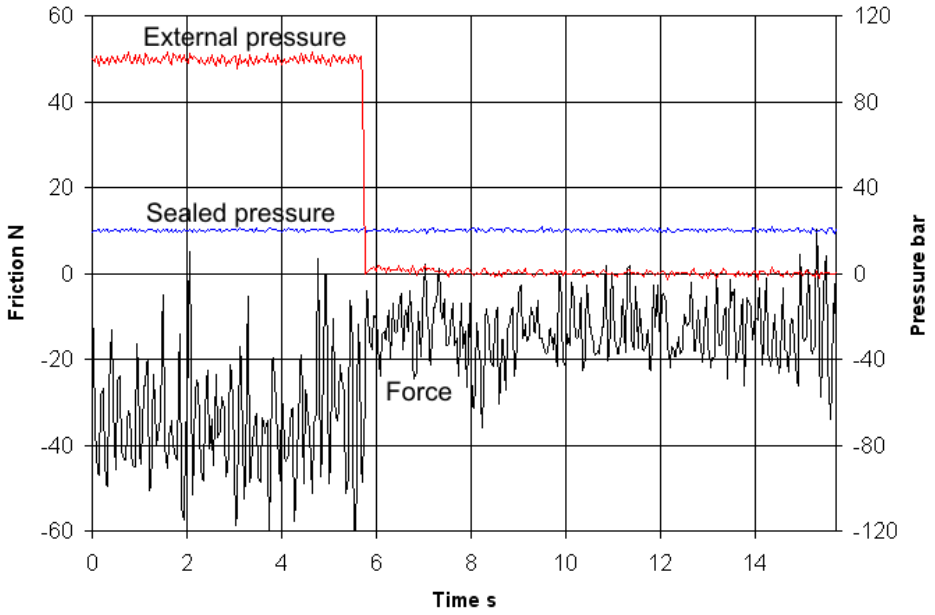

Figure 8-28: Friction for active seal with square o-ring sealing element, step removal of 100 bar external pressure during outstroke, 20 bar sealed pressure

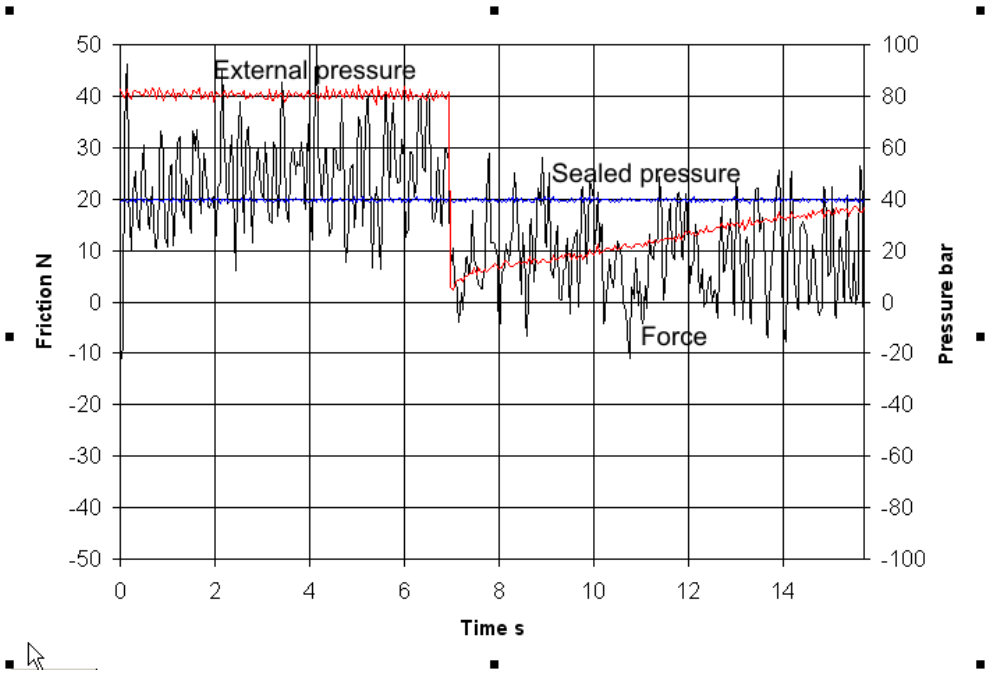

Figure 8-29: Friction for active seal with square o-ring sealing element, step removal of 80 bar external pressure during instroke, 40 bar sealed pressure

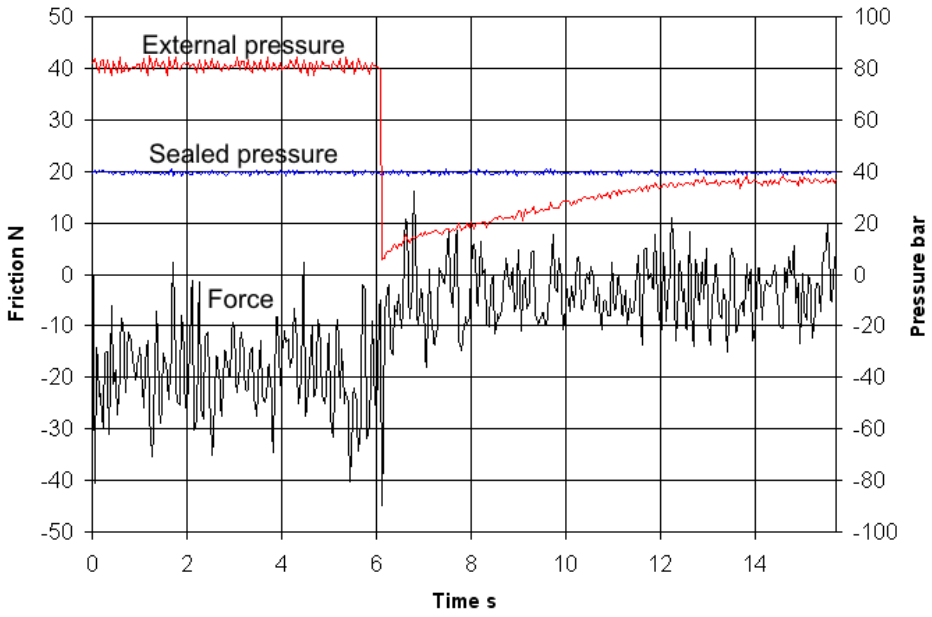

Figure 8-30: Friction for active seal with square o-ring sealing element, step removal of 80 bar external pressure during outstroke, 40 bar sealed pressure

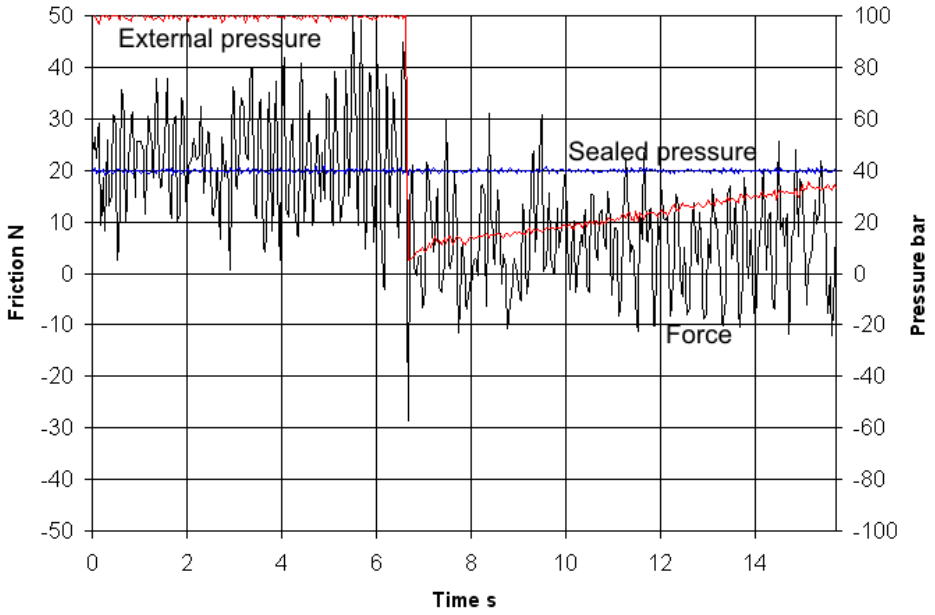

Figure 8-31: Friction for active seal with square o-ring sealing element, step removal of 100 bar external pressure during instroke, 40 bar sealed pressure

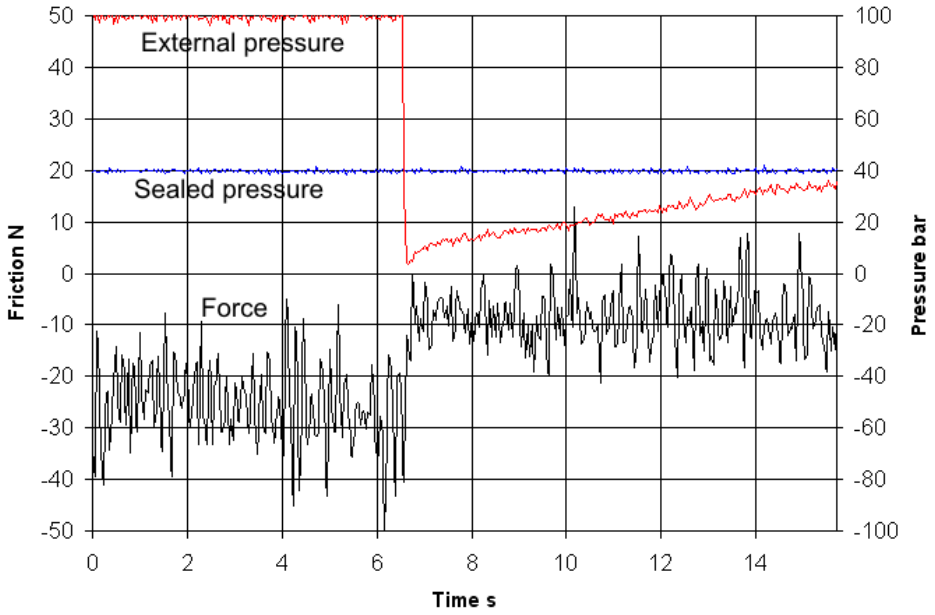

Figure 8-32: Friction for active seal with square o-ring sealing element, step removal of 100 bar external pressure during outstroke, 40 bar sealed pressure

Figures 8-25 to 8-32 show the transient behaviour in friction following the removal of the external pressure for two different sealed pressures (20 and 40 bar), each with two different initial external pressures. In all cases the friction is seen to rapidly decrease after the external pressure was removed with approximate lags of the order of a tenth of a second or lower. This indicates the seal design with the square o-ring element may be suitable for applications where the seal needs to be retracted rapidly such as when rapid movement stage follows an accurate positioning stage. The current design of seal rig is less suitable for rapid seal extension where significant increases in friction are not seen in the remainder of the stroke once an external pressure was applied. It is not possible to determine whether this persistent low friction is indicative of higher leakage with the current test rig.

For intermediate sealed pressures (approximately 40 bar or higher) the pressure measured in the outer circumferential chamber recovers towards the sealed pressure following its initial decrease after the removal of the external pressure (figures 8-29 to 8-32). This increase in measured pressure takes place over a period of approximately 10 s, indicating it to be a relatively gradual physical process compared with the pressure and frictional changes occurring immediately after the removal of the external pressure. It is deduced that the pressure recovery was caused by fluid leakage between the main sealed region and the outer circumferential housing containing the port to its pressure sensor. In order to maintain ambient pressure at the external pressure supply port it would have been necessary for the seal to extrude in a manner that sealed this external pressure from the part of the outer-circumferential chamber where the pressure measurement was taken from. Inspection of the porting to the two fluid chambers (shown on the isometric sketch in figure C-5) provides an indication of how the observed pressure differences could occur. The external pressure and pressure sensor were both ported to the outer-circumferential chamber through radial holes in the housing with perpendicular orientations to each other. Following the removal of the external pressure the seal may have extruded through the hole to the external pressure source, sealing this ambient pressure from the outer-circumferential chamber. The sealing element may also have deformed axially to allow fluid pressure to pass between the main sealed region and outer-circumferential chamber. As the pressure sensor was ported to the outer-circumferential chamber separately from the external pressure source, the pressure throughout this chamber may have been registered by the pressure sensor.

No recovery in the pressure at the outer-circumferential chamber was observed at the lowest sealed pressure of 20 bar (figures 8-25 and 8-28) after the external pressure was removed. This indicates that the sealing between the outer-circumferential and main sealed regions was maintained under these conditions. This suggests minimum sealed pressure exists that is required to sufficiently deform the sealing element to open a fluid channel between the two chambers when the external pressure is removed.

8.4 Simulation of friction levels for active seal

8.4.1 Methodology

It was considered which of the available types of friction simulation investigated would be most suitable for describing the friction characteristics of the active seals. For typical friction results for both the rectangular section and U-cup section seals (e.g. figure 8-22) there is little variation in friction with sliding speed. This occurs as a result of the experimental speed range being limited to 5 mm/s and above in order to avoid long testing periods with the novel seal assembly configurations. It was not possible to use the active seal experimental data to verify the speed dependent friction behaviour at lower speeds where significant changes in friction may have been expected. Without any significant variation in measured friction with speed, use of a model with only load dependence would be appropriate. Load-dependent friction modelling is considered in the static contact mechanics approaches explored in chapter 4.

The friction levels of the active seal with the rectangular o-ring reach a maximum value over the 20-120 bar range of external pressures (figure 8-22). This suggests the real area of contact to reach a maximum value over this load range. The model for dry rubber friction in section 4.2.4.2 allows a limiting value of friction at extreme loads and may be appropriate for this experimental data. Friction is expected to approach a limiting value at a lower external pressure with the nitrile rubber o-ring than with the polyurethane sealing element as a result of the lower elastic modulus of the rubber material. Therefore it is expected for any limiting friction behaviour to be more apparent for the sealing element with lower stiffness.

An estimate for the elastic modulus of the nitrile rubber material of 5 MPa was assumed. The friction coefficient for the nitrile rubber is assumed to be governed by the empirical relationship in section 4.2.4.2 (equation (4.11)). The effective axial length of the sealing element was taken as 3 mm with a 16 mm diameter. It is assumed that the rod-sealing element pressure would correspond with the external pressure applied on the outer circumference of the sealing element. This was justified because the simplified geometry would create an approximately uniform pressure distribution with an approximately hydrostatic pressure changes from variation in the external pressure.

8.4.2 Results

Figure 8-33 shows the simulated friction level with the empirical equation for dry rubber friction over a range of different external pressures. The experimental data in the figure includes the results with the square-section o-ring for different external and sealed pressures (from figures 8-22 to 8-24) with a sliding speed of 1 mm/s. These results show a qualitative agreement between the model and the measured data with a limiting value of friction approached at higher external pressures and lower friction levels at the lowest external pressures. This

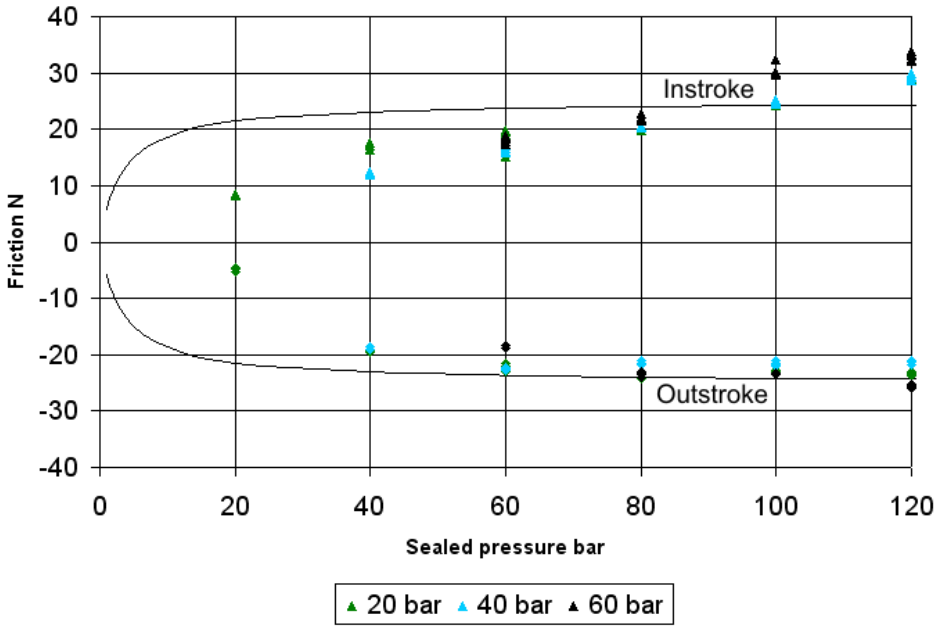

Figure 8-33: Predicted friction from $\mu = \frac{1}{C_1}\frac{1}{\left(1+15\frac{p}{E}\right)}$ and experimental results for rectangular o-ring with different external and sealed pressures, square o-ring sealing element, E=5 MPa, 1 mm/s sliding speed

provides a strong indication that the experimental friction may have reached a limiting value as a result of a saturation in the real area of contact similar to what is known to occur in dry rubbers at high loadings. The lower friction at low external pressures provides some indication of a region where the contact fraction and adhesive friction may have risen with load.

There is no accurate quantitative agreement between the model based on the rubber friction equation and the active seal experiments. Measured friction reaches a limiting value at a higher external pressure than predicted with the model. It would be possible to improve the experimental agreement by significantly increasing the elastic modulus assumed for the o-ring material. Use of a multiple of the 5 MPa elastic modulus assumed would produce a reasonable agreement, although is unlikely to be physically justified. It is possible there was some level of seal extrusion between the rod and housing that took place at intermediate external pressures (between approximately 40 and 100 bar) that may have acted to increase the nominal area of contact while the limiting contact fraction was approached across the contact length. This may have produced more significant increases in the total area of real contact at higher pressures than would occur with a constant nominal area of contact.

8.5 Closure

Two active seal test rigs have been produced, commissioned and used to investigate the frictional behaviour of a hydraulic system where the rod seal is extended or retracted by varying the pressure acting on the outer circumference of the sealing element. One of the test rigs used a double-lip polyurethane rod seal with an axial interference between the seal housing in order to allow the external pressure to be varied without affecting the main sealed pressure. A radial opening on the air side of the housing was used to supply fluid at the external pressure to the outside of the seal. Steady-state friction measurements were carried out for different combinations of sealed and external pressures. The response of the friction level to step increases and decreases in external pressure were also measured.

The alternative active seal test rig featured a square o-ring as the sealing element and a radial slot in the centre of the seal groove to supply the external pressure to the outer circumference of the sealing element. This design was intended to be more robust to low external pressures than the design with the double-lip seal as the U-cup type seal was not originally designed to create a sealed interface on its fluid side. Friction measurements were taken for steady-state conditions with different sealed pressures, each with a range of external pressures. The friction response following the removal of the external pressure was also obtained.

Friction was shown to increase with external pressure with significant increases occurring up to a 120 bar external pressure. This may have been the result of friction at the axial interference between the seal and housing lowering the rod-seal reaction force for a particular fluid pressure and necessitating higher than expected fluid pressures to produce particular rod-seal reaction forces. There was shown to be a reasonable degree of repeatability between successive strokes, indicating the assembly to have reasonable short-term stability. Friction was shown to be lower than for the passive seal tests with similar fluid pressures. This was thought to be the result of the lower rod-seal pre-squeeze produced in the active seal housing block. The friction measurements showed friction to be lower during outstroke than during instroke for the double-lip sealing element.

Experiments for applying pressure steps in the external pressure were shown to produce immediate changes in the friction level. Step increases in external pressure were shown to produce rapid increases in friction with lags of the order of a tenth of a second or lower. Step decreases in external pressure produced corresponding decreases in overall friction, although during outstroke these friction decreases occur less rapidly over periods of a few seconds. Reducing the external pressure was shown to reduce the friction to steady-state levels for the new pressure combination within the stroke. Increasing the external pressure during outstroke also produces a transition to the new steady-state friction levels before the end of the stroke. External pressure increases during instroke resulted in a friction level being

reached that was lower than the steady-state friction level in subsequent strokes.

Steady-state experiments with the square o-ring sealing element show there to have been an initial rapid increase in outstroke friction with external pressure over the lower range of pressures. Previous investigations have suggested similar rapid friction increases with square-section seals to occur during instroke. It is not certain why this discrepancy has arisen. Instroke friction was shown to continue to significantly increase with external pressure at higher pressures which was not expected from the dry friction behaviour of rubbers. This may have been caused by either friction between the seal and housing lowering the rod-seal reaction force or by seal extrusion between the rod and seal. The highest absolute friction values were lower for the square-section than the double-lip seal. This could be the result of either the higher nominal contact area between the rod and double-lip seal or the higher stiffness of the double-lip seal material.

Removing the external pressure from the active seal with the square-section sealing element was shown to cause an immediate reduction in friction. Rapidly applying a particular external pressure did not produce measurable increases in friction for the remainder of the stroke. It is uncertain whether the absence of a friction increase would have been indicative of greater leakage under these conditions. For sealed pressures higher than 20 bar the pressure in the outer-circumferential chamber was shown to gradually approach the sealed pressure over a period in the order of ten seconds after the external pressure source was removed. This may have been caused by the seal extruding into and blocking the port where the external pressure was supplied while the sealing between the outer-circumferential and main sealed regions was disrupted.

Friction for the active seal with the square o-ring sealing element was modelled using the empirical equation for dry rubber considered in chapter 4. Little speed dependence of friction was observed over the limited experimental speed range, suggesting a static contact mechanics approach may be suitable for explaining the available experimental data. This friction coefficient-loading model was able to qualitatively capture the appearance of a maximum friction level at higher external pressures, although the model predicted the limiting friction to be approached at excessively low loadings. This inaccuracy could have been the result of variation in the nominal area of contact as a result of seal extrusion.

Chapter 9

Conclusions

9.1 Conclusions

This thesis has been concerned with progress towards the development of an active sealing system for a hydraulic actuator where the sealing elements can be radially extended and retracted to vary the friction and leakage characteristics. Experimental and numerical approaches have been used to determine the friction characteristics of existing hydraulic seals to investigate improving tribology modelling techniques and allow the frictional behaviour of proposed active sealing systems to be predicted and analysed. Prototypes for active sealing concepts have also been developed and commissioned to demonstrate that the concept can be achieved in practice.

Friction measurements of specific single-lip and double-lip rod seals were carried out for constant velocities over a range of sealed pressures and sliding speeds. At higher sealed pressures there is a gradual halving of friction once the sliding speed is increased above approximately 2 mm/s. Comparison with previous studies suggests this critical sliding speed may be dependent on the physical size of the seal. Instroke and outstroke friction exhibit similar speed dependent changes in friction at higher sealed pressures for the single-lip seal.

An unexpected abrupt increase in friction during instroke is apparent at intermediate speeds, which does not have a readily identifiable cause. As a result the general decrease in friction above a critical sliding speed is not present during instroke at low sealed pressures. The double-lip seal exhibits similar friction characteristics to the single-lip seal with no abrupt instroke friction increase at intermediate sliding speeds. This suggests this unexpected change in friction may be attributable to the smaller seal geometry instead of the unusual test rig design.

Friction measurement with sinusoid motion shows the friction to approximately double at lower sliding speeds in cases where the sliding speed remains below a particular level for a reasonable period of time. This friction increase begins towards the end of outstroke motion,

reaches a peak at the stroke limit and decreases once the instroke cycle began. This is consistent with the friction measurements for constant velocity motion where higher friction is observed at low sliding speeds and friction increases during outstroke and decreases during instroke. At intermediate frequencies there is significant friction variation throughout the stroke, indicating the importance of transient effects in the seal-rod sliding friction coefficient. The theoretical "parallelogram" friction-displacement relationship with Coulomb friction does not occur as a result of these transient effects in the friction coefficient.

An approximately linear force-displacement relationship is present at the highest test frequency (60 Hz). This is consistent with rocking motion against the seal axial stiffness. The measured stiffness is 3.7 times greater than predicted from a bulk parameter model, suggesting the seal may deflect differently to simple shearing. There is also a significant measured hysteresis loop, suggesting additional sources of energy dissipation other than the material viscoelastic properties. The double-lip seal behaves similarly to the single-lip seal with slightly less friction variation across the stroke at intermediate frequencies.

Simulations were produced for sinusoid motion using a mass-spring-damper model to represent the seal inertia, axial stiffness and viscoelastic damping. Suitable values for these parameters were estimated and the natural frequency calculated as approximately 2.1 kHz, indicating the behaviour significantly below the natural frequency to be relevant for the current study. For a constant limiting value of sliding friction a "parallelogram" friction-displacement characteristic is predicted. Variation in the damping ratio does not significantly affect the simulation results and the hysteresis loop at low displacement amplitudes is predicted to be minimal.

Several different approaches were used to simulate constant velocity seal friction. Each of these simulations are dependent on the pressure distribution between the rod and seal which was obtained from FEA modelling of the seal geometry. Geometries for single-lip, double-lip and o-ring seals were modelled. Increasing the sealed pressure above a critical value was predicted to initiate contact between the rod and main body of the seal, significantly increasing the nominal area of contact. Including curvature at the seal corners produces Hertzian peaks which were relevant for EHL analysis.

Combining the contact pressure distribution with an empirical equation for rubber friction coefficients produces a reasonable agreement with experimental data between friction and sealed pressure. This friction model may be suitable for applications where prolonged periods with low sliding speeds do not take place as time delays and lags were found to be associated with the higher empirical friction at lower speeds. Friction is predicted to increase rapidly with sealed pressure once the main seal body gained contact with the rod and approach a limiting value at high sealed pressures. The rapid friction rise was observed at a higher sealed pressure than simulated, possibly due to inaccuracy in the assumed initial clearance between the rod and seal body.

A deterministic contact model with a sinusoid surface was produced to investigate a theoretical basis for the empirical relationship at high loadings. This sinusoid contact was modelled using an analytical approximation and an FEA model. Full contact between the surfaces is predicted to take place at an excessively low nominal load, suggesting a need to include a distribution of asperity heights.

The appropriateness of GW contact theory was investigated to verify the physical basis for previous mixed lubrication studies. GW theory was shown not to be appropriate for the seal material and expected loading in the current study where the theory predicts unrealistically high contact fractions. Using measured surface roughness parameters in the GW model further reduces the suitability of the model for the expected loadings. This suggests the standard GW-average Reynolds approach used in previous hydraulic seal tribology studies may not be appropriate for this application.

The established approach to seal tribology of inverse EHL theory was compared with experimental data and shown not to produce accurate friction predictions. This standard theory predicts friction to have a $u^{0.5}$ dependence on sliding speed while a negative relationship with much higher friction levels was observed in practice. The high friction levels suggest significant amounts of asperity contact may occur or the fluid film may collapse completely and cause boundary lubrication to dominate.

An alternative simulation approach was considered that includes asperity contact, hence may have been able to explain the higher measured friction values. This was the GW-average Reynolds model which has been used in previous studies of hydraulic seals. The standard model was shown not to be an accurate method of predicting the velocity dependence of friction. Excessively high friction is predicted during instroke as a result of fluid cavitation extending inwards from the air side of the seal. This may have been caused by the divergent film profile between the sealed and air sides. Similar frictional behaviour was predicted for an o-ring geometry, suggesting this behaviour to be a common feature of the modelling technique.

Modifying the GW-average Reynolds simulation to force a transition to EHL conditions where the pressure limit of GW theory is exceeded improves the experimental agreement at higher sealed pressures. Assuming a residual asperity shear stress in the regions with a transition to EHL produces a qualitative agreement across the full experimental range of sealed pressures. This agreement can be improved if a constant proportion of the overall load is assumed to be transferred to the asperities.

Derivation and use of an empirical speed dependent relationship for the asperity friction coefficient allows an accurate agreement with the friction measurements. In order to improve the evidence for a variable asperity friction coefficient it would be preferable to produce a theoretical method for predicting this variation in friction with sliding speed.

A friction model based on the point-contact EHL of single asperities was produced to

investigate whether fluid viscosity could be used to explain the higher observed friction levels without having to use boundary friction models with empirical friction characteristics. The $u^{0.388}$ dependence on friction coefficient obtained does not represent a significant improvement over conventional inverse EHL over the seal geometry. Integrating the point-contact results over a distribution of asperity heights and using these results for the asperity friction coefficient does not improve the experimental agreement.

Hysteresis friction simulations were developed following the partial success of the empirical dry rubber friction relationship in attempt to include speed-dependence in a contact mechanics model. These simulations were based on the delayed elastic recovery of the material creating asymmetrical pressure distributions between different sides of surface asperities. One set of simulations is based on a single point on the seal surface modelled as a mass-spring-damper and another set consider a repeating line contact. Friction was predicted to significantly reduce above a critical sliding speed and reach an approximately constant value at high sliding speeds, giving a qualitative agreement with the experiments at higher sealed pressures. Excessive friction coefficients were predicted at low loadings due to the excessive predicted contact fractions, similar to what is seen in the static models of sinusoid contact.

An asperity truncation modification was made to the hysteresis simulation to investigate how the excessive simulated decrease in friction between low speeds and high speeds could be reduced. This modification assumes the peaks of the sinusoid surface to be removed following run-in, increasing the contact fraction and friction at high sliding speeds. Peak truncation improves the experimental agreement for speed-dependent friction, although creates additional problems with excessive friction at low loading.

Active seal concepts were developed to demonstrate that variation in the seal frictional characteristics could be achieved in practice by varying the seal extension. Two active seal prototypes were produced, one with a double-lip sealing element and the other with a square o-ring. Both sealing systems allowed the constant velocity friction to be varied by adjusting the external pressure at the outer circumference of the sealing elements. The transient response in friction following step changes in external pressure was also obtained for both seal prototypes. External pressure increases during instroke were shown to produce an increased friction level below the steady-state value for the remainder of the stroke. Otherwise, the new steady-state friction levels were reached before the end of the stroke following the changes in external pressure.

9.2 Recommendations for further work

It would be preferable to develop and commission a test rig for rod seal friction that allows friction measurement in both directions of strokes independently while not having the end face of the rod exposed to pressurised fluid. This would allow testing at higher sealed pressures

to verify similar previous investigations and improve friction accuracy by reducing the force range required by the load cell. To achieve this it would be necessary to design a method of having the rod go through two opposite sides of the housing block with sealing at both rod-housing interfaces while only measuring friction from one of the sealing regions. It may also be worth carrying out extended run-in periods to bring the experiments into line with the run-in specifications in the ISO 7986 standard. Creep speed friction measurements could be improved by using a different actuation system such as a ball screw that is more suitable to producing low velocities.

The quality of the data from high frequency sinusoid excitation could be also improved by using a more suitable actuation system. Use of an equal-area hydraulic actuator would be expected to produce a closer approximation to sinusoid motion than the single-ended model used in the current investigation. Alternatively, an electromagnetic actuator may also provide more accurate sinusoid motion at the low displacements associated with high frequency motion. It should be possible to reliably obtain the stiffness characteristics associated with the seals if accurate sinusoid motion could be produced over a range of higher frequencies.

It was shown that an existing empirical equation can produce reasonable approximations to the friction-load characteristics for the seal. It would be preferable to determine an accurate theoretical relationship between nominal loading and contact fraction in order to obtain a scientific basis for this empirical equation. A stochastic rough surface model valid for high contact fractions appears to be the most likely form of a suitable contact model.

If a mixed lubrication method is to be used for future seal tribology simulation, it would be necessary to find an alternative to the standard GW contact model for high sealed pressures. Alternative methods of producing a load transfer from the asperities to the fluid could be explored if the existing GW-average Reynolds approach is to be used as a basis for future work. Mixed lubrication models combining the Reynolds equation with asperity contact models designed for high contact fractions could also be considered. It may also be worth investigating under what conditions and degrees of contact a continuous fluid film can exist between two contacting rough surfaces and using this to suggest a limiting condition for the validity of the Reynolds equation.

One of the main limitations of the proposed hysteresis friction model could be overcome by combining the sinusoid surface model with a distribution of asperity heights. If this could be achieved in a manner that allows nominal loads be supported at lower contact fractions this would reduce the problem of high friction coefficients being predicted at lower nominal loadings. Ideally, an experimentally accurate static contact model for the contact fraction-loading for rough surfaces would be produced and extended to include hysteresis during sliding motion. Alternative damping models to Voigt-Kelvin could also be implemented to reduce the excessive energy dissipation at higher frequencies.

The sinusoid experiments suggest standard quasi-steady-state friction modelling to have

limitations for predicting friction during varying speed. In order to produce accurate friction predictions throughout a load cycle involving elevated friction levels it would be necessary to include transient effects from the velocity history. This would be required for a comprehensive transient friction simulation or empirical lookup table technique.

Alternative designs for more practical active sealing systems could be developed to follow on from the initial experiments. It would be preferable to test new active sealing systems under conditions commonly experienced by seal-less actuators in order to empirically demonstrate the possible advantages of active sealing technology in specific applications. A detailed analysis of the friction-leakage trade-off could be carried out experimentally to determine the potential benefits.

References

[1] S. Habibi, R. Burton, and E. Sampson. High precision hydrostatic actuation systems for micro- and nanomanipulation of heavy loads. *Journal of Dynamic Systems, Measurement, and Control*, 128(4):778–787, 2006.

[2] S. Habibi and A. A. Goldenberg. Design and analysis of a new symmetrical linear actuator for hydraulic and pneumatic systems. *Transactions of the Canadian Society for Mechanical Engineering*, 23(3):377–396, 1999.

[3] T. Hunt and N. Vaughan. *The hydraulic handbook*. Elsevier Advanced Technology, Oxford, 9 edition, 1997.

[4] B. S. Nau. A historical review of studies of polymeric seals in reciprocating hydraulic systems. *Proceedings of the Institution of Mechanical Engineers Part J, Journal of Engineering Tribology*, 213(3):215–226, 1999.

[5] Y. Kawahara, Y. Ohtake, and H. Hirabayashi. Oil film formation of oil seals for reciprocating motion. Proceedings of the Ninth BHRA International Conference on Fluid Sealing, Noordwijkerhout, Netherlands, 1981. Elsevier Applied Science Publishers.

[6] R. Rana, R. Sayles, G. Nikas, and I. Jalisi. An experimental technique for investigating the sealing principles of reciprocating elastomeric seals for use in linear hydraulic actuator assemblies. Proceedings of the Second World Tribology Congress, Vienna, Austria, 2001.

[7] M. Kaneta, T. Takeshima, S. Togami, H. Nishikawa, and Y. Kanzaki. Stribeck curve in reciprocating seals. 18th International Conference of Fluid Sealing, Antwerp, Belgium, 2005. BHR Group Limited.

[8] M. Kaneta, H. Todoroki, H. Nishikawa, Y. Kanzaki, and Y. Kawahara. Tribology of flexible seals for reciprocating motion. *ASME Journal of Tribology*, 122(4):787–795, 2000.

[9] T. Papatheodorou. Influence of hard chrome plated rod surface treatments on sealing behaviour of hydraulic rod seals. *Sealing Technology April 2005*, pages 5–10, 2005.

[10] G. J. Field and B. S. Nau. Film thickness and friction measurements during reciprocation of a rectangular section rubber seal ring. Proceedings of the Sixth BHRA International Conference on Fluid Sealing, pages 45–56, Munich, Germany, 1973. BHRA. paper C5.

[11] G. J. Field and B. S. Nau. The effects of design parameters on the lubrication of reciprocating rubber seals. Proceedings of the Seventh BHRA International Conference on Fluid Sealing, Cranfield, Bedfordshire, 1975. BHRA. paper C1.

[12] D. B. Wassink, V. G. Lenss, J. A. Levitt, and K. C. Ludema. Physically based modeling of reciprocating lip seal friction. *ASME Journal of Tribology*, 123(2):404–412, 2001.

[13] K. K. Chang and J. S. Woo. Analysis of contact force and thermal behaviour of lip seals. *Tribology International*, 30(2):113–119, 1997.

[14] H. L. Johannesson. Oil leakage and friction forces of reciprocating o-ring seals considering cavitation. *Journal of Lubrication Technology Transactions of the ASME*, 105(2):288–296, 1983.

[15] C. M. Calvert, M. Tirovic, and T. Stolarski. Design and development of an elastomer-based pneumatic seal using finite element analysis. *Proceedings of the Institution of Mechanical Engineers Part J, Journal of Engineering Tribology*, 216(3):127–138, 2002.

[16] J. A. Greenwood and J. B. P. Williamson. Contact of nominally flat surfaces. *Proceedings of Royal Society of London, Ser. A*, 295:300–319, 1966.

[17] R. F. Salant, N. Maser, and B. Yang. Numerical model of a reciprocating hydraulic rod seal. *ASME Journal of Tribology*, 129(1):91–97, 2007.

[18] J. A. Greenwood and J. J. Wu. Surface roughness and contact: an apology. *Meccanica*, 36(6):617–630, 2002.

[19] M. Ciavarella, V. Delfine, and G. Demelio. A re-vitalized greenwood and williamson model of elastic contact between fractal surfaces. *Journal of the Mechanics and Physics of Solids*, 54(12):2569–2591, 2006.

[20] P. Thirion. Les coefficients d'adherence du caouchouc. *Revue Generale Caoutchouc*, 23:101–106, 1946.

[21] D. F. Denny. The influence of load and surface roughness on the friction of rubber-like materials. *Proceeding of the Physical Society- Section B*, 66(9):721–727, 1953.

[22] W. R. Chang, L. Etsion, and D. B. Bogy. An elastic-plastic model for the contact of rough surfaces. *ASME Journal of Tribology*, 109(2):257–263, 1987.

[23] M. Pullen and J. B. P. Williamson. On the plastic contact of rough surfaces. *Proceedings of Royal Society of London, Ser. A*, 327:159–173, 1972.

[24] K. Komvopoulos. Elastic finite element analysis of multi-asperity contacts. *ASME Journal of Tribology*, 114(4):823–831, 1992.

[25] H. Eid and G. G. Adams. An elastic-plastic finite element analysis of interacting asperities in contact with a rigid flat. *Journal of Physics D: Applied Physics*, 40(23):7432–7439, 2007.

[26] F. Hirano. Dynamic inverse problems in hydrodynamic lubrication. Proceedings of the Third BHRA International Conference on Fluid Sealing, Cambridge, UK, 1967. BHRA. paper F1.

[27] F. Hirano and M. Kaneta. Theoretical investigation of friction and sealing characteristics of flexible seals for reciprocating motion. Proceedings of the Fifth BHRA International Conference on Fluid Sealing, Warwick, UK, 1971. BHRA. paper G2.

[28] C. J. Hooke and J. P. O'Donoghue. Elastohydrodynamic lubrication of soft highly deformed contacts. *Proceedings of the Institution of Mechanical Engineers Part C, Mechanical Engineering Sciences*, 14(1):34–48, 1972.

[29] L. E. C. Ruskell. Rapidly converging theoretical solution of the elastohydrodynamic problem for rectangular rubber seals. *Proceedings of the Institution of Mechanical Engineers. Part C, Journal of Mechanical Engineering Science*, 22(1):9–16, 1980.

[30] G. K. Nikas. Elastohydrodynamics and mechanics of rectangular elastomeric seals for reciprocating piston rings. *ASME Journal of Tribology*, 125:60–69, 2003.

[31] G. K. Nikas and R. S. Sayles. Study of leakage and friction of flexible seals for steady motion via a numerical approximation method. *Tribology International*, 39(9):921–936, 2006.

[32] G. K. Nikas. Theoretical study of solid back-up rings for elastomeric seals in hydraulic actuators. *Tribology International*, 37:689–699, 2004.

[33] G. K. Nikas and R. S. Sayles. Modelling and optimization of composite rectangular reciprocating seals. *Proceedings of the Institution of Mechanical Engineers Part J, Journal of engineering tribology*, 220(4):395–412, 2006.

[34] K. L. Johnson, J. A. Greenwood, and S. Y. Poon. Simple theory of asperity contact in elastohydrodynamic lubrication. *Wear*, 19(1):91–108, 1972.

[35] A. Yamaguchi and H. Matsuoka. A mixed lubrication model applicable to bearing/seal parts of hydraulic equipment. *ASME Journal of Tribology*, 114(1):116–121, 1992.

[36] B. Yang and R. F. Salant. A numerical model of a reciprocating rod seal with a secondary lip. *Tribology Transactions*, 51(2):119–127, 2008.

[37] B. Yang and R. F. Salant. Numerical model of a tandem reciprocating hydraulic rod seal. *ASME Journal of Tribology*, 130(3):032201, 2008.

[38] A. Thatte and R. F. Salant. Transient ehl analysis of an elastomeric hydraulic seal. *Tribology International*, 42(10):1424–1432, 2009.

[39] J. E. Archard and E. W. Cowking. Elastohydrodynamic lubrication at point contacts. volume 180 of *Symposium on Elastohydrodynamic Lubrication Proceedings of the Institution of Mechanical Engineers*, pages 47–56, Leeds, UK, 1965. Institution of Mechanical Engineers.

[40] A. N. Grubin. *Book No. 30*. DSIR London Translation No. 337, 1949.

[41] H. P. Evans and R. W. Snidle. The elastohydrodynamic lubrication of point contacts of heavy loads. *Proceedings of Royal Society of London, Ser. A*, 382:183–189, 1982.

[42] C. H. Venner. *Multilevel solution of the elastohydrodynamic line and point contact problems*. PhD thesis, Univeristy of Twente, Netherlands, 1988.

[43] A. G. Tangena and P. J. M. Wijhoven. Finite element calculations on the influence of surface roughness on friction. *Wear*, 103:345–354, 1985.

[44] Q. V. Bui and J. P. Ponthot. Estimation of rubber sliding friction from asperity interaction modeling. *Wear*, 252(1):150–160, 2002.

[45] N. Purushothaman and I. D. Moore. Hysteresis sliding friction of rubber- finite element analysis. *Journal of Engineering Mechanics*, 116(1):217–232, 1990.

[46] N. Purushothaman. *Numerical analysis of sliding of rubber over triangular and rectangular grooved asperities- tyre pavement interaction*. PhD thesis, University of Newcastle, Newcastle, Australia, 1987.

[47] W. O. Yandell, P. Tanneranonon, and V. G. Zankin. Prediction of tireroad friction from surface texture and tread rubber properties. Technical report, American Society for Testing and Materials, 1982. ASTM Special Technical Publication 793.

[48] R. A. Schapery. Analytical models for the deformation and adhesion components of rubber friction. *Tire Science and Technology*, 6(1):3–47, 1978.

[49] R. A. Schapery. Analysis of rubber friction by the fast fourier transform. *Tire Science and Technology*, 6(2):89–113, 1978.

[50] A. J. Heilala and A. Kangasniemi. Adjustment and control of a mechanical seal against dry running and severe wear. Proceedings of the Eleventh International Conference on Fluid Sealing, pages 548–575, Canes, France, 1987. Elsevier Applied Science Publishers.

[51] R. F. Salant, A. L. Miller, P. L. Kay, J. Kozlowski, W. E. Key, and M. C. Algrain. Development of an electronically controlled mechanical seal. 11th International Conference on Fluid Sealing, pages 576–595, Cannes, France, 1987. Elsevier Applied Science Publishers.

[52] P. Wolff and R. F. Salant. Electronically controlled mechanical face seal for aerospace applications-part ii: transient tests. *Tribology Transactions*, 38(1):51–56, 1995.

[53] J. Dayan, M. Zou, and I. Green. Contact elimination in mechanical face seals using active control. *IEEE Transactions on Control Systems Technology*, 10(3):344–354, 2002.

[54] I. V. Kragelsky and V. V. Alisin. *Tribology- lubrication, friction and wear*. Professional Engineering Publications Ltd, London, UK, 2001.

[55] Parker Hannifin. *inPHorm European Packing*, 1999.

[56] Parker Hannifin. *Parker o-ring handbook*, 2007. Catalog ORD 5700.

[57] D. F. Moore. *Principles and applications of tribology*. Pergamon Press Ltd, Oxford, UK, 1975.

[58] F. L. Roth, R. L. Driscoll, and W. L. Holt. Frictional properties of rubber. *Rubber Chemistry and Technology*, 16(1):155–177, 1943.

[59] K. A. Grosch. The relation between the friction and visco-elastic properties of rubber. *Proceedings of Royal Society of London, Ser. A*, 274:21–39, 1963.

[60] C. M. Ettles and C. E. Hardie. Friction of some polymers and elastomers at high values of pressure x velocity. *ASME Journal of Tribology*, 110(4):678–684, 1988.

[61] RDP Electronics Ltd, Wolverhampton, UK. *Model 31 tension-compression load cell*. RDP catalogue.

[62] Kulite, Leonia, New Jersey, USA. *ETM-375*. Kulite catalogue.

[63] G. K. Nikas and R. S. Sayles. Nonlinear elasticity of rectangular elastomeric seals and its effect on elastohydrodynamic numerical analysis. *Tribology International*, 37(8):651–660, 2004.

[64] Parker Hannifin. *Polyurethanes- PDF ultrathan sealing compounds.*

[65] D. Dowson and P. D. Swales. Development of elastohydrodynamic conditions in a reciprocating seal. Proceedings of the Fourth International Conference on Fluid Sealing, pages 2–10, Philadelphia, PA, USA, 1969.

[66] E. Prati and A. Stozzi. Study of the elastohydrodynamic problem in rectangular elastomeric seals. *Journal of Tribology Transactions of the ASME*, 106(4):505–512, 1984.

[67] A. R. Lansdown. *Lubrication and lubricant selection a practical guide.* Professional Engineering Publications Limited, London and Bury St Edmunds, UK, 3 edition, 2004.

[68] K. L. Johnson. *Contact Mechanics.* Cambridge University Press, Cambridge, UK, 1987.

[69] R. S. Sayles and T. R. Thomas. Surface topography as a non stationary random process. *Nature*, 271:431–434, 1971.

[70] V. K. Jain. Surface topography changes in polymer-metal sliding: Ii. *Journal of Lubrication Technology Transactions of the ASME*, 105(4):526–533, 1983.

[71] J. L. McCool. Relating profile instrument measurement to the functional performance of rough surfaces. *Journal of Tribology Transactions of the ASME*, 109(2):264–270, 1987.

[72] N. Maser. Numerical model of a reciprocating rod seal, including surface roughness and mixed lubrication. Master's thesis, Georgia Tech, 2006.

[73] T. R. Thomas. *Rough surfaces.* Longman Group Ltd, London, UK, 1982.

[74] A. H. Uppal and S. D. Probert. Mean separation and real contact area between surfaces pressed together under high static loads. *Wear*, 23(1):39–53, 1973.

[75] Y. Zhao and L. Chang. A model of asperity interactions in elastic-plastic contact of rough surfaces. *ASME Journal of Tribology*, 123(4):857–864, 2001.

[76] Y. Zhao, D. M. Maietta, and L. Chang. An asperity microcontact model incorporating the transition from elastic deformation to fully plastic flow. *ASME Journal of Tribology*, 122(1):86–93, 2000.

[77] P. Sahoo. Asperity interaction in elastic-plastic contact of rough surfaces in presence of adhesion. *Journal of Physics D: Applied Physics*, 38(16):2841–2847, 2005.

[78] P. Sahoo. Asperity interaction in adhesive contact of metallic rough surfaces. *Journal of Physics D: Applied Physics*, 38(22):4096–4103, 2005.

[79] P. Sahoo. Adhesive friction for elastic-plastic contacting rough surfaces considering asperity interaction. *Journal of Physics D: Applied Physics*, 39(13):2809–2818, 2006.

[80] A. Cameron. *Basic lubrication theory*. Ellis Horwood Ltd, Chichester, UK, 3 edition, 1981.

[81] A. Cameron. *The principles of lubrication*. Longmans, London, UK, 1966.

[82] H. Okamura. A contribution to the numerical analysis of isothermal elastohydrodynamic lubrication. Proceedings of the Ninth Leeds-Lyon Symposium on Tribology, pages 313–320, Leeds, UK, 1982.

[83] K. P. Oh. The numerical solution of dynamically loaded elastohydrodynamic contact as a nonlinear complementarity problem. *ASME Journal of Tribology*, 106(1):88–95, 1984.

[84] B. J. Hamrock. *Fundamentals of fluid film lubrication*. Marcel Dekker, New York, NY, USA, 3 edition, 2004.

[85] R. F. Salant, N. Maser, and B. Yang. Numerical model of a reciprocating hydraulic rod seal. Proceedings of IJTC 2006 STLE/ASME International Joint Tribology Conference, San Antonio, Texas, USA, 2006. ASME.

[86] N. Patir and H. S. Cheng. An average flow model for determining effects of three-dimensional roughness on partial hydrodynamic lubrication. *Journal of Lubrication Technology Transactions of the ASME*, 100:12–17, 1978.

[87] N. Patir and H. S. Cheng. Application of average flow model to lubrication between rough sliding surfaces. *Journal of Lubrication Technology Transactions of the ASME*, 101:220–229, 1979.

[88] S. S. R. Harp and R. F. Salant. An average flow model of rough surface lubrication. *ASME Journal of Tribology*, 123(1):134–143, 2001.

[89] H. G. Elrod. A cavitation algorithm. *ASME Journal of Tribology*, 103:350–354, 1981.

[90] E. Ehabe, F. Bonfils, C. Aymard, A. K. Akinlabi, and J. Sainte Beuve. Modelling of mooney viscosity relaxation in natural rubber. *Polymer Testing*, 24:620–627, 2005.

[91] S. S. Yelma, B. A. Miller, and R. G. Landers. Clearance regulation of mechanical gas face seals: part ii - analysis and control. *Tribology Transactions*, 49(3):373–386, 2006.

[92] I. R. Clemitson. *Castable polyurethane elastomers*. CRC Press, Boca Raton, Florida, US, 2008.

[93] D. Dowson. Elastohydrodynamic and microelastohydrodynamic lubrication. *Wear*, 190:125–138, 1995.

[94] H. S. Cheng. On aspects of microelastohydrodynamic lubrication. Proceedings of the Fourth Leeds-Lyon Symposium on Tribology, Lyon, France, 1977. paper III.

[95] H. P. Evans and R. W. Snidle. The isothermal elastohydrodynamic lubrication of spheres. *Journal of Lubrication Technology Transactions of the ASME*, 103(4):547–557, 1981.

[96] C. H. Venner, W. E. Napel, and R. Bosma. Advanced multilevel solutions of the elastohydrodynamic line contact problem. *ASME Journal of Tribology*, 112(3):426–432, 1990.

[97] J. A. Greenwood. Film thickness in circular elastohydrodynamic contacts. *Proceedings of the Institution of Mechanical Engineers Part C, Mechanical Engineering Sciences*, 202(1):11–17, 1988.

[98] Y. H. Wijnant. *Contact dynamics in the field of elastohydrodynamic lubrication.* PhD thesis, Univeristy of Twente, 1998.

Appendix A

Modelling and simulation of seal flexing

A.1 Overview

Hydraulic rod seals are expected to have a non-zero axial compliance that results in a change in axial location of the point of contact between the rod and seal when an axial force is applied to the seal surface. The friction force between the rod and seal acts to deflect the seal in the direction of rod motion. For constant velocity motion the seal is expected to eventually reach an equilibrium deflection, hence seal flexibility is not expected to be particularly important for steady-state constant velocity conditions. If the stroke length is limited to within the order of the maximum axial deflection of the seal, the regions of varying seal deflection would be expected to be clearly visible in the friction traces of the measured data. For sufficiently short strokes it may be expected for the rod and seal to never lose contact as the static friction required to initiate motion between the rod and seal is never overcome and the rod rocks on the seal. Shorter strokes are normally associated with higher frequency reciprocating motion where the stroke length reduces to maintain a constant maximum speed or force amplitude limitation. Seal flexibility is expected to become important for reciprocating motion at relatively high frequencies.

Several analytical approaches are available to explain the behaviour of the friction experienced by a hydraulic rod during motion involving seal compliance. Analytical models can readily be used for rocking motion where there is no relative motion between the rod and seal surfaces. The seal undergoing flexing motion has been approximated as a mass-spring-damper and the expected friction profiles experienced by the rod obtained. Numerical simulations have also been carried out using this mass-spring-damper model while allowing relative motion between the rod and seal surfaces. These simulations have been carried out to give an indication of the transition region between rocking motion and longer strokes where

seal flexibility is less significant.

A.2 Simple harmonic motion analysis

For low rod displacement amplitudes there is expected to be no relative motion between the rod and seal as the friction force does not become sufficient to overcome the static friction. Under these conditions deflection of the seal is equivalent to the displacement of the rod. For sinusoidal rod motion the deflection of the seal can be expressed as a mathematical function and analytical equations can be produced for the friction force acting on the seal. The seal has been modelled as a mass-spring-damper with the flexing seal assumed to have a particular stiffness, inertia and viscous damping. Mass-spring-damper models are used extensively in engineering and represent a standard approach to dynamic analysis. There are several possible approaches to modelling how the stiffness and inertia of the flexing seal affect the force experienced by the rod.

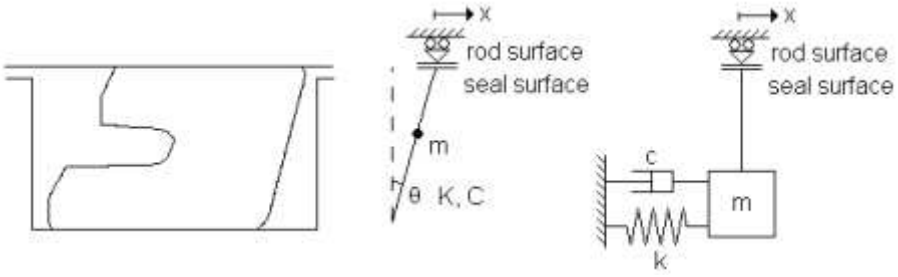

Figure A-1: Seal flexibility for model for seal flexing as a rigid body

One possible approach for the motion against a flexing seal is a rigid body vibration model. In this method the seal is modelled as flexing about a particular location on the seal body with no significant variation in the geometry of the region in motion. With this model the additional strain in the seal associated with the axial deflection occurs at the pivot location where the resulting material stresses provide the effective stiffness and damping. Figure A-1 shows this rigid body model of the seal flexing about a pivot point and its equivalent model with Cartesian coordinates. Using the equivalent Cartesian model simplifies the problem. The stiffness and damping are associated with the viscoelastic properties of the material and its capacity to store and dissipate elastic potential energy.

An alternative vibration model for the rod and seal is to allow compliance between the effective mass of the seal and the location where the excitation motion is applied. With this approach there is a second degree of freedom within the system associated with the displacement of the effective centre of mass. Figure A-2 shows a possible model allowing this type of compliance. A conventional approach to forced vibration with exciting motion is to have the excitation cause mass displacement as in figure A-2 without the additional stiffness

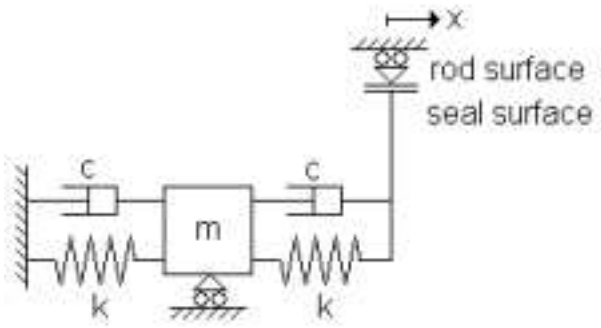

Figure A-2: Alternative seal flexibility for model for seal flexing as a particle

between the mass and the fixed support. The current problem requires this constraint as the seal is assumed to deflect from a fixed location. Allowing a compliance between the seal surface and centre of mass increases the complexity of the problem by requiring an additional parameter for the stiffness between the surface and centre of mass. It is difficult to determine a suitable relationship between the two stiffnesses in figure A-2 as the geometry variation during flexing motion is difficult to predict.

Figure A-3: Possible variance in centre of mass of seal during flexing motion

It is desirable to determine which model of the seal compliance is more suitable for modelling the friction experienced by the rod. The importance of the compliance between the seal surface and effective centre of mass is dependent on how the deformation profile of the seal varies with frequency. For a particular displacement amplitude if the seal deformation profile does not vary with frequency, the system can be approximated by the model in figure A-1 where the amplitude of the effective mass motion is fixed by the excitation amplitude. It is also possible that the seal may maintain contact with the rod with significant variation in the motion of the effective centre of mass between different frequencies. A visualisation of how compliance between the excitation motion and effective seal motion could take place is shown in figure A-3. In this illustration the displacement of the seal becomes more localised near the rod surface at higher frequencies with a corresponding lower displacement in the centre of mass. Which compliance model would be the more appropriate is dependent on the tendency of the seal to deform differently under varying dynamic conditions. The current

study assumes the seal to axially flex on its housing in a similar manner at high frequencies as at lower frequencies and static deflection cases.

The force acting on the seal Q (of equal magnitude and opposite direction to the friction force exerted on the rod) is given by

$$Q = m\ddot{x} + c\dot{x} + kx \tag{A.1}$$

For sinusoidal rod motion

$$Q = a_1\left(k - m\omega^2\right)\sin\omega t + c\omega\cos\omega t \tag{A.2}$$

Assuming the steady-state friction profile to be sinusoidal with amplitude Q_0 and phase lag ψ, equation (A.2) becomes

$$Q_0\sin\left(\omega t - \phi\right) = a_1\left(k - m\omega^2\right)\sin\omega t + c\omega\cos\omega t \tag{A.3}$$

From trigonometric identities, the coefficients in equation (A.3) are

$$Q_0 = \sqrt{(k - m\omega^2)^2 + (c\omega)^2} \tag{A.4}$$

and

$$\psi = \arctan\left(\frac{-c\omega}{k - m\omega^2}\right) \tag{A.5}$$

The coefficients for equation (A.3) can also be expressed in terms of the dimensionless parameters natural frequency $\omega_n = \sqrt{\frac{k}{m}}$ and damping coefficient $\zeta = \frac{c}{2m\omega_n}$ as

$$\frac{Q_0}{m} = \omega_n^2\sqrt{\left(1 - \left(\frac{\omega}{\omega_n}\right)\right)^2 + \left(2\zeta\frac{\omega}{\omega_n}\right)^2} \tag{A.6}$$

and

$$\psi = \arctan\left(\frac{-2\zeta\frac{\omega}{\omega_n}}{1 - \left(\frac{\omega}{\omega_n}\right)^2}\right) \tag{A.7}$$

A.2.1 Estimation of parameter values for modelling seal rocking motion

Suitable values of effective mass, stiffness and damping are required for the seal compliance model in order to simulate an accurate representation of the seal behaviour. These parameters are estimated by considering a lumped parameter model for the shearing of the seal. The seal is assumed to deflect under the effect of the axial frictional shear stress as shown in figure A-

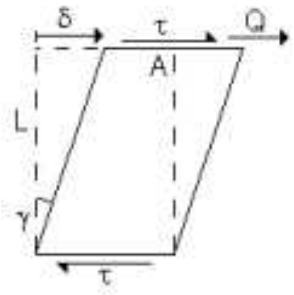

Figure A-4: Simple shear strain model of seal flexibility

4. The length L_y associated with the effective thickness of the region of the seal undergoing flexing motion could be dependent on the type of seal deflection taking place. One possibility is for the seal to deflect between the rod and the outer bore of the housing. For this case the effective length is known to be 4 mm from the geometry of the seal groove in the housing block. Another possibility is for the seal to deflect between the rod and inner bore of the housing which would give a much lower effective L_y length of 0.3 mm. In the latter case the deflecting region within the seal would be limited to the region near the surface in contact with the rod.

It is difficult to deduce which of the two possible values of effective thickness L_y is likely to be more accurate. One possibility is for the seal to have different effective axial stiffness between instroke and outstroke. During outstroke the seal may be expected to be partially extruded through the narrow clearance between the rod and inner bore of the housing. In this case the lower L_y length of 0.3 mm may be expected to be dominant. For instroke motion the shear stress would act in the opposite direction and would be expected to deflect the seal surface towards the fluid side. This deflection would not be constrained by the inner bore of the housing and may be expected to correspond to the longer effective L_y value of 4 mm. It is also possible that, for repeating cyclic motion, the seal may settle towards a non-zero mean deflection that may allow one of the two types of deflection to dominate throughout the cycle. Cyclic motion where there is some degree of sliding between the rod and seal may be expected to favour an equilibrium position biased towards the lower stiffness. This is because the limiting friction is expected to occur at a higher deflection against the lower stiffness than for the higher stiffness. Therefore the lower stiffness would be expected to dominate for the majority of the displacements during the load cycle. The current investigation assumes an effective L_y length of 4 mm corresponding with the lower value of axial stiffness.

The effective axial length of the seal L_x was taken as 5.7 mm from the maximum axial dimension of the seal quoted in the relevant component catalogue [55]. This introduces some inaccuracy as contact between the rod and seal was not expected to occur over the full maximum axial length. This inaccuracy is expected to result in an over-prediction of

friction for any particular axial deflection by increasing the area of contact over which the frictional shear stress τ acts. There is also the complication that the U-cup geometry of the seal differs from a simple rectangular section, having a reduced axial length at the radial location between the two seal lips. Therefore the bulk parameter model may have a higher axial stiffness than would occur with the actual seal geometry. An effective diameter D of 20 mm was assumed for the cross section as the midpoint of the rod diameter of 16 mm and the outer bore of the seal groove (24 mm).

An elastic modulus E of 12.1 MPa was assumed for the seal material in common with the other areas of the current investigation. The shear modulus G is calculated from

$$G = \frac{E}{2\left(1+\nu\right)} \tag{A.8}$$

Where the Poisson ratio ν was taken as 0.49 in accordance with a near-incompressible material. This produces a shear modulus of 4.06 MPa for the polyurethane seal material.

It is possible to obtain the effective stiffness of the model from the selected dimensions and elastic properties of the seal geometry. This is carried out by considering the standard mechanics of the bulk parameter material element shown in figure A-4. The seal axial stiffness k is defined as the stiffness coefficient between the total frictional shear force Q and seal axial deflection x according to

$$Q = kx \tag{A.9}$$

The shear force Q is related to the shear stress τ and the area A of the seal in contact with the rod by

$$\begin{aligned} \tau &= \frac{Q}{A} \\ \tau &= \frac{Q}{L_x D} \end{aligned} \tag{A.10}$$

The Hooke's Law relationship for shear stress is

$$G = \frac{\tau}{\gamma} \tag{A.11}$$

For the geometry shown in figure A-4 the shear strain γ and axial deflection x are related by

$$\gamma = \frac{x}{L_y} \tag{A.12}$$

Combining equations (A.9)-(A.12) produces the relationship for axial stiffness

$$k = \frac{GL_xD}{L_y} \tag{A.13}$$

Substituting the estimated dimensions and shear modulus into equation (A.13) gives an estimation for the seal axial stiffness of 115.7 N/mm.

The effective mass of the element is given by

$$m = L_xL_yD\rho \tag{A.14}$$

With the seal dimensions previously inferred and assuming a density of the seal material of 1.4×10^3 kg/m^3 an effective mass can be calculated as 0.638×10^{-3} kg.

A.3 Natural frequency associated with seal flexibility

It is possible to calculate the natural frequency of the element representing the flexible seal from its mass and stiffness. According to the standard $\omega_n = \sqrt{\frac{k}{m}}$ relationship the seal is predicted to have a natural frequency of 13.5×10^3 rad/s (2.14 kHz). This value of natural frequency is significantly greater than the normal operating frequency range for hydraulic actuation systems of approximately 100 Hz or lower. From this analysis it would not be expected for inertia effects to become significant over the range of actuation frequencies investigated. Therefore it was necessary to investigate only frequencies significantly lower than the natural frequency in the mixed sticking-sliding model produced in section A.5 for experimental comparison.

A.4 Derivation of damping parameters for seal flexibility

It is relatively difficult to infer a suitable damping coefficient for the seal flexibility model. The approach taken is to assume a particular damping ratio ζ and calculate the corresponding damping coefficient c. The relationship between the dimensionless parameters ω_n and ζ and the damping coefficient c can be obtained by equating the coefficients in the force balance equation (equation (A.1)) with its dimensionless form

$$\frac{Q_0}{m}\sin\omega t = \ddot{x} + 2\zeta\omega_n\dot{x} + \omega_n^2x \tag{A.15}$$

Equating the coefficients of $\dot{x}$ gives the damping coefficient as

$$\frac{c}{m} = 2\zeta\omega_n \tag{A.16}$$

It is possible to calculate the damping coefficient from equation (A.16) if the damping ratio ζ is known. A value for ζ of 0.05 was proposed as other authorities have suggested

this to be typical for polyurethanes [92]. This damping ratio corresponds with a c damping coefficient of 0.859 Nm/s. There was thought to be significant uncertainty in the damping coefficient assumed as material damping properties are not frequently quoted in literature. In order to take account of the uncertainty in damping level it is necessary to carry out simulations for a range of different values of ζ.

A.5 Simulation of friction with mixed rocking and sliding on seal

A.5.1 Simulation description

A numerical simulation was produced in AMESim 8.1.0 to investigate the friction behaviour under operating conditions where sliding motion takes place between the rod and seal while seal flexibility remains important. The seal was modelled as a mass-spring-damper as shown in figure A-1 with a single degree of freedom in the axial direction of the rod. Values for system mass, stiffness and damping were used as calculated in section A.2.1. Sliding motion was allowed to take place between the rod and seal surfaces where the limiting maximum value of friction was reached. Friction at the rod-seal interface was modelled with a dry Coulomb friction model. The static friction coefficient was assumed to be equivalent to the dynamic friction coefficient. A maximum value of friction was set at 150 N in accordance with the approximate friction level known to be experienced in the current seal type at high sealed pressures.

Sinusoidal excitation was applied at the rod surface and the resulting simulated force acting on the rod over a single cycle was obtained. The force variation with time was recorded for a single cycle carried out after steady-state conditions had been reached. A total of ten cycles were carried out to reach steady-state conditions for the oscillatory motion. An excitation frequency of 10 Hz was used for all simulations while the amplitude of the motion was varied. This frequency was thought to be appropriate for the simulations as all the experimental frequencies were significantly below the theoretical natural frequency and varying the simulated frequency over the experimental range was not expected to significantly affect the simulated friction characteristics. For each damping ratio ζ a range of different excitation amplitudes were used in order to capture the transition between rocking and sliding motion. With no damping the limiting friction force (150 N) was expected to be exceeded for an excitation amplitudes in excess of 1.30 mm. Displacement amplitudes of 1, 2, 5, 10 and 20 mm were simulated accordingly. This range of excitation amplitudes was used for damping ratios ζ of 0, 0.05, 0.3, 1, 2 and 3, representing a wide range of possible damping ratios to account for the uncertainty in this parameter.

The Coulomb friction model was simulated using an AMESim FRT-011-1 component

with a discrete transition between static and dynamic friction within the integrator. A convergence tolerance (as defined by the AMESim standard integrator) of 10^{-9} was used for all simulations. Each simulation was run for a total of ten cycles and the steady-state results recorded from the final cycle. It was found that the initial transients in the force amplitudes experienced by the rod decayed within ten cycles for the stiffness and damping parameters considered.

A.6 Simulation results for mixed sliding and sticking motion

A.6.1 Comparison with fundamental mass-spring cases

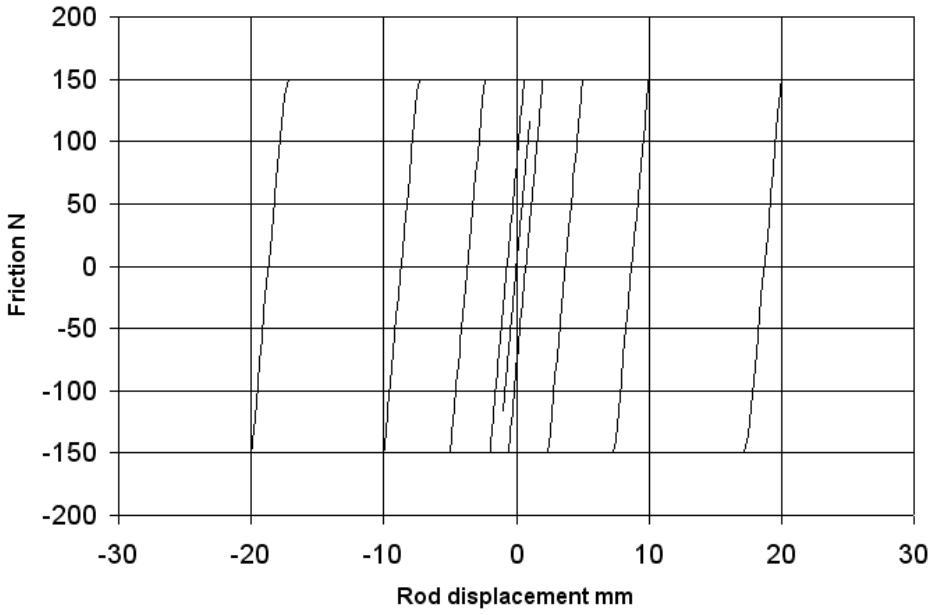

Figure A-5: Simulated friction against rod displacement for sliding mass-spring-damper seal flexibility model, 10 Hz excitation, ζ=0

Figures A-5 to A-8 show the simulated friction behaviour for the seal modelled as a mass-spring-damper with a maximum friction value for three limiting cases; no damping $\zeta = 0$ and high damping $\zeta = 3$. For both damping ratios the friction behaviour for low displacement amplitudes is approximately equivalent to the fundamental cases with no sliding motion. For small displacements there is an approximately proportional relationship between displacement and friction force. Increasing the excitation amplitude within the seal rocking region extends the approximately linear force-displacement relationship over a greater range of displacements. This suggests the damping characteristics of the seal material to be relatively

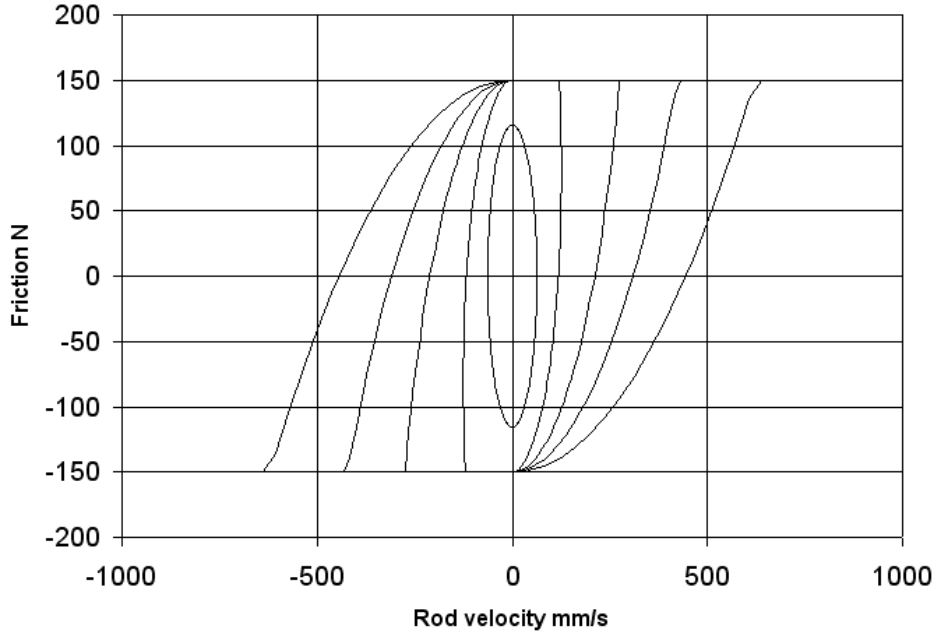

Figure A-6: Simulated friction against rod velocity for sliding mass-spring-damper seal flexibility model, 10 Hz excitation, ζ=0

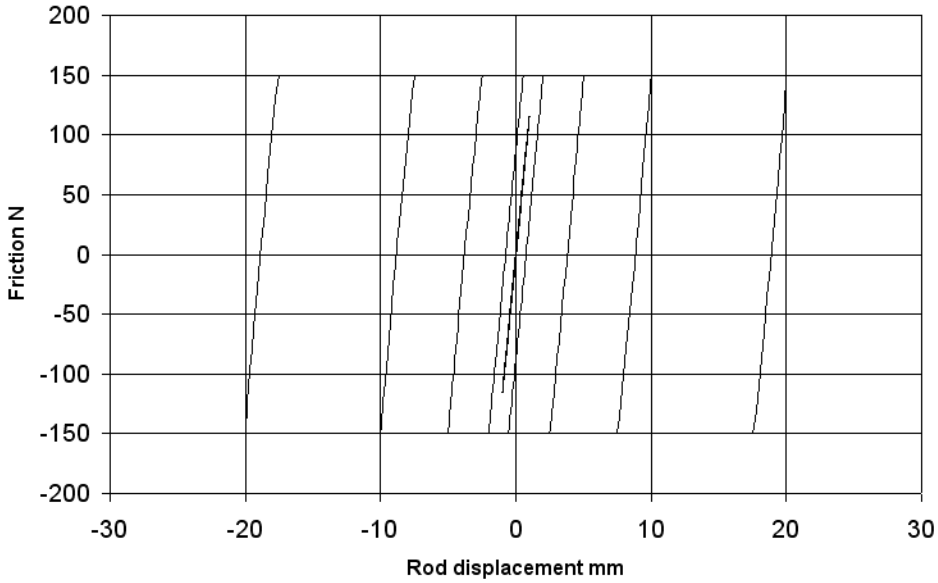

Figure A-7: Simulated friction against rod displacement for sliding mass-spring-damper seal flexibility model, 10 Hz excitation, ζ=3

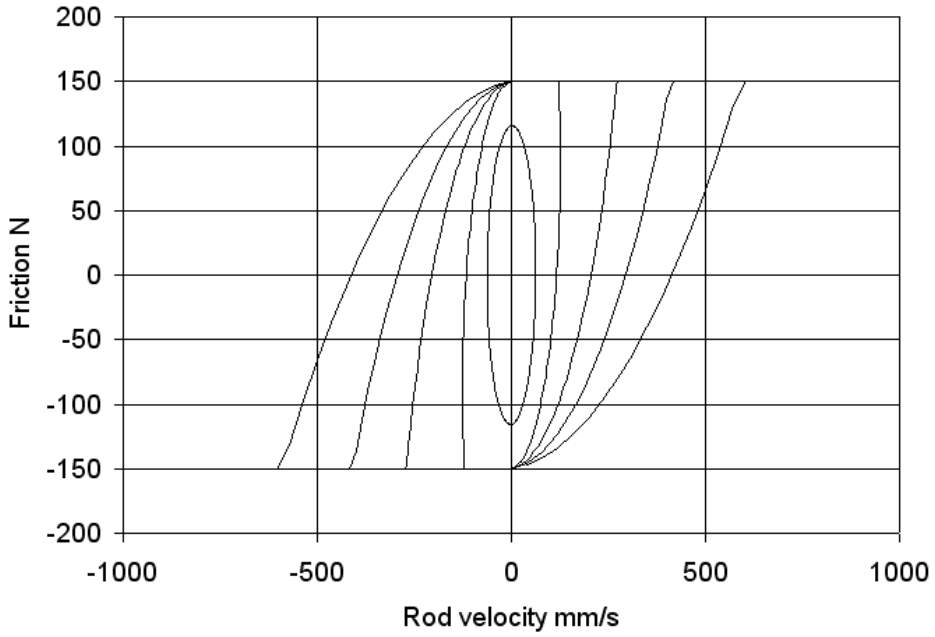

Figure A-8: Simulated friction against rod displacement for sliding mass-spring-damper seal flexibility model, 10 Hz excitation, ζ=3

unimportant for the friction characteristics of the seal rocking motion for most excitation frequencies of practical interest.

Figure A-9 shows an enlargement of the rocking motion region of figure A-7 for the excitation of the mass-spring-damper system with a relatively high ζ damping ratio of 3. This graph indicates a minor hysteresis loop to be present as a result of the damping. The effect of damping is to increase the force magnitude required during extension from the mean point and lower the force magnitude during the following retraction. Even for the case of the over-damped system the energy dissipation enclosed by the hysteresis loop is minimal compared with the overall energy stored in the spring, represented by the area between the force curve and its zero axis. This suggests that significant dissipation and hysteresis loops would not be expected for low-displacement rocking motion providing the high natural frequency calculated is within the correct order of magnitude.

A.6.2 Friction characteristics of transition region

There are consistent friction characteristics near the limits of the stroke for different excitation amplitudes. At the maximum displacements the transition between the positive and negative values of the Coulomb friction constant takes the form of an approximately constant gradient between displacement and force experienced by the rod. This produces an overall force-

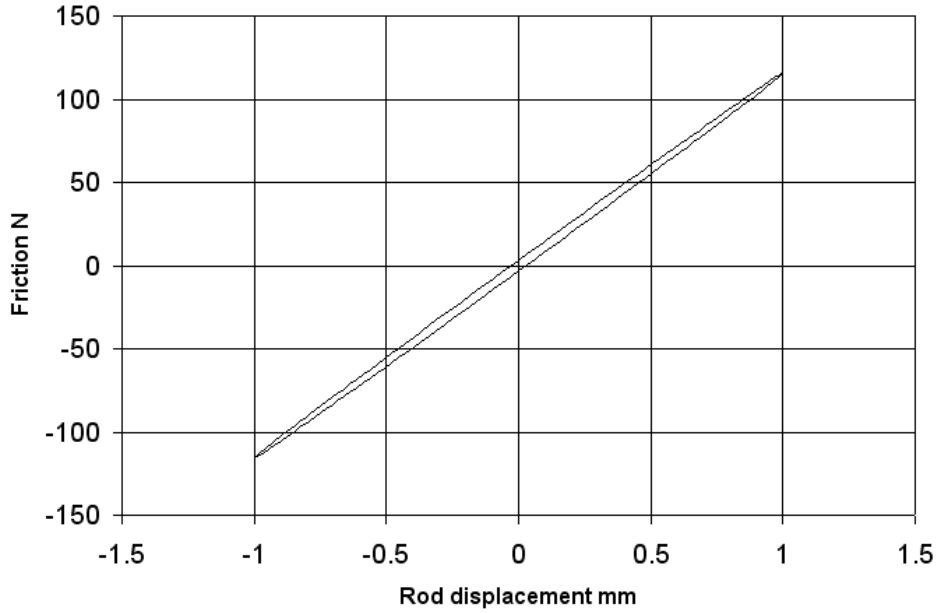

Figure A-9: Detail of rocking motion for mass-spring-damper seal flexibility simulation, 10 Hz excitation, ζ=3

displacement characteristic with a "parallelogram" appearance such as is shown in figure A-5. This region with a linear relationship between force and displacement occurs as a result of the seal deflection reversing direction during a period of sticking contact between the rod and seal surfaces. The gradient of this region remains constant and equivalent to the static stiffness of the seal for different amplitudes of exciting displacement. This constant effective stiffness for different displacement amplitudes and sliding speeds indicates damping not to significantly affect the friction characteristics.

The damping ratio ζ has little effect on the frictional characteristics when there is significant mixed sticking and sliding motion. Comparing the frictional characteristics for no damping and super-critical damping (figures A-5 and A-7 respectively) shows there to have been no significant differences. This suggests the seal material damping properties to be relatively unimportant for all types of motion that are significantly below the system natural frequency.

Appendix B

Point-contact EHL simulation

B.1 Point-contact EHL overview

Point-contact EHL encompasses the lubrication of contacting bodies with two-dimensional surfaces. The standard problem of a contact between a hemisphere and a rigid flat has traditionally been used in the development of point-contact EHL simulations. This standard situation serves as a point of reference for the EHL of contacting bodies with alternative geometries and for demonstrating typical characteristics of EHL theory. The current investigation has considered whether point-contact EHL could be used to explain the measured friction characteristics in seal friction by considering the lubrication of micron-scale contact between surface asperities. Inverse EHL theory over the whole contact length between the rod and seal is shown to predict much lower friction than observed in practice (section 5.1.6). It has been investigated whether the thinner fluid films between contacting asperities may be able to use an EHL mechanism to help explain the higher observed friction levels.

Few previous studies have applied the EHL lubrication of point contact to the micron-scale contact of an asperity. Most previous investigations of micron-scale EHL have been concerned with randomly generated rough surfaces with a large number of surface asperities within the fluid domain. The history of micro-EHL history has been reviewed in publications such as Dowson [93] and Cheng [94]. Dowson concluded the flattening of asperities under micro-EHL effects can maintain EHL conditions with film thicknesses similar to or lower than the average roughness height under unloaded conditions. This finding may be interpreted as supporting the current approach of assuming a fluid film to be maintained between contacting asperities, although EHL conditions would also have to be maintained to the higher loadings experienced in seals if the model is to have a valid physical basis. A recent study of reciprocating seal tribology [30] looked at two-dimensional EHL with a randomly generated two-dimensional roughness profile imposed on the mean surface separation. This latter study used a two-dimensional fluid domain to allow direct contact between the two surfaces without creating

a flow discontinuity that would occur in a one-dimensional model. Direct contact between asperities was allowed for the purposes of film shape determination, although the direct contribution of asperity shear to overall friction was not considered. The current investigation is concerned with the EHL friction occurring at similar contact regions.

A single-asperity EHL based approach presents a deterministic alternative to investigating micro-EHL compared with most previous approaches where stochastic models of a surface profile were considered. This approach enables a relatively simple fluid domain geometry to be used and also allows previous studies of standard contact problems to be used as a basis for methodology and expected results. Micro-EHL represents a method for exploring whether the mechanism of fluid shear stress can be used to explain the high friction levels in hydraulic seals. In principle the method is capable of making predictions concerning friction levels without relying on empirical friction relationships. The parameters required by the model (asperity geometry and fluid viscosity) can be obtained without reference to the measured seal friction levels, allowing a scientific basis for friction prediction. The alternative approach to EHL is boundary lubrication where the fluid film is assumed to break down and friction generate from the shear stress between the absorbed boundary layers at each surface. It is relatively difficult to predict friction levels during boundary lubrication without using empirical measurements of the friction coefficient. Therefore micro-EHL represents a method of friction simulation with a more scientific theoretical basis than the main alternative approach of boundary lubrication.

Most previous studies of EHL point contact have used a parabolic approximation to a hemisphere for the deformable body. The geometry of a parabola approximates to the geometry of a hemisphere for small deflections, although is less accurate where the deflection becomes significant relative to the radius of curvature. This difference in geometries is expected to be less of an issue for typical asperity geometry where only gentle slopes (hence small deflections relative to the radius of curvature) are expected. One reason for using a parabolic body profile has been to allow an analytical solution to the deflection from the well known Hertzian equations.

B.2 Numerical approaches for point contact

In order to obtain a solution to point-contact EHL the two-dimensional Reynolds equation is discretised with a finite difference approximation. The Reynolds equation is solved numerically for a particular film thickness distribution to obtain the corresponding fluid pressure distribution. Additionally, the film thickness distribution that would be produced by the new pressure is calculated from the compliance equations associated with the solid body. The film thickness is adjusted using an iterative method until the fluid pressure distribution from the solution of the two-dimensional Reynolds equation is compatible with the pressure required

to produce the corresponding deformation. There have been problems with numerical stability and convergence throughout the early history of point contact analysis. The standard technique of successive overrelaxation of the film thickness distribution is known not to be convergent, necessitating the use of more sophisticated numerical methods.

One of the first studies to obtain solutions for the EHL of hemispherical contact was carried out by Archard [39] in the 1960s. This investigation used an approximation to the film thickness adapted from Grubin's method in line contact [40]. The variation in film thickness across the contact length was assumed correspond with that occurring under dry contact conditions. The central film thickness on which this variation was imposed was iterated until a pressure distribution from the Reynolds equation solution corresponded with the load required. Use of the modified Grubin method is known to produce reasonable approximations to the average film thickness. However, there is a shortcoming that a contraction in the film thickness normally occurs near the outlet which cannot be modelled with the assumption of a fixed film shape with an variable offset. This approach may provide a reasonable approximation to the minimum film thickness and fluid shear stress, although would not be ideal for accurate solutions.

Evans [95] was later able to obtain solutions for moderate loads without using simple approximations for the film thickness distribution. In a following study [41] the same authors were also able to obtain solutions for high loads using a new solution technique. The numerical method was to use the inverse Reynolds equation over the dry contact region and the finite difference method outside the dry contact region. This technique subsequently became standard for highly loaded point-contact problems. An alternative method was first proposed in [42] where two different finite differencing methods were combined to produce a solution. Gauss-Seidel iteration was used in high pressure regions and Jacobi distributive relaxation outside the high pressure zones. The latter technique of using two finite difference methods is relatively easy to implement compared with combined inverse and finite difference methods. Multigrid techniques were later introduced in [96] to improve computational efficiency.

B.3 Values of dimensionless groups for seal materials

Most previous point-contact EHL studies have used material properties consistent with contact between metals. Typical seal polymer materials have elastic moduli four orders of magnitude lower than steels and other common metals. Simulations carried out in the current investigation have a typical Moes speed parameter L (which incorporates material properties) of 0.04. Greenwood's review of previous point-contact EHL studies [97] indicates L parameters lower than 1 to have seldom been considered. This shows the current investigation to be concerned with dimensionless parameters significantly outside the range of previously published results. It is uncertain whether the relationships obtained from earlier studies could

be reliably extrapolated to the ranges of L parameters in the current study. Therefore it was necessary to carry out simulations with the desired L parameters instead of using results from previous investigations.

B.4 Dimensionless units

Several dimensionless groups have become conventional in point-contact EHL. The dimensionless Dowson material parameter G is important to the current study. This parameter relates the pressure required to deform the solid material to the variability of viscosity with respect to pressure. For a fixed deformation a higher G value is associated with greater variation in fluid viscosity across the contact zone. It has been established that a pressure spike can appear near the outlet in point-contact EHL as a result of viscosity variation. This pressure spike is known not to occur with an isoviscous fluid (with a G parameter of zero). The outlet pressure spike is expected to become less pronounced as the G parameter is reduced. The current investigation is concerned with G parameters significantly lower than most previous studies due to the low elastic modulus of seal elastomers and polymers. The reduced fluid viscosity variation may be expected to reduce the significance of the outlet pressure spike and produce differences in results compared with those reported in previous investigations.

The most commonly used dimensionless speed U parameter has been

$$U = \frac{\eta_0 u \left(1 - \nu^2\right)}{4RE} \tag{B.1}$$

The dimensionless speed and material parameters are usually combined together to produce a single dimensionless group. Most studies have used the Moes lubricant parameter L where

$$L = G(2U)^{\frac{1}{4}} \tag{B.2}$$

Combining the material and relative speed properties into a single dimensionless group is not a preferable option if the effects of varying both speed and material properties are to be studied in detail. For the application of seal tribology little variation is expected in the material parameter compared to the speed parameter. In the current study the lubrication parameter is treated as effectively being a speed parameter.

Dimensionless deflection Δ has special relevance for the current study, having not been considered as physically important in most previous point-contact investigations. For steady-state point-contact it is conventional to specify an overall load and iterate the deflection until a solution with the required load is obtained. This procedure essentially uses deflection as the independent variable with this deflection adjusted until the desired load is obtained. An alternative approach is to specify deflections only and obtain the load with each desired

deflection. In most cases the normal load is considered to be a more useful parameter than the initial interference between the two surfaces. The current study considers the effective properties of a particular distribution of asperity heights and corresponding differences in deflection in section B.7. For this particular analysis it is desirable to express friction and loading in terms of deflection, hence the parameter Δ is used as an independent variable.

For the current investigation loading is non-dimensionalised with respect to the Hertzian contact force. The proportional increase in load relative to the corresponding Hertzian load may be an appropriate dimensionless group as it allows the analysis in section B.7 to be presented similarly to the GW-contact model on which the analysis was based. The Hertzian load is calculated from the deflection using the Hertzian equation for dry contact. The additional load over and above the Hertzian load is required to deflect the body further than in the zero film thickness case to open up a film for the fluid. Dimensionless increase in load compared with the dry Hertzian case was found to produce a more accurate fit to a power law relationship in the simulation results compared with the total dimensionless load.

B.5 Simulation methodology

B.5.1 Point contact methodology overview

B.5.1.1 Overview

To obtain a solution for the coupled sets of equations in point-contact it is necessary to use a relaxation-based iterative scheme. At any particular iteration a new fluid pressure is calculated from the Reynolds equation using the values of film thickness from the previous iteration. The current pressure distribution is then adjusted towards the newly calculated pressures with a suitable relaxation technique. A new film thickness distribution is then calculated from the elasticity equations and the current film thickness values, applying a different relaxation factor. The process is repeated until the magnitude of the pressure changes falls within the specified tolerance.

B.5.1.2 Film thickness calculation

The film thickness distribution is calculated from the numerical evaluation of the equations governing the deformation of the parabolic body. For a two-dimensional, semi-infinite parabolic body the local surface height at point (X, Y) is governed by

$$H(X,Y) = H_0 + \frac{X^2}{2} + \frac{Y^2}{2} + \frac{2}{\pi^2}\int_{-\infty}^{\infty}\int_{-\infty}^{\infty}\frac{P(X',Y')}{\sqrt{(X-X')^2+(Y-Y')^2}}dX'dY' \qquad \text{(B.3)}$$

The integration on the right hand side of equation (B.3) determines the local deflection

under the effect of a pressure distribution applied across the surface. This equation can be represented as a summation series given in [98] as

$$H_{i,j} = H_0 + \frac{X_i^2}{2} + \frac{Y_j^2}{2} + \frac{2}{\pi^2}\sum_{k=0}^{n_x}\sum_{l=0}^{n_y} K_{ikjl}P_{k,l} \tag{B.4}$$

where the discretisation coefficients K_{ikjl} are calculated from

$$\begin{aligned} K_{ikjl} = &|X_p|\text{arcsinh}(\frac{Y_p}{X_p}) + |Y_p|\text{arcsinh}(\frac{X_p}{Y_p}) \\ &-|X_m|\text{arcsinh}(\frac{Y_p}{X_m}) - |Y_p|\text{arcsinh}(\frac{X_m}{Y_p}) \\ &-|X_p|\text{arcsinh}(\frac{Y_m}{X_p}) - |Y_m|\text{arcsinh}(\frac{X_p}{Y_m}) \\ &+|X_m|\text{arcsinh}(\frac{Y_m}{X_m}) + |Y_m|\text{arcsinh}(\frac{X_m}{Y_m}) \end{aligned} \tag{B.5}$$

where

$$X_p = X_i - X_k + \frac{h_x}{2} \tag{B.6}$$

$$X_m = X_i - X_k - \frac{h_x}{2} \tag{B.7}$$

$$Y_p = Y_j - Y_l + \frac{h_y}{2} \tag{B.8}$$

$$Y_m = Y_j - Y_l + \frac{h_y}{2} \tag{B.9}$$

A relaxation factor is applied when updating the film thickness calculated from equation (B.4). In this case simple underrelaxation is used to give the new value of film thickness as

$$H_{new} = H_{old} + K_H(H - H_{old}) \tag{B.10}$$

A relaxation factor K_H of 0.1 was found to be suitable for most cases.

B.5.1.3 Reynolds equation

The behaviour of the fluid across the contact is assumed to be governed by the dimensionless Reynolds equation

$$\frac{\partial}{\partial X}(\epsilon\frac{\partial P}{\partial X}) + \frac{\partial}{\partial Y}(\epsilon\frac{\partial P}{\partial Y}) - \frac{6\eta_0 U R^2}{a^3 p_h}\frac{\partial H}{\partial X} = 0 \tag{B.11}$$

where

$$\epsilon = H^3 e^{-\alpha P p_{max}} \tag{B.12}$$

Using the Reynolds equation to investigate tribology on the scale of surface microgeometry has several problems. It is uncertain whether continuum mechanics are applicable to sub-micron film thicknesses. If the molecular length of the lubricant is within the order of the film thickness it may not be appropriate to treat the fluid as a continuum.

There may also be shortcomings in the model from not taking intramolecular attraction into account. At separations significantly less than a nanometre the two surfaces would begin to be attracted by strong intramolecular forces. If the surfaces approach to molecular-scale separations there will be significant forces acting on each surface other than from the lubricant and the Reynolds equation will not be valid.

An additional limitation of the Reynolds equation in the current investigation is the simplification of Newtonian fluid behaviour. It is well known that a boundary layer (normally a few molecules thick) forms on each surface through either chemical reaction or molecules of the fluid being physically absorbed into surface pores. This boundary layer may significantly influence micron-scale lubricant flow if the film becomes sufficiently thin to allow the two boundary layers to interact.

The boundary layers could provide an alternative means of load support and friction generation if full EHL conditions are not satisfied. If there is significant direct contact between the two surfaces part of the load will be transferred through contact stress instead of fluid pressure. In this case there will be adhesive bonding between the two boundary layers on the contacting surfaces. Shearing of the boundary layers in contact regions would contribute to total friction in addition to the viscous shear stress from the fluid. Boundary lubrication is expected to occur if the film becomes sufficiently thin to allow direct contact of the boundary layers or if there is insufficient fluid to maintain a full film.

B.5.1.4 Numerical method for solving Reynolds equation

The dimensionless Reynolds equation (equation (B.11)) is discretised using a central difference method as

$$\frac{1}{h_x^2}(\epsilon_{i-\frac{1}{2},j}(P_{i-1,j} - P_{i,j}) + \epsilon_{i+\frac{1}{2},j}(P_{i+1,j} - P_{i,j}) + \epsilon_{i,j-\frac{1}{2}}(P_{i,j-1} - P_{i,j}) + \epsilon_{i,j+\frac{1}{2}}(P_{i,j+1} - P_{i,j}) - \frac{1}{2h_x}\frac{6\eta_0 U R^2}{a^3 p_h}(H_{i+1,j} - H_{i-1,j})) = 0 \tag{B.13}$$

Outside the Hertzian contact zone the discretised equation is solved using Gauss-Seidel iteration. With this method the pressure values are continuously updated as the matrix of

pressure values is swept through according to

$$P_{i,j} = \frac{1}{\epsilon_{i-\frac{1}{2},j} + \epsilon_{i+\frac{1}{2},j} + \epsilon_{i,j-\frac{1}{2}} + \epsilon_{i,j+\frac{1}{2}}}(\epsilon_{i-\frac{1}{2},j}P_{i-1,j} + \epsilon_{i+\frac{1}{2},j}P_{i+1,j} + \epsilon_{i,j-\frac{1}{2}}P_{i,j-1} + \epsilon_{i,j+\frac{1}{2}}P_{i,j+1} - \frac{3h_x\eta_0 UR^2}{a^3 p_h}(H_{i+1,j} - H_{i-1,j})) \quad \text{(B.14)}$$

A relaxation factor is applied to the pressure results obtained from equation (B.14) to update the pressure values at the previous iteration. The standard successive overrelaxiation method is used with a factor of 0.4 for most of the simulations carried out. The relaxation scheme used is described by

$$P_{i,j}^{n+1} = K_{rel}P_{i,j}^{new} + (1 - K_{rel})P_{i,j}^{n} \quad \text{(B.15)}$$

Inside the dry contact region Jacobi iteration is used with a distributive relaxation scheme applied to the results. The Reynolds equation is discretised in the same manner as outside the Hertzian region (equation (B.13)) and a similar solution procedure was used. The new pressure values are calculated in a similar manner to the Gauss-Seidel method in equation (B.14), although the pressure values used in the calculations are not continuously updated as the spatial positions were swept through.

The new pressure distribution calculated from Jacobi is then subject to a distributive relaxation procedure. The new pressure at each node is calculated from taking an average of the pressure changes calculated from Jacobi at the neighbouring nodes

$$\overline{P}_{i,j} = \overline{P}_{i,j} + \delta_{i,j} - \frac{1}{4}(\delta_{i+1,j} + \delta_{i-1,j} + \delta_{i,j+1} + \delta_{i,j-1}) \quad \text{(B.16)}$$

After distributive relaxation is applied, the new pressure distribution from equation (B.16) is further relaxed against the previous iteration to calculate the pressure distribution. This method of relaxation is similar to the underrelaxation with the Gauss-Seidel solution (equation (B.15)), although a different relaxation coefficient was used (0.2 for most conditions).

B.5.2 Combined iterative procedure

Once the new pressure distribution is calculated from the combined Gauss-Seidel and Jacobi distributive relaxation methods, a new film thickness profile is calculated from equation (B.4). The film thickness from the previous iteration is then updated according to the relaxation relationship

$$H_{new} = H_{old} + K_H(H - H_{old}) \quad \text{(B.17)}$$

A relaxation factor K_H of 0.05 was found to be suitable for most of the investigation.

The film thickness is iterated with each new pressure distribution until the changes in fluid pressure between different iterations in the outer loop fall within the convergence tolerance. For the overall loop a mean absolute change in dimensionless pressure P of 0.1×10^{-6} was used as the tolerance. The inner loop tolerance for the pressure distribution from a particular iteration of film thickness was set as 5×10^{-6} of the mean proportional change in fluid pressure at each node.

B.5.3 Values of simulation parameters and range of independent variables

Results were produced adjusting the relative speed and deflection about an operating point of 10 mm/s and 30 nm deflection. The relative speed was varied between 5 mm/s and 100 mm/s while maintaining a constant deflection of 30 nm. The deflection was also varied between 20 and 50 nm for a constant relative speed of 10 mm/s. An asperity radius of 1 μm was assumed to correspond with the value taken in the GW integration procedure in section B.7. A mesh of 121 nodes in both X and Y directions was used with equal spacing between adjacent nodes. The fluid domain was simulated as extending four times the Herzian contact radius from the centre of contact in both X and Y directions. Power law relationships were determined for the friction coefficients and additional load from least-squares curve fitting to the data points.

An additional set of simulations was carried out maintaining an approximately constant load at the operating point and varying the relative speed between 5 mm/s and 100 mm/s. The deflection was varied to maintain a constant load according to equation (B.18). This enabled a loading of $\pm 10\%$ of the operating point to be maintained for a range of deflections. The loading was also varied for a particular relative speed of 10 mm/s. Least-squares curves were fitted for a power law relationship between loading and friction coefficient.

B.6 Results for single asperity EHL

The relationships obtained for the effect of deflection and sliding speed variation on additional load and friction coefficient are

$$\left(\frac{P}{Pmax} - 1\right) = 29.0 L^{2.59} \left(\frac{\delta}{R}\right)^{-1.15} \tag{B.18}$$

$$\mu = 7.01 L^{1.57} \left(\frac{\delta}{R}\right)^{-0.408} \tag{B.19}$$

And for loading and sliding speed on friction coefficient

$$\mu = 0.2388 L^{1.55} w^{-0.3039} \tag{B.20}$$

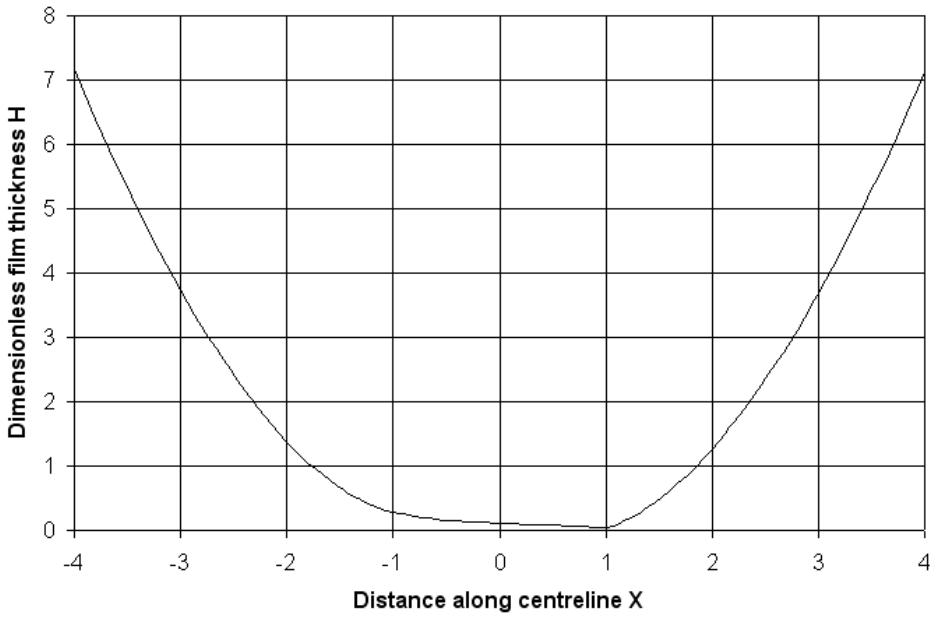

Figure B-1: Centreline dimensionless film thickness at operating point $\delta = 30$ nm, u=10 mm/s

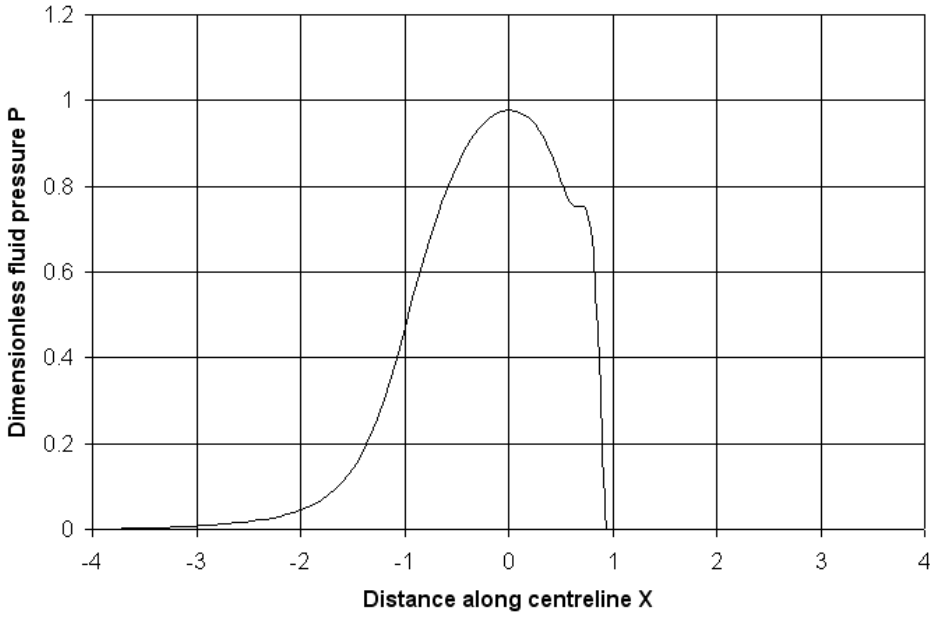

Figure B-2: Centreline dimensionless fluid pressure at operating point $\delta = 30$ nm, u=10 mm/s

The relationship between friction coefficient and lubrication parameter (equation (B.20))

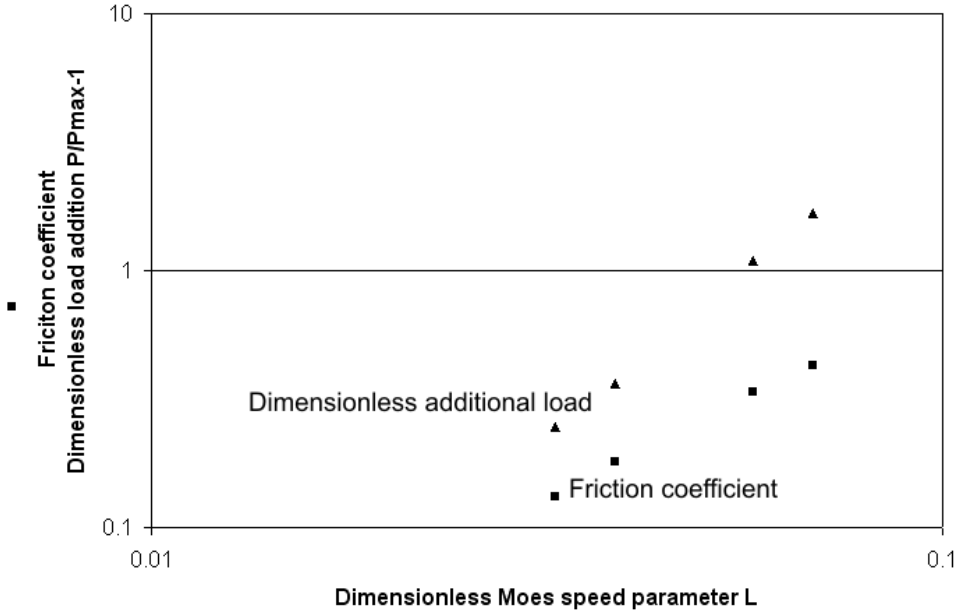

Figure B-3: Dimensionless load addition and friction coefficient for varying Moes speed parameter

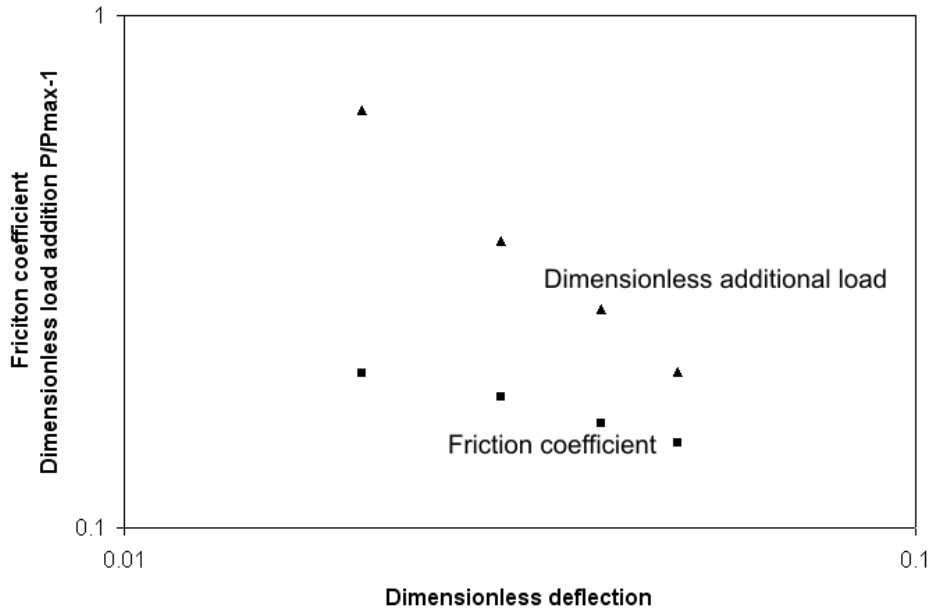

Figure B-4: Dimensionless load addition and friction coefficient for varying deflection

indicates there to be a $u^{0.388}$ relationship between sliding speed and friction coefficient for an unvaried load. The measurements from the seal test rig (figure 2-18 showing friction at

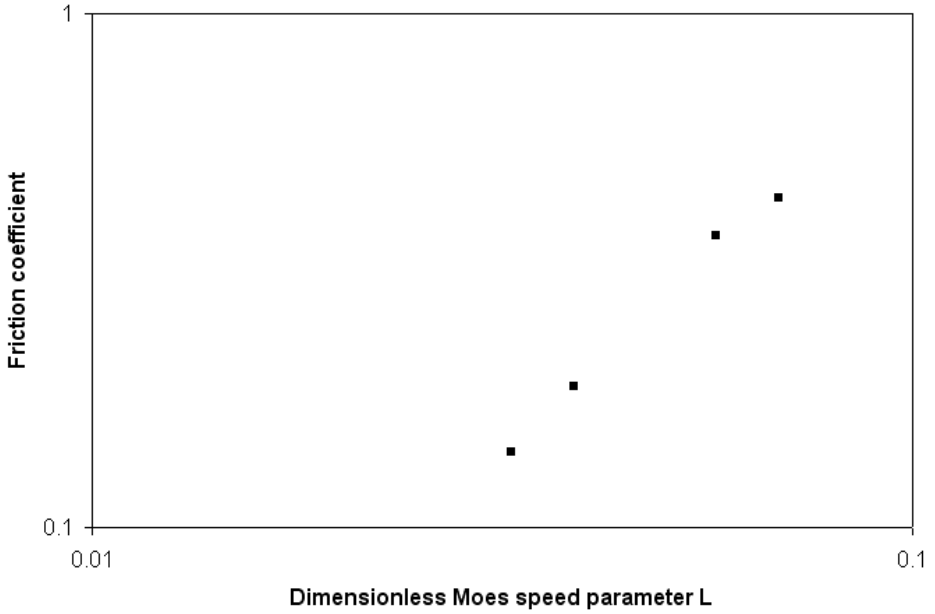

Figure B-5: Friction coefficient for varying Moes speed parameter

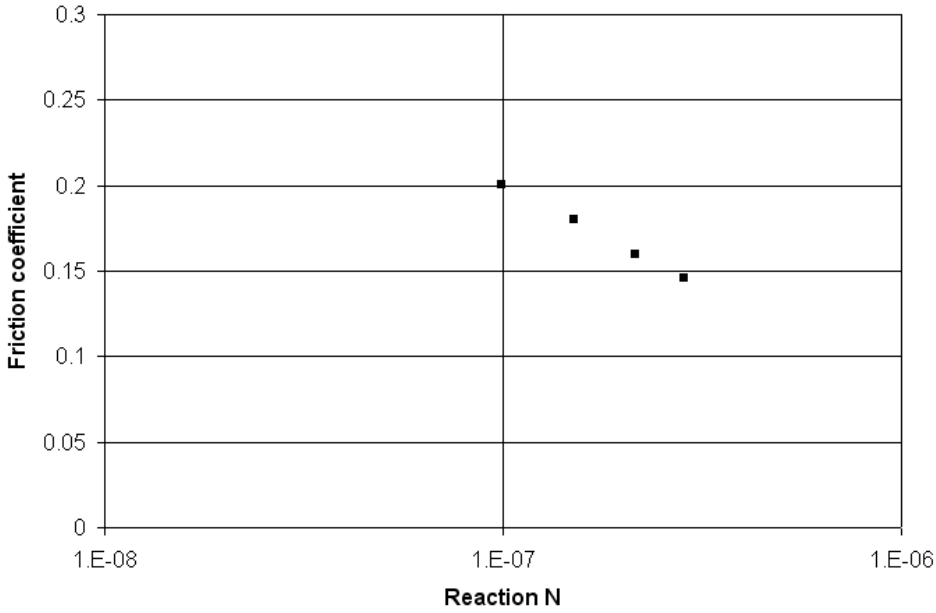

Figure B-6: Friction coefficient for varying load

80 bar sealed pressure being typical) indicate there to be no general positive relationship between friction and speed over the service range of sliding velocities. If EHL simulation is to

provide physically realistic results for velocity-dependence a near-zero or negative power law between friction coefficient and lubrication parameter be required in equation (B.20). A $u^{0.388}$ dependence of friction coefficient does not offer much of an improvement in experimental agreement compared with the inverse EHL simulations. Both $u^{0.388}$ and $u^{0.5}$ power laws produce large increases in friction over the four orders of magnitude of speed range which are not observed in practice. It is considered whether the velocity-dependence of friction could be reduced by integrating the results over a particular asperity distribution in section B.7.

Equation (B.20) also suggests the friction coefficient to decrease with increasing loading. For this relationship a power law of -1 would indicate friction to be invariant with loading while a power law of zero would suggest an abidance to Coulomb's friction law of load being proportional to friction. The -0.304 value for the power law suggests the friction to increase significantly with loading, although not as highly as under a Coulomb friction model. A single power law may not be an appropriate relationship for modelling the effects of loading on seal friction for the complete range of loadings experienced during service. At high sealed pressures asperity interaction is expected to become important as the real area of contact begins to saturate. A single asperity lubrication model that does not consider asperity interaction is less likely to be physically accurate at higher sealed pressures. For the seal material in the current study asperity interaction is expected to become significant above a few tens of bar of sealed pressure where the $p << E$ condition is not satisfied.

Equations (B.18) and (B.19) describe the variation in loading and friction coefficient with respect to the deflection of the body under dry Hertzian conditions. Expression of the friction and load dependence in this form is used to calculate the effective loading-friction and speed-friction relationships for a particular distribution of asperities in section B.7. A particular height distribution of the asperity peaks is assumed in this model with a corresponding distribution of asperity deflections. For this rough surface model it is relatively straightforward to introduce the EHL simulation results where the friction and loading were functions of deflection.

Figure B-2 indicates there to be a small region near the outlet where the fluid pressure becomes significantly greater than the Hertzian pressure distribution at the corresponding location. Near this location there is known to usually be a pressure spike as a result of the pressure-dependence of fluid viscosity. Variation in fluid viscosity is known to be less significant than in most previous point-contact investigations due to the lower maximum pressures associated with deflecting the body. This may explain why the pressure gradient on the positive velocity axis never becomes positive in the pressure spike region while most previous studies report a pronounced spike.

Inspection of the centre-line film thickness distribution at the operating point (figure B-1) indicates there to be significant variation in the film thickness across the Hertzian region while many previous studies report a near-constant film thickness in this region. There are

two possible explanations for this occurrence. Firstly, most previous studies have considered situations where large increases in fluid viscosity take place inside the high pressure region. Grubin suggested the fluid pressure approximates to the Hertzian pressure distribution where the fluid viscosity tends to high values and under these conditions the film thickness is approximately uniform. At high viscosities the speed-dependent Couette term in the Reynolds equation dominates over the pressure-dependent Poiuseulle term and necessitates a near-uniform film thickness to maintain flow continuity. For the lower viscosity changes in the current study there may be expected to be a greater influence of fluid pressure on flow in the thinner film region, hence less uniform film profiles. It is also possible that, as the current study has unusually high sliding speeds relative to the asperity dimensions, this may increase the sensitivity of the pressure distribution to changes in sliding velocity and lower the effective loading.

B.7 Integration of point-contact results over rough surface

B.7.1 Overview

A novel approach has been considered for the effective friction of a rough surface where the mechanism of friction is characterised by the point-contact EHL of surface asperities. This analysis is based on the GW asperity contact theory described in section 4.2.2. GW contact theory is used to estimate the contact fraction and effective loading corresponding with different mean surface separations for static conditions. The standard contact theory is modified to include effects of the changes in loading and shear stress that would occur if a lubricating fluid becomes entrained underneath the asperities. Friction and loading at each contacting asperity are assumed to be determined by the relationships from the point-contact EHL analysis in section B. The EHL friction and loading of each asperity is then integrated over the expected distribution of asperity contacts according to the normally distributed asperity heights in GW theory. This produces the effective friction and loading from EHL effects associated with particular mean surface separations.

Integrating point-contact EHL with GW contact theory offers a method for exploring how fluid entrainment underneath asperities and its effects on friction could be modelled. If the simulation results were to show similar trends to the measured seal friction under certain operating conditions this may be indicative of micro-EHL taking place at the asperity peaks and being a dominant source of friction generation. The integration over a particular asperity distribution may have been expected to negate particular characteristics of the load-dependent behaviour of a single asperity, possibly improving the physical realism of the single asperity EHL results. This is the case in standard GW theory where the real contact area of a single asperity varies with loading as $w^{\frac{2}{3}}$, while with a more physically accurate w^1 following

the integration over an asperity distribution. Additionally, it is considered whether this EHL approach to friction from asperity contact could be used to improve the experimental agreement of the results from the GW-average Reynolds simulations in section 5.2.6.

B.7.2 Friction coefficient from GW integration

Modifications were made to the GW contact model in order to incorporate the relationships between sliding speed, deflection, loading and friction obtained from point contact EHL. The loading of a single asperity for a particular deflection in the unmodified GW model is given by Hertzian contact theory in equation (4.5). For the EHL simulations of a single asperity a relationship between this Hertzian load, operating conditions, the normal load from fluid pressure was produced (equation (B.18)). The loading for a single asperity under EHL conditions (g_{EHL}) can be expressed in a form similar to that in standard GW theory as

$$g_{EHL} = \frac{4}{3}\frac{E}{(1-\nu^2)}\left(\frac{P}{P_{max}} - 1 + 1\right) R^{\frac{1}{2}}\delta^{\frac{3}{2}} \tag{B.21}$$

The corresponding friction from fluid shear stress for a contacting asperity is

$$S_{EHL} = \mu g_{EHL} \tag{B.22}$$

Where the friction coefficient μ is a function of the deflection and sliding speed as defined by equation (B.19) from the point-contact EHL analysis. The friction and reaction forces for a particular asperity deflection are then combined with the probability density function for the location of the asperity peaks to give the effective friction and load for a normal distribution of asperity peaks. Carrying out the integration procedure for the GW contact model described in section 4.2.2 produces the relationship for effective contact pressure

$$P_c = \frac{4}{3}\frac{1}{(1-\nu^2)}\hat{\sigma}^{\frac{3}{2}}\frac{1}{\sqrt{2\pi}}\int_H^\infty \left(29.02L^{2.5866}\left(\frac{\sigma_h\,(Z-H)}{R}\right)^{-1.1506} + 1\right)(Z-H)^{\frac{3}{2}}e^{-\frac{Z^2}{2}}dZ \tag{B.23}$$

The effective friction force for the rough surface is obtained similarly by using the EHL relationship for shear force (equation (B.22)) instead of the normal force in the substitution into equation (B.21). This effective friction is

$$S_{EHL} = \frac{4}{3}\frac{1}{(1-\nu^2)}\hat{\sigma}^{\frac{3}{2}}\frac{1}{\sqrt{2\pi}}\int_H^\infty 7.011L^{1.5652}$$
$$\left(\frac{\sigma_h\,(Z-H)}{R}\right)^{-0.408}\left(29.02L^{2.5866}\left(\frac{\sigma_h\,(Z-H)}{R}\right)^{-1.1506} + 1\right)(Z-H)^{\frac{3}{2}}e^{-\frac{Z^2}{2}}dZ \tag{B.24}$$

The effective friction coefficients were calculated for a range different sliding speeds between 0.1 mm/s and 300 mm/s corresponding with the experimental range of rod velocities. Each of these sliding speeds were simulated for mean dimensionless surface separations H between zero and three times the RMS asperity height. This allows the relationship between sliding speed, surface separation and effective friction coefficient to be visualised for the single asperity EHL version of the GW contact model. Values of roughness parameters corresponding with the mixed GW-average Reynolds simulations in section 5.2.1.3 were assumed.

The effective friction coefficient for asperity EHL is integrated over the expected contact distribution for the single-lip seal in order to predict the seal friction characteristics. A contact pressure distribution corresponding with the single-lip seal at 80 bar sealed pressure (figure 4-11) was used for the analysis. Initially, the simulated distribution of total pressure between the rod and seal was assumed to be produced through the mechanism of EHL-induced pressure increases underneath the contacting asperities. The fluid between the rod and seal outside regions of asperity contact was assumed to be at ambient pressure, making no contribution to the total effective pressure acting on the seal. For each rod speed the shear stress corresponding to the normal pressure at each node was calculated from the relationships obtained between pressure, shear stress and lubrication parameter in equations (B.23) and (B.24).

The simulation results from the mixed lubrication GW-average Reynolds contact model were integrated with the friction coefficients obtained for point-contact EHL of rough surfaces. In this approach the asperity friction coefficient (assumed to have a constant value in the GW-average Reynolds analysis in section 5.2) is assumed to be variable according to the rough surface EHL relationship in equation B.23. The GW-average Reynolds simulation was solved for a single-lip seal with a sealed pressure of 80 bar over a range of sliding speeds and the converged fluid and asperity contact pressures obtained for each sliding velocity. During postprocessing the asperity contact pressure P_c is assumed to be equivalent to the effective pressure load experienced by the asperities through EHL lubrication. This contact pressure is converted to a corresponding shear stress according to B.24 at each node along the contact length to give the shear stress distribution. The fluid shear stress is then numerically integrated along the contact length with respect to this displacement to obtain the overall friction.

B.7.3 Results from GW-point-contact EHL simulations

Figure B-7 shows the effective friction contributions for integrating the relationships from point-contact EHL over a normal distribution of asperity heights. The results show there to be a positive linear relationship between mean surface separation and friction coefficient with a moderate change in friction coefficient taking place over the range of separations and

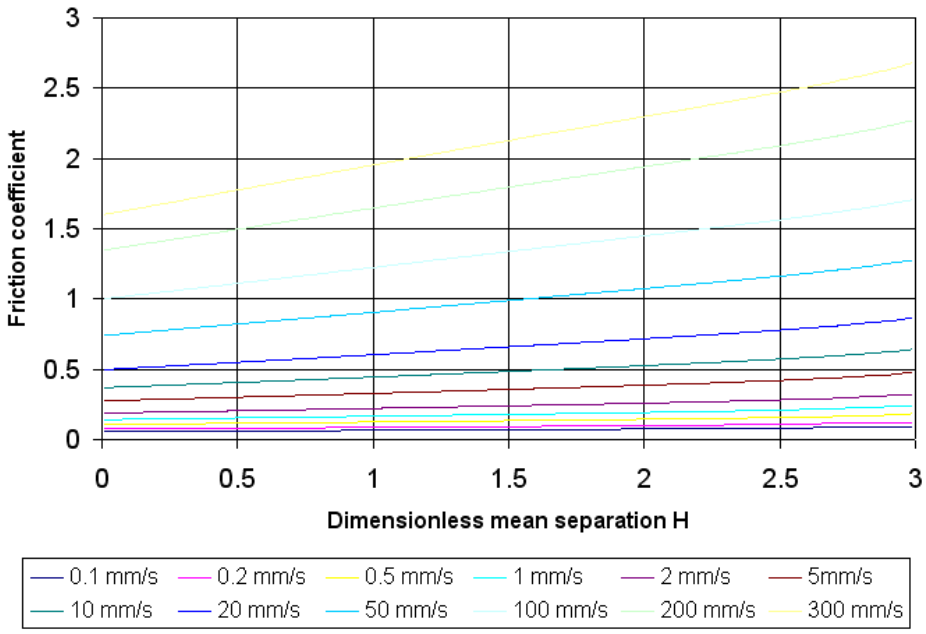

Figure B-7: Friction coefficients for integration of point-contact EHL results over GW asperity contact model

loading. This indicates there to be a small reduction in friction coefficient at higher loading, although the decrease is not sufficient to explain the saturation in friction levels that has been reported in hydraulic seals at higher pressures. There also remain significant increases in friction coefficients with sliding speed. A power law of approximately $u^{0.43}$ exists between sliding speed and friction. This suggests the integration over the roughness distribution does not significantly reduce the speed dependence of friction that limits the physical accuracy of the single-asperity EHL model.

Combining the EHL friction coefficients for a rough surface with a seal geometry pressure distribution produces the friction results shown in figure B-8. A similar power law relationship exists between friction and sliding speed compared with the single asperity and general rough surface. The velocity-dependence of friction is approximately independent of loading for the all analysis based on the EHL of a single asperity. As a result similar friction-speed Stribeck curves would be expected for alternative seal geometries and sealed pressures. The experimental friction results show much lower velocity dependence than the simulations and a negative relationship between friction and speed, indicating the modelling technique not to predict physically realistic results for sealing applications. This suggests single-asperity EHL not to be a dominant source of friction in hydraulic seals.

Using the EHL friction coefficients as an alternative for the asperity contact friction coefficient in the GW-average Reynolds simulations further reduces the experimental agreement.

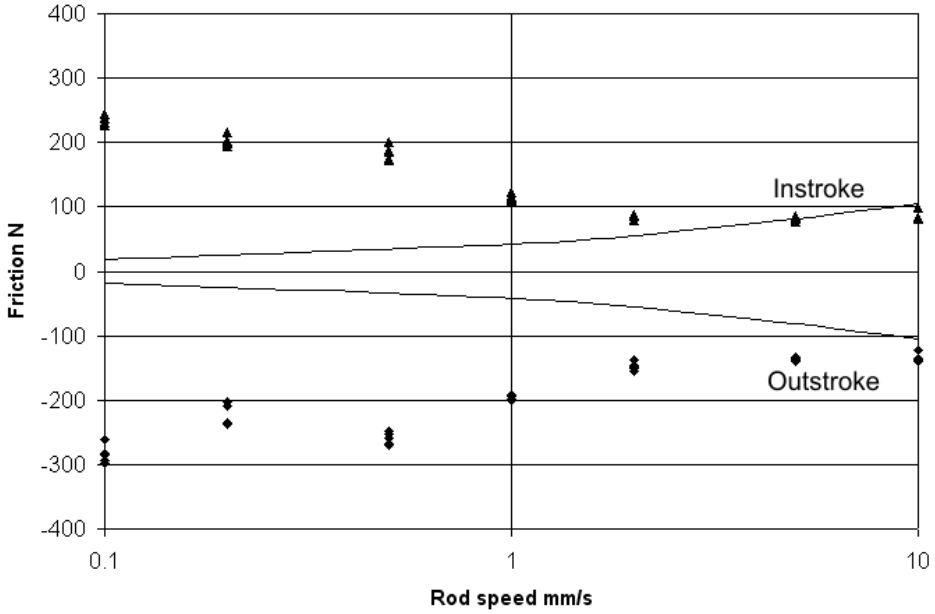

Figure B-8: Simulated seal friction with friction coefficient function from GW point-contact model, single-lip seal, 80 bar sealed pressure

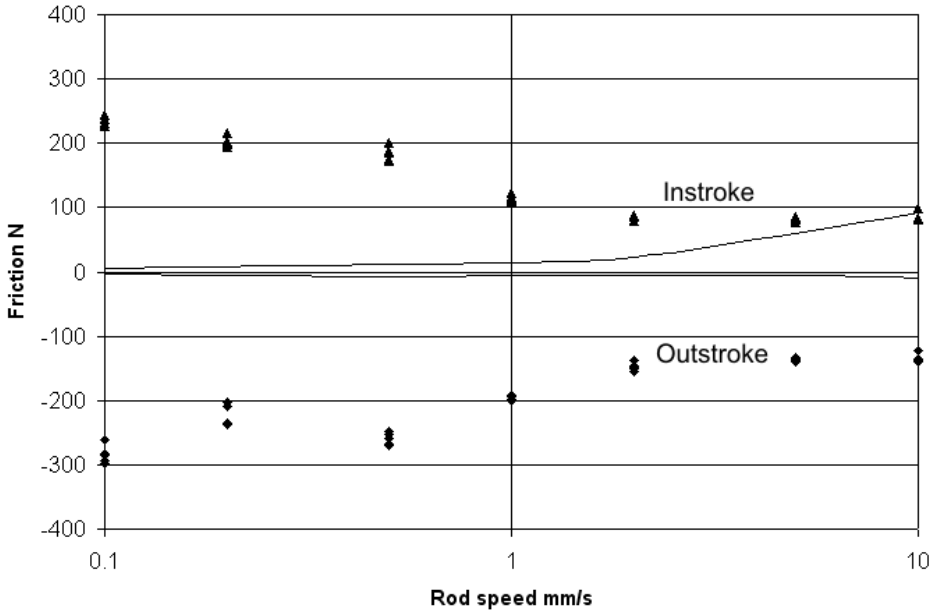

Figure B-9: Simulated seal friction for GW-average Reynolds with friction coefficient function from GW point-contact model, single-lip seal, 80 bar sealed pressure

Figure B-9 shows the results of using the variable friction coefficient for the asperity contact in simulations of a single-lip seal. There is no improved agreement in the relative levels of instroke and outstroke friction as the friction coefficient experiences only minor decreases at higher loadings. The EHL-based trend of increasing friction with sliding speed reduces the experimental agreement by introducing this relationship into the simulation while no significant positive relationship between speed and friction is observed in practice.

There are several possible explanations for the poor experimental agreement between the single-asperity EHL simulations and the seal friction measurements. Whether the lubricant behaves as a Newtonian fluid at the micron-scale dimensions associated with the asperities is discussed in section B.5.1.2. The main limitation could be the presence of a boundary layer of fluid at each of the contacting surfaces which may resist motion in regions of narrow films.

Limitations of the point-contact assumptions of non-interacting hemispherical contacts are discussed in section 4.2.3.3. In this analysis it is shown that the GW model may not be appropriate for hydraulic sealing applications due to the high loading conditions where significant contact fractions and asperity interaction are expected. Any theory based on no interaction between asperities is likely to have its accuracy limited to lower sealed pressures in hydraulic sealing applications.

Appendix C

Housing blocks for passive and active seal test rigs

C.1 Rod seal housing block for passive seal

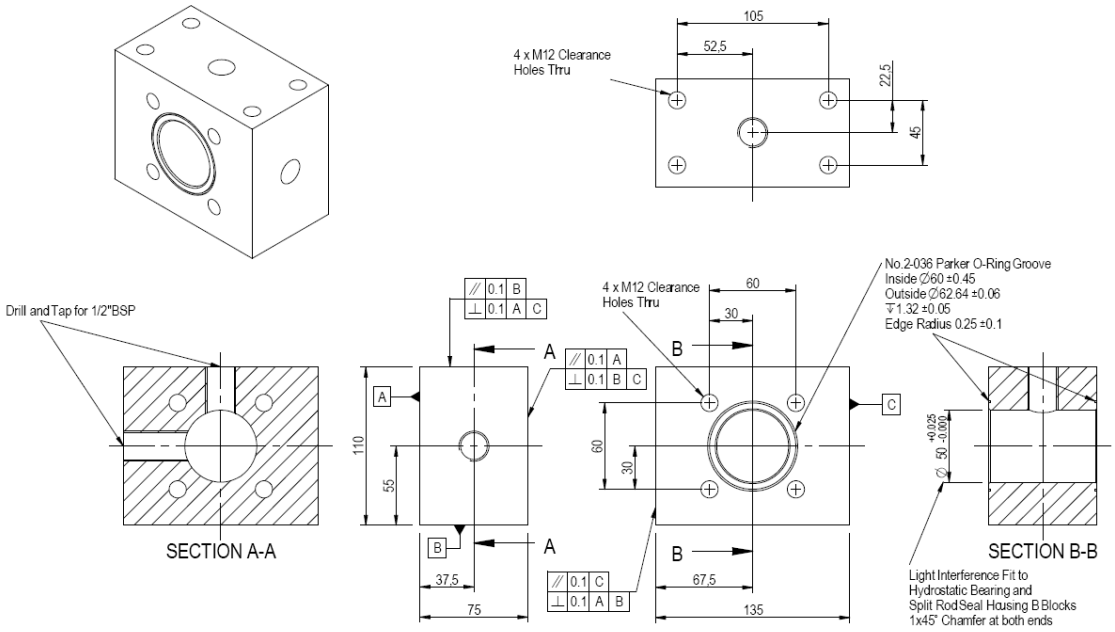

Figure C-1: Central housing block enclosing main sealed region

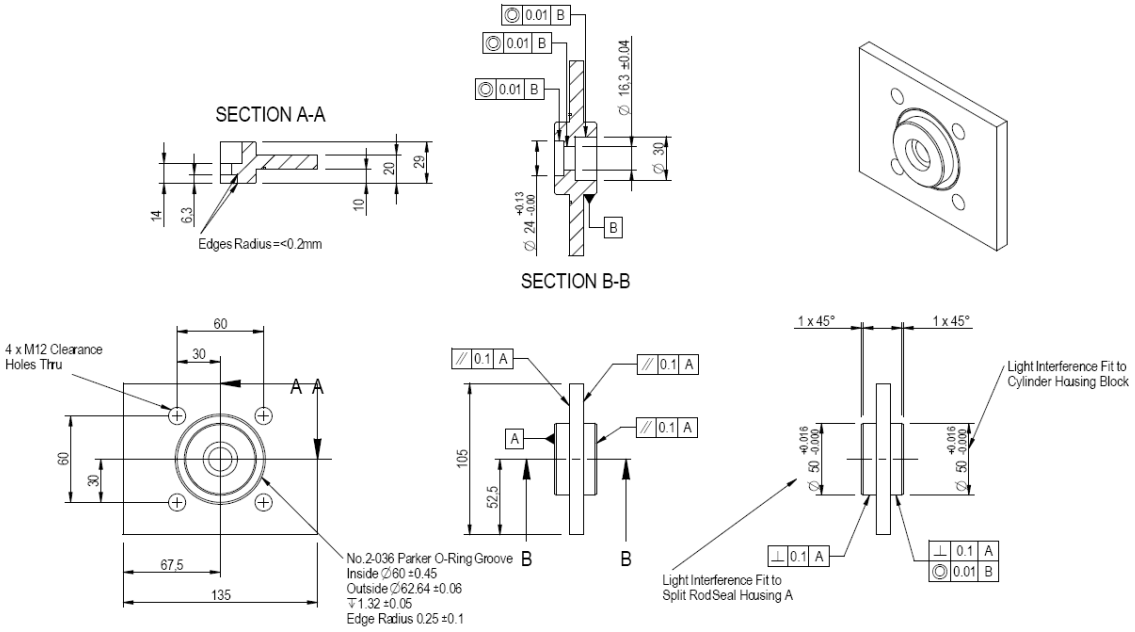

Figure C-2: Internal housing block containing groove for rod seal

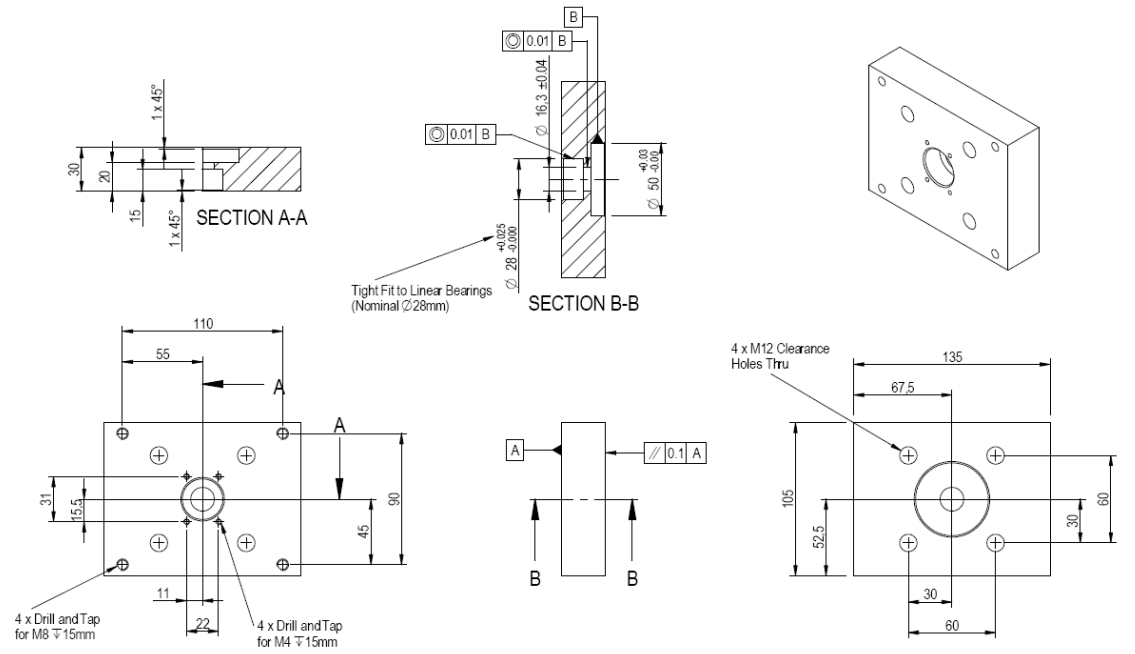

Figure C-3: End housing block forming one of the faces of the seal groove

C.2 Seal housing block for active seal with double-lip sealing element

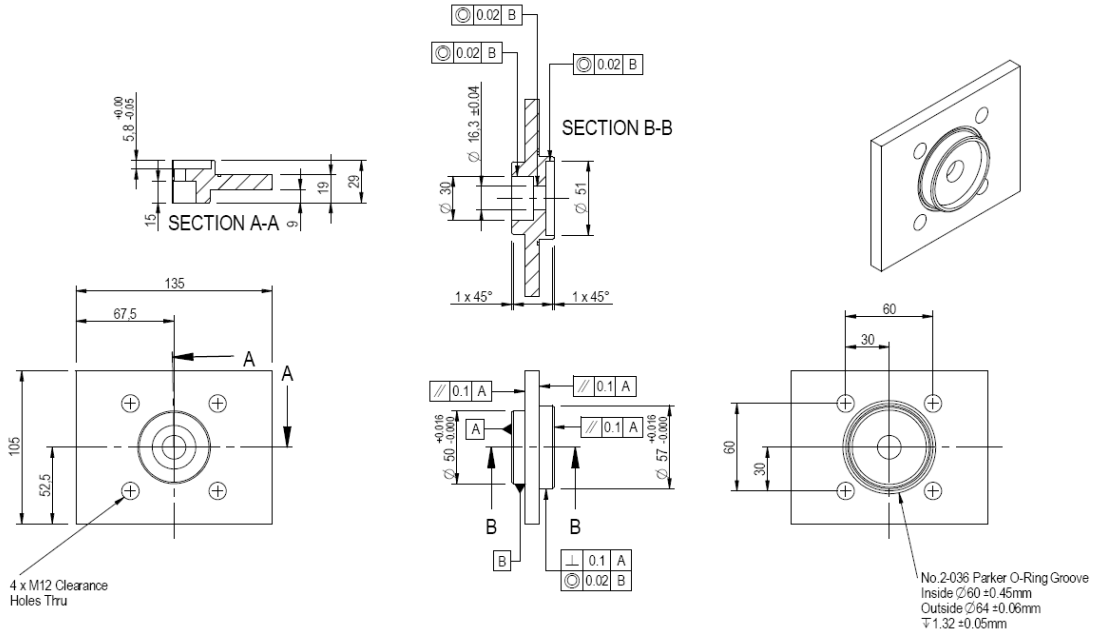

Figure C-4: Internal housing block forming one of the faces of the seal groove in active seal assembly

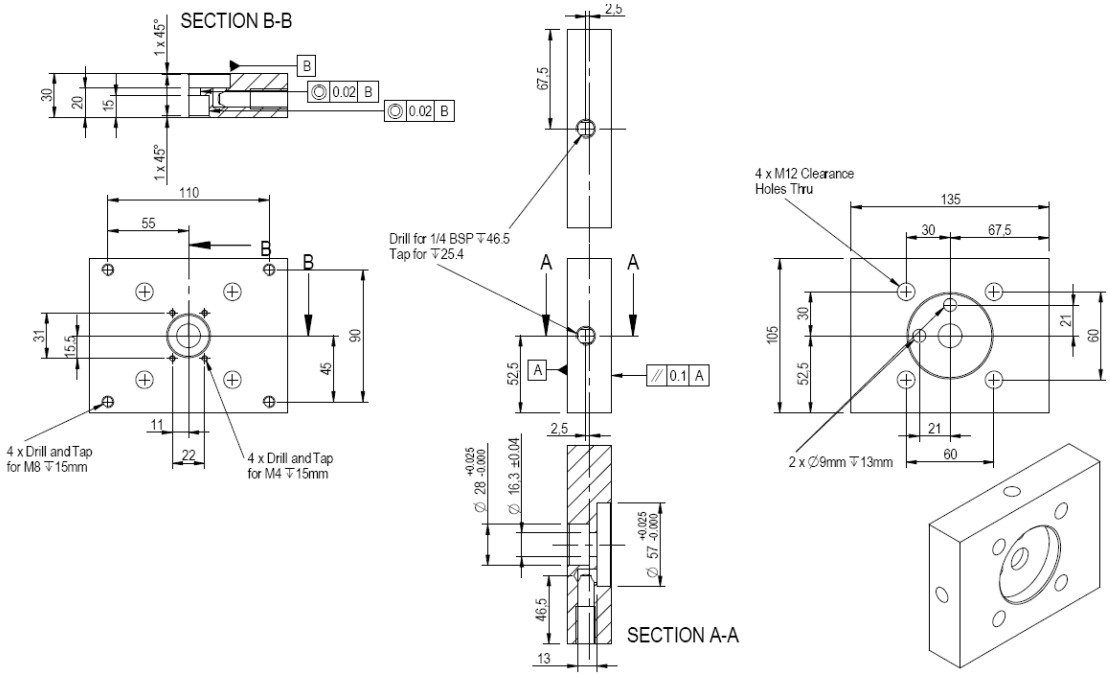

Figure C-5: End housing block containing seal groove in active seal assembly

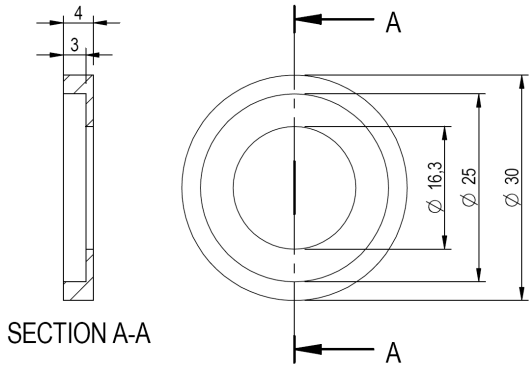

Figure C-6: Additional housing component to provide radial constraint to double-lip seal in active seal assembly

C.3 Seal housing block for active seal with rectangular-section sealing element

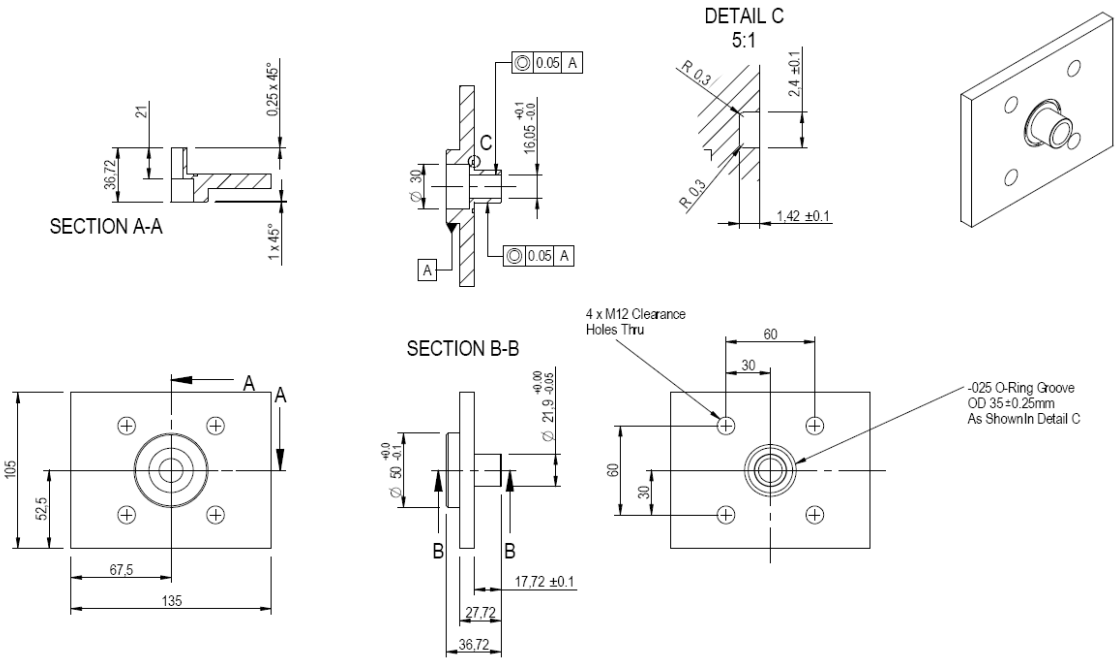

Figure C-7: Internal housing block for active seal assembly with square o-ring sealing element

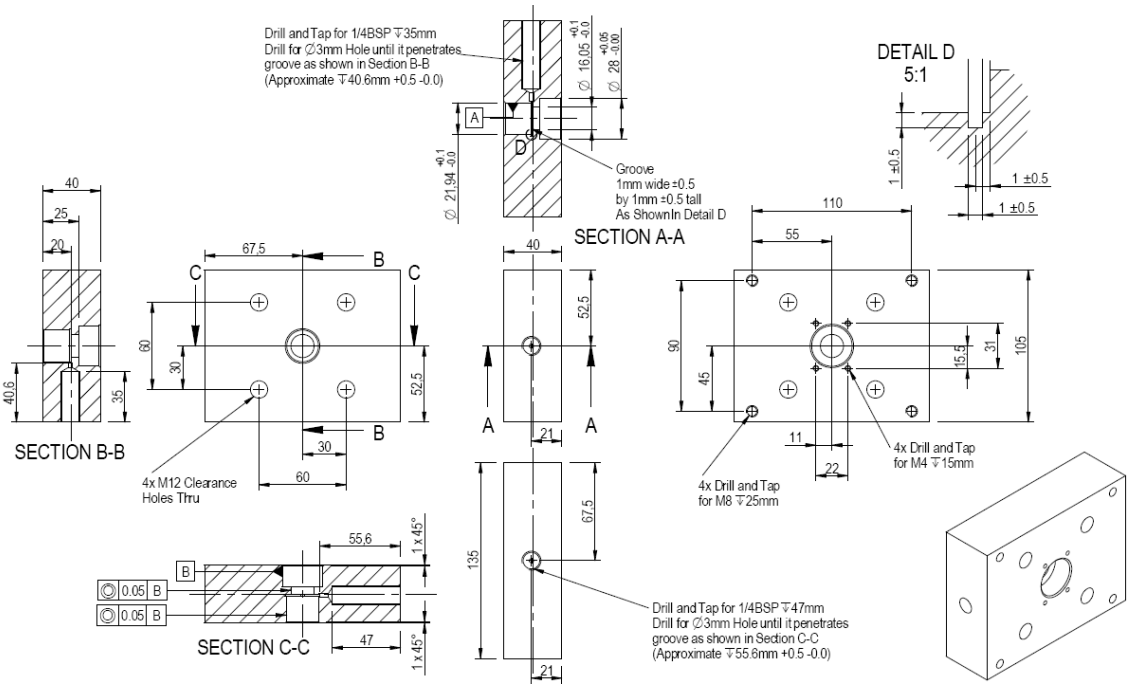

Figure C-8: End housing block for active seal assembly with square o-ring sealing element